Searching for neutrinoless double-beta decay of germanium-76 in the presence of backgrounds

Alexis G. Schubert

A dissertation submitted in partial fulfillment of
the requirements for the degree of

Doctor of Philosophy

University of Washington

2012

Reading Committee:

John F. Wilkerson, Chair

Jason A. Detwiler

Nikolai R. Tolich

Program Authorized to Offer Degree:
Department of Physics

University of Washington

Abstract

Searching for neutrinoless double-beta decay of germanium-76
in the presence of backgrounds

Alexis G. Schubert

Chair of the Supervisory Committee:
Professor John F. Wilkerson
Physics

The neutrino, an elementary particle, has been the subject of experimental investigation for over 50 years. Recent experiments have shown that neutrinos have mass and oscillate, but questions about fundamental properties of the neutrino remain. The observation of neutrinoless double-beta decay ($0\nu\beta\beta$) could determine whether lepton number is violated, discover whether the neutrino is its own antiparticle, and provide information about the absolute scale of neutrino mass. The MAJORANA Collaboration will search for $0\nu\beta\beta$ of germanium-76 in an array of germanium detectors. Previous experiments indicate that the half life of this decay mode is greater than 10^{25} years. To be sensitive to this rate, MAJORANA must construct an ultra-low-background detector. MAJORANA is building the DEMONSTRATOR, a 40-kg detector array, at the Sanford Underground Research Facility in Lead, South Dakota.

The $0\nu\beta\beta$ of ^{76}Ge would produce ^{76}Se and two electrons with 2039 keV of energy. The physics reach of the DEMONSTRATOR will be determined by the background count rate in a 4-keV energy region surrounding the 2039-keV Q-value. MAJORANA has a background goal of less than three counts in the energy region of interest per tonne-year of DEMONSTRATOR exposure. Projections of the DEMONSTRATOR's sensitivity are determined from a background energy-spectrum model based on material assay data and Monte Carlo simulation results. Understanding and minimization of backgrounds is critical to the success of the

DEMONSTRATOR.

MAJORANA Collaborators operate a low-background detector in a shielded environment at the Kimballton Underground Research Facility near Ripplemeade, Virginia. The contents of the detector cryostat are well known, making it a good candidate for testing the MAJORANA background model. This dissertation describes the creation of a background energy-spectrum model for the Kimballton detector. Energy spectra measured with the detector at Kimballton are compared to results of the background model, and implications for the DEMONSTRATOR are explored.

TABLE OF CONTENTS

LIST OF FIGURES

LIST OF TABLES

GLOSSARY

$0\nu\beta\beta$: neutrinoless double-beta decay. A theorized process in which two protons in a nucleus are converted to two neutrons; two electrons and no neutrinos are emitted.

$2\nu\beta\beta$: two-neutrino double-beta decay. A process in which two protons in a nucleus are converted to two neutrons; two electrons and two neutrinos are emitted. This process has been observed for many nuclei, including ^{76}Ge.

BEGE: Broad-Energy Germanium detector; a p-type point-contact germanium diode detector produced by CANBERRA.

CLHEP: a Class Library for High Energy Physics. A set of physics-specific C++ libraries maintained by the Large Hadron Collider Computing Grid [1].

DAQ: data acquisition.

DAWN: Drawer for Academic WritiNgs; a renderer for visualization of 3D geometrical data. DAWN output can be produced from GEANT4 geometry models.

DEMONSTRATOR: an experiment of the MAJORANA Collaboration, searching for neutrinoless double-beta decay of ^{76}Ge using 40 kg of germanium detectors.

GAT: Germanium Analysis Toolkit; a library of C++ modules for processing ORCA and Monte Carlo results. Developed by the MAJORANA Collaboration and based on TAM and ROOT [2].

GEANT4: a C++ Monte Carlo toolkit for the simulation of particle interactions in matter [3], [4].

GERDA: GERmanium Detector Array; an experiment to search for double-beta decay of ^{76}Ge using germanium detectors in a liquid argon shield [5].

GSS: Generic Surface Sampler, a tool for uniformly sampling surfaces of volumes; part of MaGe [6].

ICP-MS: inductively coupled plasma mass spectrometry; a type of mass spectrometry.

KURF: Kimballton Underground Research Facility; an underground laboratory near Ripplemead, Virginia.

LN: Liquid Nitrogen.

MAGE: MAjorana-GErda software package; a C++ physics simulation software framework based on Geant4 and ROOT; jointly developed by Majorana and Gerda [7].

MAJORANA: a collaboration searching for neutrinoless double-beta decay of ^{76}Ge.

MALBEK: MAjorana Low-background BEGe at KURF; a modified low-background BEGe detector located in a shielded underground environment at KURF.

MGDO: MAjorana-GErda Data Objects; a library of C++ data objects for storage and analysis of Monte Carlo simulation results and DAQ data [8].

MJOR: MAjorana-ORCARoot. A Majorana C++ toolkit based on ROOT, ORCARoot, and MGDO. Used to write ORCA data into MGDO objects saved in ROOT files.

NERSC: National Energy Research Scientific Computing Center; a scientific computing center in Berkeley, California, for the U.S. Department of Energy's Office of Science.

ORCA: Object-oriented Real-time Control and Acquisition; a data-acquisition application developed at the University of North Carolina [9].

ORCAROOT: a ROOT-based C++ toolkit used to write ORCA data into ROOT files.

P-PC: P-type Point Contact; a type of germanium detector with a small (point-like) signal contact.

PDSF: Parallel Distributed Systems Facility; a networked distributed computer cluster at NERSC used for simulation and analysis.

ROOT: an object-oriented C++ framework for efficient storage and analysis of large amounts of data; developed for the high-energy physics community [10].

SURF: Sanford Underground Research Facility; a deep underground research laboratory in the Homestake Mine in Lead, SD.

TAM: Tree Analysis Modules; a modular framework for analysis of ROOT TTrees. Developed at MIT [11].

ACKNOWLEDGMENTS

So many people lent their time and expertise to help me. Thank you to everyone at CENPA for making the lab such a wonderful place to work and learn, especially John Amsbaugh, Greg Harper, Hamish Robertson, and Doug Will. I enjoyed many useful discussions about statistics and data analysis with Nikolai Tolich. Mike Miller, I appreciated your software expertise and advice. Jarek Kaspar, thanks for fixing so many things. Tom Burritt, it was greato work with you and see all of your beautiful designs for the Canary Cage and MAJORANA.

Thank you to everyone in the UNC ENPA group for being so helpful and welcoming. Mark Howe, thanks for responding so quickly to my requests and for being such a friendly presence at UW and UNC.

I'm grateful to everyone in MAJORANA for all of your feedback and help. David Radford, thanks for your advice about slow pulses, waveform processing, and germanium detectors. Kareem Kazkaz, I'm grateful for all of your help with the Clover detector. Dongming Mei, I'm glad you could share your expertise about neutron interactions with me.

Steve Elliott, Vic Gehman, and Vince Guiseppe, thanks for all of your help. I learned so much by working and corresponding with you. I enjoyed working with all of you on the Canary Cage and on MAJORANA. Steve, thank you for answering my questions so quickly and for your advice about all sorts of things.

Jonathan Leon, it's been excellent working with you. You're a wonderful officemate.

Jason Detwiler, thank you for teaching me so many things about C++, ROOT, and physics, and for being so patient while doing so. You've been an excellent mentor.

John Wilkerson, I'm grateful for so many things you've done for me. Thanks for always finding time to help me.

Mike Marino and Rob Johnson, it was excellent to be your officemates. It was great to work, learn, and travel with you.

Paddy Finnerty and Graham Giovanetti, I can't thank you enough. You did all of the dirty work at KURF, including bringing MALBEK to CANBERRA and collecting all of the data I could ask for. Your careful documentation and valuable input were so helpful. Graham, thanks for that ^{241}Am measurement. Paddy, writing software with you was excellent; it was great to collaborate with you. I enjoyed visiting UNC and working with you two. You were such gracious and entertaining hosts.

Michael, thanks for making everything fun.

DEDICATION

For my family.

Chapter 1

NEUTRINOLESS DOUBLE-BETA DECAY AND MAJORANA

1.1 Introduction

Observation of the neutrino has been a challenging task in experimental physics. First postulated in 1930, the neutrino avoided detection for over 25 years. Recent experiments involving solar, atmospheric, and reactor neutrinos have shown that neutrinos have mass and oscillate. These experiments determined the mass-squared differences between the three neutrino mass eigenstates and determined the mixing matrix relating neutrino mass and flavor eigenstates. Several questions about the neutrino remain:

- Is lepton number a conserved quantity?
- Is the neutrino its own antiparticle (a Majorana particle)?
- What is the absolute mass scale of the neutrino?
- What is the neutrino mass hierarchy?

The observation of a process called neutrinoless double-beta decay could answer these questions.

Double-beta decay is a nuclear process in which the number of protons in a nucleus increases by two, and the number of neutrons decreases by two. Double-beta decay has been observed to occur with the emission of two neutrinos, and may occur without neutrino emission. In the process of two-neutrino double-beta decay ($2\nu\beta\beta$), a nucleus, N, with Z protons and A nucleons decays by emitting two electrons (betas) and two antineutrinos:

$$N(Z,A) \Rightarrow N(Z+2,A) + e^- + e^- + \overline{\nu}_e + \overline{\nu}_e \tag{1.1}$$

Double-beta decay is observable when some nuclei with even numbers of protons and neutrons decay [12]. A diagram depicting this decay mode appears in Figure 1.1a. Unstable nuclei may undergo $2\nu\beta\beta$ if single β-decay is energetically forbidden or highly suppressed by conservation of angular momentum. This process has been observed in many nuclei and has a half-life on the order of 10^{19} to 10^{21} years. For $2\nu\beta\beta$ of ^{76}Ge, the spectrum of the sum of the electron energies is shown in Figure 1.2a. Experiments observing $2\nu\beta\beta$ are sensitive to the emitted electrons, and not the weakly interacting neutrinos, so the sum of electron energies is shown in the figure.

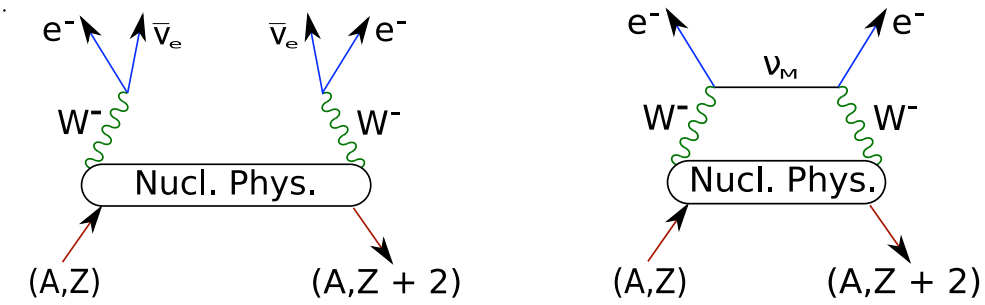

(a) (b)

Figure 1.1: Diagrams describing $2\nu\beta\beta$ (a) and $0\nu\beta\beta$ (b).

Neutrinoless double-beta decay ($0\nu\beta\beta$) is a process in which a nucleus decays by emitting two electrons and no antineutrinos:

$$N(Z, A) \Rightarrow N(Z + 2, A) + e^- + e^- \tag{1.2}$$

It is not known whether this decay mode exists. This process does not occur in the Standard Model of particle physics, and is forbidden by lepton number conservation. For this process to occur, the neutrino and antineutrino must be indistinguishable; the neutrino must be a Majorana particle. Since no neutrinos are emitted in this process, the sum of the energies of the emitted electrons is equal to the total energy released in the decay. A

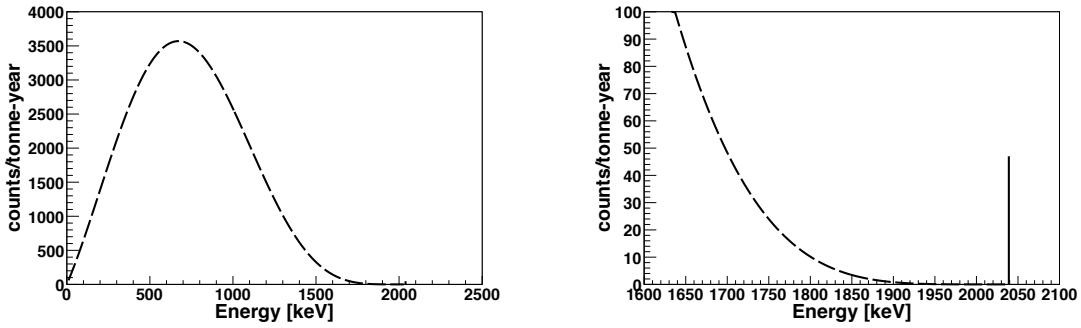

(a) (b)

Figure 1.2: Sum spectra of electron energies for $2\nu\beta\beta$ (dashed line) and $0\nu\beta\beta$ (solid line) in ^{76}Ge. The $0\nu\beta\beta$ peak is barely visible in the plot on the left; the plot on the right shows a closer view of the endpoint energy, 2039 keV. The $0\nu\beta\beta$ half-life is assumed to be 10^{26} years, approximately ten times the current lower limit. The two-neutrino double-beta decay spectrum was calculated using the Primakoff-Rosen approximation [12] for the $2\nu\beta\beta$ half-life of 1.5×10^{21} years [13]. Spectra are calculated for emitted electrons; detector resolution is not included. Rates are calculated for germanium enriched to 86% ^{76}Ge; there are 47 counts in the $0\nu\beta\beta$ peak and 3.2×10^6 counts in the $2\nu\beta\beta$ spectrum per tonne-year.

spectrum of the sum of the electron energies is shown in Figure 1.2b for $0\nu\beta\beta$ of ^{76}Ge, for an assumed value of the decay half-life.

Figure 1.1b describes $0\nu\beta\beta$ if the process is mediated by the exchange of a light Majorana neutrino. In this case, the decay half life is [12]:

$$\left[T^{0\nu}_{1/2}\right]^{-1} = G^{0\nu}(E_0, Z)\left|M^{0\nu}\right|^2 \langle m_{\beta\beta}\rangle^2 \tag{1.3}$$

$$= G^{0\nu}(E_0, Z)\left|M^{0\nu}_{GT} - \frac{g_V^2}{g_A^2} M^{0\nu}_F\right|^2 \langle m_{\beta\beta}\rangle^2 \tag{1.4}$$

In this expression, $G^{0\nu}$ is a calculable quantity which includes the phase space for the decay, E_0 is the Q-value of the decay, Z is the number of protons in the nucleus, $M^{0\nu}_{GT}$ and $M^{0\nu}_F$ are the Gamow-Teller and Fermi nuclear matrix elements, and g_V and g_A are the vector and axial-vector coupling constants.

The effective neutrinoless double-beta decay mass, $m_{\beta\beta}$, is described by the neutrino masses and neutrino mixing matrix:

$$\langle m_{\beta\beta}\rangle = |U_{e1}|^2 m_1 + |U_{e2}|^2 m_2 e^{i\phi_2} + |U_{e3}|^2 m_3 e^{i\phi_3} \tag{1.5}$$

$$= |\cos\theta_{12}\cos\theta_{13}|^2 m_1 + |\sin\theta_{12}\cos\theta_{13}|^2 m_2\, e^{i\phi_2} + |\sin\theta_{13}|^2 m_3\, e^{i\phi_3} \tag{1.6}$$

where U_{ei} are elements of the leptonic mixing matrix, m_i are the masses of the neutrino mass eigenstates, and ϕ_2 and ϕ_3 are the relative Majorana phases. The elements of the mixing matrix are described by three angles determined from neutrino oscillation experiments.

Oscillation experiments can also determine the mass-squared differences of the neutrino mass eigenstates. The current values are [14]:

$$\Delta m^2_{21} \equiv m^2_2 - m^2_1 = 7.50 \pm 0.20 \times 10^{-5}\ \text{eV}^2 \tag{1.7}$$

$$\left|\Delta m^2_{32}\right| \equiv \left|m^2_3 - m^2_2\right| = 2.32^{+0.12}_{-0.08} \times 10^{-3}\ \text{eV}^2 \tag{1.8}$$

$$\sin^2(2\theta_{12}) = 0.857 \pm 0.024 \tag{1.9}$$

$$\sin^2(2\theta_{23}) > 0.95\ (90\%\ \text{CL}) \tag{1.10}$$

$$\sin^2(2\theta_{13}) = 0.098 \pm 0.013 \tag{1.11}$$

The sign of Δm^2_{32} is unknown; m_3 may be more massive than m_1 and m_2 (normal hierarchy) or less massive than m_1 and m_2 (inverted hierarchy). The absolute scale of the masses is also unknown, although there are some constraints. The value of $m_{\beta\beta}$ described by Equation 1.5 is shown in Figure 1.3 as a function of the mass of the lightest neutrino, where the mixing matrix elements and other masses are taken from the values above. It is important to note that Figure 1.3 depends on the mechanism by which $0\nu\beta\beta$ proceeds. Observation of $0\nu\beta\beta$ could provide information about the absolute mass scale of neutrinos and the neutrino mass hierarchy.

To search for $0\nu\beta\beta$, one must obtain a candidate isotope and monitor it for decays of this mode. The most sensitive $0\nu\beta\beta$ searches to date have been performed with isotopes of germanium, ^{76}Ge, and xenon, ^{136}Xe. The Heidelberg-Moscow Collaboration set a limit of $T^{0\nu}_{1/2} > 1.9 \times 10^{25}$ years (90% CL) using ^{76}Ge [15]. The International Germanium Experiment (IGEX) set a similar limit of $T^{0\nu}_{1/2} > 1.6 \times 10^{25}$ years (90% CL) using ^{76}Ge [16]. A subset of the Heidelberg-Moscow Collaboration claimed observation of $0\nu\beta\beta$ with a half-life of $2.23^{+0.44}_{-0.31} \times 10^{25}$ years [17]. This result remains unconfirmed. The EXO-200 Collaboration set a limit using ^{136}Xe of $T^{0\nu}_{1/2} > 1.6 \times 10^{25}$ years (90% CL) [18]. Recently, KamLAND-Zen also set a limit using ^{136}Xe, $T^{0\nu}_{1/2} > 1.9 \times 10^{25}$ (90% CL) [19]. If $0\nu\beta\beta$ proceeds by the exchange of a light Majorana neutrino, the xenon results are in tension with the claim of $0\nu\beta\beta$ in ^{76}Ge [18] [19].

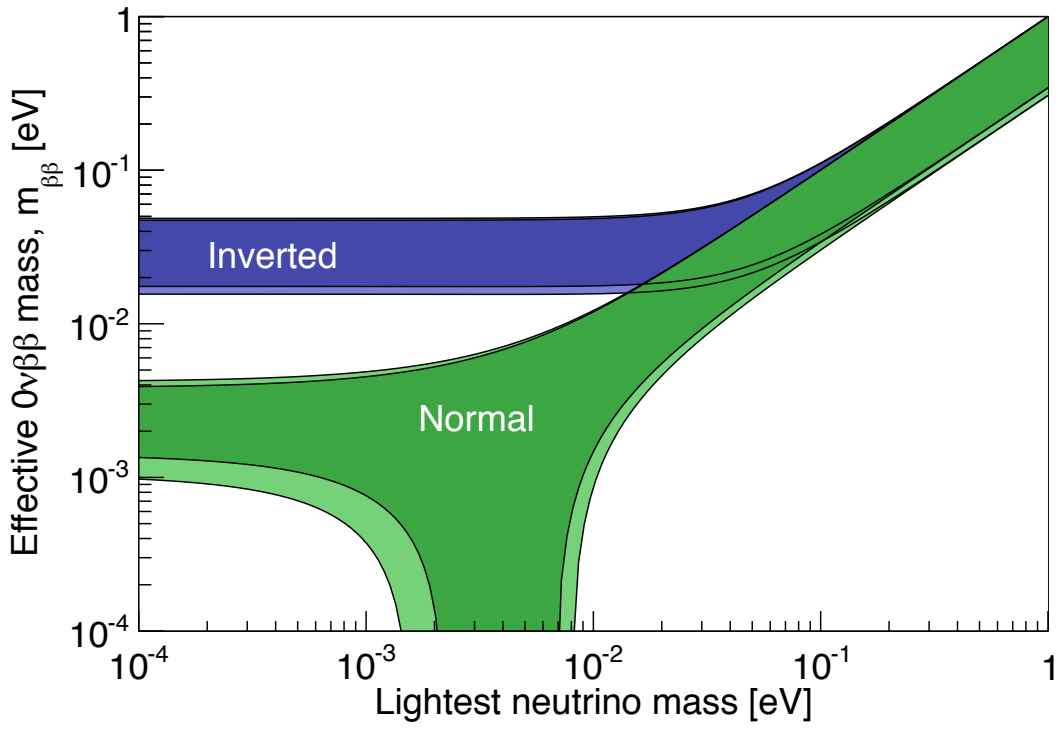

Figure 1.3: Effective $0\nu\beta\beta$ mass as a function of the mass of the lightest neutrino, according to Equation 1.5. Values of neutrino mixing parameters are from the Particle Data Group [14]. The green region describes the case of the normal hierarchy; the blue region describes the inverted hierarchy. The dark-colored bands are the regions allowed by the best-fit values and limits on mixing parameters. The thickness of the dark bands at each value of $m_{\beta\beta}$ is due to the CP-violating phases. The light-colored regions contain areas allowed by experimental uncertainties.

1.2 The MAJORANA DEMONSTRATOR

The MAJORANA Collaboration [20] [21] [22] will search for neutrinoless double-beta decay ($0\nu\beta\beta$) of ^{76}Ge with an array of germanium crystals. Germanium detectors are a well-established and commercially available technology that has been used to observed two-neutrino double-beta decay of ^{76}Ge and generate limits on the $0\nu\beta\beta$ half life. The choice of germanium will allow MAJORANA to directly test the claimed observation of $0\nu\beta\beta$ in ^{76}Ge.

MAJORANA is constructing the DEMONSTRATOR, which will contain 40 kg of germanium crystals. The DEMONSTRATOR will be located deep underground at the 4850-foot level of the Sanford Underground Research Facility (SURF) in the former Homestake Mine in Lead, SD. At least 30 kg of the germanium will be enriched to 86% in ^{76}Ge. The DEMONSTRATOR will consist of two independent vacuum cryostats, which will be shielded from backgrounds with active and passive shielding. In order of proximity to the detectors, these layers will be: electro-formed copper, modern lead, a radon-exclusion box, an active scintillator veto, and polyethylene. The DEMONSTRATOR is shown in Figure 1.4.

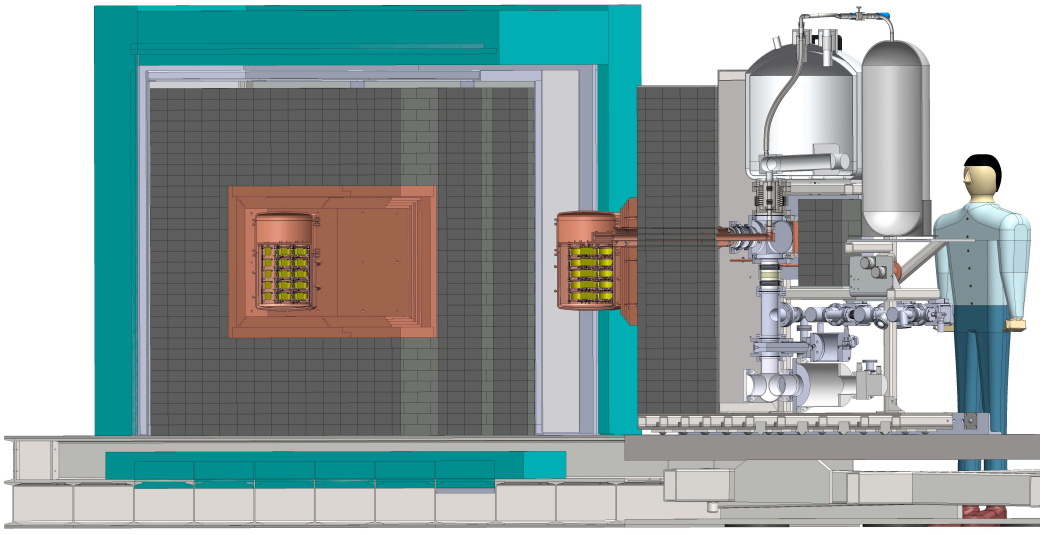

Figure 1.4: The MAJORANA DEMONSTRATOR, shown in cross section. Layers of copper, lead, and polyethylene shielding surround two copper cryostats. In this image, the cryostat module on the right is pulled out of the shielding.

Within each cryostat, the germanium crystals will be mounted in strings, rigid columns of detectors suspended from an electro-formed copper cold plate. Each cryostat will contain seven strings. Each string will hold three to five germanium crystals in a close-packed geometry. Each cryostat is cooled by a thermosyphon that extends outside of the shield to a liquid nitrogen dewar.

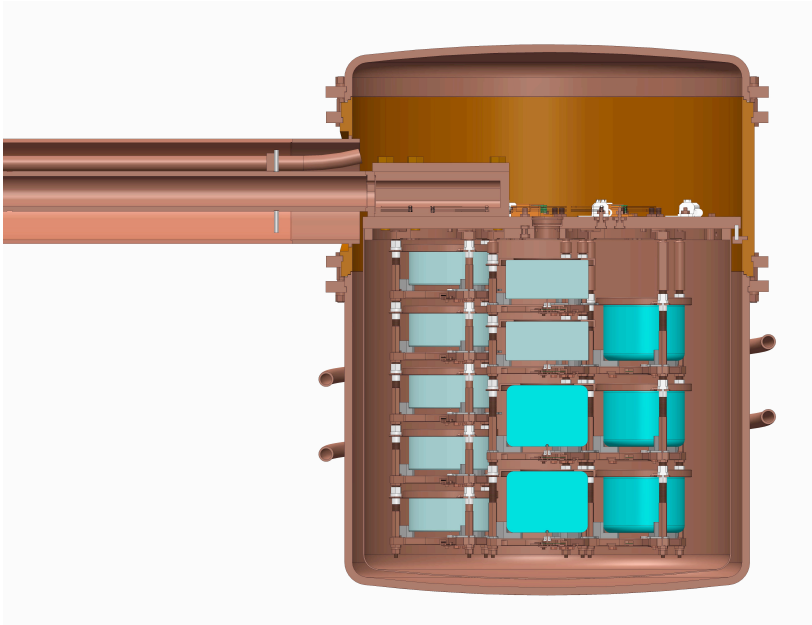

Figure 1.5: A DEMONSTRATOR cryostat containing strings of germanium crystals.

Cryostats will be deployed in the DEMONSTRATOR in three phases. In the first phase, scheduled for early 2013, two strings of natural germanium crystals will be deployed in a prototype cryostat. The prototype cryostat was fabricated from commercial copper. A cryostat named Cryostat One, created from electroformed copper and containing seven strings, of which three will be enriched, is planned for Fall of 2013. Cryostat Two, made of electroformed copper and containing seven strings of enriched crystals, will be deployed in Fall of 2014. Construction of the prototype cryostat is complete, and electroforming of copper parts for Crystat One has also been completed.

If the DEMONSTRATOR verifies the technical readiness of the design, MAJORANA will proceed with a larger experiment. The MAJORANA and GERDA collaborations are working together to pursue a joint goal of a tonne-scale ^{76}Ge experiment. The GERDA (GERmanium Detector Array) Collaboration is investigating $0\nu\beta\beta$ in ^{76}Ge with an alternative background-shielding method [5]. While the MAJORANA detectors will be housed in conventional vacuum cryostats surrounded by compact shielding, GERDA is deploying detectors directly in liquid argon. The joint experiment intends to select one method of detector deployment.

The signal of $0\nu\beta\beta$ is a peak at the ^{76}Ge double-beta decay endpoint, 2039 keV. The DEMONSTRATOR has a background goal of less than three counts per tonne-year in a 4-keV region of interest centered around the endpoint energy. For a tonne-scale experiment, this will translate to approximately one count per tonne-year. The additional background suppression for the tonne-scale experiment will be gained by operating deeper underground, reducing cosmogenic exposure of components, and including more detector strings in each cryostat. The inclusion of more detector strings in each cryostat increases the efficiency of a crystal-to-crystal analysis cut described in Section 1.5.2. Sensitivity to the $0\nu\beta\beta$ signal is limited by the background count rate in the energy spectrum surrounding the double-beta decay endpoint energy. The sensitivity of a ^{76}Ge experiment to the $0\nu\beta\beta$ half-life is shown in Figure 1.6. After 30 kg-years of exposure, the DEMONSTRATOR will exclude or confirm the claimed observation of $0\nu\beta\beta$ in ^{76}Ge.

1.3 Germamium detectors

Germanium semiconductor detectors are well-understood and commercially available technology. They are widely used for detection of ionizing radiation. Germanium detectors have several characteristics that make them useful for $0\nu\beta\beta$ searches. They feature excellent energy resolution, on the order of 0.2% at 2 MeV, which is essential for separating the $0\nu\beta\beta$ peak from the $2\nu\beta\beta$ continuum. To function as a semiconductor, a germanium crystal must have extremely low levels of impurity atoms. This requirement ensures that the crystal has very low levels of intrinsic contamination with radioisotopes. Fabrication of crystals from germanium enriched to 86% in ^{76}Ge has been demonstrated, which allows the germanium crystals to act as both source and detector.

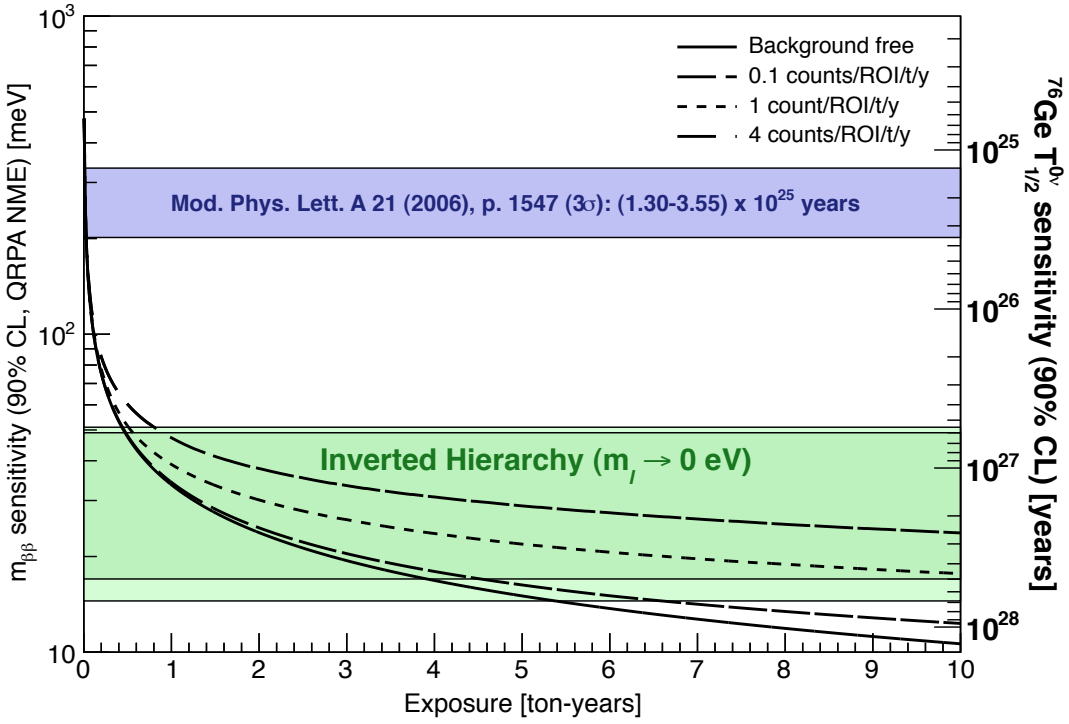

Figure 1.6: The sensitivity of a search for $0\nu\beta\beta$ with ^{76}Ge. The sensitivity is shown as a function of exposure for various background rates in a 4-keV wide energy region of interest centered around the $0\nu\beta\beta$ endpoint energy. The blue region corresponds to a claimed observation of $0\nu\beta\beta$ in ^{76}Ge [17]. The phase space permitted by the inverted hierarchy is shown in green, assuming the mass of the lightest neutrino is near zero. The relationship between $m_{\beta\beta}$ and $T^{0\nu}_{1/2}$ was determined from Equation 1.3, using $G^{0\nu}m_e^2$ of 6.31×10^{-15} y^{-1} [23] and $M^{0\nu}$ of 4.5 [24]. Figure generated from code by Jason Detwiler [25].

A diagram of a germanium crystal is shown in Figure 1.7. Crystals used as germanium detectors have masses on the order of 1 kg and may be several centimeters in length and diameter. To operate a germanium crystal as a radiation detector, a reverse bias of approximately 5 kV is applied across two electrical contacts. Ionizing radiation interacting in the depleted region of the crystal liberates electron-hole pairs. The holes and electrons drift to the electrical contacts under the influence of the electric field. The number of electron-hole pairs created is proportional to the amount of energy deposited [26]. A waveform from a 500 keV energy deposit in a germanium detector is shown in Figure 1.8. The energy of the deposit is calculated from the waveform height.

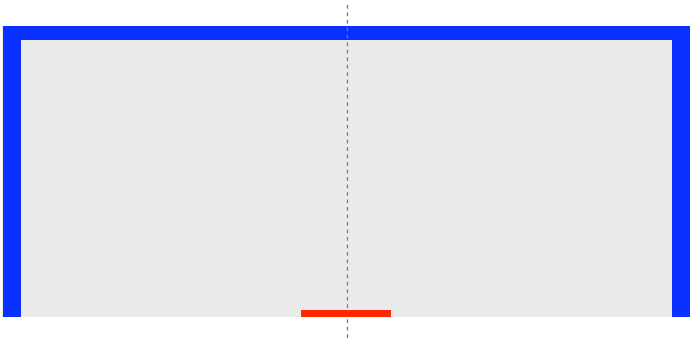

Figure 1.7: A diagram of a germanium crystal for use as a detector. The crystal is shown in cross section; it is cylindrically symmetric about the axis represented as a dashed line. A bias voltage is applied to the large electrical contact shown in blue. The signal is read out from the contact shown in red.

A typical energy spectrum from a germanium detector is shown in Figure 1.9. This spectrum of background radiation was collected in a laboratory at the University of Washington. The prominent peaks at 511, 1461, and 2615 keV are due to gamma rays released in positron-electron annihilation, ^{40}K decay, and ^{208}Tl decay, respectively. The continuum above 2615 keV is due primarily to cosmic-ray-induced interactions, which also contribute at lower energies. The low-energy cutoff near 50 keV is due to the threshold of the data acquisition system.

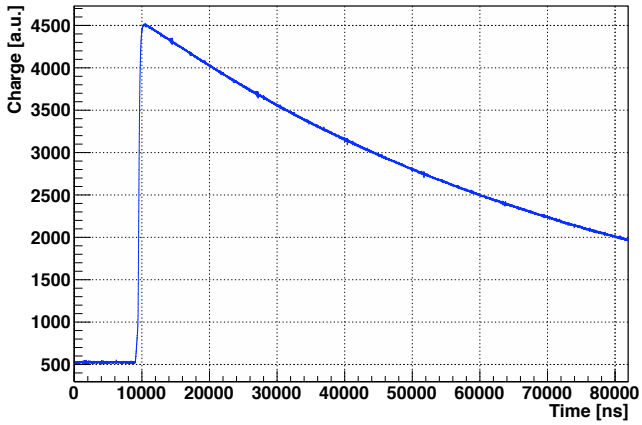

Figure 1.8: A sample waveform from a germanium detector. This waveform is from an energy deposit of approximately 500 keV.

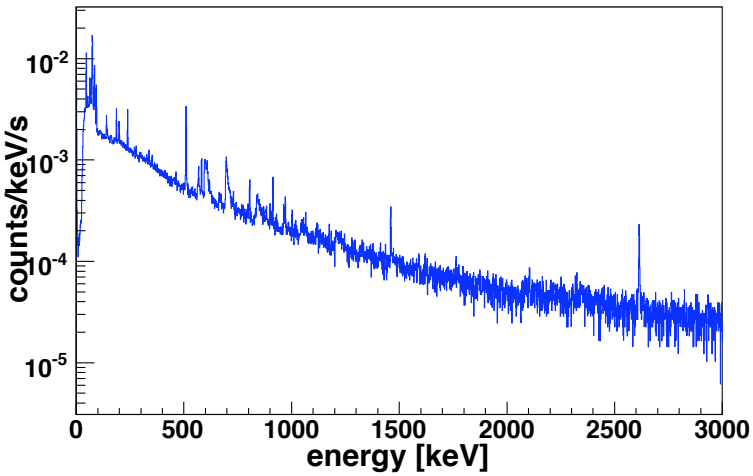

Figure 1.9: A 5.6-day background energy spectrum measured in the UW MAJORANA lab. The spectrum was measured with a 1-kg commercial germanium detector shielded by six inches of lead.

MAJORANA has chosen p-type point-contact (P-PC) germanium crystals for use in the DEMONSTRATOR. These detectors have many advantages over conventional germanium detectors [27] [28]. P-PC crystals have a small signal contact that results in low capacitance and therefore low electronics noise. The electric field configuration results in long drift times, which allows good separation of signals from energy deposits at different radial locations within a crystal. This capability is useful for identifying events produced by multiple interactions in a crystal.

A P-PC detector has a large n^+ electrical contact, as shown in blue in Figure 1.7. The electrical contacts in the figure are not to scale. This contact is typically made by evaporating and diffusing lithium into the surface [26]. The n^+ layer may have a thickness of one millimeter or more. The point contact is a p^+ layer, often produced by implantation of boron ions. The p^+ layer may be a few tenths of a micron in thickness. These electrical contacts are dead layers of the germanium crystal. Radiation entering the detector may be attenuated in the dead layers before reaching the active region. For P-PC detectors, which have thick n^+ contacts covering much of the surface of the germanium crystal, the dead layer can have a significant effect on the efficiency for detecting radiation.

Some waveforms collected from germanium detectors have long rise times and may be degraded in energy. The n^+ contact of P-PC detectors has been identified as a source of these slow-rising energy-degraded pulses [29] [30] [31]. The n^+ dead layer can consist of a truly dead layer, where energy deposits do not give rise to signal pulses, and a partially dead layer, where energy deposits in a region of weak field give rise to slow energy-degraded signals. Various parametrizations of charge collection in the dead layer as a function of depth into the germanium crystal can be found in the literature. An example dead layer parametrization by Aalseth et al. [30] is shown in Figure 1.10. In the figure, the region between 0 and approximately 1 mm appears to be a truly dead layer; no charge is collected from interactions in this region. Between approximately 1 and 3 mm deep is the partially dead layer, where energy deposits give rise to energy-degraded signals. In this dissertation, the layer that includes both the truly dead and partially dead layers will be refered to as the *total* dead layer.

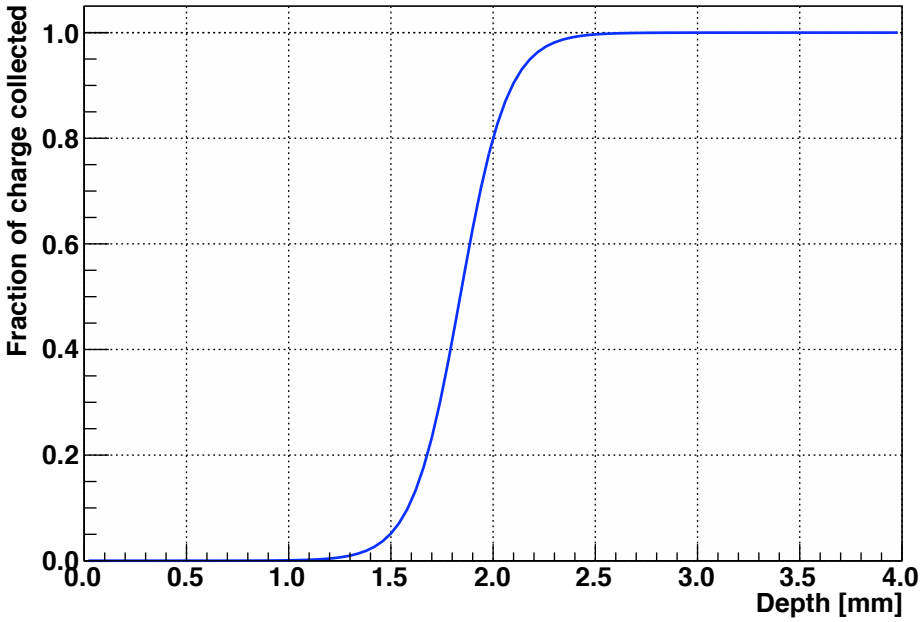

Figure 1.10: A parametrization of charge collection efficiency as a function of interaction depth in the n^+ contact of a P-PC germanium detector. This figure is based on a parametrization by Aalseth et al. [30].

1.4 Backgrounds to neutrinoless double-beta decay in germanium-76

If a ^{76}Ge nucleus in a detector in the MAJORANA DEMONSTRATOR array undergoes neutrinoless double-beta decay, two electrons will be emitted from the nucleus and will deposit their energy in the detector within a few millimeters of the decay site. The combined energy of the electrons will be equal to the Q-value of the decay, 2039 keV. If several such decays occur, they would create a peak in the energy spectrum measured with the DEMONSTRATOR. The MAJORANA Collaboration will look for a signal from $0\nu\beta\beta$ in a region of interest approximately 4 keV wide surrounding the Q-value. The sensitivity of the experiment is limited by backgrounds in this region of interest.

To show the level of background reduction that is necessary, the background spectrum from Figure 1.9 is reproduced in Figure 1.11, and compared to the $2\nu\beta\beta$ signal rate and a potential $0\nu\beta\beta$ signal of a magnitude allowed by current limits on the $0\nu\beta\beta$ half-life. The background rate in Figure 1.11 is many orders of magnitude too high for a successful $0\nu\beta\beta$ experiment. Background-reduction methods developed in previous $0\nu\beta\beta$ searches with germanium can provide significant improvement. MAJORANA requires approximately 100 times lower backgrounds than the levels that have been achieved previously, and will use novel methods for reducing backgrounds. Backgrounds and methods for their minimization are described below.

For a tonne-scale experiment, MAJORANA has a background goal for the energy region of one count or less per tonne-year after analysis cuts. For background rates as high as several counts per tonne-year, the background rate does not have much influence on the sensitivity of the DEMONSTRATOR. However, at the one-tonne scale, the background rate can significantly impact the final sensitivity of the experiment, as shown in Figure 1.6.

Radiation entering a germanium crystal may deposit part or all of its energy in the crystal. Radiation with energy greater than the ^{76}Ge Q-value is a potential background in a $0\nu\beta\beta$ search, but lower-energy radiation is also problematic, because it can obscure low-energy peaks used to identify backgrounds that can deposit energy near the $0\nu\beta\beta$ Q-value.

A good description of backgrounds to germanium detector experiments is given by G. Heusser in reference to the GALLEX and Heidelberg-Moscow experiments [32]. The

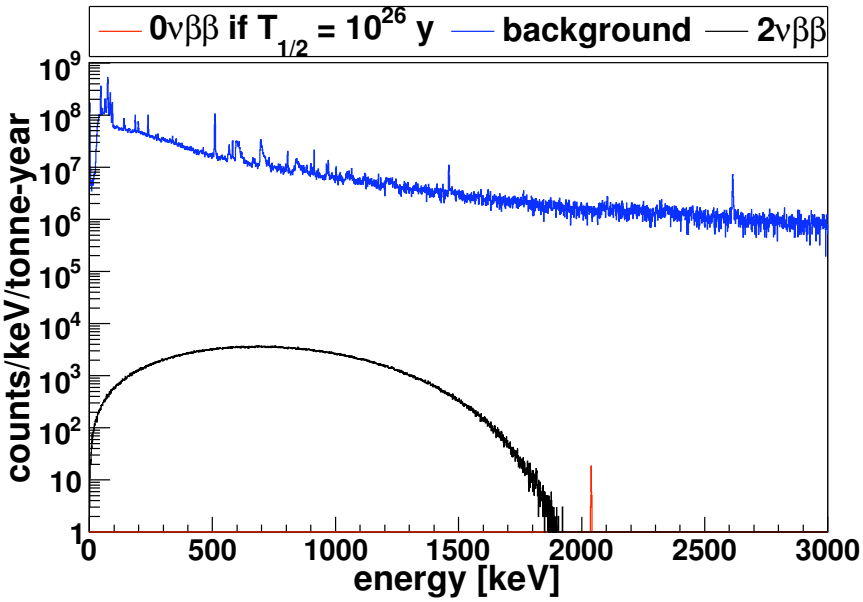

Figure 1.11: Signal rates for $2\nu\beta\beta$ (black) and $0\nu\beta\beta$ (red), if the $0\nu\beta\beta$ half-life is 10^{26} years. For comparison, the background rate from Figure 1.9 is shown (blue), scaled to one tonne-year of operation.

paper classifies backgrounds into six categories, roughly ordered by importance:

- Environmental gamma radiation
- Radioimpurities in the materials of the detector
- Radioimpurities in the shielding
- Cosmic rays: nucleons, muons, and activation
- Radon and its progenies
- Neutrons from natural fission and (α, n) reactions

These backgrounds arise from primordial contamination of materials with the long-lived isotopes ^{238}U, ^{232}Th, and ^{40}K, and from cosmic rays. Backgrounds can be reduced by shielding the detector from environmental radiation, carefully selecting and fabricating materials, and limiting cosmogenic exposure. The backgrounds listed above are described below, and backgrounds in a 100 keV region surrounding the ^{76}Ge $0\nu\beta\beta$ Q-value are tabulated in Table 1.1.

Uranium-238, Thorium-232, Potassium-40 are naturally-occurring radioactive isotopes with extremely long half-lives, greater than 10^9 years. Potassium-40 decays to either ^{40}Ca or ^{40}Ar, which are stable. However, both ^{238}U and ^{232}Th decay to stable isotopes by a series of several alpha and beta decays. The ^{238}U and ^{232}Th decay chains are shown in Figures 1.12 and 1.13. Several isotopes in the decay chains emit radiation with energies greater than the $0\nu\beta\beta$ Q-value. The decay products ^{214}Bi and ^{208}Tl are of special concern because of the energies of gammas emitted in their decays. Thallium-208 appears in the ^{232}Th decay chain and beta decays, emitting a 2.6-MeV gamma 99% of the time. Bismuth-214 appears in the ^{238}U decay chain and emits a 2.2-MeV gamma 5% of the time. The decay of ^{214}Bi is particularly problematic because it produces several high-energy gammas. The simulated response of a germanium detector to a point source of monoenergetic 2.6-MeV gammas is shown in Figure 1.14a. This figure shows how the 2.6-MeV gamma contributes counts at lower energies. The simulated response to ^{214}Bi and ^{208}Tl is shown in Figure 1.14b.

Alpha and beta radiation from the ^{238}U and ^{232}Th decay chains can be attenuated by small thicknesses of material, so these backgrounds are typically only a problem in materials very close to the germanium crystals. The copper and lead shielding surrounding the DEMONSTRATOR cryostats will attenuate gamma radiation from the experimental hall. While the lead shielding will attenuate environmental gamma backgrounds, it will also serve as a potential source of background. Measured values of ^{210}Pb contamination in commercially available lead span many orders of magnitude, and may reach 2500 Bq/kg [32]. This contamination is believed to occur during lead production. To mitigate contamination with ^{210}Pb, lead may be produced in clean conditions, or ancient lead (produced long ago compared to the ^{210}Pb half life of 22.2 years) may be used. MAJORANA will attenuate backgrounds from the lead shielding by lining the lead with commercial copper, and by

Table 1.1: Selected background contributions to the DEMONSTRATOR energy spectrum near the $0\nu\beta\beta$ endpoint of 2039 keV. Contributions are listed for the energy region between 1990 and 2090 keV. Q-values and gamma energies are from NuDat [33] unless otherwise specified.

Source	**Energy [keV]**	**Description**
^{214}Bi	1994.6	γ peak; ^{238}U daughter
^{214}Bi	2010.8	γ peak; ^{238}U daughter
^{214}Bi	2016.7	γ peak; ^{238}U daughter
^{214}Bi	2021.6	γ peak; ^{238}U daughter
^{76}Ge(n,n$'\gamma$)	2023	γ peak
^{206}Pb(n,n$'\gamma$)	2041	γ peak
^{214}Bi	2052.9	γ peak; ^{238}U daughter
^{214}Bi	2085.1	γ peak; ^{238}U daughter
^{214}Bi	2089.7	γ peak; ^{238}U daughter
^{76}Ge $2\nu\beta\beta$	continuum	2039-keV Q-value, two βs
^{214}Bi	continuum	2204.1-keV and other γ peaks; ^{238}U daughter
^{208}Tl	continuum	2614.5-keV γ peak; ^{232}Th daughter
^{68}Ga	continuum	2921.1-keV Q-value; produced in Ge
^{60}Co	continuum	2823.6-keV Q-value; produced in Ge, Cu
^{210}Po	continuum	5304.3-keV α, radon plate-out product
cosmogenic μs	continuum	interactions in Ge, other materials

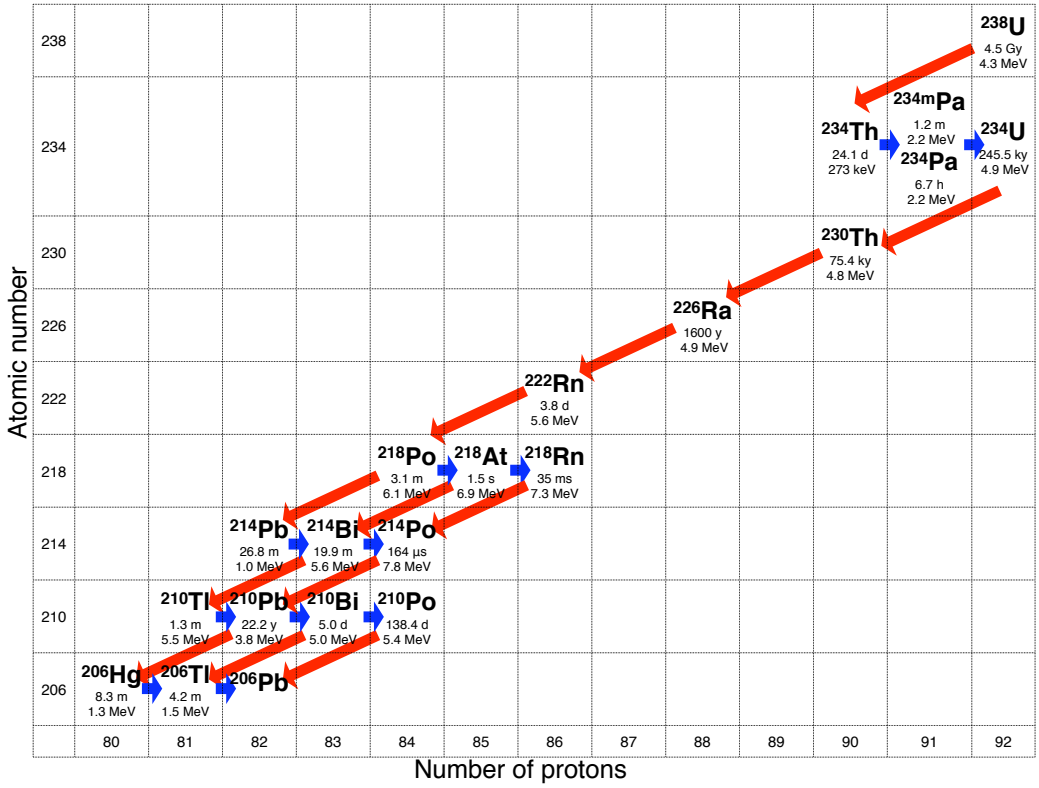

Figure 1.12: The ^{238}U decay chain. Red arrows indicate alpha decays; blue arrows indicate beta decays. The half life and Q-value are listed for each isotope. Where more than one decay mode is possible the larger Q-value is listed. Half lives and Q-values are from the NuDat decay radiation database [33].

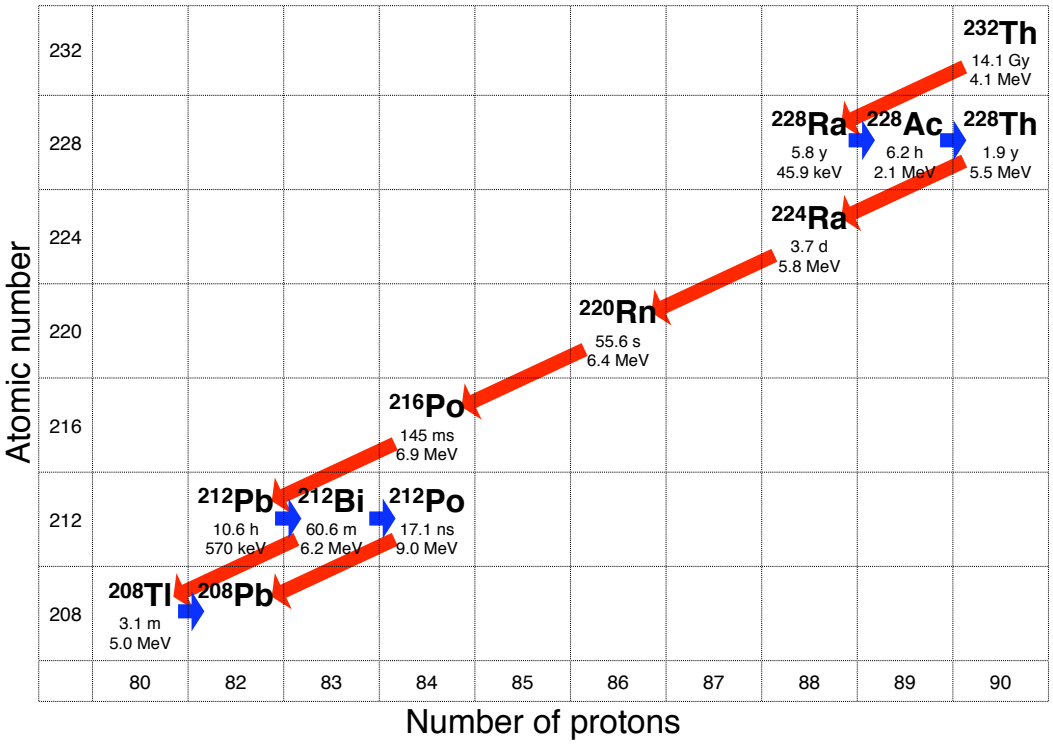

Figure 1.13: The ^{232}Th decay chain. Red arrows indicate alpha decays; blue arrows indicate beta decays. Half life and Q-value are listed for each isotope. Where more than one decay mode is possible the larger Q-value is listed. Half lives and Q-values are from the NuDat decay radiation database [33].

using an inner layer of ultra-clean electroformed copper.

Only materials that meet stringent radiopurity requirements will be placed within the shielding. Some plastics, such as Parylene and PTFE, have intrinsically low levels of radioactivity and may be used in small amounts near the detectors. Components inside the shield will be fabricated in a cleanroom, cleaned and etched, and will be handled according to clean procedures. Component mass is minimized to reduce radioactive contaminants and to facilitate the granularity analyis cut described below. All materials considered for use in the DEMONSTRATOR are certified by a MAJORANA material assay campaign.

Electroformed copper has been demonstrated to have extremely low levels of radioactive contamination. In the electroforming process, sacrificial copper anodes are plated onto a stainless-steel cathode mandrel in the shape of the desired part. Electroforming is done in an acid bath in a cleanroom environment. The process is performed underground to reduce cosmogenic activation of the copper. Continuous purification of the acid bath removes impurities. The cryostats and structural components of the detector strings are fabricated from electroformed copper.

Radon, in the form of ^{222}Rn from the ^{238}U decay chain, is a noble gas present in mine air. Radon daughters, including the long-lived ^{210}Pb, may plate out on surfaces exposed to contaminated air. To avoid contamination, machining of DEMONSTRATOR components is performed in cleanroom conditions. After machining, components are cleaned and etched to remove any radon deposition on the surfaces. The clean components are then double bagged and sealed in nylon bags. Assembly will take place in a glovebox that is purged with liquid nitrogen boil off. A gas exclusion volume surrounding the DEMONSTRATOR cryostats will be purged with nitrogen gas to keep radon away from the germanium crystals.

Cosmic rays create backgrounds for MAJORANA in multiple ways. The DEMONSTRATOR is operated deep underground, at the 4850-foot level of SURF. At this depth, the cosmic-ray flux is greatly attenuated and consists of high-energy muons. Muons interacting in the germanium crystals or shielding can be identified by the active muon veto. A bigger challenge is presented by muon-induced neutrons, which may be produced in the rock at SURF, and then interact in the shielding or germanium crystals. A layer of passive polyethylene shielding will moderate the flux of these secondary neutrons.

Exposure of detector materials to cosmic rays is problematic even long before data-taking starts, because it may produce long-lived unstable isotopes within the material. Cosmogenic activation of germanium can produce many long-lived isotopes, including ^{56}Co, ^{57}Co, ^{58}Co, and ^{68}Ge. To mitigate these delayed cosmic-ray backgrounds, electroformed copper is produced underground. Enrichment of germanium eliminates cosmogenics, so the exposure of enriched material and fabricated detectors is carefully controlled.

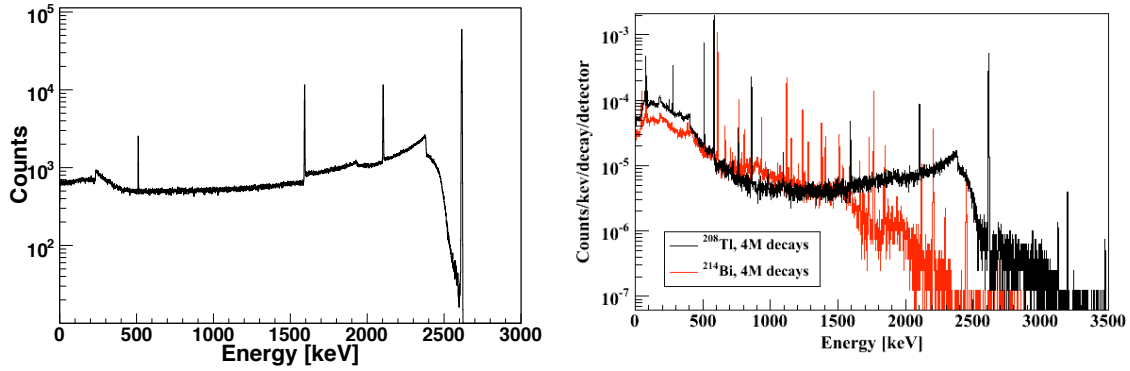

(a) (b)

Figure 1.14: Response of a germanium detector to radiation from the ^{232}Th and ^{238}U decay chains, simulated with the MAJORANA and GERDA package MAGE. The germanium crystal in the simulation was 80 cm in diameter and 30 cm in length. Radiation was emitted from a point source 5 mm from the end of the crystal. In (a), response is shown to monoenergetic gammas of 2615 keV, the energy of a gamma emitted in the decay of ^{208}Tl, from the ^{232}Th chain. In (b), response is shown to ^{214}Bi and ^{208}Tl.

1.5 Techniques for background mitigation

Careful material selection and several layers of shielding will minimize backgrounds that may deposit energy in the DEMONSTRATOR. Even after these background reduction efforts, some irreducible backgrounds remain. A potential $0\nu\beta\beta$ of ^{76}Ge would emit two electrons, with a total energy of 2039 keV inside of a germanium crystal. These electrons would typically

travel a few millimeters within the crystal before depositing their energy. Several offline analysis techniques will distinguish between $0\nu\beta\beta$ signal events and background events in data from the germanium detectors.

1.5.1 Single-site time correlation

Some radioisotopes decay into short-lived daughter nuclei, and these decays may be identified with a single-site time-correlation analysis. For example, ^{68}Ge is a cosmogenic activation product that may be present in germanium crystals. Germanium-68 decays to ^{68}Ga by electron capture with a half life of 271 days and a Q-value of 106 keV. Gallium-68 decays to ^{68}Zn with a halflife of 67.7 minutes and a Q-value of 2.9 MeV. The decay of ^{68}Ga may deposit energy in the $0\nu\beta\beta$ region of interest.

Analysis of the times, energies, and crystal locations of deposits in the detector array can identify the correlated ^{68}Ge and ^{68}Ga decays as background events; this analysis is called single-site time correlation (SSTC).

1.5.2 Granularity

A gamma with energy on the order of the $0\nu\beta\beta$ endpoint has a high probability of Compton scattering. Such a gamma may deposit energy in one germanium crystal, exit the crystal, and deposit energy in a second crystal. Other background radiation, such as neutrons and muons, may also interact in multiple crystals. Since the background rate in the MAJORANA experiment will be very low, an event that deposits energy in the $0\nu\beta\beta$ region of interest in one crystal in coincidence with an event in a separate crystals is unlikely to be a random coincidence. Such background events will be rejected with a crystal-to-crystal granularity cut. The close-packed geometry of the MAJORANA experiment allows for high efficiency of this cut.

1.5.3 Pulse-shape analysis

Background radiation, including high-energy gammas, may interact in multiple locations in a single germanium crystal. Due to the electric field configuration in a P-PC detector,

interactions from different radial locations in the detector can arrive at the signal contact separated by hundreds of nanoseconds. These multi-site events can be identified with pulse-shape analysis (PSA) and can be discriminated from the single-site nature of $0\nu\beta\beta$.

1.6 Backgrounds surrounding the energy region of interest

For MAJORANA to set a lower limit on the half-life of $0\nu\beta\beta$ or to claim observation of a $0\nu\beta\beta$ signal, it will be necessary to understand the background energy spectrum surrounding the small energy region of interest. The current background budget for the DEMONSTRATOR is 2.9 counts in a 4-keV region of interest per tonne-year of exposure. Contributions to this total are listed in Table 1.2. The background budget is based on material assay information and the results of a simulation campaign to determine efficiency for backgrounds to deposit energy in the region of interest. To support a result, the collaboration should be able to explain features in the full spectrum, and reductions in the spectrum due to analysis cuts.

The collaboration must also understand backgrounds outside of the small region of interest to verify the performance of the DEMONSTRATOR. The DEMONSTRATOR will consist of 30 kg of germanium, and will operate for a few years, reaching approximately 0.1 tonne-yr of exposure. For the DEMONSTRATOR, MAJORANA has a background goal of less than three counts per tonne-year in the $0\nu\beta\beta$ energy region on interest. If this background goal is achieved, less than one count is expected in the region of interest during the operation of the DEMONSTRATOR. Based on backgrounds in the full energy spectrum of the MAJORANA DEMONSTRATOR, the collaboration should be able to predict the rate in the $0\nu\beta\beta$ region of interest for a one-tonne-scale experiment.

Table 1.2: Count rate estimates for the DEMONSTRATOR and a tonne-scale experiment in the $0\nu\beta\beta$ ROI after application of analysis cuts, and upper limits prior to cuts in a 1.9-3.0 MeV window. Central values in columns 2 and 3 are based on achievable purity levels and anticipated values of parameters. Uncertainties include assay sensitivity and potential sample variability. The numbers in parentheses are estimates after an SSTC cut and a cut to remove ^{60}Co events. The final row conservatively adopts a linear summation of uncertainties. Table and caption adapted from MAJORANA review document [34].

	ROI Background [counts/ROI/t/y]		Rate in 1.9-3.0 MeV
Detector Component	DEMONSTRATOR	Tonne-Scale	[counts/(kg-month)]
	Naturally Occurring Radioactivity		
Electroformed Cu	$0.89^{+2.20}_{-0.89}$	$0.48^{+1.20}_{-0.48}$	$0.10^{+0.16}_{-0.10}$
OFHC Cu	$0.29^{+2.91}_{-0.29}$	$0.01^{+0.14}_{-0.01}$	$0.03^{+0.25}_{-0.03}$
Lead Shielding	$0.20^{+8.31}_{-0.20}$	$0.01^{+0.43}_{-0.01}$	$0.01^{+0.56}_{-0.01}$
Cables	$0.22^{+0.85}_{-0.22}$	$0.16^{+0.59}_{-0.16}$	$0.03^{+0.13}_{-0.03}$
Front Ends	$0.19^{+0.19}_{-0.10}$	$0.13^{+0.13}_{-0.07}$	$0.05^{+0.05}_{-0.03}$
Ge, Plastics, Others	$0.10^{+0.20}_{-0.10}$	$0.09^{+0.14}_{-0.09}$	<0.03
	Cosmogenic Activation		
Enriched Ge	0.18 ± 0.05	0.05 ± 0.01	0.89 ± 0.26 (0.15 ± 0.05)
^{60}Co in Copper	$0.11^{+0.11}_{-0.06}$	0.01 ± 0.01	$1.61^{+1.61}_{-0.81}$ $(0.09^{+0.09}_{-0.05})$
	External and Environmental Contributions		
External γ and (α,n)	$0.10^{+0.10}_{-0.05}$	0.01 ± 0.01	0.01 ± 0.01
Rn and Surface αs	$0.05^{+0.16}_{-0.05}$	$0.05^{+0.15}_{-0.05}$	<0.01
	in situ *Muon-Induced and ν Background*		
(n,n$'\gamma$)	$0.21^{+0.63}_{-0.16}$	$0.02^{+0.06}_{-0.02}$	$0.08^{+0.23}_{-0.06}$
Ge(n,n)	$0.17^{+0.51}_{-0.13}$	$0.02^{+0.05}_{-0.01}$	$0.02^{+0.04}_{-0.01}$
Ge(n,γ)	$0.13^{+0.26}_{-0.09}$	$0.01^{+0.03}_{-0.01}$	$0.01^{+0.04}_{-0.01}$
Direct μ, ν, other	<0.04	<0.01	<0.01
Totals	$2.9^{+16.5}_{-2.4}$	$1.06^{+2.96}_{-0.95}$	$2.8^{+3.4}_{-1.3}$ $(0.59^{+1.62}_{-0.41})$

1.7 Conclusions and outline of this dissertation

MAJORANA will search for neutrinoless double-beta decay with the DEMONSTRATOR, an array of germanium detectors enriched in ^{76}Ge. The signal of $0\nu\beta\beta$ is a peak at the ^{76}Ge $0\nu\beta\beta$ endpoint in the DEMONSTRATOR energy spectrum. The sensitivity of a low-background experiment like the DEMONSTRATOR is determined by the background count rate in the region of interest. To make a convincing $0\nu\beta\beta$ limit or claim, MAJORANA must have a thorough understanding of backgrounds in the $0\nu\beta\beta$ energy region of interest and throughout the energy spectrum. This will require a model of the DEMONSTRATOR energy spectrum, accounting for the total spectrum expected from all background contributions. This background model is also necessary to make projections of background rates for a future tonne-scale germanium experiment based on measurements with the DEMONSTRATOR. A MAJORANA simulation campaign is currently underway to simulate the energy spectrum response of the DEMONSTRATOR. MAJORANA is building a background model of the DEMONSTRATOR energy spectrum, using Monte Carlo simulations of detector response from the simulation campaign and information about material radiopurity.

Our ability to model a background energy spectrum can be validated with an existing germanium detector. This validation is an important test of the simulation software and of our understanding of backgrounds. MAJORANA Collaborators at the University of North Carolina at Chapel Hill (UNC) operate a good candidate detector for a validation study: a low-background germanium detector in a shielded underground environment. The detector is located at the Kimballton Underground Research Facility (KURF) in Chemical Lime Company's Kimballton Mine near Ripplemeade, VA. The detector, the MAJORANA Low-background BEGe at KURF (MALBEK) is a modified Broad-Energy Germanium (BEGe) detector, a p-type point-contact detector manufactured by CANBERRA. MALBEK is ideal for the study of backgrounds because it is a low-background detector, the contents of the cryostat are well known, and it is operating stably underground.

This dissertation describes the creation of a model of the background energy spectrum for MALBEK. The model is compared to energy spectra collected with MALBEK at KURF, discrepancies are described, and implications for the MAJORANA DEMONSTRATOR back-

ground energy spectrum are discussed.

Chapter 2

THE MALBEK DETECTOR AND DATA ACQUISITION SYSTEM

2.1 Introduction

The MAJORANA Low-background BEGe at KURF (MALBEK) detector is a modified Broad-Energy Germanium (BEGe) detector located at the Kimballton Underground Research Facility (KURF) [35], [36]. This chapter will describe the MALBEK detector and explain the data acquisition system. Chapter 3 will give an overview of the software used for MALBEK data processing. Details of data processing are described in Chapter 4.

2.2 The MALBEK detector

MALBEK is a p-type point-contact (P-PC) detector produced by CANBERRA [37] based on a similar detector developed in conjunction with Juan Collar of the University of Chicago. MALBEK was carefully designed to ensure minimal radioactive contamination of the cryostat and to achieve a low energy threshold.

Detailed information about most commercially produced germanium detectors is difficult to obtain. Detector manufacturers are often reluctant to share proprietary details about germanium crystal geometry and cryostat contents. MALBEK is unusual in this respect because CANBERRA and Juan Collar provided engineering drawings, photographs, and other information about the contents of the detector. In addition, MAJORANA Collaborators from UNC traveled to CANBERRA with MALBEK in October of 2011. During the trip, the MALBEK cryostat was opened, the dimensions of several parts were measured, and the cryostat contents were photographed. The goal of this dissertation is to validate MAJORANA's understanding of backgrounds to an ultra-clean germanium detector experiment. The MALBEK detector, with its low-background design and well-understood cryostat, is an excellent test stand for this validation project.

The MALBEK detector consists of a dipstick-style vacuum cryostat containing a germanium crystal mounted in copper and Teflon cups. Components inside the cryostat and near the crystal include small amounts of tin solder for electrical connections, a front-end electronics package, and commercially available connectors and resistors. To minimize detector capacitance, MAJORANA Collaborators John Wilkerson of UNC and David Radford of ORNL specified custom dimensions and a minimal point-contact diameter. The choice of dimensions was based on simulations by David Radford. Juan Collar provided input into the front-end electronics design and supplied low-background copper, lead, and Teflon parts for use in the cryostat. Properties of MALBEK are listed in Table 2.1.

In the experimental hall at KURF, the MALBEK detector stands in a 30-liter dewar of liquid nitrogen (LN) and is shielded by several layers of lead. A one-inch-thick layer of ancient lead surrounds the detector. The ancient lead is surrounded by four to eight inches of modern lead. The lead shielding is supported by an aluminum stand and enclosed in an acrylic box that serves as a radon exclusion volume. The exclusion volume is purged with a continuous flow of nitrogen boil off from a second 30-liter dewar of LN. A 10-inch-thick stack of polyethylene surrounds the lead shielding and the detector stand. A diagram of the detector and lead shielding appears in Figure 2.1. A photo of the detector in its lead shielding and radon exclusion box appears in Figure 2.2. The MALBEK installation at KURF was constructed by MAJORANA Collaborators at UNC. The conceptual design of the shield was generated by Reyco Henning and Padraic Finnerty at UNC and the detailed design was created by Gary Swift, an engineer at TUNL [42].

A small hole through the modern lead shielding allows a calibration source to be inserted near the detector. The hole ends above the detector, centered over the cryostat. The hole does not penetrate the ancient lead shield. During calibration runs, a ^{133}Ba source on a wire was inserted into the source hole.

Table 2.1: Properties of the MALBEK detector.

General Information	
Manufacturer	CANBERRA
Detector model	modified BE2830/S [38]
Detector serial number	8498 [39]
Preamp model	PSR SL [39]
Preamp serial number	13000010 [39]
Crystal Characteristics	
Crystal height	30 mm [38]
Crystal diameter	60.6 mm [38]
Crystal pull date	26 Oct 2007 [40]
Depletion voltage	+2700 V [39]
Operating voltage	+3500 V [39]
Point contact (p^+) dead layer thickness	0.3 μm [37]
Outer (n^+) dead layer thickness:	
Nominal value	1 mm [41]
Measured value	0.93 $\pm$ 0.09 mm (Chapter 6.4)
Total crystal mass:	
Nominal value	465 g [38]
Measured value	455.5 $\pm$ 15.8 g (Chapter 6.6)
Active crystal mass	404.2 $\pm$ 15.5 g (Chapter 6.6)

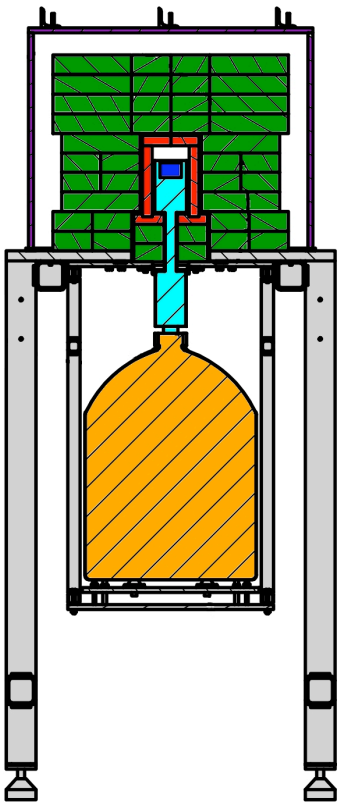

Figure 2.1: The MALBEK detector in shielding. The detector (light blue) sits in an LN dewar (orange). The germanium crystal (blue) is shielded by layers of ancient lead (red) and modern lead (green). The dewar and shield are supported by a stand (gray). This cross-sectional image was modified from an engineering drawing by Gary Swift [42].

Figure 2.2: The MALBEK detector. The portion of the cryostat containing the germanium crystal is surrounded by lead shielding and a radon exclusion box. The detector is cooled with an LN dewar.

2.3 Data acquisition from MALBEK

Data from the MALBEK detector are collected with a MAJORANA-like data acquisition (DAQ) system [43]. A computer running an Object-oriented Real-time Control and Acquisition (ORCA) [9] application controls the experiment and collects data. The DAQ has three main functions: to record digitized waveform data from the detector, to provide high voltage to the detector and to maintain LN levels in the two dewars. The MALBEK DAQ builds on work by other MAJORANA Collaborators and ORCA developers and was modeled after previous setups used by Michael Marino [44], [29]. UNC students Padraic Finnerty and Graham Giovanetti worked with John Wilkerson and Mark Howe to implement the MALBEK DAQ and experimental setup. A schematic of the MALBEK DAQ is shown in Figure 2.3. Details are explained below.

The following terms will be used to describe data recorded by the DAQ:

Waveform a digitized voltage signal as a function of time.

Event the response of a detector array during a specified time window. For analysis of DEMONSTRATOR data, an event may contain waveforms collected from multiple crystals. In this MALBEK analysis, each event contains one waveform.

Run a set of data recorded with the DAQ. MALBEK runs are typically one hour in duration.

MALBEK has a small front-end electronics package within the cryostat and an external integrated transistor reset preamplifier. The charge-sensitive preamplifier provides a voltage output proportional to integral charge collected from the germanium crystal. The integrating circuit of the preamplifier resets after reaching a certain level. The integral charge includes contributions from the leakage current and from charge created by ionizing radiation. For clarity, the preamplifier voltage signal that is proportional to the integral charge will be referred to as the *ionization energy* signal in the rest of this chapter. The preamplifier has an inhibit output, which provides a logic signal when the integrator re-

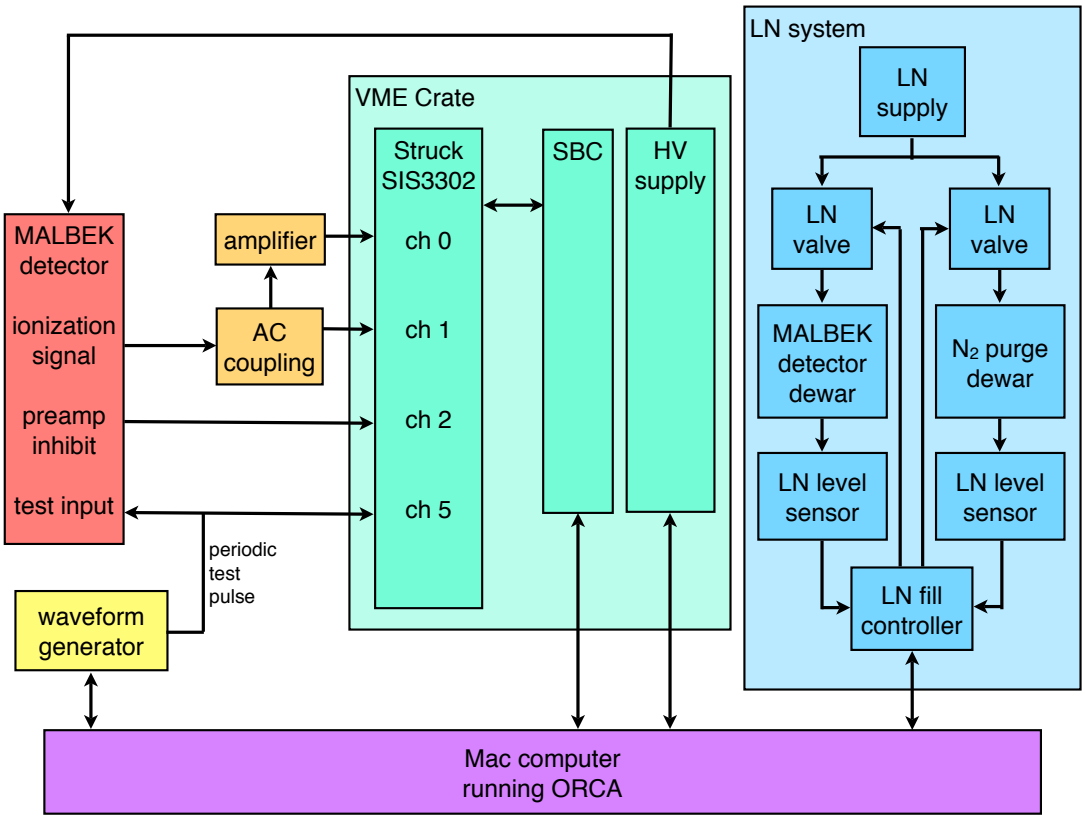

Figure 2.3: MALBEK data acquisition system. Output from the waveform generator passes through attenuators, which are not shown.

sets. The preamplifier also has a test input, which can be used to inject a pulse into the electronics.

Data from the MALBEK detector are recorded with an SIS3302, an eight-channel 100-MS/s 16-bit digitizer produced by Struck Innovative Systeme. The SIS3302 resides in a VME crate and is read out with a Concurrent Technologies Single Board Computer (SBC). The SIS3302 is configured to trigger internally. Each channel triggers independently. Four channels of the SIS3302 are active during data taking. These channels are summarized in Table 2.2.

Table 2.2: Inputs to the Struck SIS3302 digitizer. The SIS3302 samples at 10 Ms/s. Short waveforms are collected from the inhibit and pulser channels because only the time stamps are used.

Channel	**Input**	**Number of samples**
0	amplified ionization energy signal	8192
1	unamplified ionization energy signal	8192
2	inhibit signal	4
5	periodic pulser signal	4

The ionization energy signal from the preamplifier is AC coupled and then input to a Phillips Scientific 777, which splits the signal. One output from the 777 is sent to channel 1 of the SIS3302; this unamplified signal is used to collect waveforms in an energy range up to ∼3 MeV. A second output from the 777 is sent through an amplifier to channel 0 of the SIS3302; this signal is used to collect waveforms of energies up to ∼160 keV. The amplified signal uses the full range of the digitizer to store low energy waveforms, which reduces noise associated with digitization. The amplified signal is used for a dark matter search and also for low-energy single-site time-correlation background rejection [35]. The unamplified ionization energy signal is used for the work in this dissertation: understanding

the full energy spectrum response of MALBEK to backgrounds at KURF. The rest of this dissertation will focus on the unamplified ionization energy signal.

The inhibit signal from the preamplifier is input to channel 2 of the SIS3302. During a reset of the preamplifier, the ionization energy signal is noisy and unusable. In later analysis, the time stamps of inhibit signals are used to identify and veto events in the ionization energy channels that are coincident with preamplifier resets.

An Agilent 33220A function generator provides periodic test pulses at a frequency of 0.1 Hz. These test pulses are used to measure the live time of the experiment and to study the energy resolution of the detector. Output from the pulser is split in two. The MALBEK preamplifier test input receives one signal. The other pulser signal is sent to channel 5 of the SIS3302. Pulses input into the preamplifier test port are visible in the ionization energy channels and appear at approximately 35 keV in the energy spectrum. The signal in channel 5 provides timing information that is used to identify pulser waveforms in the detector signals in channels 0 and 1.

The MALBEK dipstick cryostat resides in an LN dewar. The level of LN in this dewar is monitored and maintained via an American Magnetics, Inc. (AMI) 286 multi-channel liquid level controller. The level controller also maintains the LN level in the radon purge dewar.

Data from the SBC, level controller, function generator, and high-voltage supply are collected by ORCA in one-hour runs. The output from each run is saved to disk as a single file.

Early data-taking efforts with MALBEK at KURF found that ORCA files were extremely large ($\sim$1 GB per run). These file sizes were dominated by inhibit-related waveforms in the amplified and unamplified ionization energy channels of the SIS3302. To reduce file sizes, an ORCA script discards inhibit-like waveforms from the energy channels before ORCA data are written to disk. The waveforms are identified by characteristic large negative-polarity pulses, which differ significantly from the positive-polarity ionization energy signal. Discarding the inhibit-related waveforms reduces the average file size to approximately 30 MB per run.

2.4 Lead-210 contamination

When MALBEK began operating underground in shielding at KURF in 2010, it was clear that an unexpected source of ^{210}Pb contamination was near the detector. The first shielded energy spectra from KURF included features characteristic of ^{210}Pb and its progeny: a 46.5-keV gamma peak due to ^{210}Pb, Pb x-ray lines between 70 and 90 keV, and a bremsstrahlung continuum [45] [46] [47]. The high intensity of the Pb x-rays and the presence of the bremsstrahlung continuum suggested that the ^{210}Pb contamination was in lead near the cryostat or inside it. An energy spectrum collected between September and November of 2010 is shown in Figure 2.4. The generation of this energy spectrum from MALBEK data is described in Chapter 4, and the spectrum is shown out to higher energies in Figure 4.1.

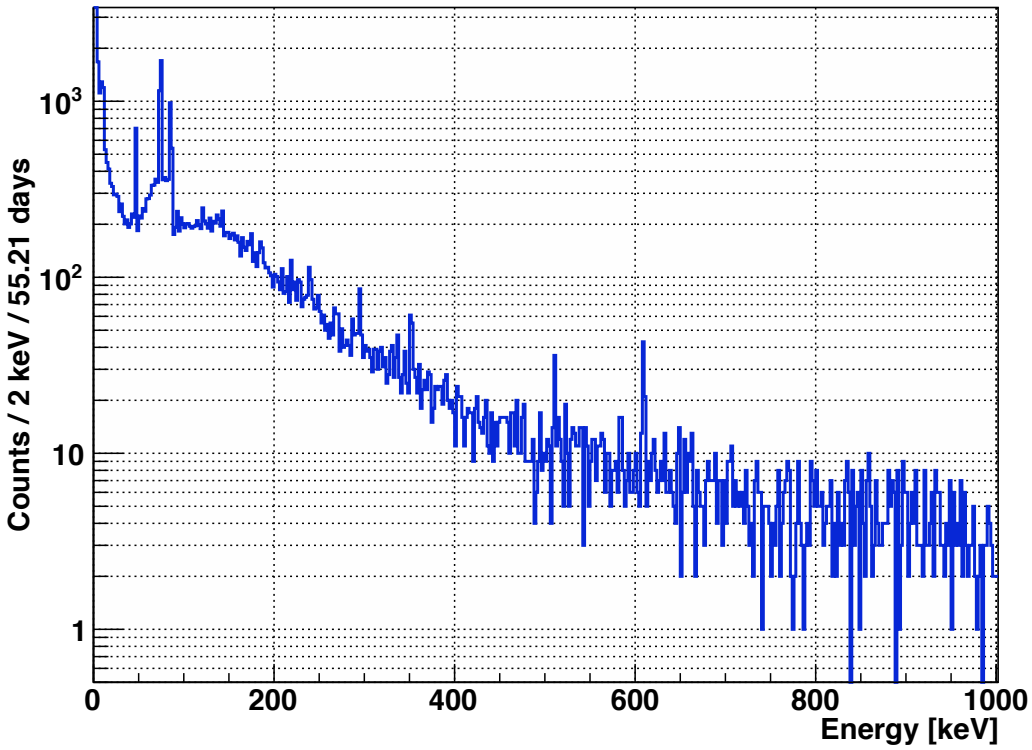

Figure 2.4: Evidence of ^{210}Pb contamination in a shielded MALBEK energy spectrum collected underground at KURF. Some visible features include a ^{210}Pb gamma peak at 46.5 keV, Pb x-ray lines between 70 and 90 keV, and a ^{214}Bi gamma peak at 609 keV.

A paper by G. Heusser describes ^{210}Pb contamination and includes a spectrum of germanium-detector response to ^{210}Pb in a sample of lead bricks [32]. Part of the discussion is summarized here to explain features observed in the MALBEK energy spectrum. With a half life of 22.2 years, ^{210}Pb is a long-lived isotope in the ^{238}U decay chain. During fabrication, ^{210}Pb may be introduced into materials and is often present in lead bricks and tin solder at concentrations exceeding secular equilibrium. The energy-spectrum response of a germanium detector to ^{210}Pb is characterized by the beta decay of ^{210}Pb to ^{210}Bi and the subsequent beta decay of ^{210}Bi to ^{210}Po. In 4.3% of ^{210}Pb decays, a 46.5-keV gamma is emitted. Other low-energy electrons and photons are emitted in this decay, but typically they are attenuated before reaching the active volume of the detector. The beta decay of ^{210}Bi produces a beta with an endpoint of 1.1 MeV. If the decay occurs in lead, the high-energy beta will induce bremsstrahlung and Pb x-rays. The bremsstrahlung continuum has a maximum near 170 keV, and the lead x-rays have energies of 72.8, 75.0, 84.9, and 87.4 keV.

The presence of ^{210}Pb in the MALBEK energy spectrum was surprising. MALBEK was custom fabricated by CANBERRA to the specifications established by UNC, in collaboration with Juan Collar. MALBEK was a second-generation prototype detector, based on a previous prototype fabricated by CANBERRA and delivered to the University of Chicago. The University of Chicago prototype detector is used in the CoGeNT experiment at Soudan [48] [49] [29]. The count rate observed in MALBEK at KURF in 2012 was much higher than the count rate in the University of Chicago detector at Soudan, and the Soudan detector did not show signs of ^{210}Pb contamination [50].

Many possibilities for the source of MALBEK's ^{210}Pb contamination were hypothesized by Juan Collar, Reyco Henning, John Wilkerson, and Mike Yocum of CANBERRA [51] [50]. The presence of a significant quantity of lead within the cryostat was first noticed when it was noticed that the activity of the lead x-ray lines was much higher on the surface of the earth than underground, in response to the higher cosmic-ray flux on the earth's surface [52]. This observation supported the idea that lead contaminated with ^{210}Pb was inside the MALBEK cryostat. The following components were discussed as likely sources of the contamination:

1. Small amounts of solder are present in the MALBEK detector on the point contact, the HV connection, and in the front-end electronics. This solder was believed to be made from ultra-low-background tin, but other solder, which contains lead and has high concentrations of ^{210}Pb, could have been used accidentally. Low-background tin has ^{210}Pb specific activity below 2 Bq/kg, but activities on the order of 1 kBq/kg have been measured in other solder [53].

2. The copper cup surrounding MALBEK's germanium crystal is a custom component. The standard version of the cup has a small-diameter through-hole. The central signal pin passes through this hole to the point contact. MALBEK's copper cup has a larger diameter hole than usual. This was done in an attempt to reduce the capacitance of the detector. The larger diameter exposes the central contact and surrounding surface of MALBEK's germanium crystal to radiation from electronic components in the cryostat, including brass pogo pins and connectors. The brass components near the crystal were known to contain 3–4% lead [54] [55].

3. Lead patches, which serve as centering shims, were installed directly against the outer lithiated contact of the detector. These patches were used to protect the detector from set screws that hold it in place. The patches were believed to have been fabricated from ultra-low-background lead foil provided by Juan Collar to CANBERRA, with a ^{210}Pb specific activity less than 0.013 Bq/kg [56] [57]. If modern lead was accidentally used instead, the ^{210}Pb levels would be higher. The activity of ^{210}Pb in various samples of modern lead range from undetectable levels up to 2500 Bq/kg [32].

Discussion at a Low Energy Spectrum Workshop held at UNC on August 26, 2010 helped to identify the source of ^{210}Pb contamination. At the time of the meeting, an early version of the MALBEK background model contained a contribution to the MALBEK energy spectrum from the lead patches, based on the assumption that the patches were fabricated from ancient lead with activity at the upper limit of the PNNL measurement, 0.013 Bq/kg. After looking at the MALBEK background model, the simulated response of MALBEK to ^{210}Pb in the patches, and the comparison between the model and the spectrum

collected at KURF, Juan Collar suggested using an order-of-magnitude estimate for ^{210}Pb in modern lead, 100 Bq/kg, as the specific activity of ^{210}Pb for the lead patches in the background model to see whether this could explain the spectrum measured at KURF. The shape of the simulated energy spectrum of MALBEK response to ^{210}Pb in the patches was similar to the spectrum measured with MALBEK at KURF, and, using the suggested activity value, the magnitude of the contribution was also similar. Similar tests were done for the solder and brass components, but the spectral shapes were not similar to the spectrum measured at KURF. These results from the MALBEK background model supported the idea that ^{210}Pb from the lead patches was the likely source of contamination. This is discussed in more detail in Section 7.4.1, where the background model is explained.

This work with the MALBEK background model supported the decision to open the MALBEK cryostat and remove the lead patches. This was done in October of 2011, during a trip to CANBERRA by Paddy Finnerty, Graham Giovanetti, Reyco Henning, and John Wilkerson [58]. The lead patches were replaced with Teflon shims and the cryostat was resealed. MALBEK was returned to KURF, where data-taking resumed and the background count rate was significantly reduced.

Chapter 3

SOFTWARE OVERVIEW

3.1 Introduction

The goal of this dissertation is to demonstrate and quantify MAJORANA's understanding of backgrounds to $0\nu\beta\beta$. To achieve this, a measured energy spectrum of the MALBEK detector response to backgrounds at KURF will be compared to a model of the background energy spectrum created from Monte Carlo simulation results.

Data collected from the MALBEK detector with the data acquisition system (DAQ) are processed to perform operations including calculation of energies from digitized waveforms, calibration of energies, and removal of unwanted counts, such as preamplifier-related noise, from the energy spectrum. Similarly, the results of Monte Carlo simulations must be processed to convert them to a format suitable for comparison with the DAQ data. This includes determining total energies from sets of information about energy deposits in the detector active volume, handling energy deposits in dead layers of the germanium detector, and performing other operations to simulate the response of MALBEK.

Monte Carlo simulations of MALBEK response were performed for the backgrounds listed in Appendix K. After processing, a background model was created from the simulation results and compared to data from the MALBEK DAQ. An overview of the Monte Carlo data processing is given in later sections of this chapter. Chapter 4 describes the MALBEK data acquisition system and data processing in depth. Chapter 5 explains details of the Monte Carlo software and processing of simulation results.

3.2 Software packages

MAJORANA uses many software packages for data processing. The packages are discussed in the following sections of this chapter. A brief description of each package is given in the list below. Dependencies between the software packages are shown in Figure 3.1.

ROOT is an object-oriented C++ framework designed for the storage and analysis of high-energy physics data [10].

CLHEP is the Class Library for High Energy Physics, a set of physics-specific C++ libraries [1].

ORCA is the Object-oriented Real-time Control and Acquisition software, an application written in Objective-C for Apple's OSX [9]. ORCA is used to control elements of a data acquisition system and to record their output.

OrcaROOT is a C++ toolkit for converting ORCA output to ROOT files.

MGDO is the MAJORANA GERDA Data Objects, a set of C++ libraries developed by the MAJORANA and GERDA Collaborations for storage and analysis of DAQ and Monte Carlo data [8]. MGDO contains a set of classes for encapsulation of data (e.g. digitized waveforms) and processors for performing common operations on the data (e.g. trapezoidal filtering).

MJOR is the MAJORANA-OrcaROOT software package and is based on OrcaROOT and MGDO. MJOR is a C++ package that performs the conversion of ORCA files to MGDO objects stored in ROOT files.

GEANT4 is a set of C++ libraries for the Monte Carlo simulation of interactions of particles in matter [3], [4].

MAGE is a C++ software framework based on MGDO, ROOT, and GEANT4. MAGE is jointly developed by the MAJORANA and GERDA Collaborations [7].

TAM is the Tree Analysis Modules package, a modular framework for analyzing ROOT `TTrees` [11].

GAT is the Germanium Analysis Toolkit, a collection of C++ libraries and python scripts developed by MAJORANA for processing of MJOR and MAGE output. GAT is based on MGDO, ROOT, and TAM.

MJBM is the MAJORANA Background Model code, which is included as part of GAT.

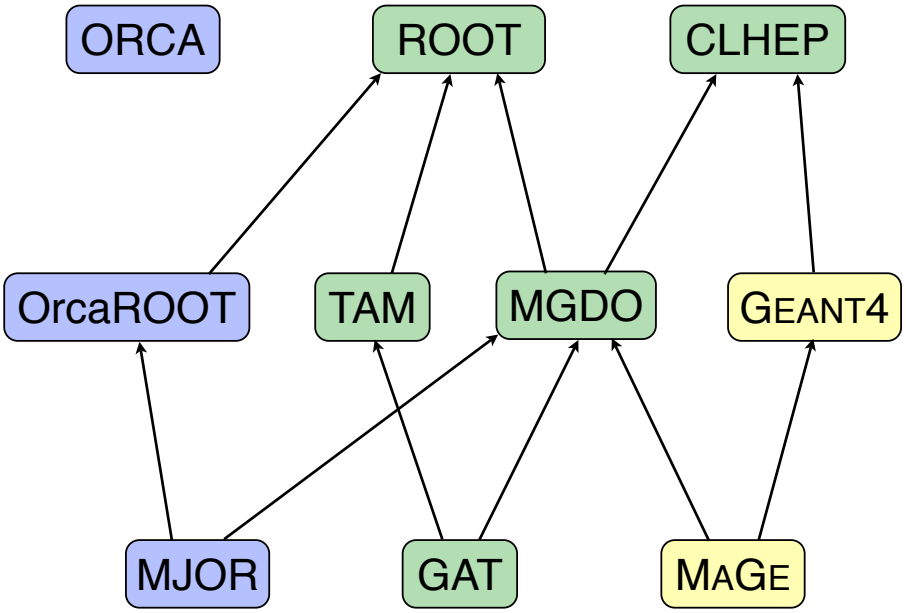

Figure 3.1: Software dependencies. Each rounded rectangle represents a software package. Arrows represent dependencies, e.g. MJOR depends on OrcaROOT and MGDO. Blue packages are used for collection and processing of DAQ data. Yellow packages are used for generation and processing of Monte Carlo data. Green packages are used for both DAQ and Monte Carlo data. No packages depend explicitly on ORCA, but OrcaROOT is developed concurrently with ORCA and is used to decode ORCA files. MAJORANA develops MJOR and GAT; MGDO and MAGE are developed jointly with GERDA.

3.3 Tiered data processing

Data from the MALBEK DAQ is typically recorded in consecutive "runs" of about one hour. Each run produces an output file that is stored on disk and is identifiable by a run number. A run is processed in three steps, shown in the left side of Figure 3.2. The steps and software involved will be described later in this chapter. Each processing step produces a new "tier" of data for the run. Runs are processed separately until after Tier 3, when multiple runs are combined into data sets. Separate processing of runs allows quick generation of data tiers on a computing cluster.

The goal of processing the DAQ data is to produce a reduced dataset of calculated quantities for each waveform, e.g. energy and time stamp, where spurious events have been removed and live time is well understood. Each step in the data processing has a specific purpose, and the steps are ordered so that processing time and file size decrease until the final tier is produced. To ensure that the effects of each processing step are identifiable and reproducible, waveforms are assigned unique identifiers so that they may be traced from the original digitized version to the final tiers. Software version information is also recorded at each step.

Results of Monte Carlo simulations are processed in a tiered approach similar to the DAQ data stream, but the Monte Carlo tiers are distinct from ORCA data tiers. Each Monte Carlo run is produced for a specified number of trials of similar events, such as ^{60}Co decay in a specified volume. Only two data tiers of Monte Carlo data are required, and they are shown in the right side of Figure 3.2. The goal of the Monte Carlo data processing is to produce a final tier that can be compared to final tier DAQ data. Like the DAQ process, event identifiers and software version information are carried through to the final tier of Monte Carlo results. This chapter will give an overview of the processing steps for the DAQ and Monte Carlo data.

3.4 Tiers of data from the MALBEK DAQ

Data from the MALBEK detector are collected with a Struck waveform digitizer, controlled by a computer running ORCA. Details of the DAQ are given in Section 2.3. The ORCA

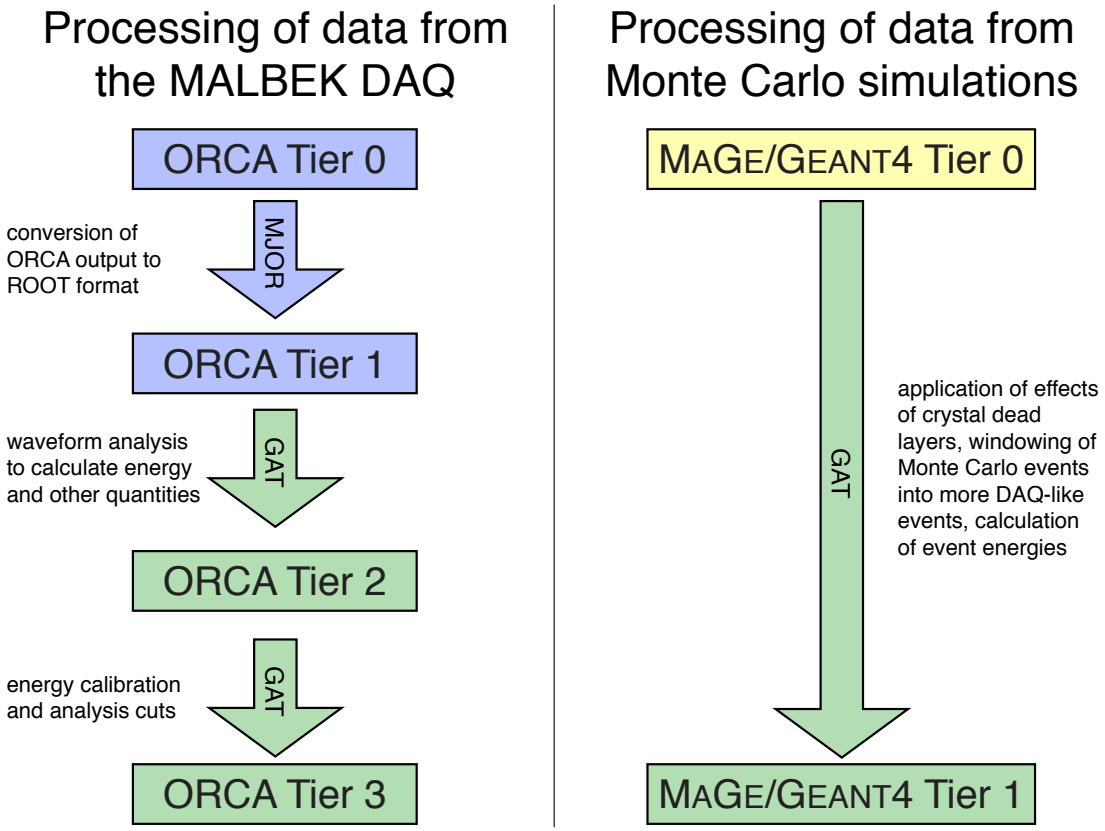

Figure 3.2: Overview of ORCA and MAGE/GEANT4 data tiers and processing steps. Data tiers and processing steps of ORCA data from the MALBEK DAQ are on the left. Tiers and processing steps of Monte Carlo (MC) results of MAGE/GEANT4 simulations are on the right. Arrows represent processing steps that generate a data tier. Rectangles represent a tier of ORCA or MAGE/GEANT4 data stored on disk. Blue data tiers are files containing data objects that are exclusive to ORCA data. Yellow tiers contain data objects exclusive to MC data. Green tiers contain combinations of ORCA-specific or MC-specific data objects and objects common to ORCA and MC data.

data tiers are summarized in Table 3.1 and described in more detail below.

3.4.1 ORCA Tier 0 output

Each ORCA run produces a Tier 0 output file that consists of an ORCA XML header and data from a waveform digitizer and LN-fill controller. ORCA minimizes run-time processing of the data, so the ORCA file contains data in the format in which it is output from the digitizer and fill controller. After a run is recorded by ORCA, the output file is transferred to a remote computer for processing.

3.4.2 ORCA Tier 1 output

In the first step of ORCA data processing, Tier 0 ORCA output files are converted to ROOT output using MJOR. The Tier 1 ORCA output produced by MJOR consists of ROOT files of data encapsulated in MGDO classes. The data are stored in a ROOT `TTree`, where each event is an entry in the tree. ROOT output is useful because arbitrary distributions can be easily visualized in histograms or graphs and ROOT files are a portable, widely accessible format. MGDO provides a convenient ROOT-based format for storing data that is independent of DAQ or Monte-Carlo simulation software.

3.4.3 ORCA Tier 2 output

Tier 1 ORCA output from MJOR is processed with GAT. The GAT script `process_malbek-_mjor_files_high_e_only.py` produces Tier 2 data for this analysis. At this processing step, baseline subtraction, pole-zero correction, and trapezoidal filtering are performed. Waveform rise-times are measured and the energy of the waveform, which is proportional to the waveform height, is calculated. The Tier 2 data consist of MGDO and GAT objects. Tier 2 data files do not contain raw waveforms, but do contain information extracted from the waveforms such as average baseline value, rise time, and energy. For each waveform, timing information relative to the preamp inhibit signal (time to next inhibit and time since last inhibit) are written to file. Similar timing information relative to the pulser is also written.

Table 3.1: Summary of ORCA data tiers. The monospace font indicates C++ objects. MGDO classes have the prefix `MG`; GAT classes have the prefix `GAT`; ROOT classes have the prefix `T` and ROOT data types have the suffix `_t`.

Contents	**Description**
Tier 0: ORCA output file	
XML header	run-level information
Struck SIS3302 digitizer output	digitized waveform data
AMI LN level sensor output	LN level data
Tier 1: MJOR output ROOT file	
`TTree MGTree`	tree of waveform data; one entry per event with:
`MGTRun run`	run-level information
`MGTEvent event`	each waveform in the event
`TTree ami`	tree of LN fill data; one entry per event with:
`Float_t level`	LN level
`UInt_t time`	time of measurement
`UShort_t channel`	channel of measurement
Tier 2: GAT output ROOT file	
`TTree fTree`	wfm. analysis results; one entry per event with:
`GATAnalysisEvent fAnalysisEvent`	waveform time stamp, calculated energy
`GATMalbekEvent fMalbekEvent`	detailed waveform analysis results
`GATMalbekEventFlag fEventFlag`	flags to identify anomalous waveforms
`GATTimeDifference pulserTimeDiff`	time since last/to next event in pulser channel
`GATTimeDifference inhibitTimeDiff`	time since last/to next event in inhibit channel
`GATTimeDifference highEnergyTimeDiff`	time since last/to next event in energy channel
`GATMalbekSlowControlData fSlowControlData`	LN level and accelerometer information
Tier 3: GAT output ROOT file	
Same as Tier 2	energies calibrated; vetoes applied to remove pulser-coincident and inhibit-coincident events

3.4.4 ORCA Tier 3 output

Tier 2 ORCA output from GAT is processed with another GAT script, `malbek_tier3_creator.py`, to produce Tier 3 output. The Tier 3 data format is the same as Tier 2, but timing information is used to remove events coincident with the MALBEK preamp inhibit signal.

3.5 Tiers of Monte Carlo data

Monte Carlo simulation results are produced with the MAJORANA-GERDA software package MAGE. MAGE is described in Section 5.3. The MAGE/GEANT4 data tiers are summarized in Table 3.2 and described below.

3.5.1 MAGE/GEANT4 Tier 0 output

The result of a MAGE/GEANT4 simulation is a Tier 0 ROOT data file containing locations, energies, and other information about simulated energy deposits in the germanium crystal. The encapsulation of MAGE/GEANT4 results for storage in Tier 0 Monte Carlo output files is described in Chapter 5.

3.5.2 MAGE/GEANT4 Tier 1 output

Each ROOT file of MAGE/GEANT4 output is processed with GAT to generate a ROOT file of MAGE/GEANT4 Tier 1 results. GAT contains a set of C++ libraries that perform operations on MAGE/GEANT4 results such as the application of dead layers, quenching corrections for energy deposited by nuclei, and other processing to make Monte Carlo results more similar to DAQ data. GAT processing of MAGE/GEANT4 results is explained in Section 5.9.

3.6 Final processing of data from the MALBEK DAQ

After the tiered data processing, where each ORCA run is handled separately, multiple runs are combined into a dataset in a single file, which can be compared with Monte Carlo simulation results. Several datasets are discussed in this dissertation, including shielded

Table 3.2: Summary of MAGE/GEANT4 data tiers. The monospace font indicates C++ objects. MGDO classes have the prefix `MG`; GAT classes have the prefix `GAT`.

Contents	**Description**
Tier 0: MAGE/GEANT4 output ROOT file	
`TTree fTree`	tree of results; one entry per event with:
`MGTMCRun fMCRun`	run-level information
`MGTMCEventHeader eventHeader`	event-level information
`MGTMCEventSteps eventSteps`	data for each interaction in the crystal
`MGTMCEventSteps eventPrimaries`	primary particle data
Tier 1: GAT output ROOT file	
`TTree fTree`	tree of results; one entry per event with:
`MGTMCRun fMCRun`	run-level information
`GATAnalysisEvent fAnalysisEvent`	event time stamp, energy
`GATEventWeight fMCEventWeight`	importance-sampling track weight data
`GATRandomValues fRandomValues`	Gaussian-distributed random values
`MGTCrystalData MGTCrystalData`	description of crystal geometry and dead layers

data from 2010, unshielded background data from August 2011, and calibration source data from August 2011. When runs are combined into a single dataset, the Tier 3 data format is maintained, but all runs are merged into one file. Anomalous runs (with short run times or high event rates) are discarded, and the total live time is computed. This final data processing is described in Chapter 4.

3.7 Comparing data from the MALBEK DAQ to Monte Carlo results

The energy spectrum from a MALBEK ORCA dataset is the sum of many contributions from different sources, typically radioactive decays. Each contribution can be characterized as the response of the detector to a single contaminant, e.g. ^{60}Co in a copper component inside the cryostat. An energy spectrum of detector response can be simulated for each contribution using MaGe/Geant4. An arbitrary number of Monte Carlo trials may be performed in a given run, and an arbitrary number of runs may be generated. The final tier of MaGe/Geant4 data for the runs can be used to produce a histogram of the simulated energy spectrum of MALBEK response to the specified number of decays.

An ORCA energy spectrum can be compared to the MaGe/Geant4 energy spectrum using the Majorana Background Model (MJBM) code contained in GAT. An energy spectrum histogram is produced from a set of MaGe/Geant4 runs describing the same contribution. The MJBM code normalizes each MaGe/Geant4 energy spectrum contribution to represent detector response to the number of decays expected in the ORCA dataset. The number of expected decays must be calculated from the live time of the ORCA dataset and the expected decay rate, which is determined from the component mass, radiopurity data for the component material, and possibly additional data such as the cosmogenic exposure history of the component. The simulation results determine the efficiency for a decay to deposit a given amount of energy in the detector.

Using the MJBM code, the results of many MaGe/Geant4 simulations of MALBEK response to expected backgrounds are combined to produce a composite background model. This process is explained and results are presented in Chapter 7.

Chapter 4

MALBEK ORCA DATA PROCESSING

4.1 Introduction

This chapter describes processing of MALBEK data into an energy spectrum that can be compared to Monte Carlo results. The production of each data tier, introduced in Chapter 3, is explained in detail. Data cuts to remove spurious counts are described.

Three sets of shielded background data collected at KURF are discussed in this dissertation. All MALBEK datasets described in this dissertation were collected at KURF with the ORCA DAQ. These datasets contain the measured energy-spectrum response of MALBEK to background radiation from the detector and experimental hall at KURF. Each of these datasets were collected while MALBEK was in the lead shielding described in Chapter 2:

Dataset I was collected October through November of 2010, while MALBEK was in a lead and polyethylene shield at KURF.

Dataset II was collected during 2011, after Dataset I. This dataset is similar to Dataset I, but contains more exposure.

Dataset III was collected in late 2011 and in 2012, after the cryostat was opened at CANBERRA.

Dataset I was studied extensively during development of the analysis software and data cuts. Datasets II and III were blinded until results of background modeling, including fits of Monte Carlo results to the Dataset I energy spectrum, were complete. Information about these three datasets is summarized in Table A.1. Dataset I is presented in this chapter and will be used to demonstrate waveform processing and cuts that are applied to produce an energy spectrum from DAQ data. The energy spectrum generated from Dataset I appears

in Figure 4.1. The spectrum will be shown in more detail in the following sections. The same processing methods were used to generate energy spectra from Datasets II and III.

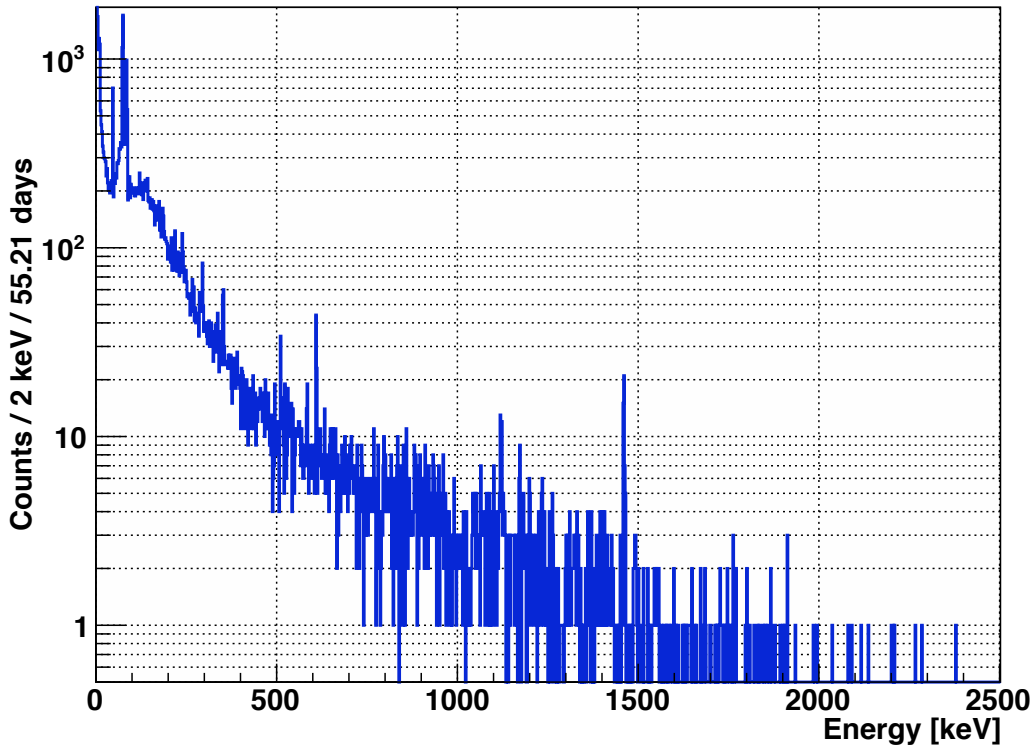

Figure 4.1: The Dataset I energy spectrum. This energy spectrum was created from the unamplified ionization energy channel. Pulser-related and preamplifier-related counts have been removed. Some visible features include a ^{210}Pb gamma peak at 46 keV, Pb x-ray lines near 80 keV, a ^{214}Bi gamma peak at 609 keV, and a ^{40}K gamma peak at 1461 keV. Due to the pulsed-reset preamplifier, there are no counts above 2500 keV.

Some datasets collected while MALBEK was unshielded at KURF will be discussed in this chapter. Information from these datasets will also be used in later chapters. These datasets contain high-statistics data that are useful for characterizing MALBEK:

ORCA/Struck ^{133}Ba (+ backgrounds): measurement of a ^{133}Ba calibration source.

ORCA/Struck ^{60}Co (+ backgrounds): measurement of a ^{60}Co calibration source.

ORCA/Struck unshielded backgrounds: measurement of background radiation underground at KURF.

The ^{133}Ba and ^{60}Co datasets include background environmental radiation from the KURF experimental hall; the unshielded background dataset is a measurement of these backgrounds.

4.2 Production of ORCA Tier 1 data with MAJORANA-ORCARoot

ORCA data are processed in a tiered approach, as introduced in Chapter 3. Each ORCA run produces a Tier 0 ORCA output file, and MAJORANA-ORCARoot (MJOR) is used to create a Tier 1 ROOT file from each ORCA file. ORCA Tier 1 data files contain the same information as ORCA Tier 0 data files, but the Tier 1 data is in a more convenient ROOT format. An overview of the contents of the ORCA data tiers was given in Table 3.1 in Chapter 3. The ORCA data tiers and data processing are explained in more detail in this chapter.

Several applications are included with MJOR. The MJOR application `majorcaroot_basic_malbek` is used to process MALBEK ORCA data. The MALBEK MJOR application stores data from the Struck SIS3302 in a ROOT `TTree`. The `TTree`, called `MGTree`, consists of the following branches, which contain one entry per event recorded by the SIS3302:

- `run`: an MGDO `MGTRun` object of run-level information, including the ORCA run number and run start time.

- `event`: an MGDO `MGTEvent` object of event-level information. For each waveform in the event, the `MGTEvent` contains a pair of objects:

  - An `MJTSIS3302` digitizer data object, which contains the time stamp of the waveform, a number to identify the digitization channel, and an index identifying the waveform within the run.
  - An `MGTWaveform` waveform data object, which includes the length of the recorded waveform, the ADC value of the waveform at every sampled point, and the sampling frequency.

The MALBEK data analyzed here contains only one pair of waveform and digitizer objects per event.

In addition to the ROOT `TTree` of digitized waveform data, a `TTree` of data from the MALBEK AMI LN controller is created. This tree, called `ami`, contains one entry per LN level data point. Each entry contains the channel number in which the LN level was measured, the LN level as a percentage, and the time of the measurement. LN levels are recorded every 10 seconds from the detector dewar and the radon purge dewar.

4.3 Production of ORCA Tier 2 data with GAT

Each ROOTified ORCA Tier 1 file is processed with the GAT Python script `process_malbek_mjor_files_high_e_only.py` to generate an ORCA Tier 2 data file. This second stage of ORCA data processing has two main purposes: to calculate energies and other quantities from waveforms and to calculate timing information that can be used later to identify pulser-related and inhibit-related events.

In the Python script, the GAT processor `GATMGTEventMalbekWfmProc` is used to extract information from MALBEK waveforms. This processor uses an instance of the GAT class `GATMGTEventMalbekWfmChannelProc` to determine energy and rise time of waveforms in the unamplified ionization energy channel. This section describes waveform processing and the calculation of relative timing information.

4.3.1 Waveform energy calculation

The following steps are performed to calculate the waveform energy:

1. *Baseline removal*: the first samples of the waveform are averaged to determine the baseline. This baseline value is subtracted from each data point in the waveform using MGDO's `MGWFBaselineRemover`.

2. *Pole-zero correction*: the baseline-subtracted waveform is convolved with a function to account for exponential decay using MGDO's `MGWFPoleZeroCorrection`.

3. *Trapezoidal filtering*: a trapezoidal filter is applied to the baseline-subtracted, pole-zero-corrected waveform using the MGDO processors `MGWFTrapezoidalFilter` and `MGWFExtremumFinder`. The energy of the waveform, in arbitrary units, is calculated from the maximum value of the trapezoidal-filtered waveform. This energy is stored in the Tier 2 output.

Each step in the calculation of waveform energy is shown for an example waveform in Figure 4.2. The parameters used for waveform processing are listed in Table 4.1.

Table 4.1: Waveform processing parameters for Dataset I.

Parameter	**Value**
Baseline-averaging region	0 – 4 μs
Pole-zero correction time constant	69.88 μs
Trapezoidal filter ramp time	11 μs
Trapezoidal filter gap time	5 μs
Number of samples for median filtering	11

4.3.2 Waveform rise time determination

The rise time of a waveform is useful for identifying slow, energy-degraded pulses that originate from interactions in the transition dead layer. For small amplitude (low energy) waveforms, the ability to identify slow pulses is limited by noise. To mitigate the effects of noise, we calculate the 10–90% rise time. Even on a relatively noisy waveform, the 10% and 90% heights can be identified accurately. Using a large range (80%) of the waveform's amplitude ensures an accurate estimate of rise time.

At energies on the order of 100 keV, the 10–90% rise time becomes a less accurate identifier of signals from the transition dead layer. Many of the counts in the Dataset I

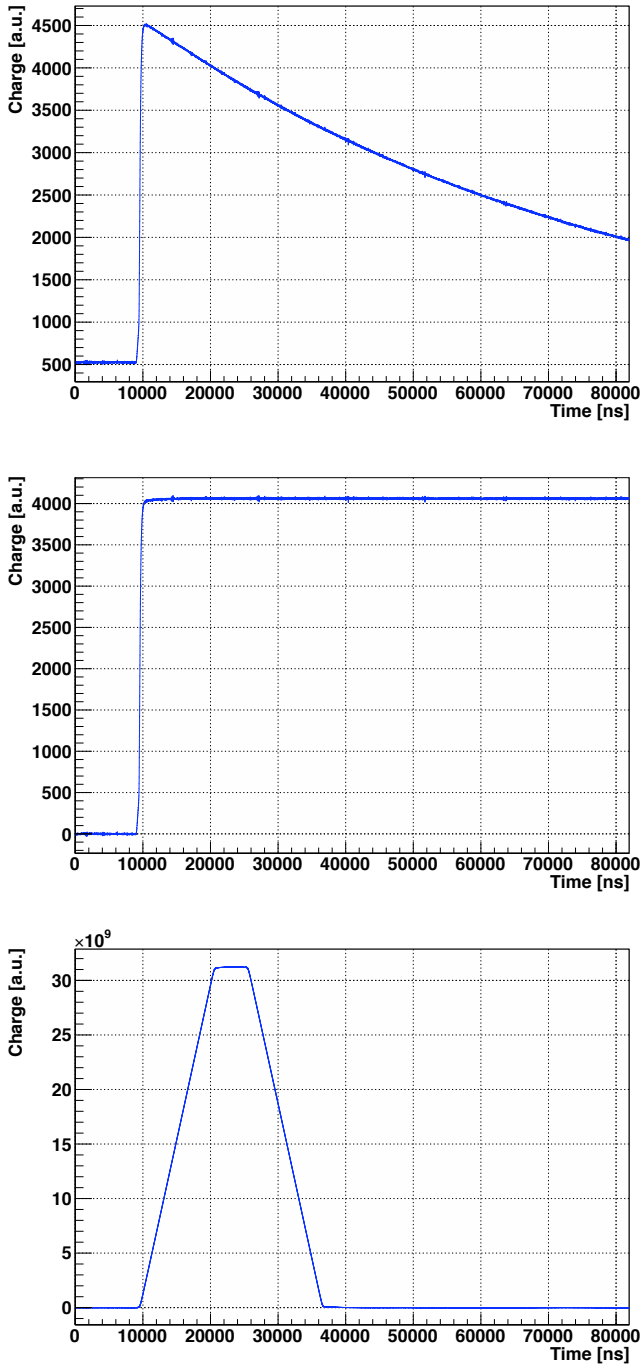

Figure 4.2: Processing a sample waveform to calculate energy. The waveform is shown before any processing (top), after baseline subtraction and pole-zero correction (middle) and after trapezoidal filtering (bottom). The energy of this waveform is 500 keV.

energy spectrum are due to gamma interactions in the germanium crystal. High-energy gammas have a large probability of Compton scattering in germanium, and they will often interact in multiple locations. Monte Carlo simulations by Roth et al. showed that full-energy gamma peaks in a germanium detector are dominated by multi-site events down to energies of about 150 keV [59]. Figure 4.3, from the paper, shows the fraction of single-site and multi-site contributions to a full-energy photopeak as a function of photopeak energy.

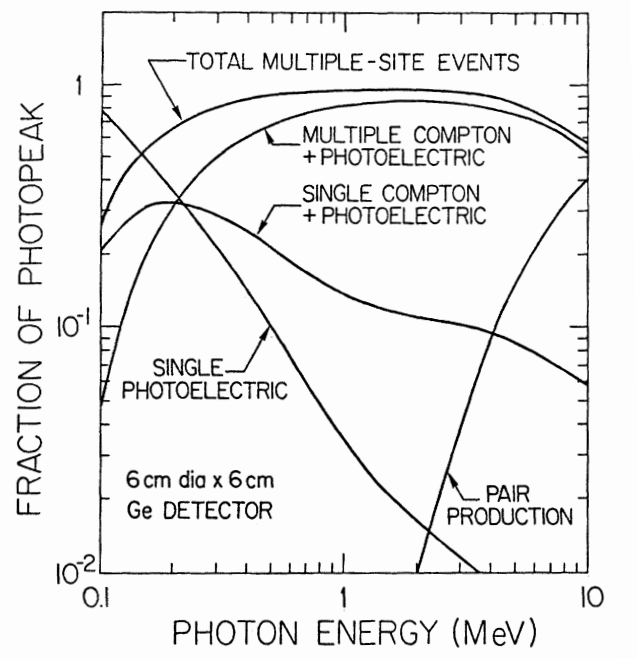

Figure 4.3: Contributions of energy-loss mechanisms to a full-energy photopeak. Reproduced from Roth et al. © 1984 IEEE [59].

Due to the long drift times characteristic of PPC detectors, ionization charge created by energy deposits at two locations in the detector can arrive at the point contact separated by a few microseconds. Using the 10–90% rise time, these multi-site waveforms are indistinguishable from slow pulses. David Radford of ORNL proposed an alternate metric for identifying high-energy slow pulses: the 80–100% rise time. Both the 10–90% and 80-100% rise times are calculated for each waveform in the unamplified ionization-energy channel.

The 10–90% rise time is calculated with the following procedure:

1. A copy is created of the baseline-subtracted and pole-zero corrected waveform used during energy calculation.

2. An 11-sample median filter is applied to remove any single-sample spikes in the waveform. The MGDO processor `MGWFMedianFilter` is used to perform the median filter.

3. The full height of the median-filtered waveform is calculated with MGDO's `MGWFExtremumFinder`. The time points at which the waveform reaches 10% and 90% of its full height are calculated using MGDO's `MGWFRisetimeCalculation`. The difference in these values is the 10–90% rise time.

The 80–100% rise time is calculated with a procedure developed by David Radford. This method is notably different from the 10–90% rise-time calculation because it starts with a baseline-subtracted (but not pole-zero-corrected) waveform and uses the derivative to find the 100% point. The 80–100% rise time is calculated with the following procedure:

1. A copy of the baseline-subtracted waveform is processed with a `MGWFTrapezoidalFilter` instance. The waveform is trapezoidal filtered with a ramp time of 400 ns and a gap time of 20 ns. This processing is comparable to taking the derivative of the waveform and performing some smoothing.

2. The time at which the waveform reaches 100% is calculated from the zero crossing of the derivative waveform. MGDO's `MGWFExtremumFinder` is used to find the time at which the derivative waveform is at its maximum. The first zero crossing after the maximum is found. This time location is reported as the 100% time.

3. A copy of the baseline-subtracted waveform is smoothed with the `MGWFMedianFilter` 11-sample median filter.

4. The full height of this smoothed, baseline-subtracted waveform is calculated with `MGWFExtremumFinder`. The time at which the waveform reaches 80% of its full height is found with `MGWFRisetimeCalculation`. This time is reported as the 80% time.

5. The difference between the 80% and 100% times is reported as the 80–100% rise time.

Rise time calculations for two example waveforms are shown in Figure 4.4. Both of these waveform are "fast" pulses that did not originate from the transition layer of the detector. One of the example waveforms is a 10-keV single-site event. The noise in this trace is substantial compared to the height of the pulse, so the determination of the 80–100% rise time is difficult. The second example is a 1236-keV multi-site waveform. The 10–90% rise time of this waveform is relatively long as it is composed of energy depositions in two separate locations in the germanium crystal, which took different amounts of time to reach the signal contact.

4.3.3 ORCA Tier 2 Data storage

Each Tier 2 file is a ROOT file, which contains a `TTree` of data extracted from the Struck SIS3302 waveforms. The information stored in a Tier 2 file is described below. The `TTree`, named `fTree`, contains the same number of entries as the Tier 1 `TTree`: one entry per waveform recorded by the Struck card. Each `fTree` entry contains the following:

- `fAnalysisEvent`: a `GATAnalysisEvent` object of event-level information, including run and event identification numbers. The `GATAnalysisEvent` contains one `GATAnalysisEventData` object with information about the waveform in the event, including the energy and time stamp. The `GATAnalysisEvent` and `GATAnalysisEventData` classes are described in Tables E.1 and E.2, respectively.

- `fMalbekEvent`: a `GATMalbekEvent` object that contains a pair of objects with information about waveform processing:

  - `GATMalbekWaveformProcessingPars`: the settings used to process waveforms, e.g. trapezoidal filter ramp time and gap time.
  - `GATMalbekWaveformAnalysisData`: the results of waveform processing, e.g. waveform energy and rise time.

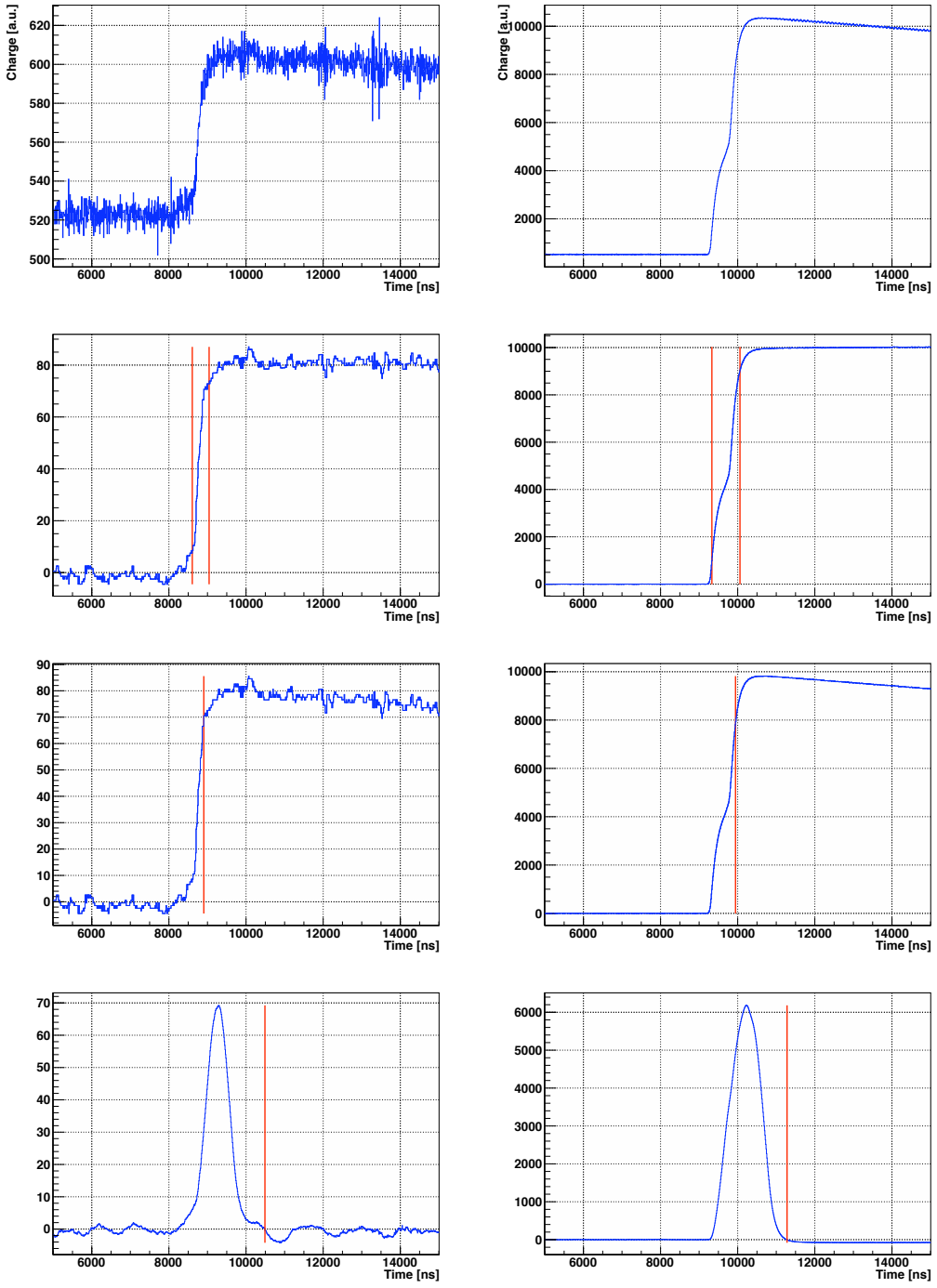

Figure 4.4: Processing sample waveforms to calculate rise time. From top to bottom: the raw waveform; the 10% and 90% locations; the 80% location; the 100% location. Left: a 10-keV single-site waveform with 10–90% rise time of 0.44 μs and 80–100% rise time of 1.59 μs. Right: a 1236-keV multi-site waveform with 10–90% rise time of 0.73 μs and 80–100% rise time of 1.34 μs.

- `pulserTimeDiff`: a `GATTimeDifference` object containing timing information relative to the pulser channel, including the time to next and time since last pulser waveform.

- `inhibitTimeDiff` a `GATTimeDifference` object containing timing information relative to the inhibit channel.

- `highEnergyTimeDiff` a `GATTimeDifference` object containing timing information relative to the unamplified ionization energy channel.

- `fSlowControlData` information about the LN levels in the detector dewar and purge dewar.

4.4 Production of ORCA Tier 3 data with GAT

The goal of Tier 3 data processing is to reduce the size of the dataset and to ensure that runtime and live-time are well understood. The structure of ORCA Tier 3 ROOT files is similar to the Tier 2 files, but events in the inhibit and pulser channels are removed from the `TTree` of SIS3302 data. Events from the amplified ionization energy channel are also removed, since they are not used in this analysis. After these cuts, only events from the unamplified ionization energy channel remain. Some additional cuts are applied to the unamplified ionization energy channel data to remove events associated with the preamplifier. These "timing" cuts rely on coincidence information and are described below.

4.4.1 Timing cuts

Counts associated with the pulser and preamplifier resets contribute to the energy spectrum. These counts are identified using information in the `GATTimeDifference` timing objects in the Tier 2 data. The counts are then removed with a series of timing cuts, performed in the order listed below. Histograms of time and energy distributions are created and retained so that some information about vetoed events is available in the Tier 3 data.

1. *Run edges*

   Waveforms in the unamplified energy channel that occur before the first signal and

after the last signal in the pulser channel are removed. This creates well-defined run start and stop times. Prior to this cut, the run stop time is not known and the run duration is not well defined. This cut discards a small amount of livetime, typically 10 seconds out of 3600 seconds, or 0.28%.

2. *Inhibit-coincident counts*

   Waveforms in the unamplified energy channel with timestamps within ±1 ms of a waveform in the inhibit channel are discarded. A typical interval between resets is 40 ms, so 5% of livetime is removed. The time distribution of unamplified energy counts relative to inhibit counts is shown in Figure 4.5.

3. *Long inhibit intervals*

   Inhibit signals from the pulse-reset preamplifier typically occur every 40 ms or less. These signals are recorded by channel 2 of the SIS3302. If two counts in the inhibit channel are separated by a time interval of more than 60 ms, it is assumed that the inhibit channel failed to record a signal. Unamplified ionization energy data in the time interval between the two counts are discarded. This occurs approximately once every 10^5 resets.

4. *Long pulser intervals*

   The 0.1-Hz (10-second period) pulser signal is sent into channel 5 of the Struck SIS3302. If two counts in channel 5 are separated by a time interval of more than 10.1 seconds, it is assumed that the SIS3302 failed to record a signal from the pulser. This occurs for approximately 0.16% of signals in the pulser channel in Dataset I. Unamplified energy channel data in the time interval between the two counts are discarded.

5. *Pulser-coincident counts*

   Waveforms in the unamplified energy channel with timestamps within 1.0 μs of a waveform in the pulser channel are identified. The time distribution of unamplified energy counts relative to pulser counts is shown in Figure 4.6. These counts are

identified in the Tier 3 data, but are not removed because they are useful for measuring livetime and energy resolution in later data processing. Identifying information in the Tier 3 data can be used to remove these counts if needed.

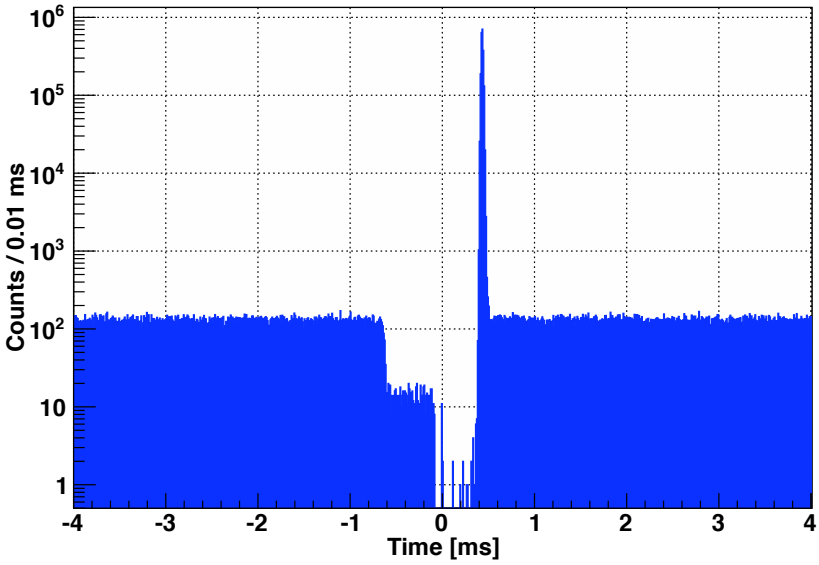

Figure 4.5: Time distribution of counts in the unamplified ionization-energy channel relative to counts in the inhibit channel. This plot was created from Dataset I. There are three main features in the distribution: a flat continuum below -1 ms and above 1 ms, a sharp peak near 0.4 ms, and a decrease in counts between -0.6 and 0.4 ms. Random coincidences create the flat continuum. The unamplified ionization-energy channel triggers on noise associated with the resets of the preamplifier, which causes the peak. The ORCA script that removes inhibit-related waveforms creates the deficit in counts.

The energy spectrum before and after application of these five cuts is shown in Figure 4.7. Visible features in the spectra include reset-related peaks at 2 and 40 keV, peaks due to ^{68}Ge near 10 keV, the pulser peak at 35 keV, a ^{210}Pb gamma peak at 46 keV, and Pb x-ray lines near 80 keV. The energy spectra of counts removed by each cut are shown in

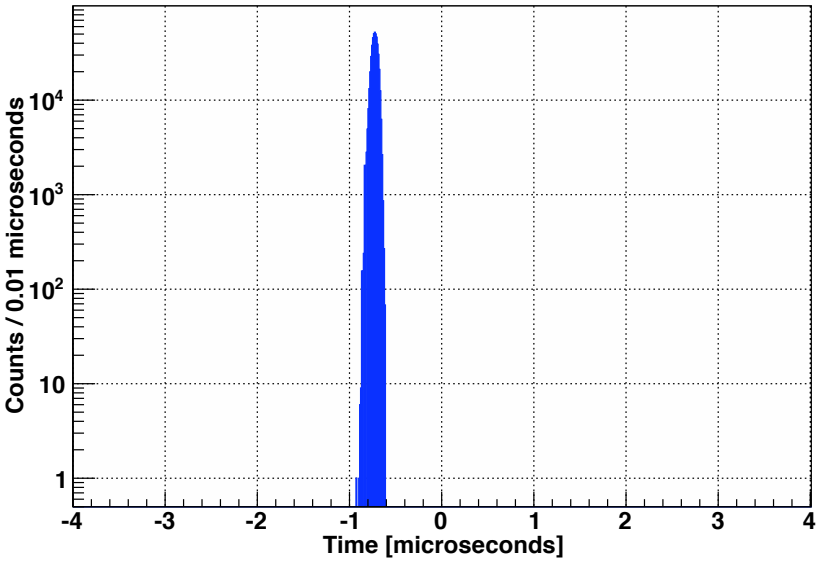

Figure 4.6: Time distribution of counts in the unamplified ionization-energy channel relative to counts in the pulser channel. This plot was created from Dataset I. The distribution is a narrow peak near -0.8 μs. The peak is offset from zero because test pulses observed in the unamplified ionization-energy channel have slightly earlier time stamps than the test pulses observed in the pulser channel.

Figure 4.8. Each of these energy spectra are shown separately in Figure 4.9. The effects of the cuts are summarized in Table A.2.

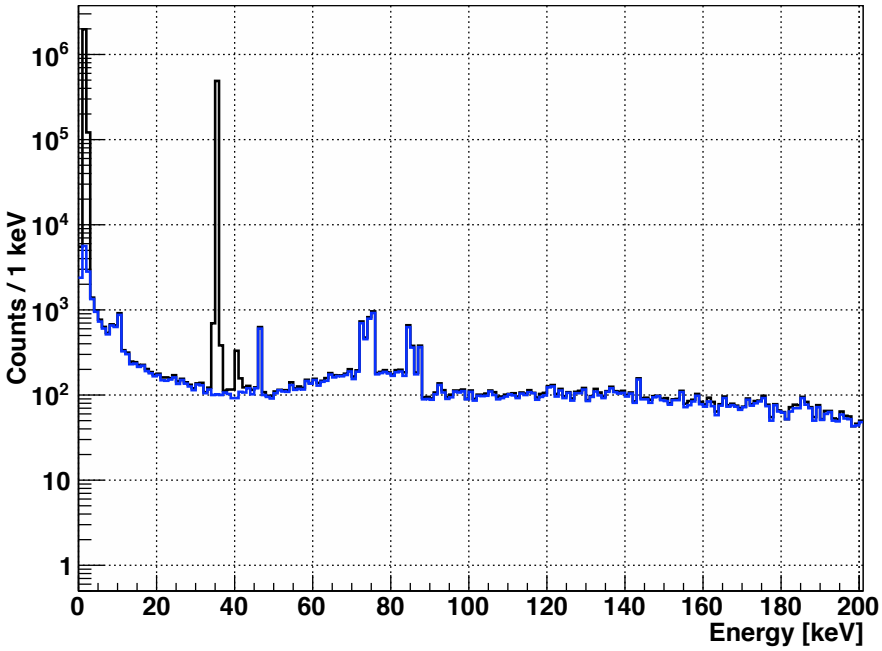

Figure 4.7: The energy spectrum before and after cuts, below 200 keV. The shielded background dataset, Dataset I, is shown before (black) and after (blue) timing cuts.

4.5 Creation of datasets

After ORCA Tier 3 data processing has been performed, datasets are generated from the Tier 3 data files using a Python script. Each dataset, e.g. Dataset I, is a single ROOT file in which the Tier 3 ROOT files from each run in the dataset have been combined using ROOT's `hadd` command-line utility. Each dataset has the same structure as a Tier 3 file: the `TTree`s `fTree` and `ami` and histograms of energy and time distributions for all events in the dataset. The majority of data-processing has been performed during the generation of Tiers 1–3, but a few cuts are applied and additional information is calculated:

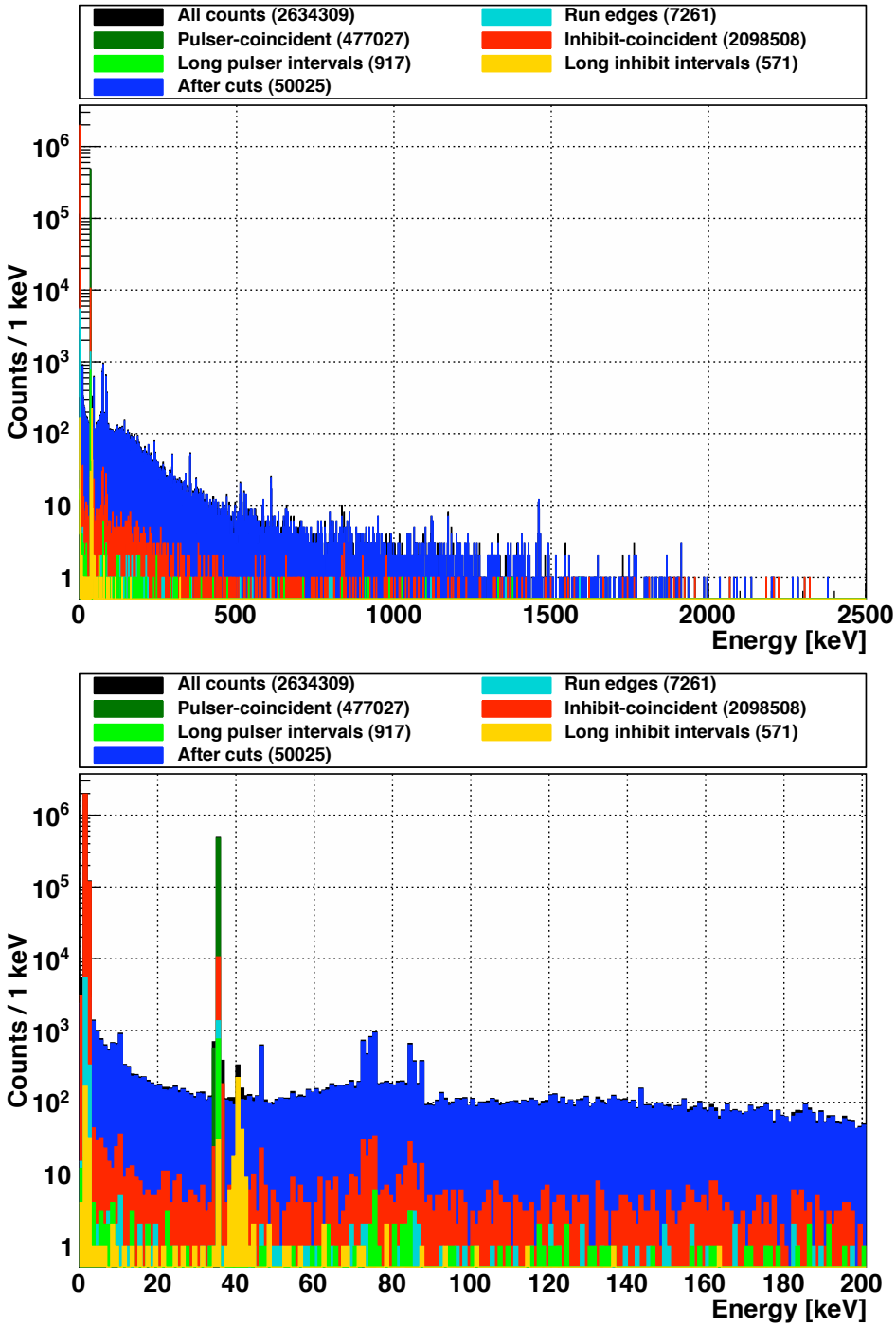

Figure 4.8: Effects of timing cuts on the energy spectrum. For each histogram, the number of counts at all energies is listed in parentheses. These plots were created from Dataset I.

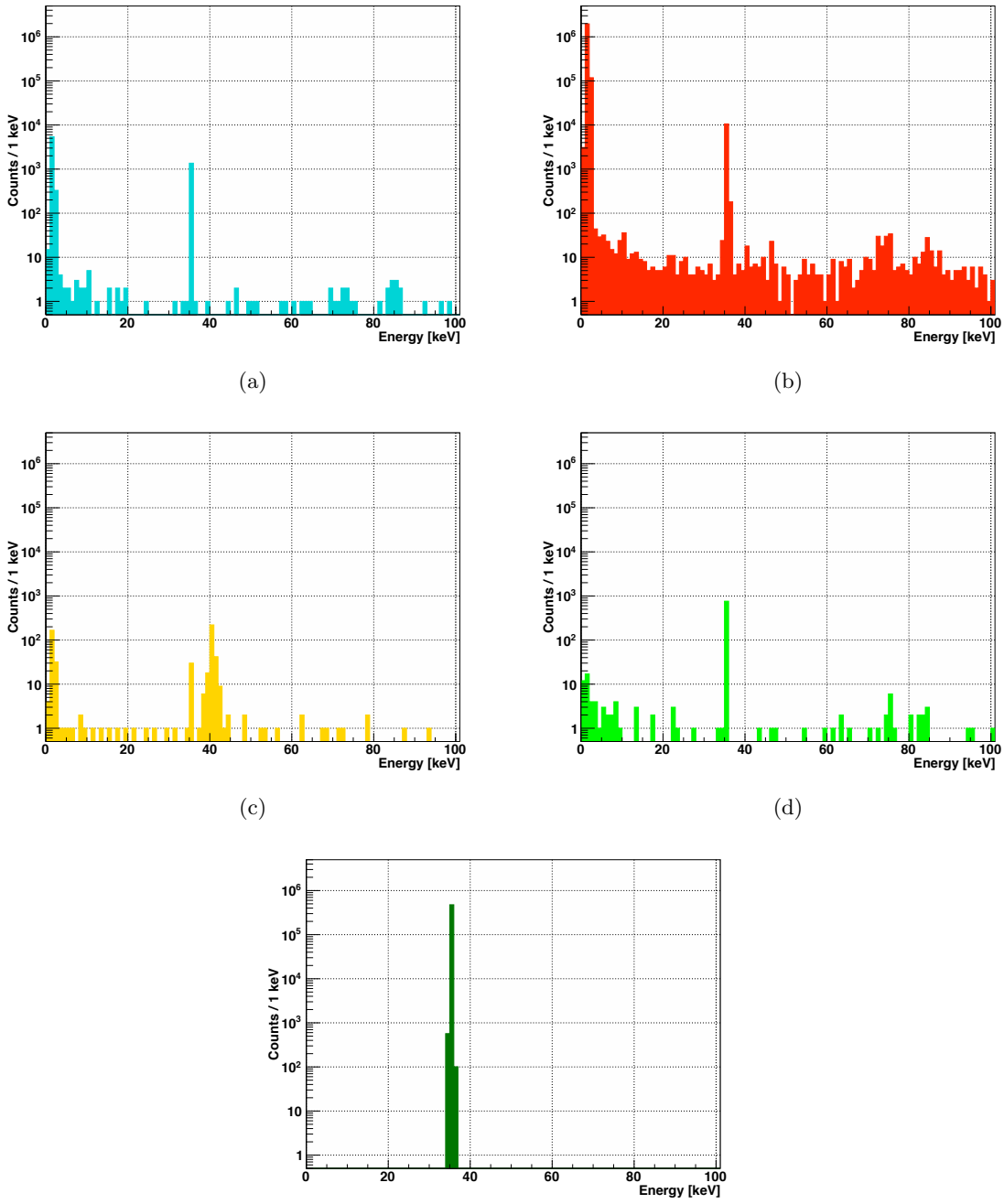

Figure 4.9: Energy spectra of counts vetoed by timing cuts, below 200 keV. Counts removed by each timing cut are shown: run edges (a), coincident with pulsed-reset inhibit signal (b), in long pulsed-reset inhibit intervals (c), in long pulser signal intervals (d), and coincident with pulser (e). These plots were created from Dataset I.

- Short runs, those less than 95% of the nominal run length, are removed. These runs may be the result of ORCA crashes, which we would like to exclude. In Dataset I, 14 of 1412 runs were removed by this cut.

- To remove burst-type noise, the distribution of number of counts above 5 keV in each run is fit with a Poisson distribution. Runs with anomalously high number of counts, greater than 99.99% of the Poisson distribution, are removed. Dataset I has a mean of 26.4 counts per run. Runs with greater than 47 counts were removed. This cut removed zero runs from Dataset I. The fit result for Dataset I is shown in Figure 4.10. In general, this cut should be used carefully because it could have a small biasing effect.

- The cumulative live time is calculated from the area of the pulser peak. Cumulative run time and live time information are stored in a `GATRunTimeInfo` object and saved in the ROOT file.

4.6 Identification of slow pulses

As described in Section 4.3.2, two rise times are calculated for each waveform: the 10–90% rise time and the 80–100% rise time. The rise time of a waveform is useful for identifying energy deposits in the transition layer of the detector, which are degraded in energy. The distribution of rise time as a function of energy is shown for Dataset I in Figure 4.11. In the figure, there is a band of fast pulses with a 10–90% rise time of approximately 0.4 μs and an 80–100% rise time of approximately 1.4 μs. At low energies, the bands widen as it becomes difficult to measure the rise time of small amplitude pulses. At all energies, a continuum of counts is visible at large rise times.

The two rise time distributions look similar for Dataset I. The ^{60}Co dataset is useful for comparison because it has two high-intensity gamma peaks at 1173 and 1332 keV. The rise-time distributions for the ^{60}Co dataset are shown in Figure 4.12. In the 10–90% distribution, many counts in the two gamma peaks have large rise times. In the 80–100% distribution, most counts in the gamma peaks are confined to the band of fast pulses. The 10–90% rise

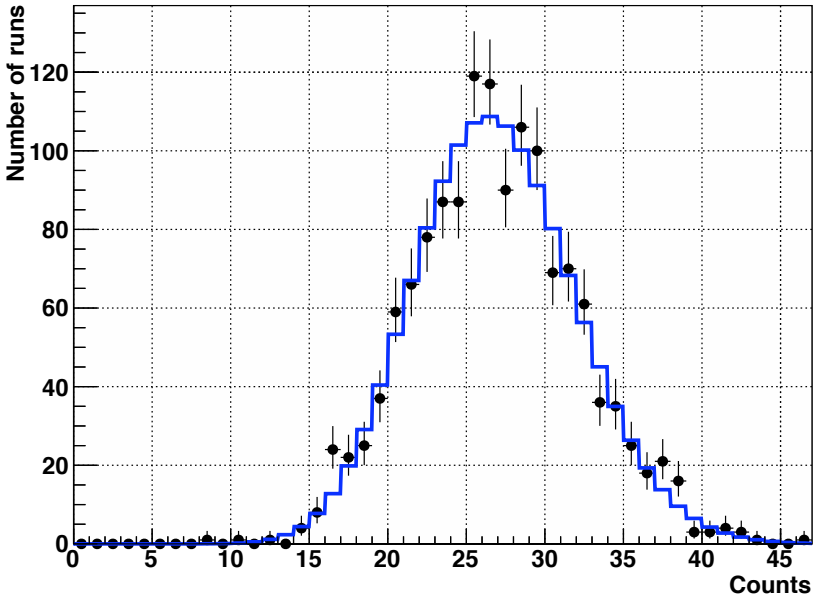

Figure 4.10: The distribution of counts per run above 5 keV in the 1398 runs in Dataset I. The distribution is well-described by a Poisson function with a mean of 26.4: χ^2 is 29.3 per 46 degrees of freedom (the reduced χ^2 is 0.66) and the P-value is 0.97.

time misidentifies multi-site events, which contribute to the gammas peaks, as slow events, as in Figure 4.4. The 80–100% rise time is better at discriminating multi-site events from slow pulses.

To eliminate slow pulses across the full range of the energy spectrum, both the 10–90% and 80–100% rise times will be used. The 10–90% rise time is useful at low energies, where electronics noise reduces the accuracy of the 80-100% rise time calculation and multi-site events are uncommon. The 80–100% rise time is useful at high energies, where the prevalence of multi-site events limits the usefulness of the 10–90% rise time. Figure 4.13 shows the ^{133}Ba energy spectrum. In the figure, the following spectra are shown: all counts, slow counts as identified with a 655.6 ns 10-90% rise-time cut, and slow counts as identified with a 1.85 μs 80–100% rise-time cut. The 655.6 ns 10–90% rise-time cut was determined by Padraic Finnerty in a study of MALBEK with a test pulser. This cut retains 99.7% (3 sigma) of fast waveforms at low energies, up to ∼10 keV [60]. The 1.85 μs 80–100% rise-time cut was chosen to make the energy spectra of slow pulses agree in the region around 60 keV, as identified with the 80–100% and 10–90% rise times. This agreement is consistent in both the high-statistics ^{133}Ba and ^{60}Co energy spectra. The value of 60 keV was chosen because it is in a region where both rise time cuts perform well. The location of 60 keV also avoids the location of any peaks in the ^{133}Ba dataset, ^{60}Co dataset, or Dataset I.

A combined rise-time cut was developed from the 10–90% and 80–100% rise times:

$$\left(\frac{t_{90-10}}{T_0}\right)[1-f(E)]+\left(\frac{t_{100-80}}{T_1}\right)f(E)<1 \tag{4.1}$$

where t_{90-10} is the 10–90% rise time, t_{100-80} is the 80–100% rise time, T_0 and T_1 are the cut values determined from rise-time studies, and $f(E)$ is a function that transitions between the 10–90% rise-time cut and the 80–100% rise-time cut. The function $f(E)$ is a function of the energy of the waveform, E:

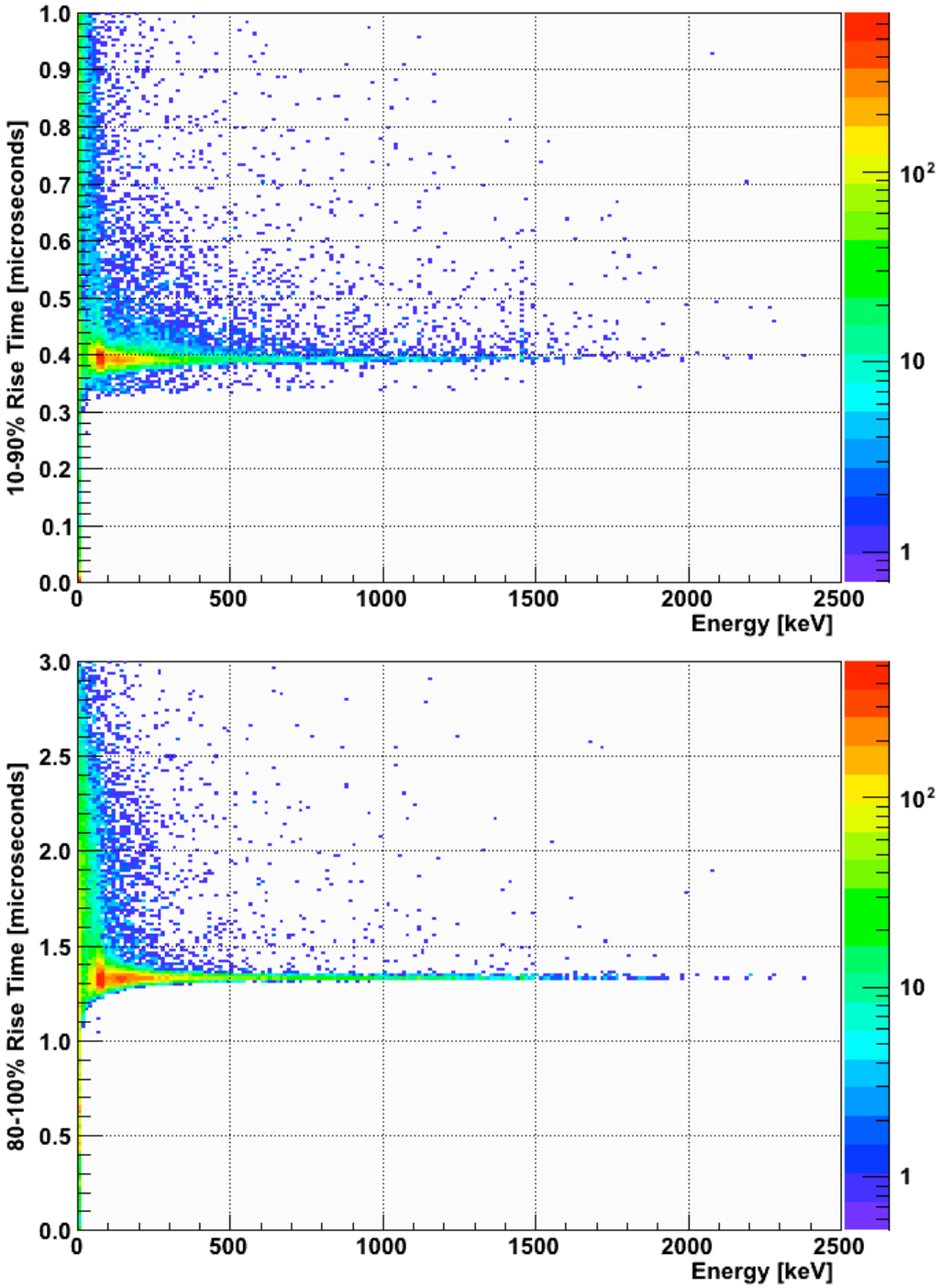

Figure 4.11: Rise time as a function of energy for Dataset I. The 10–90% rise time (top) and the 80–100% rise time (bottom) are shown for comparison. Pulser-related and inhibit-related counts have been removed.

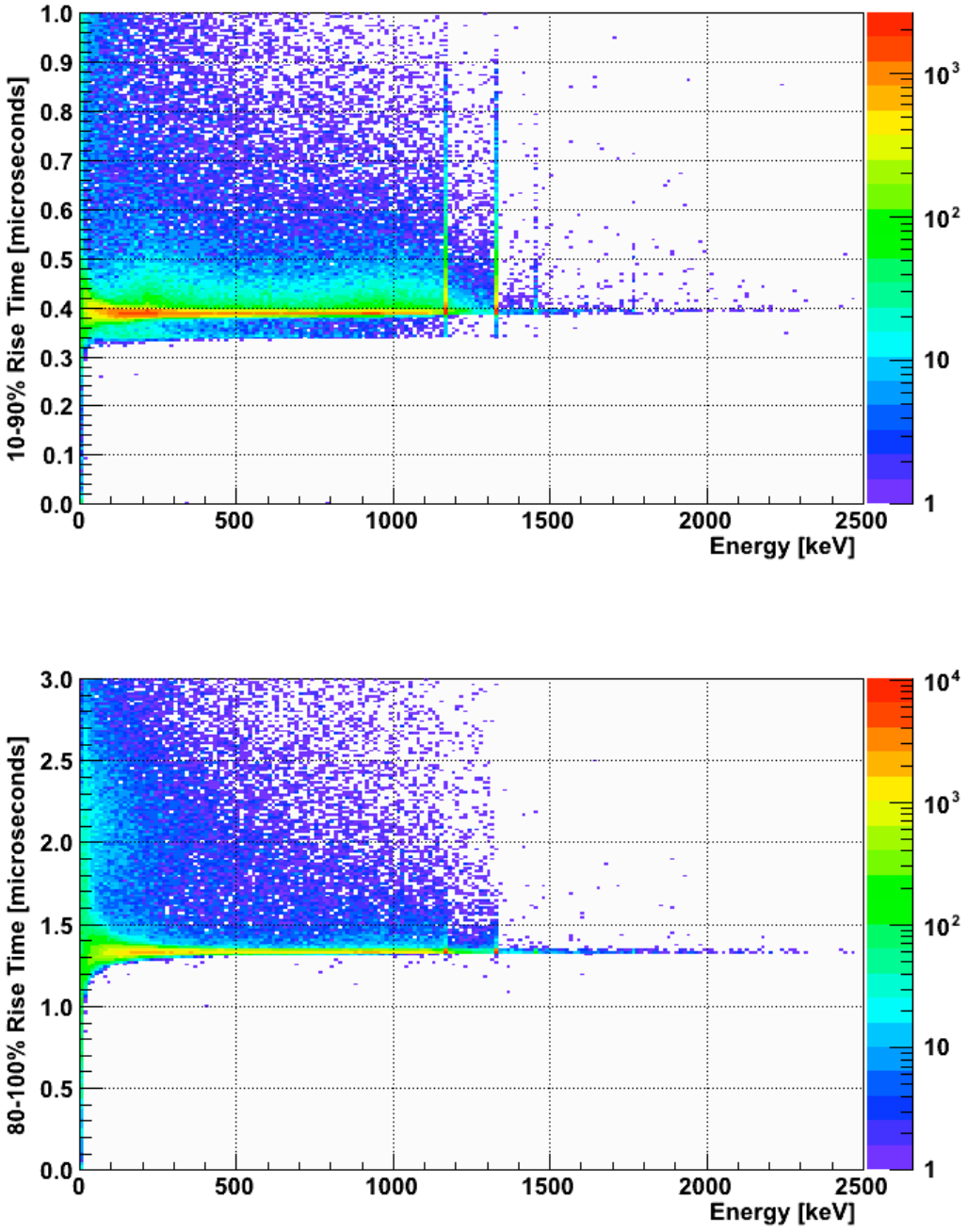

Figure 4.12: Rise time as a function of energy for the ^{60}Co dataset. The 10–90% rise time (top) and the 80–100% rise time (bottom) are shown for comparison.

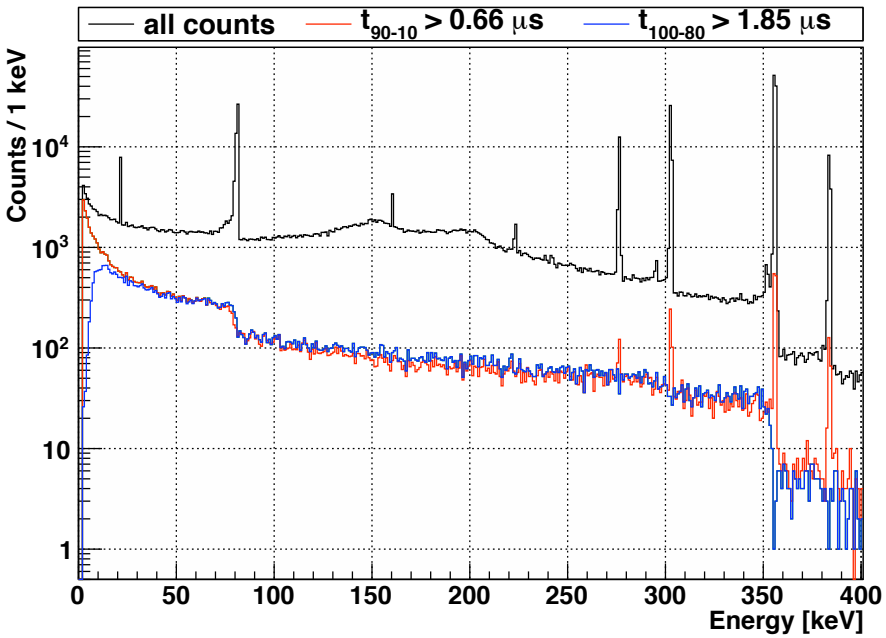

Figure 4.13: All counts and slow counts in the ^{133}Ba dataset energy spectrum. Slow counts have been identified with two measures of the rise time: the 10–90% rise time and the 80–100% rise time. Using the 10–90% rise time, the multi-site events in the gamma peaks are misidentified as slow; the 80–100% rise time avoids this problem.

$$f(E) = 0.5\left[1 + \mathrm{Erf}\left(\frac{E - E_0}{W}\right)\right] \tag{4.2}$$

where E_0 is the transition energy, and W is the width of the transition. The function $f(E)$ provides a smooth transition from the 10–90% rise time cut to the 80–100% rise time cut. The parameter values are listed in Table 4.2. In Figure 4.14, the ^{133}Ba energy spectrum is shown. All counts and the slow and fast counts identified with the combined rise-time cut are shown.

Table 4.2: Parameters used in the combined rise time cut, described by Equations 4.1 and 4.2.

Parameter	**Description**	**Value**
T_0	Slow-pulse cut for 10–90% rise time	655.6 ns
T_1	Slow-pulse cut for 80-100% rise time	1.85 μs
E_0	Energy of transition	60 keV
W	Width of transition	5 keV

4.7 The energy spectrum

The Dataset I MALBEK unamplified energy spectrum is shown in Figures A.1, A.2, and A.3. These figures show more details of the energy spectrum from Figure 4.1. The timing cuts and pulser veto have been applied, but slow pulses have not been removed. Prominent peaks are identified in Table C.1.

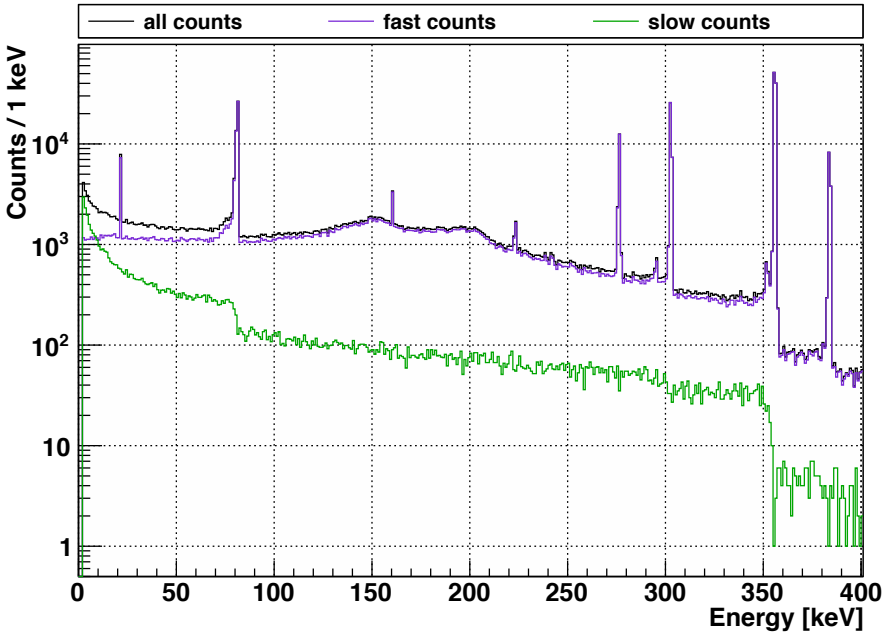

Figure 4.14: The ^{133}Ba dataset energy spectrum. The energy spectrum of slow counts that are rejected with the combined rise-time cut is shown. The spectrum of fast counts retained by the combined cut is also shown.

4.7.1 Peak fitting

After the combined rise-time cut has been applied, locations of possible peaks are identified with the peak-scanning algorithm described in Appendix B. These peaks are then fit to determine their area and width. This information is used for energy calibration and to determine energy resolution.

For each peak, a fit region is constructed based on MALBEK's approximate energy resolution at this location. The fit region extends 10σ above and below the peak in energy. If the fit regions of two or more peaks overlap, the peaks are fit simultaneously. The following function is used to describe the fit region:

$$a_0 + a_1 E + \sum_{i=0}^{k} \frac{N_i}{\sigma_i \sqrt{2\pi}} \exp\left[-\left(\frac{E - x_i}{\sqrt{2}\sigma_i} \right)^2 \right] \tag{4.3}$$

where E is energy. The first two terms, a_0 and a_1, are a linear continuum. The sum includes k Gaussian peaks, where the ith peak has N_i counts, centroid x_i, and width σ_i. The parameters are initialized using estimates of their values and errors, and are allowed to float freely in the fit.

The Python script `fitPeaks.py` is used for peak fitting. An unbinned extended maximum likelihood fit is performed with ROOT's RooFit package, version 3.14, using ROOT's `TMinuit` fitter.

For each peak, a measure of significance is calculated:

$$significance = \frac{N}{\sigma_N} \tag{4.4}$$

where N is the number of counts in the peak and σ_N is the uncertainty in the number of counts, as reported by the fitter. Peaks with significance greater than 3.0 are identified using the Table of Isotopes and NuDat, and their fit results are tabulated. The results of peak fits to Dataset I appear in Table C.1.

To evaluate the goodness of fit, the energy spectrum of the ORCA/Struck dataset is drawn with five bins per FWHM. The fit function is also drawn, and χ^2 per degree of freedom is calculated. With the exception of the pulser peak, all of the Dataset I peaks have reasonable P-values (between 0.14 and 1.0) and reasonable values of reduced χ^2 (between 0.3 and 1.3). Some example fits are shown in Figures 4.15 and 4.16.

The fit to the pulser peak is shown in Figure 4.16. The residual has an asymmetrical, undulating shape, implying that the peak is non-Gaussian. This shape could be the result of a shift in detector gain or a change in other parameters. Dataset I was reviewed on a run-by-run basis in an attempt to identify times at which parameters may have shifted considerably. The dataset was subdivided based on recorded times of LN fills, detector rebiasing, and changes to the DAQ. No correlation with these events was found. The pulser peak may be subject to changes that do not affect other peaks in the energy spectrum. Other peaks in the energy spectrum have count rates that are $\sim 10^3$ times lower than the pulser, so it is difficult to draw conclusions from these low-statistics data. During future data-taking with the MALBEK detector, it would be useful to take periodic high-statistics calibration data, so that changes in gain or other parameters may be identified.

4.7.2 Energy calibration

The criteria for using a peak in energy calibration or in a fit of the energy resolution function are listed below:

1. The peak must be due to ionizing energy deposits in the detector. This excludes the pulser.

2. The peak must be the result of a single contribution. This excludes the peak at 511 keV, which is due to e^+-e^- annihilation and ^{208}Tl.

3. The peak must be separated from nearby peaks by at least three sigma.

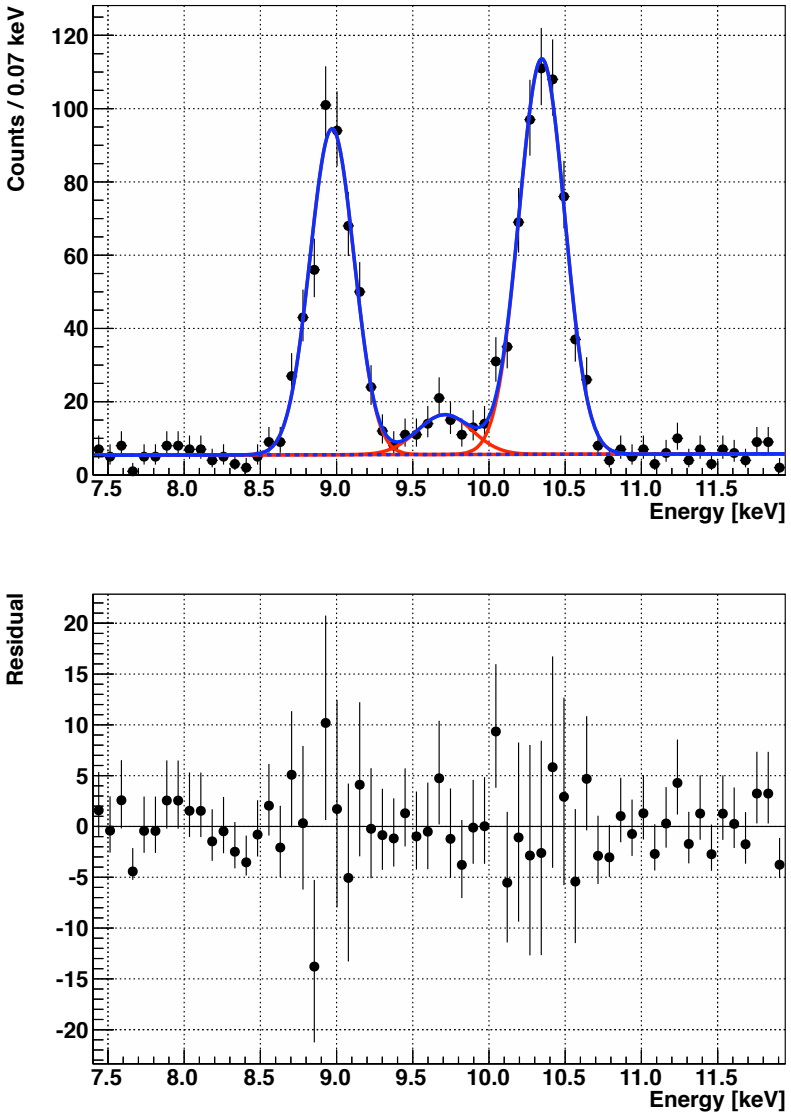

Figure 4.15: Fit of the 8.98-keV ^{65}Zn, 9.66-keV ^{68}Ga, and 10.37-keV ^{68}Ge peaks in Dataset I. This fit has χ^2 of 35.2 per 49 degrees of freedom (reduced χ^2 of 0.72) and a P-value of 0.93.

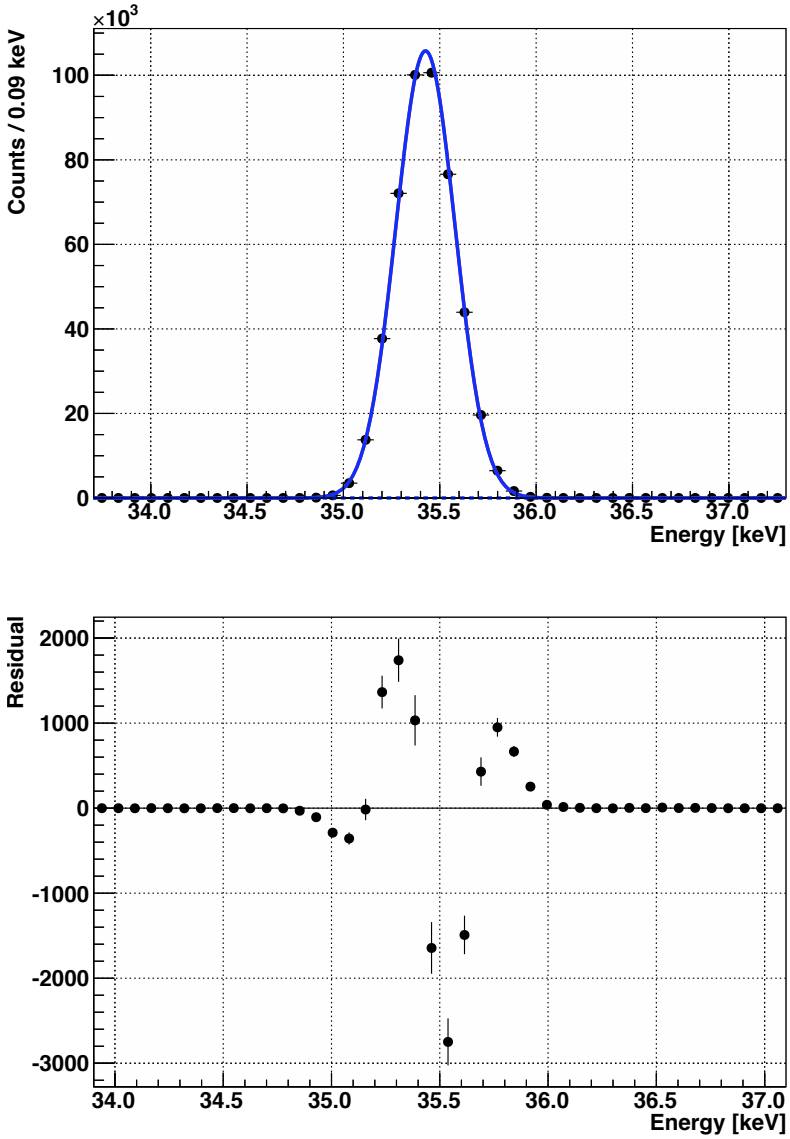

Figure 4.16: Fit of the pulser peak in Dataset I. This fit has χ^2 of 663.9 per 36 degrees of freedom (reduced χ^2 of 18.4). The gain of the detector may have drifted during data taking.

4. The number of counts in the peak must be at least five times greater that the uncertainty in number of counts reported by the fitter or the statistical uncertainty in the number of counts, whichever is greater.

5. The fitter must not return any error codes and must have converged.

The 10 Dataset I peaks used for energy calibration are labeled in Table C.1. To determine the energy calibration, a linear function was fit to the graph of fit centroid vs. published energy. For Dataset I, this fit has a χ^2 value of 36.9 and 8 degrees of freedom ($\chi^2/\mathrm{DOF} = 4.6$), which corresponds to a P-value of 1.2×10^{-5}. This is poor agreement. While reviewing the MALBEK data, David Radford of ORNL recognized that the issues in energy calibration are the result of inherent non-linearities in the Struck digitizer. During future data taking, it might be possible to improve the energy calibration with dedicated studies of the Struck digitizer.

The published and calibrated energies are shown in Figure 4.17. Adding additional terms (up to fourth order in energy) to the fit does not bring the reduced χ^2 below 3 or the P-value above 0.01, so the linear energy calibration is used. While the goodness of fit is poor, the difference between calibrated and published energies is on the order of 0.1 keV for most peaks.

4.7.3 Energy resolution

A standard expression for the energy resolution, σ, of a germanium detector is [26]:

$$\sigma(E) = \sqrt{c_0^2 + \epsilon F E} \tag{4.5}$$

where c_0 is an electronics noise component, ϵ is the average energy to create an electron hole pair, 2.96 eV at 77 K , and F is the Fano factor. Measured values of the Fano factor in germanium range from 0.057 to 0.129 [26].

Some MALBEK data collected over long periods of time are better described by an energy resolution function that includes a higher-order term:

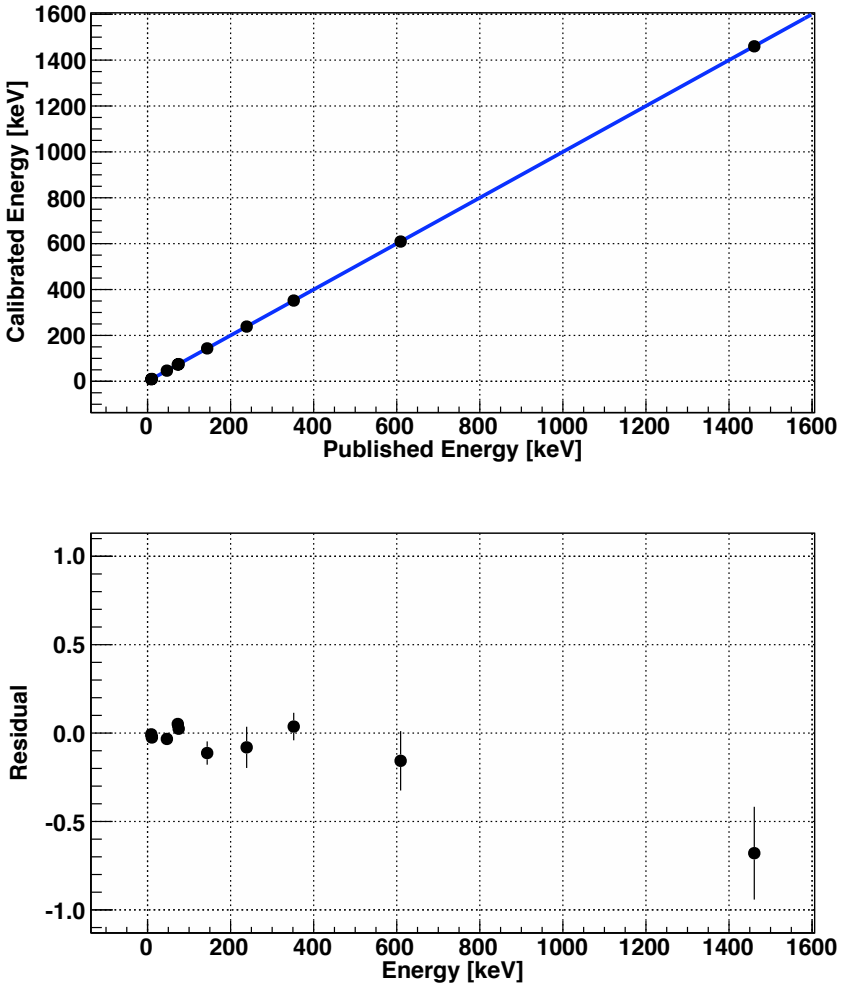

Figure 4.17: Energy linearity of Dataset I.

$$\sigma(E) = \sqrt{c_0^2 + \epsilon c_1 E + c_2 E^2} \tag{4.6}$$

The additional term with coefficient c_2 can describe a drift in energy calibration. This term can also describe effects like charge trapping. The Fano factor has been relabeled c_1, since this term may include contributions that are not due to the Fano factor.

Each dataset is fit with Equation 4.6, using ROOT's `TMinuit` fitter to minimize χ^2. The value of c_0 is determined from the width of the pulser peak and is constrained in the fit. Fits are performed with and without the c_2 term, to determine which form of the equation best describes each dataset.

Dataset I is best described by Equation 4.6 when all three terms are included. Figure 4.18 shows the energy-dependent energy resolution and the residuals from a fit with Equation 4.6. This fit has a χ^2 value of 15.5 and 8 degrees of freedom (χ^2/DOF = 1.9), which is a P-value of 0.05. Without the c_2 term, χ^2 is 39.8 per 9 degrees of freedom (χ^2/DOF = 4.4) – a P-value of 8×10^{-6}.

The ^{133}Ba dataset is well described by Equation 4.6 without the c_2 term: χ^2/DOF = 1.52, P-value = 0.08. The energy resolution of the ^{133}Ba dataset is shown in Figure 4.19. The ^{60}Co dataset is also well described without the c_2 term: χ^2/DOF = 2.99, P-value = 0.88. The ^{60}Co energy resolution is shown in Figure 4.20.

These two datasets may be well described without the c_2 term because they were collected over much shorter time periods than Dataset I. Note that 5-σ significant peaks from each dataset were used to determine the energy calibration and the functional form of the energy-dependent energy resolution. As a result, different peaks were used from each dataset, e.g. the strong ^{133}Ba gamma lines were used when characterizing the ^{133}Ba dataset, but these lines were not present in Dataset I.

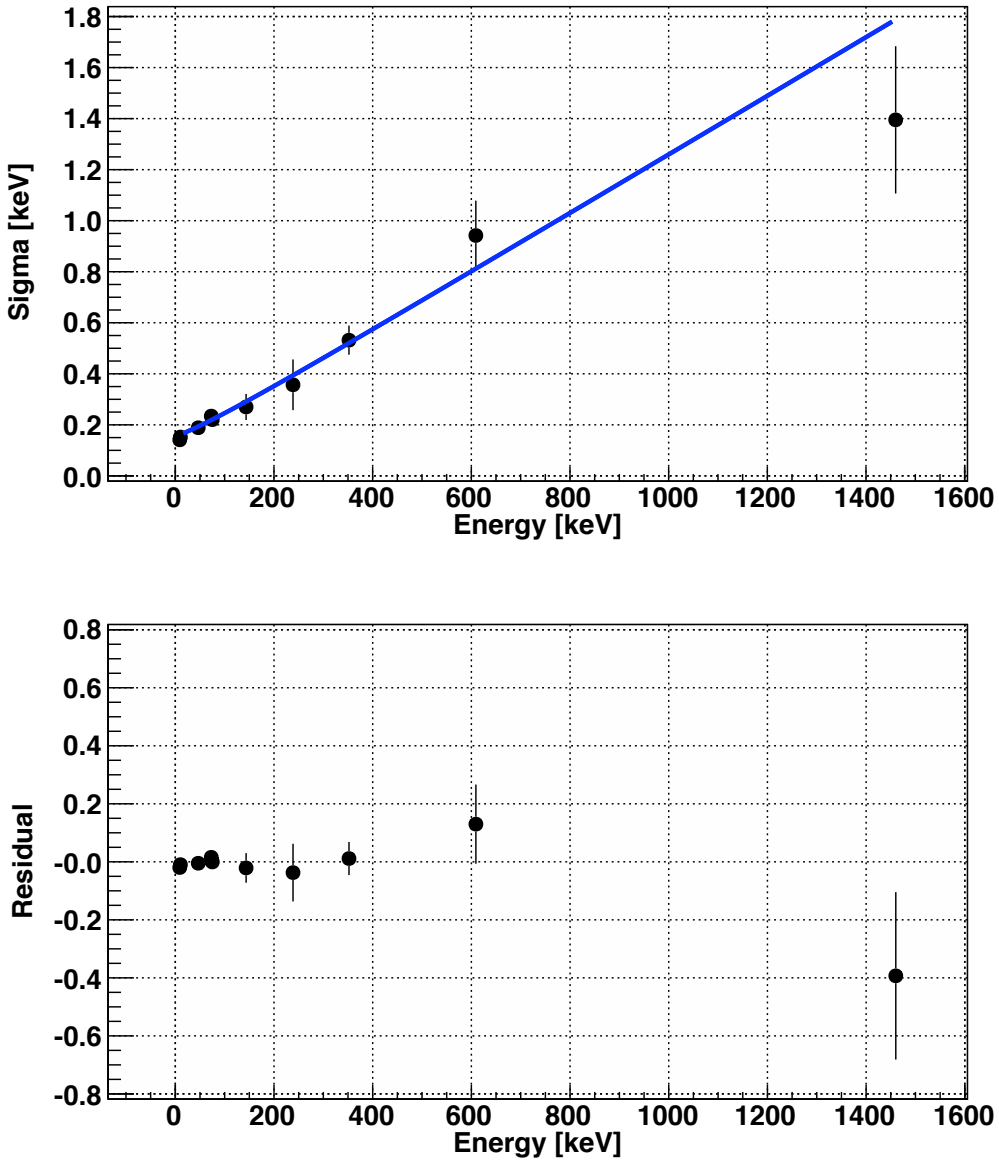

Figure 4.18: Energy resolution of Dataset I.

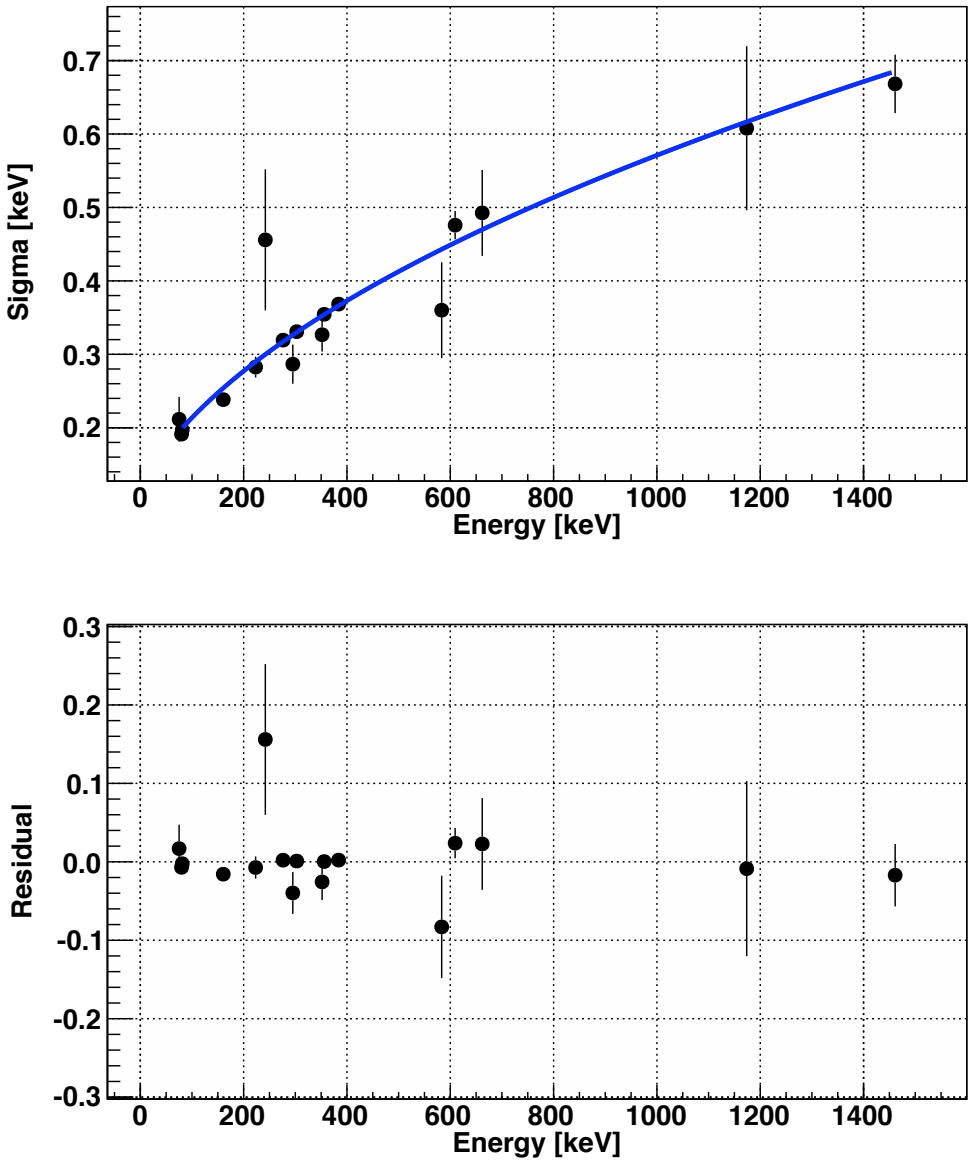

Figure 4.19: Energy resolution of ^{133}Ba dataset.

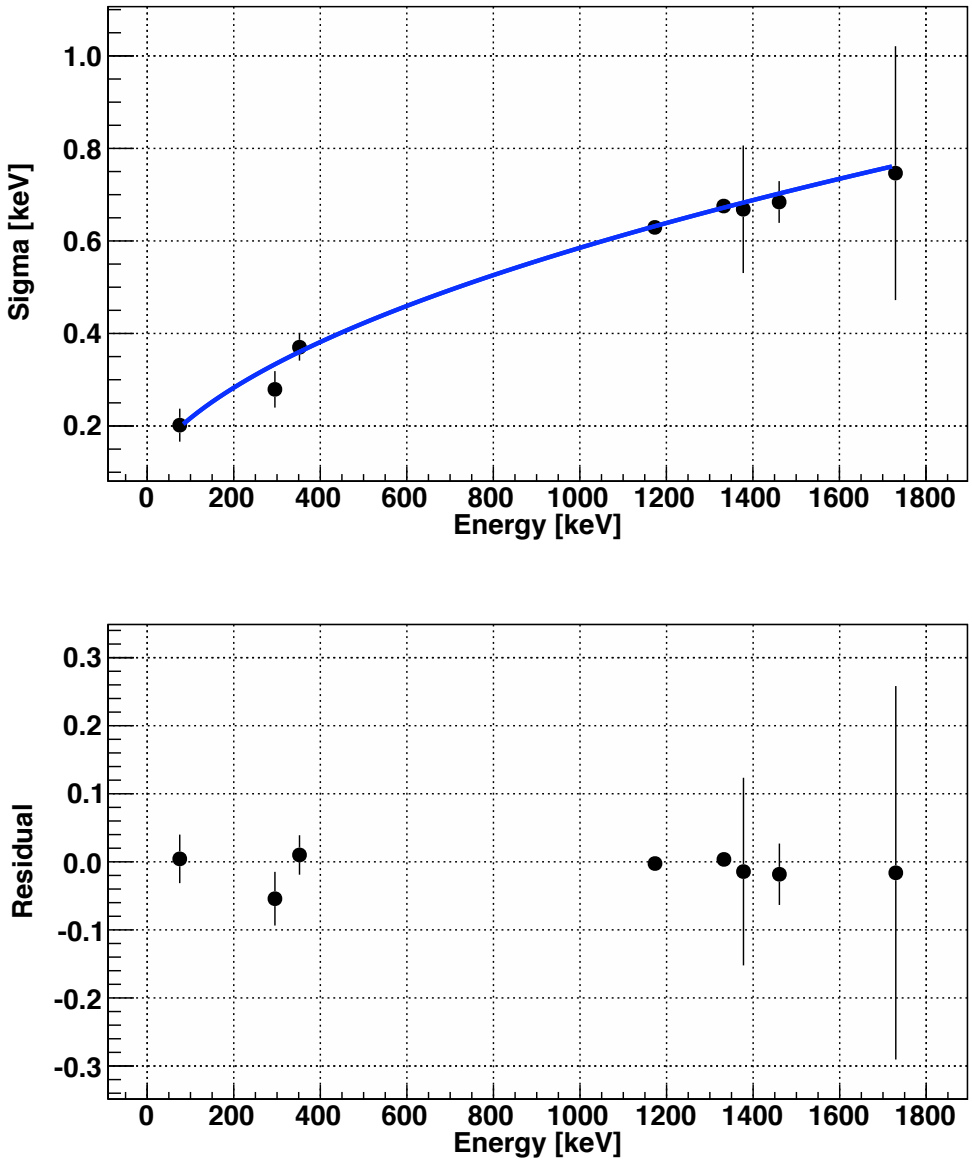

Figure 4.20: Energy resolution of ^{60}Co dataset.

4.8 The pulsed-reset preamplifier

The pulsed-reset preamplifier has two effects on the MALBEK energy spectrum: it contributes to the dead time and it affects the shape of the energy spectrum. This section describes both effects.

The preamplifier resets when the following condition is met:

$$tA_{leakage} + \sum_i Q_i \geq Q_R \tag{4.7}$$

where t is the time since last reset, $A_{leakage}$ is the leakage current of the detector, Q_i are the charge deposits due to ionizing radiation, and Q_R is the charge at which the preamplifier resets, which is a characteristic of the preamplifier.

Equation 4.7 can be expressed in terms of energy:

$$\frac{\epsilon t A_{leakage}}{e} + \sum_i E_i \geq E_R \tag{4.8}$$

where E_R is the reset energy, e is the electron charge, and ϵ is the average energy to create an electron-hole pair.

If there are no ionizing deposits in the detector, the preamplifier will reset in a characteristic time, which will be labeled T_R:

$$T_R \equiv \frac{eE_R}{\epsilon A_{leakage}} \tag{4.9}$$

This definition is useful because T_R can be measured during MALBEK data taking and can be used to study the leakage current.

Figure 4.21 shows the duration of intervals between preamplifier resets in Dataset I. Only intervals that do not contain events in the unamplified ionization channel are shown; this selects intervals where the reset was caused only by the leakage current. The main peak near 42 ms is due to leakage-current-induced resets. This peak has some width because the leakage current changes with time. There is a tail on the left side of the peak, probably due to resets that were caused by an energy deposit but made it into this selection because the unamplified ionization channel waveform was discarded by the ORCA script described in Chapter 2. A small fraction of the time, the inhibit channel of the SIS3302 fails to record a reset, creating the peak at 84 ms. The mode of this distribution is 42.1 ms. One percent of counts fall below 37.9 ms and 1% are above 47.1 ms.

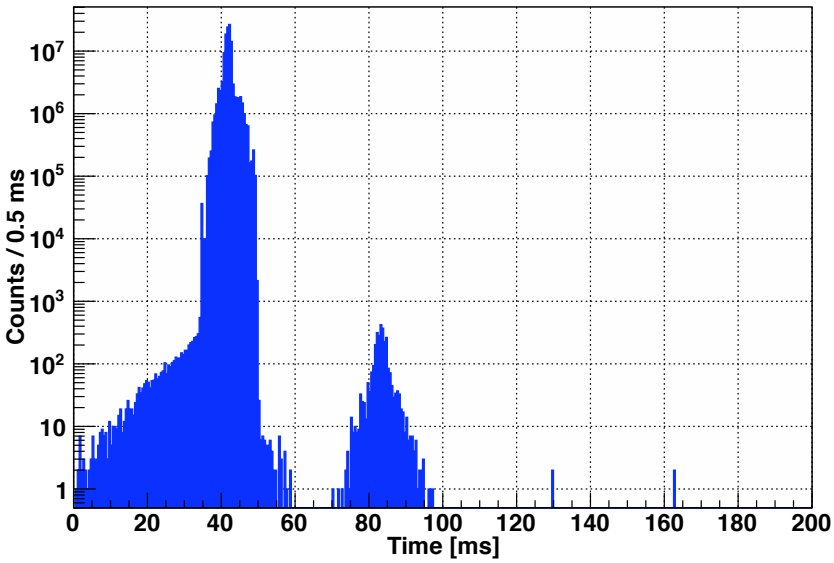

Figure 4.21: Time duration between preamplifier resets in Dataset I.

A veto of 1 ms is applied before and after each reset to remove noise from the energy spectrum. MALBEK operates with a reset rate of approximately 25 Hz, so the dead time due to this cut is typically 5% and can be calculated from the rate in the inhibit channel. In addition to this dead time, there is an energy-dependent efficiency: high-energy waveforms

are more likely to cause a reset than low-energy ones. Equation 4.8 is useful for understanding the preamplifier's effect on the energy spectrum. Energy deposits that cause the preamplifier to reset are not observable with MALBEK. This means that energies greater than E_R are not observed and an energy deposit less than E_R may be observed, depending on the amount of leakage-current charge that has accumulated and the amount of energy that has been deposited since the last reset.

While shielded, the rate of ionizing energy deposits in MALBEK is below 10 mHz and the reset rate is typically 25 Hz, so the probability that an interval between resets contains more than one waveform from the ionizing energy channel is very small. This simplifies things, because we can calculate the energy-dependent efficiency for this situation. An energy deposit with energy E_i at time t_i can be observed if:

$$t_i > \frac{T_{veto}}{2} \tag{4.10}$$

$$t_i < T_R \left(1 - \frac{E_i}{E_R}\right) - \frac{T_{veto}}{2} \tag{4.11}$$

where T_{veto} is the total duration of the veto, 2 ms.

From Equations 4.10 and 4.11, the maximum energy that can be observed is:

$$E_{max} \equiv E_R \left(1 - \frac{T_{veto}}{T_R}\right) \tag{4.12}$$

this waveform would have to occur at $t_i = T_{veto}/2$.

In Figure 4.22, the time duration between inhibits is plotted as a function of energy for waveforms in the unamplified ionization energy channel in Dataset I. This distribution should fall along a line, where the y-intercept is T_R and the x-intercept is E_R. Since T_R varies, there is some spread along the y-axis. No points lie along the x-axis since the maximum observable energy is less than E_R.

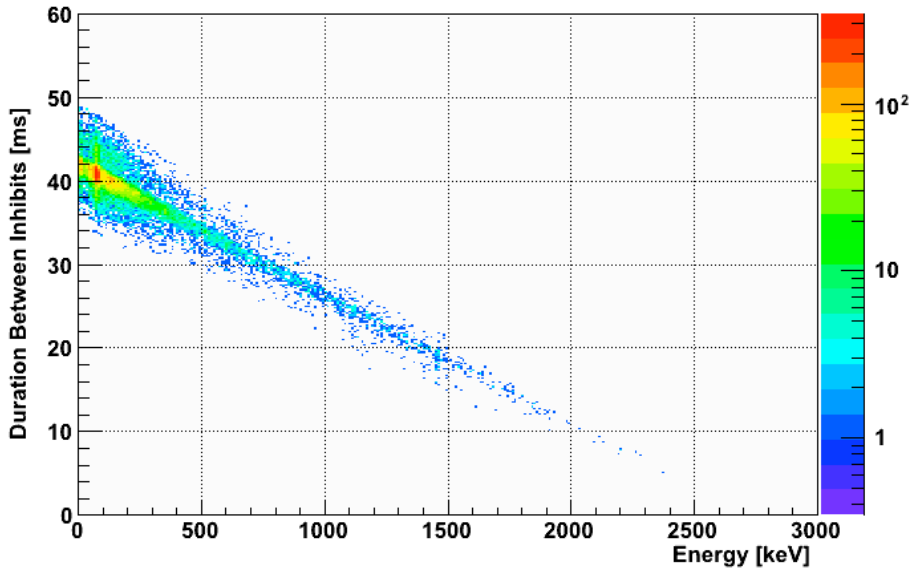

Figure 4.22: Distribution of time and energy between inhibits. This plot was created from inhibit intervals in Dataset I with exactly one high-energy channel trigger. Slow pulses have been removed and the pulser has been vetoed.

In Figure 4.23, the same data have been used to determine the reset energy. For each 50-keV energy slice, the duration between resets was histogrammed into 1 ms bins, and the mean, variance, and mode were calculated. The reset energy was calculated from a fit to a graph of the mode of each energy slice, where the square root of the variance was used as an estimate of the error in the mode. Energy slices with fewer than two counts were excluded. The reset energy calculated from Dataset I with this method is 2721.3 ± 19.9 keV.

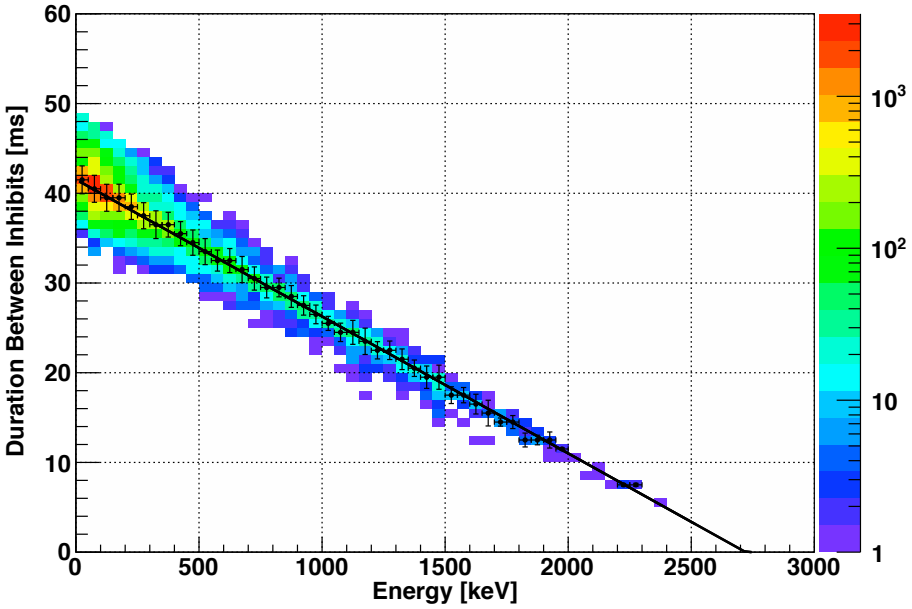

Figure 4.23: A fit to determine the preamplifier reset energy. The distribution of time and energy between inhibits was created from inhibit intervals in Dataset I with exactly one high-energy channel trigger. Slow pulses have been removed and the pulser has been vetoed.

A fit of four datasets, shown in Figure 4.24, found a reset energy of 2702.4 ± 13.7 keV. For a typical reset time of 42.1 ms, the maximum observable energy from Equation 4.12 is 2574.0 ± 13.0 keV. This is below the energy of the 2614.5-keV gamma from ^{208}Tl, which is often a prominent feature in background energy spectra collected with germanium detectors.

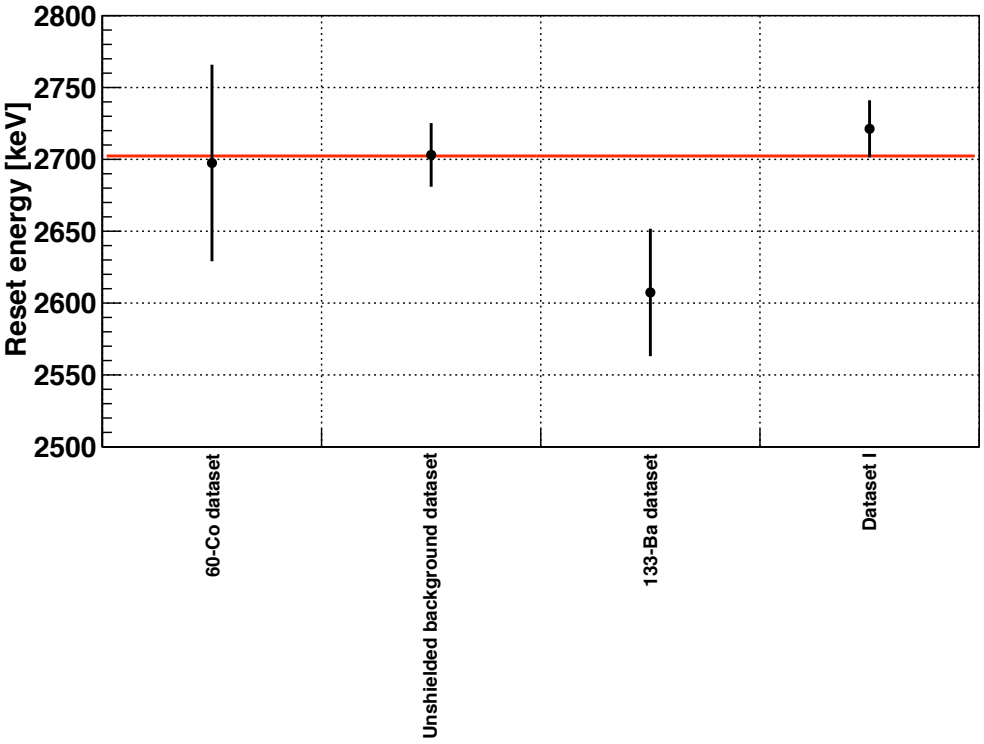

Figure 4.24: MALBEK preamplifier reset energy, determined from four datasets: 2702.4 ± 13.7 keV. This fit has a χ^2 value of 5.5 per 3 degrees of freedom and a P-value of 0.14.

For waveforms that are uniformly randomly distributed in time, the efficiency for detecting a waveform is:

$$\epsilon_{preamp}(E) = \begin{cases} 1 - \frac{E}{E_{max}} & \text{for } E \leq E_{max} \\ 0 & \text{for } E > E_{max} \end{cases} \tag{4.13}$$

The efficiency is linear in energy. Things are a little complicated because the maximum observable energy, E_{max} depends on the reset time, T_R, which is not a constant. Figure 4.25 shows the preamplifier efficiency as a function of energy for three reset times: 37.9, 42.1, and 47.1 ms. Across most of the usable energy range, the efficiency curves are similar for all three times. It should be noted that a preamplifier with these settings would not be useful for a $0\nu\beta\beta$ search, given the decreased efficiency at the ^{76}Ge Q-value of 2039 keV.

4.9 Leakage current

The detector leakage current can be calculated from Equation 4.9. The time between resets changes somewhat over time, but for a typical reset time of 42.1 ms and reset energy of 2702.4 keV, the MALBEK leakage current is:

$$A_{leakage} = \frac{eE_R}{\epsilon T_R} \tag{4.14}$$

$$= \frac{\left(1.60 \times 10^{-19}\text{ C}\right)\left(2702.4\text{ keV}\right)}{\left(2.96 \times 10^{-3}\text{ keV/e-hole pair}\right)\left(42.1 \times 10^{-3}\text{ s}\right)} \tag{4.15}$$

$$= 3.5\text{ pA} \tag{4.16}$$

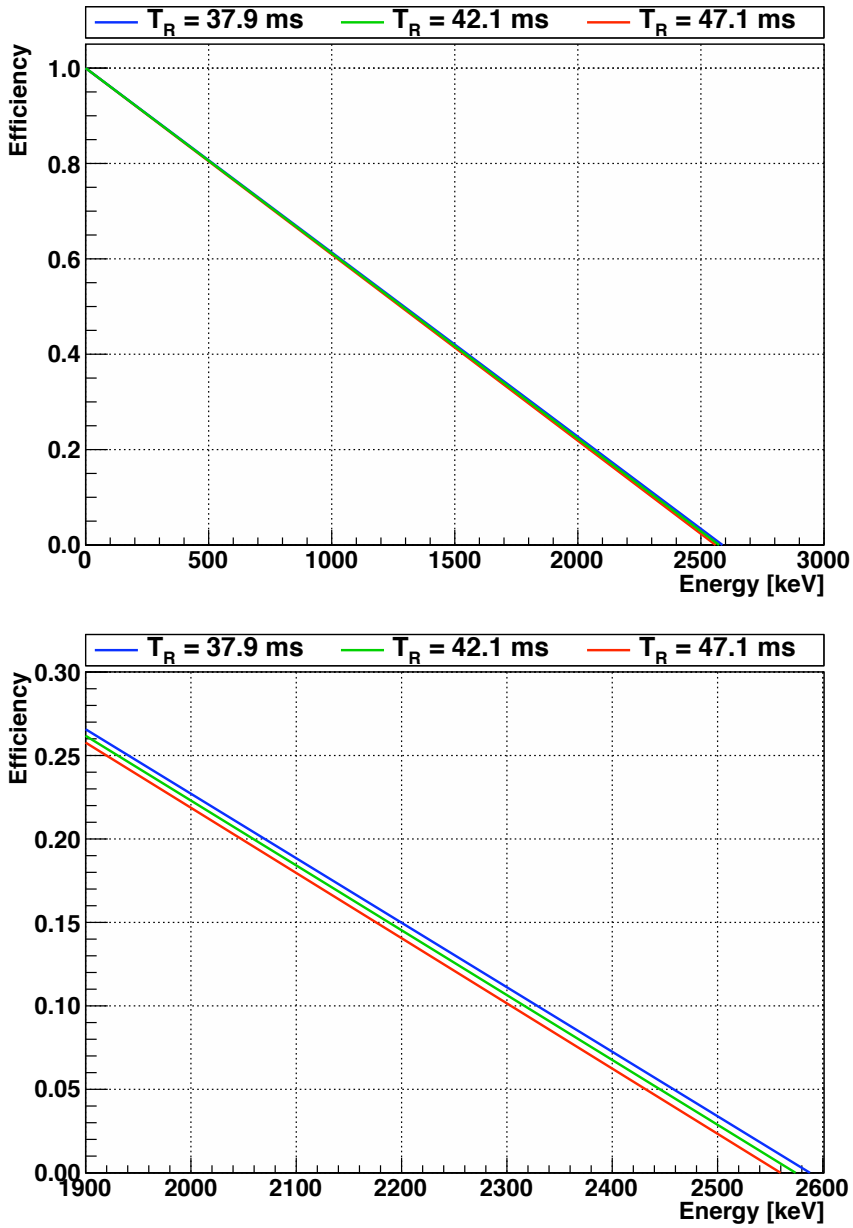

Figure 4.25: The preamplifier efficiency for three different reset times. Efficiency curves are shown for all energies with non-zero efficiency (top) and near the maximum observable energy (bottom).

Chapter 5

MaGe/Geant4 SIMULATIONS OF MALBEK RESPONSE

5.1 Introduction

This chapter will describe MaGe/Geant4 simulations of MALBEK response. Additions and improvements to the Majorana-Gerda software tools were completed in preparation for the Demonstrator simulation campaign. Simulations of MALBEK detector response were performed with this new software. The MALBEK simulation work has served as a validation of the new code and a dry run for the Demonstrator simulation campaign.

5.2 Example simulations

An overview of the process used to generate an energy spectrum of simulated MALBEK detector response is given in this section for two examples: cosmogenically produced ^{68}Ge in the germanium crystal and primordial ^{40}K in a Teflon insulator inside the cryostat. Details of the simulation and data processing are given in subsequent sections. The two examples presented below will be referenced in later sections to explain various aspects of the simulation process.

5.2.1 Germanium-68 in the germanium crystal

Germanium-68 is an unstable isotope that is created by cosmogenic activation of naturally occurring germanium. Germanium-68 is a problematic contaminant for Majorana because it can be produced in germanium crystals, is relatively long-lived, and can deposit energy in the ^{76}Ge $0\nu\beta\beta$ region of interest. Germanium-68 decays by electron capture to ^{68}Ga with a half life of 270.95 days and a Q-value of 106 keV. The ^{68}Ga atom produced by ^{68}Ge decay is in an excited state and de-excites by emission of Auger electrons and x-rays. The electron capture probabilities and resulting emitted energies are [61], [62]:

- K-shell: 10.4 keV (86.25 $\pm$ 0.22 %)

- L-shell: 1.2 keV (11.45 ± 0.20 %)

- M-shell: 0.12 keV (1.92 ± 0.08 %)

The decay of ^{68}Ge is not a potential background for $0\nu\beta\beta$ because it can only deposit a small amount of energy in a detector. The subsequent decay of ^{68}Ga is a potential background because it has a Q-value of 2921.1 keV and may deposit energy in the $0\nu\beta\beta$ region of interest around 2039 keV [33]. Gallium-68 decays with a half life of 67.7 minutes to ^{68}Zn, which is stable. The decay may proceed by electron capture or positron emission. A positron with endpoint energy 1899.1 keV is emitted in 87.9% of decays.

MAGE/GEANT4 was used to simulate the response of MALBEK to 100,000 decays of ^{68}Ge uniformly distributed in the bulk of the germanium crystal. The Tier 0 and Tier 1 energy spectra are shown in Figure 5.1. The spectra are dominated by a continuum extending to the ^{68}Ga decay Q-value. The shape of the simulated spectra depends on the nuclear and atomic data sets used by GEANT4, the geometry and materials of the MAGE model, and the location of the decays. Each count in the Tier 0 energy spectrum represents the sum of all energy deposited in the MALBEK crystal during a one-day time period. This is typically the sum of multiple interactions in the crystal. Often the energy deposited by the decays of ^{68}Ge and ^{68}Ga are summed together in a single count.

During GAT processing of Tier 0 Monte Carlo results, energy deposits resulting from a simulated decay of ^{68}Ge and ^{68}Ga are grouped into multiple events based on the time of each interaction. Each event in the Tier 1 Monte Carlo output spans no more than 10 μs, to approximate the maximum time separation of energy deposits that might contribute to a waveform collected from MALBEK with the DAQ.

Some differences in the Tier 0 and Tier 1 energy spectra are apparent in Figure 5.1. In the continuum and x-ray peaks, the Tier 1 spectrum has fewer counts at high energy and more counts at low energy than the Tier 0 spectrum. During GAT processing, a 1.1-mm-thick dead layer was applied at the outer n^+ contact of the germanium crystal. In the Tier 0 results, the dead layer is not yet considered. Counts in the energy spectrum may contain energy deposits from multiple locations within the crystal; when the dead layer is

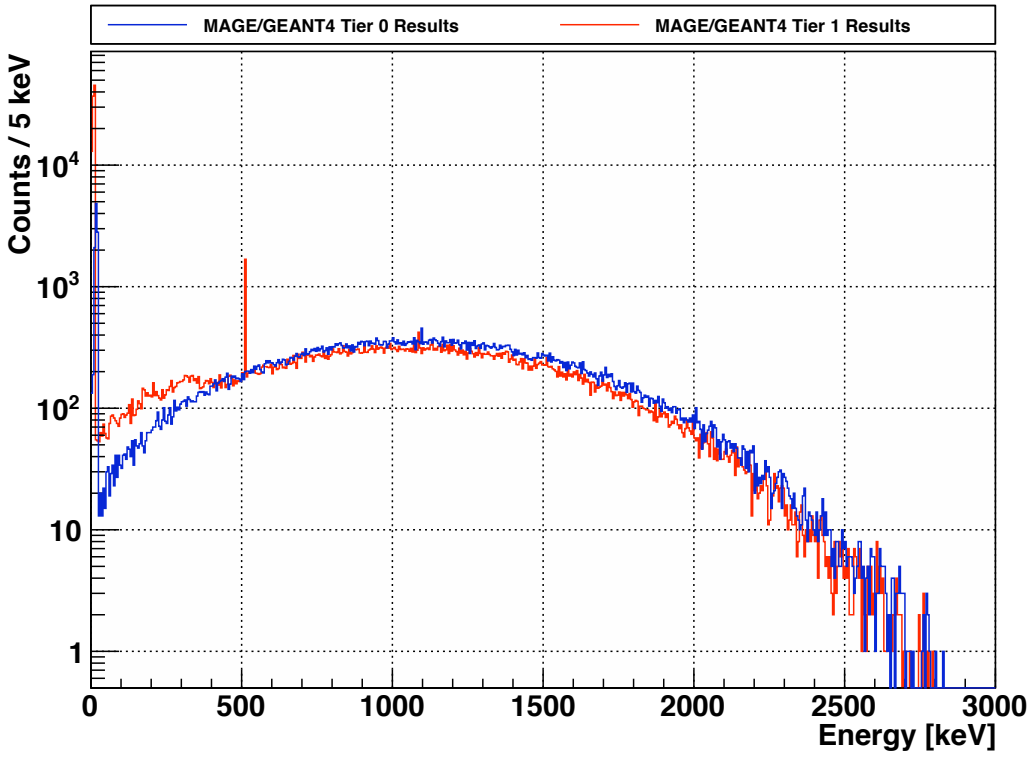

Figure 5.1: Simulated energy spectrum of MALBEK response to 10^6 decays of ^{68}Ge. The ^{68}Ge was uniformly distributed in the volume of the germanium crystal. Results are shown as produced by MAGE/GEANT4 (Tier 0) and after processing with GAT (Tier 1). During GAT processing, events are time windowed, dead layers are applied, and other operations are performed to make the Monte Carlo results reflect a realistic detector.

applied, interactions in dead regions will not contribute and the total energy of many counts will decrease. The Tier 1 spectrum contains an e^+-e^- annihilation peak at 511 keV that is not apparent in the Tier 0 spectrum. Approximately 89% of ^{68}Ga decays emit a positron, which can annihilate with an electron and produce two back-to-back 511-keV photons. For a ^{68}Ga decay that occurs in the crystal dead layer, frequently only one 511-keV photon will deposit energy in the active volume of the detector.

5.2.2 Potassium-40 in a Teflon insulator

Potassium-40 is a naturally occurring isotope of potassium, with an abundance of 0.0117 % [63] and a half life of 1.2×10^9 years [33]. Trace amounts of ^{40}K are found in many materials. Potassium-40 may decay by one of two modes [33]:

- β^- decay to ^{40}Ca, with a branching ratio of 89.3% and a Q-value of 1311.1 keV
- β^+ decay or electron capture to ^{40}Ar, with a branching ratio of 10.7% and a Q-value of 1504.7 keV

A 1460.8 keV gamma is emitted in 10.66% of decays. Low-energy x-rays, Auger electrons, and βs may also be emitted.

Five-million decays of ^{40}K were simulated in the bulk of a small Teflon insulator located below the germanium crystal in the MALBEK cryostat, named *connectorInsulatorPhysical1* in the MaGe/Geant4 MALBEK model. The Tier 0 and Tier 1 spectra of simulated detector response are shown in Figure 5.2. Both spectra show the full-energy gamma peak at 1460.8 keV and a Compton continuum at lower energies. A small annihilation peak is visible at 511 keV. The energy spectrum describes the response of MALBEK to the 1460.8-keV gammas emitted in the decay of ^{40}K. Any betas emitted in the decay would be attenuated within the Teflon insulator or other material between the insulator and the germanium crystal. The shapes of the spectra depend on the solid angle, geometry of the germanium crystal, and the materials surrounding the crystal, which attenuate and scatter gammas. The Tier 1 spectrum contains fewer counts in the full-energy peaks and continuum

than the Tier 0 spectrum; this is due to the application of the dead layer. The Tier 0 and Tier 1 spectra are fairly similar, in contrast to the ^{60}Co results in Figure 5.1.

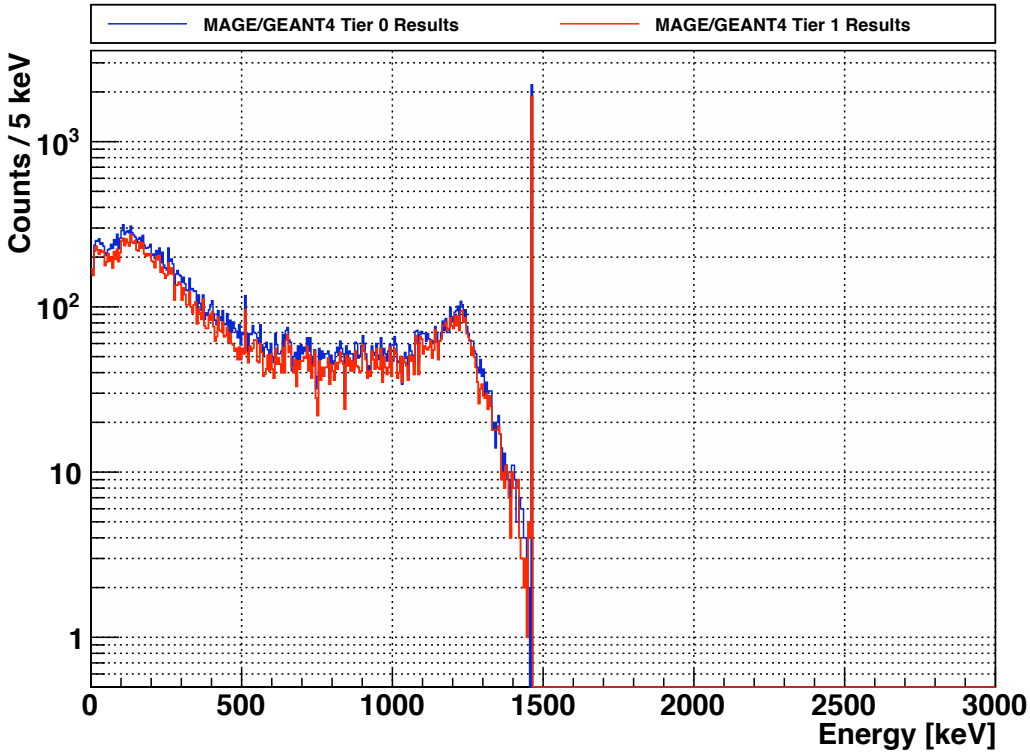

Figure 5.2: Simulated MALBEK response to 5×10^6 decays of ^{40}K in a Teflon insulator. The ^{40}K was uniformly distributed in the Teflon insulator, which was located below the germanium crystal in the cryostat. Results are shown as produced by MAGE/GEANT4 (Tier 0) and after processing with GAT (Tier 1). The GAT-processed spectrum has fewer counts in the full-energy peak at 1460.8 keV due to the application of the dead layer.

5.3 The MAJORANA-GERDA software package (MAGE)

MAGE is based on GEANT4, and is used by MAJORANA and GERDA to simulate response of a germanium detector to ionizing radiation. MAGE defines generators of primary event distributions, models of various detector geometries, and a choice of several output formats

for storage of simulated detector response. MAGE uses the GEANT4 framework to simulate interactions of particles in matter. A GEANT4 simulation consists of the following parts:

- *Monte Carlo run*: a set of trials of the same process, e.g. many simulated decays of ^{60}Co near a detector
- *Monte Carlo event*: one trial, e.g. a simulated decay of ^{60}Co and all resulting interactions in a detector and surrounding materials
- *Monte Carlo track*: the path of one particle in an event, e.g. a gamma from the ^{60}Co decay
- *Monte Carlo step*: a description of a particle before and after an interaction, e.g. the Compton scatter of a gamma

MAGE compiles as a single executable. When MAGE is run from the command line, it takes a single argument: the name of a macro file. Commands in the macro specify the detector, output format, primary particle(s), and other parameters of the simulation. MAGE/GEANT4 can simulate a variety of primary particles, and the distributions of energy, momenta, and position of the primary particles can be specified. The primary particle in a background simulation is usually an unstable isotope or a cosmic-ray muon. Unstable isotopes are handled by the `MGGeneratorRDM` generator, simulated initially at rest, uniformly distributed on a surface or in the bulk of a volume. GEANT4 provides an algorithm for distributing events uniformly in the bulk of a volume, but the distribution of primary events on the surface of a volume is handled within MAGE, using the Generic Surface Sampler (GSS) [6]. The energy, direction, and angular distribution of incident muons is handled by the `MGGeneratorCosmicRays` generator. The MAGE macro used to simulate ^{68}Ge decays in Section 5.2.1 appears in Appendix G.

A new MAGE output class, `MGOutputMCRun`, was created to store MAGE output in the MGDO Monte Carlo objects described in Section 5.4. For each MAGE run, `MGOutputMCRun` creates a Tier 0 ROOT file that contains a `TTree` of MAGE results, described in Table 3.2.

The `TTree` consists of the following branches, which are filled with one entry per Monte Carlo event.

- `fMCRun`: a `MGTMCRun` object of run-level info
- `eventHeader`: a `MGTMCEventHeader` object of event-level info
- `eventPrimaries`: a `MGTMCEventSteps` object with one `MGTMCStepData` for each primary particle in the event
- `eventSteps`: a `MGTMCEventSteps` object with one `MGTMCStepData` for each interaction in the event

By default, step data is saved only for those interactions that deposit energy in detector volumes. It is possible to save data for all steps in a run, but this consumes large amounts of disk space.

Tier 0 ROOT output produced by `MGOutputMCRun` depends on MGDO but is independent of the MAGE software. The MAGE libraries or executable are not necessary to read the `MGOutputMCRun` output files. This is convenient for processing of `MGOutputMCRun` output, since MAGE and its dependencies do not need to be installed on machines that will do the processing.

5.4 MAJORANA-GERDA Data Objects for Monte Carlo results

Several MGDO classes encapsulate results of Monte Carlo simulations for storage in ROOT `TTree`s. These classes were created for the DEMONSTRATOR simulation campaign. The classes were created in collaboration with Jason Detwiler, a MAJORANA member at LBNL, and with feedback from other members of MAJORANA and GERDA. The MGDO classes are typically used to encapsulate results from GEANT4, but are generic enough that they could be used to store information from other Monte Carlo packages as well.

The names of MGDO classes for storage of Monte Carlo results have the prefix `MGTMC` to indicate that they belong to MAJORANA-GERDA software and are ROOT-based classes

for encapsulation of Monte Carlo results. The MGDO classes `MGTMCRun` and `MGTMCEvent-Header` encapsulate Monte Carlo run and event information. Data members of these classes are described in Table D.1 and Table D.2. The class `MGTMCEventSteps` encapsulates all step data for an event, and contains an array of `MGTMCStepData` objects, where each `MGTMCStepData` element describes a particle at the beginning or end of a Monte Carlo step. `MGTMCEventSteps` and `MGTMCStepData` are described in Tables D.3 and D.4. Data members are in the system of units used by CLHEP [1]. Energies are in MeV; lengths are in mm. Classes for encapsulation of Monte Carlo data are a useful addition to MGDO because class methods and algorithms operating on these classes can be included in MGDO for the use of all MAJORANA and GERDA collaborators.

The `MGTMCEventHeader` data member `fTotalEnergy`, which represents the total energy deposited in active detector volumes during a Monte Carlo event, was used to make the Tier 0 spectra for the example of ^{68}Ge decay in the germanium crystal, shown in Figure 5.1, and ^{40}K decay in a Teflon insulator, shown in Figure 5.2. Each histogram count represents one `TTree` entry.

5.5 A MAGE model of the MALBEK detector

A model of the MALBEK detector geometry was added to the MAGE simulation package as the `MJGeometryKURFBEGeDetector` class. The `MJGeometryKURFBEGeDetector` geometry describes the materials, dimensions, and locations of components of the MALBEK detector. The `MJGeometryKURFBEGeDetector` class can be used for MAGE/GEANT4 simulations of MALBEK detector response and to generate images of the MALBEK geometry. Cross-sectional visualizations of the MALBEK cryostat were produced with GEANT4's RayTracer and appear in Figures 5.3 and 5.4.

Information for the MALBEK MAGE model was collected from technical drawings from CANBERRA and Juan Collar, a MAJORANA Collaborator at the University of Chicago. CANBERRA supplied detailed drawings of some parts and assembly-level drawings of the MALBEK cryostat. Drawings of some CANBERRA parts are proprietary, so dimensions of these parts were estimated by digitizing assembly-level drawings containing the parts. Dimensions were also collected by MAJORANA Collaborators at UNC, who traveled to

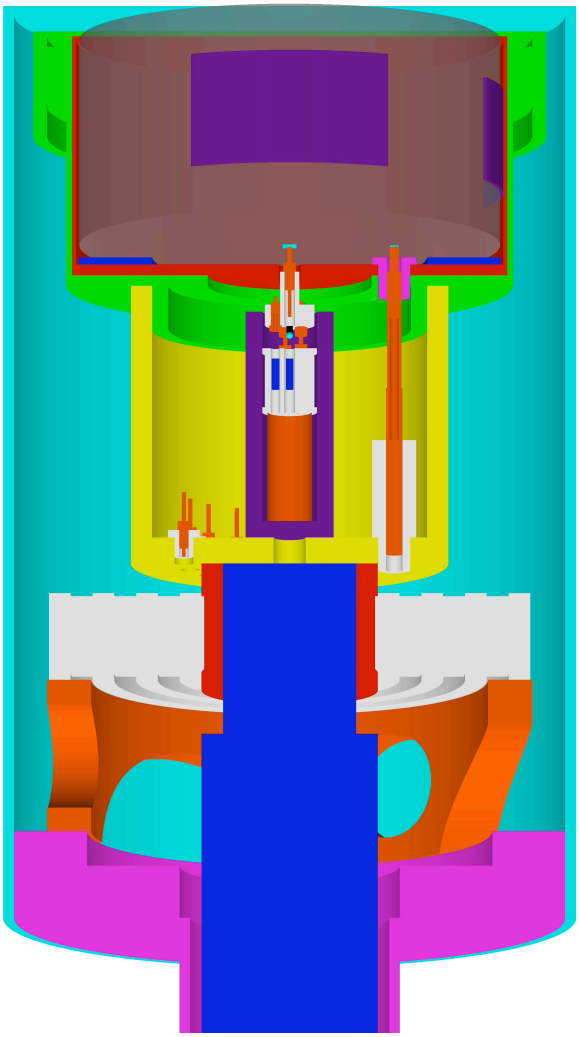

Figure 5.3: MAGE geometry model of the MALBEK detector, viewed from the side and slightly below the germanium crystal. Colors distinguish individual component volumes. The detector is shown in cross-section with the exception of the germanium crystal, which is not sectioned to show the positions of the lead patches. The patches appear as purple rectangles on the face of the crystal.

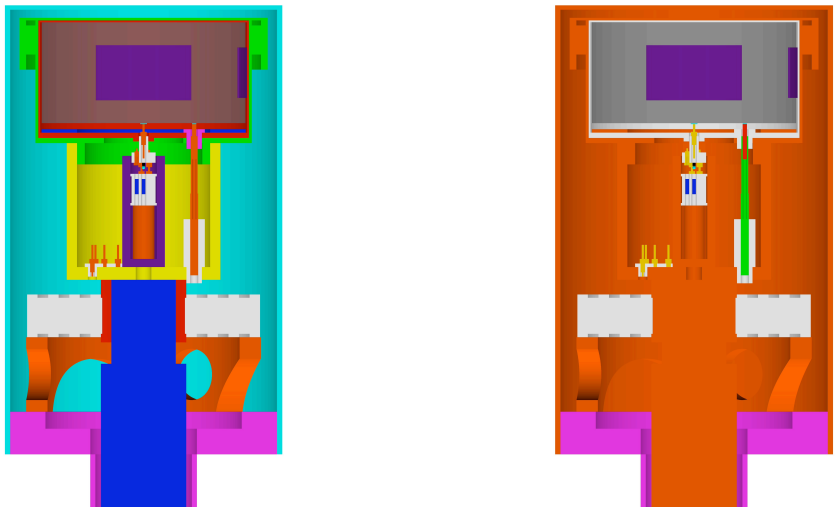

(a) (b)

Figure 5.4: MAGE geometry model of the MALBEK detector. In (a), colors distinguish individual components. In (b), colors distinguish materials: germanium (grey), copper (orange), PTFE (white), brass (yellow), resistors (blue), tin solder (cyan), FET (black), stainless steel (magenta), lead patches (violet), nickel silver (green), and beryllium copper (red). Most of the mass surrounding the crystal is copper.

CANBERRA with MALBEK in October of 2011 to open the cryostat and remove lead patches.

MaGe's `MJGeometryKURFBEGeDetectorInShield` class inherits from `MJGeometryKURFBEGeDetector` and describes the MALBEK detector surrounded by its polyethylene and lead shielding at KURF. A list of the included components with their materials and masses appears in Appendix I. A RayTracer cross-sectional image of MALBEK in shielding appears in Figure 5.5. Information about the lead shielding was taken from technical drawings by Gary Swift, an engineer at Triangle Universities National Laboratory [42]. Dimensions of the polyethylene shielding and scintillator come from measurements made at KURF by Paddy Finnerty. A RayTracer image of MALBEK in the experimental hall at KURF appears in Figure 5.6.

5.6 Simulation of the thorium-232 and uranium-238 decay chains

The isotopes ^{232}Th and ^{238}U are long-lived naturally occurring contaminants, each with a decay chain of many daughter products. If decays of either ^{232}Th or ^{238}U are simulated in MaGe/Geant4 without special handling, they would proceed through several intermediate products to the stable isotopes ^{208}Pb or ^{206}Pb, respectively. Simulating all decays in a chain at once is only appropriate if the decay chain is in secular equilibrium, which is not a valid assumption for many materials with ^{232}Th or ^{238}U contamination.

Disequilibrium in the decay chains can be studied by breaking the chains into multiple steps and simulating each one separately. When studying detector response to ^{232}Th or ^{238}U, the contributions from each step can be recombined. Majorana Collaborators chose to simulate ^{232}Th decay using the steps listed in Tables 5.1 and shown in Figure 5.7. The steps for ^{238}U are listed in Table 5.2 and shown in Figure 5.8. The bounds of the steps were determined by the half lives of the involved isotopes, radiochemistry concerns, and the type of decays. Within each step, half lives of the daughter isotopes are short relative to the half life of the parent isotope, so that secular equilibrium is a valid assumption.

When simulating detector response to ^{232}Th or ^{238}U, each step is a separate MaGe run. The bounds of a step in a decay chain are specified in a MaGe macro using a Geant4 command with arguments A_{min}, A_{max}, Z_{min}, and Z_{max}, which specify mass numbers and proton

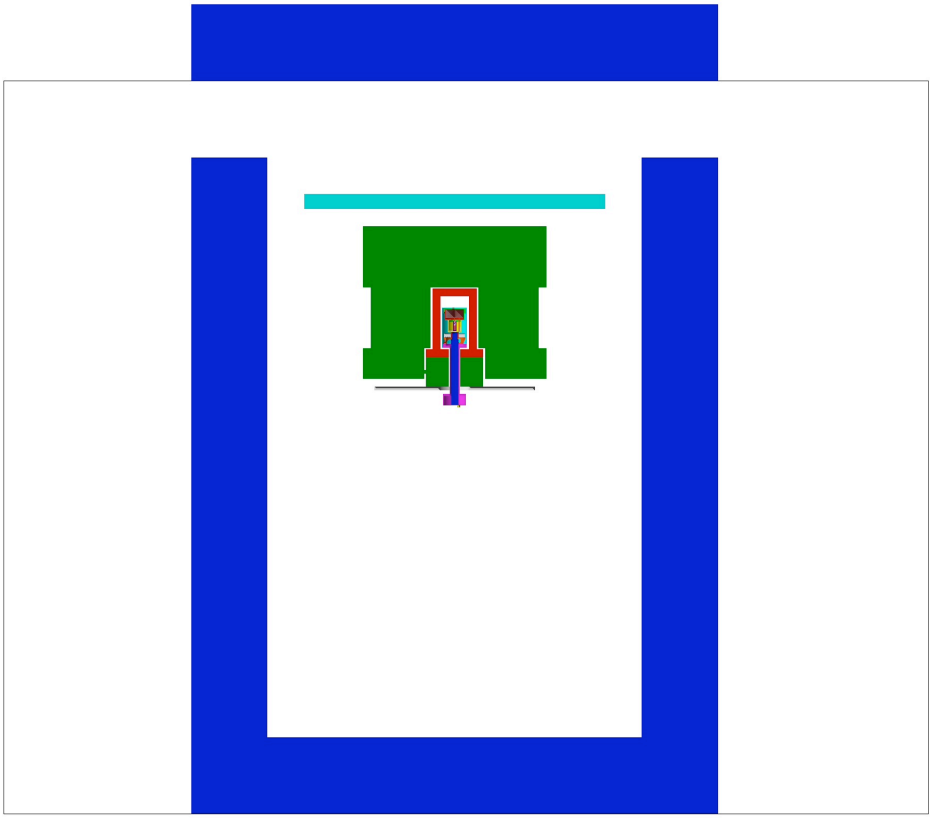

Figure 5.5: MAGE model of the MALBEK detector in shielding at KURF, shown in cross section. Materials are indicated by color: polyethylene (blue), scintillator (cyan), modern lead (green), ancient lead (red), aluminum (dark gray), steel (gray). The multicolored detector from Figure 5.4 is inside the ancient lead shield; the cold finger protrudes. The top section of the polyethylene shield rests on top of a steel trailer. The rest of the polyethylene shield is inside the trailer. The white empty space is air, except inside the detector, where it is vacuum.

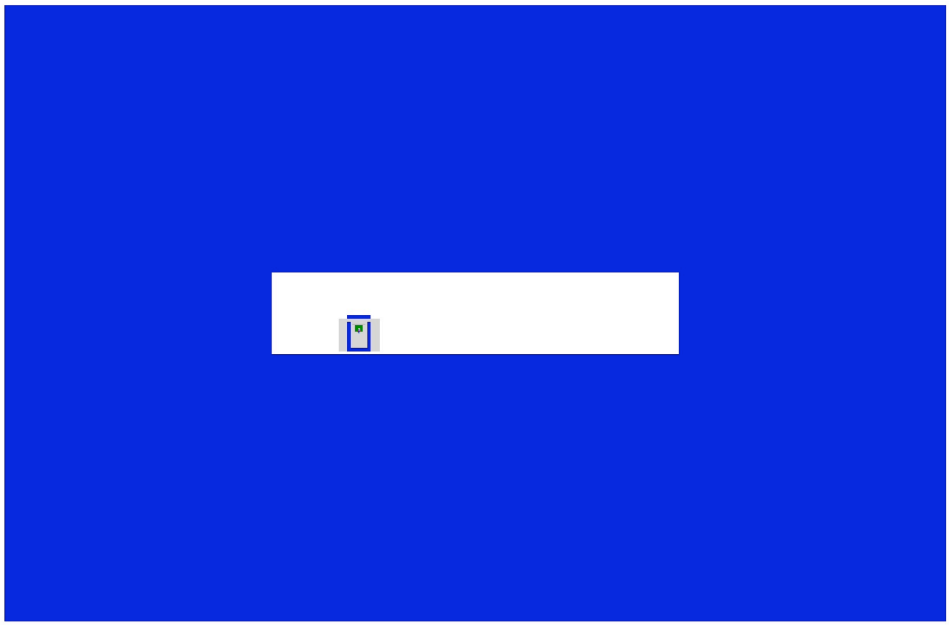

Figure 5.6: MAGE model of the experimental hall at KURF, shown in cross section. The large blue volume is rock. The experimental hall is a large cavity in the rock. The MALBEK trailer and shielding from Figure 5.5 are visible in this cavity.

Table 5.1: Steps used for simulation of the ^{232}Th decay chain.

Step	Description	Classification
1	^{232}Th to ^{228}Ra	
2	^{228}Ra to ^{228}Th	^{232}Th upper chain
3	^{228}Th to ^{224}Ra	
4	^{224}Ra to ^{208}Pb	^{232}Th lower chain

numbers of isotopes that are allowed to decay. The command is shown in Appendix G. For example, step 4 in the ^{232}Th decay chain describes the decay of ^{224}Ra to stable isotope ^{208}Pb. Step 4 extends from $A_{min} = 208$ and $Z_{min} = 81$ to $A_{max} = 224$ and $Z_{max} = 86$.

It is not always possible to break a decay chain in the desired places by specifying A_{min}, A_{max}, Z_{min}, and Z_{max}, as in the case of steps 6 and 6a in the ^{238}U decay chain. Step 6a, the decay of ^{210}Tl, is expected to be in equilibrium with step 6, but if step 6 were defined with $A_{min} = 208$ and $Z_{min} = 81$, then ^{210}Pb, ^{210}Bi, and ^{210}Po would also decay, which is undesirable because of the long half lives of these isotopes. For this reason, steps 6 and 6a are simulated separately and later recombined.

5.7 Importance sampling and parallel geometries

Simulating the response of the MALBEK detector to muon-induced neutrons and gamma-emitting radioactive sources outside the lead shielding is computationally expensive. It is necessary to simulate many events to produce a single simulated hit in the detector. GEANT4 contains an event-biasing framework for reducing variance and increasing statistics in situations like these.

One event-biasing method provided by GEANT4 is geometry importance sampling. In this method, volumes in a geometry model are assigned importance values. The user selects a particle of interest, typically a gamma or neutron, for biasing. When the track of a biased

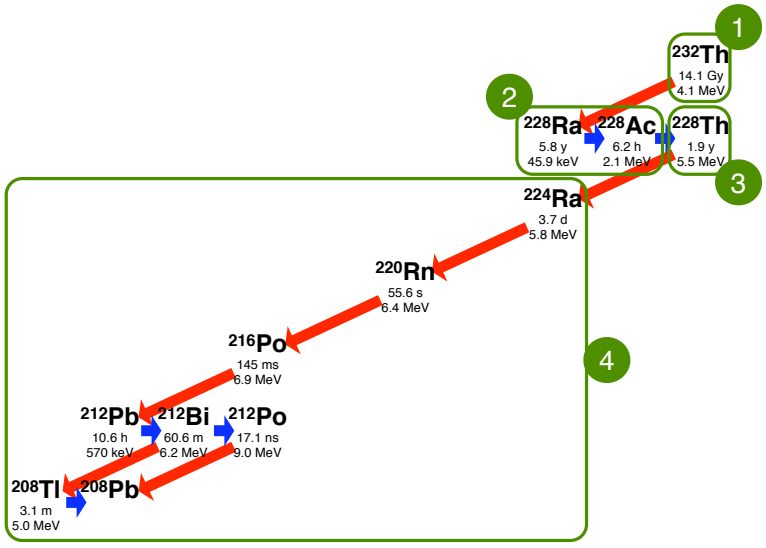

Figure 5.7: Steps used for simulation of the ^{232}Th decay chain. Red arrows indicate alpha decays; blue arrows indicate beta decays. Split steps are indicated in green. For each step, all isotopes within the box are allowed to decay. Half life and Q-value are listed for each isotope. Where more than one decay mode is possible the larger Q-value is listed. Half lives and Q-values are from the NuDat decay radiation database [33].

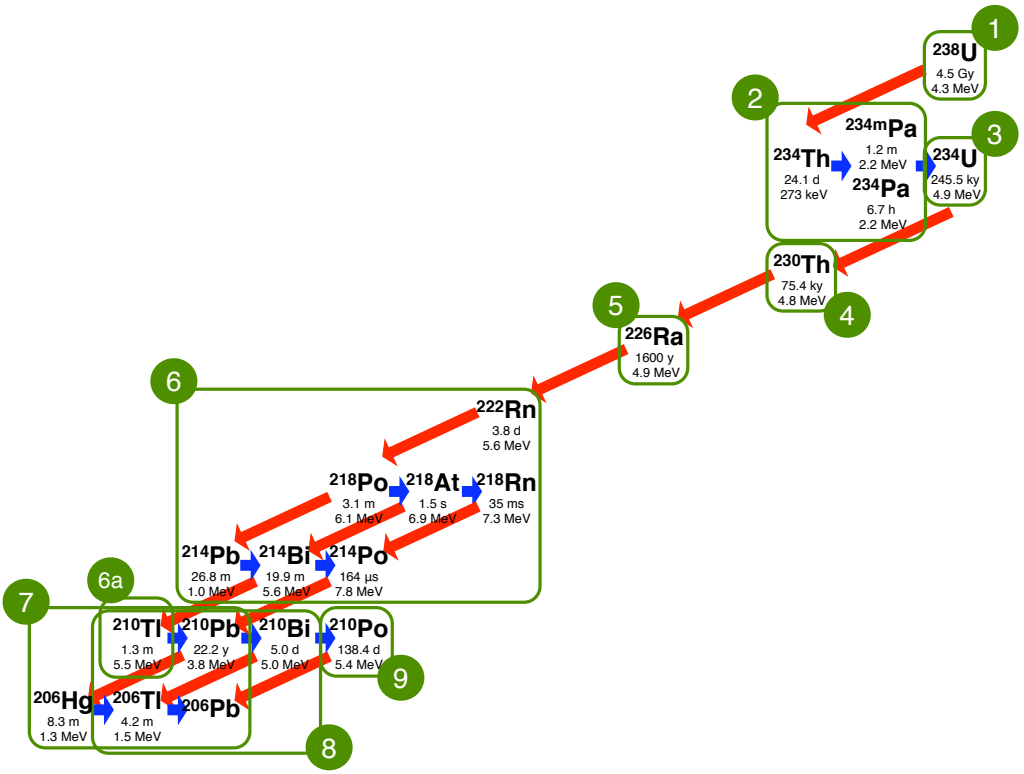

Figure 5.8: Steps used for simulation of the ^{238}U decay chain. Red arrows indicate alpha decays; blue arrows indicate beta decays. Split steps are indicated in green. For each step, all isotopes within the box are allowed to decay. Half life and Q-value are listed for each isotope. Where more than one decay mode is possible the larger Q-value is listed. Half lives and Q-values are from the NuDat decay radiation database [33].

Table 5.2: Steps used for simulation of the ^{238}U decay chain.

Step	**Description**	**Classification**
1	^{238}U to ^{234}Th	^{238}U upper chain
2	^{234}Th to ^{234}U	
3	^{234}U to ^{230}Th	
4	^{230}Th to ^{226}Ra	
5	^{226}Ra to ^{222}Rn	^{238}U lower chain I
6	^{222}Rn to ^{210}Tl or ^{210}Pb	
6a	^{210}Tl to ^{210}Pb	
7	^{210}Pb to ^{210}Bi or ^{206}Pb	^{238}U lower chain II
8	^{210}Bi to ^{210}Po or ^{206}Pb	
9	^{210}Po to ^{206}Pb	

particle crosses a boundary between two importance volumes, it is evaluated by GEANT4 and the track may be killed or split. The algorithm for modifying the track is described by Dressel [64]; part of the explanation is repeated here for the case used in the MALBEK simulations. For a track with weight w passing from volume m, with importance value I_m, to volume n, with importance value I_n, the following steps are taken:

1. A ratio of importance values, $r = I_n/I_m$, is calculated.

2. One of the following actions is performed, depending on the value of r:

   - If $r = 1$, no action is taken.
   - If $r < 1$, the particle is killed with probability $1 - r$.

- If $r > 1$ and an integer, the track is split into r identical tracks.[1]
- The weights of all resulting tracks are set to w/r.

The MAGE class `MGOutputMCRun` records track weight in `MGTMCStepData` with other step information, so that the correct energy spectrum can be reconstructed from importance-sampled Monte Carlo results.

To increase the number of counts in a detector, volumes far from a detector are typically assigned low importance values, and higher importance values are assigned to volumes near the detector. Volumes are usually arranged in an onion-layer structure around the detector; each inner volume is surrounded by a larger volume of lower importance.

The geometries of many detectors are not conducive to an onion-like layering scheme, where importance values increase with proximity to the detector. The onion-like scheme is not feasible for the MALBEK geometry; shown in Figure 5.5. None of the shielding forms an unbroken layer around the detector and the same air volume that borders the cryostat also exists between the lead and polyethylene shields. Also, it would be useful to have volumes with different importance values in the shielding, to increase the probability for incident radiation to reach the detector. Fortunately, GEANT4 provides a solution: parallel geometries.

A GEANT4 geometry model contains the standard "mass" world, which typically consists of volumes of air, lead, germanium, etc. GEANT4 also allows the creation of additional "parallel" or "ghost" worlds that coexist with the mass worlds. Volumes in a parallel world can be used for geometry importance sampling.

A virtual base class for parallel worlds, `MGGeometryParallelWorld`, was created for MAGE. This class describes a parallel world that can be used with a MAGE geometry class. The class `MJGeometryKURFBEGeDetectorInShieldParallelWorld` derives from `MGGeometryParallelWorld` and describes a parallel world for the MALBEK geometry, `MJGeometryKURFBEGeDetectorInShield`. A MAGE macro command was developed to turn the parallel world on at run-time and is shown in Appendix G.

[1] Other behavior is possible for non-integer r, but importance values for the MAGE MALBEK and DEMONSTRATOR geometries were chosen so that r was either 0.5 or 2.0.

Visualizations of the MALBEK MAGE/GEANT4 model with and without the parallel world were produced with GEANT4 and Drawer for Academic WritiNgs (DAWN) and are shown in Figure 5.9. The parallel world consists of multiple volumes throughout the polyethylene and lead shielding. The spacing and position of these volumes were chosen to propagate $\sim$ 1 MeV gammas from the experimental cavern toward the detector. The outermost parallel volume has an importance value of 1.0. The importance value of each parallel volume is twice that of the parallel volume that surrounds it.

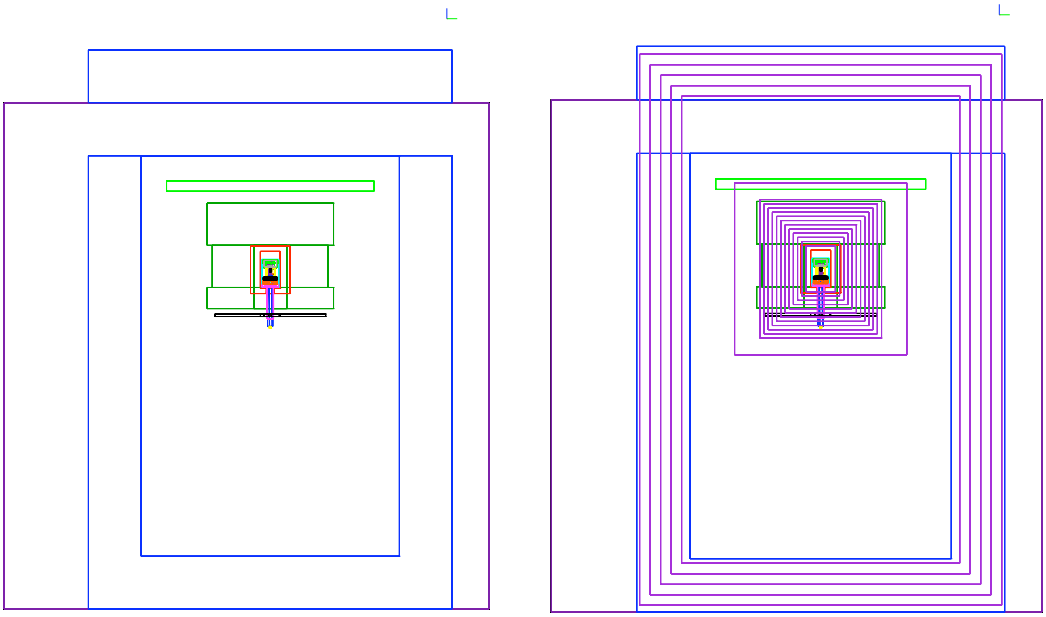

(a) (b)

Figure 5.9: DAWN wireframe visualizations of the MAGE/GEANT4 geometry model of the MALBEK detector in shielding. In (a), the shielding and cryostat volumes from Figure 5.5 are visible. In (b), parallel volumes have been added in violet.

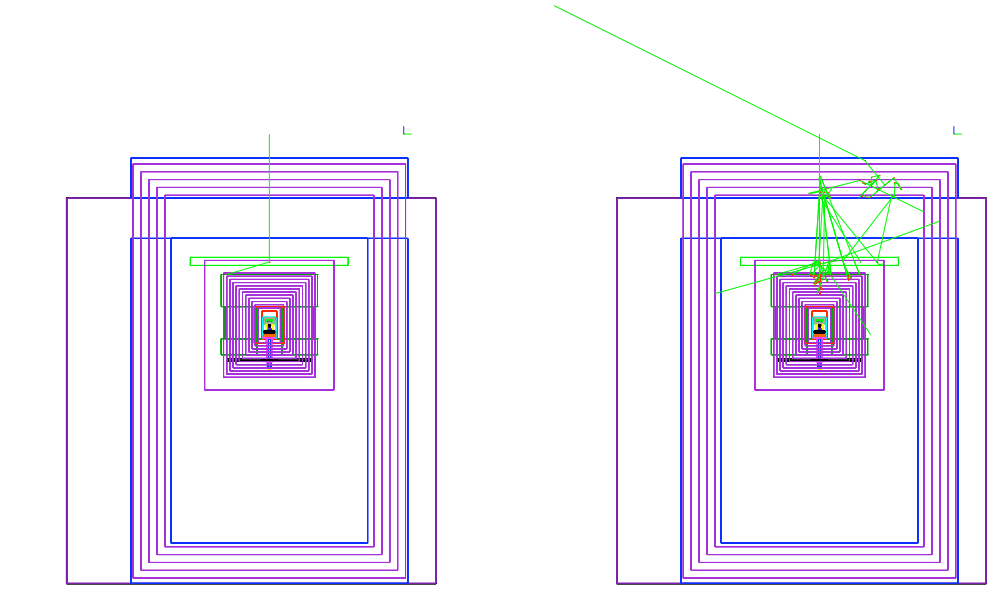

(a) (b)

Figure 5.10: An example of geometry importance sampling with the MAGE/GEANT4 MALBEK model. Both images show DAWN wireframe visualizations of the MAGE/GEANT4 MALBEK model with parallel volumes. In both images, a single 2-MeV gamma is fired at the detector from above the polyethylene shielding. Parallel volumes are shown in both images. Importance sampling is turned off in (a) and on in (b). There are more particle tracks in (b), but tracks do not reach the detector in either image.

5.8 Event windowing

When geometry importance sampling is used, a track crossing from a region of low importance to a region of high importance can be split into multiple tracks. Multiple split tracks may deposit energy in the detector, leading to an unphysical energy spectrum of detector response. Since typically only steps in the detector are written to output, it is not possible to study the MAGE output after the simulation has run and determine which split tracks produced which energy deposits.

To mitigate this issue, additional functionality was added to the MAGE output manager `MGVOutputManager`. MAGE output classes, including `MGOutputMCRun` derive from `MGVOutputManager` and inherit this functionality. The added functionality "windows" split tracks into new events. Each time a track is split by the GEANT4 importance sampling process, MAGE creates a new entry in the output `TTree`. Multiple entries that result from a single windowed event have the same event number, and are identifiable in the MAGE output as originating from the same primary particle. The track windowing would not be appropriate for events that multiple particles that may hit the detector.

Event windowing capability existed in MAGE to window energy deposits that are separated in time. Time windowing is used to maintain timing precision for energy deposits that occur after decays of particles with long half lives. MALBEK simulations use MAGE time windowing with a window length of one day. Importance sampling windowing built on this existing functionality.

5.9 Processing MAGE results with GAT

Results from MAGE simulations of detector response require processing before they can approximate data collected from a detector with a DAQ setup. This processing is performed with the GAT software package. MAGE ROOT output from `MGOutputMCRun` contains one `TTree` entry per Monte Carlo event, and each event contains an array of step data, where steps may be in multiple detector crystals (MALBEK has one crystal, so each array contains one element). In contrast, results in Tiers 1–3 of the ORCA data stream contain one `TTree`

entry per DAQ event, and each event contains an array of waveforms, where each waveform corresponds to one crystal.

The GAT module `GATMGTMCEventToAnalysisEvent` processes MAGE/GEANT4 Tier 0 `TTree` to create a Tier 1 `TTree` of `GATAnalysisEvent` and other objects. `MGTMCRun` data for each event is copied into the `TTree` of GAT output. The MAGE/GEANT4 Tier 1 format is similar to Tiers 2 and 3 of the ORCA data stream. The MAGE/GEANT4 data tiers are listed in Table 3.2.

The GAT Python script process_malbek_mage_results.py is used to process `MGOutputMCRun` results from MAGE. The script processes the Tier 0 ROOT `Tree` with the `GATMGTMCEventToAnalysisEvent` module. For each `TTree` entry, `GATMGTMCEventToAnalysisEvent` combines step data for each crystal to calculate the total energy per crystal and to produce events with an array of waveform-like data based on the MAGE/GEANT4 results. In addition, the following operations are performed on MAGE/GEANT4 results with GAT modules:

- *Time windowing*: a waveform recorded by a DAQ digitizer may be ~ 10 to 100 μs long, while a time-windowed MAGE/GEANT4 MALBEK event may span one day. A single entry in a `MGOutputMCRun TTree` may be split to form several `GATAnalysisEvent` objects, each spanning no more than a specified digitization time.

- *Dead layers*: all steps in detectors are recorded by MAGE's `MGOutputMCRun`. Dead layers are defined in GAT. GAT can be configured to use different dead layer models so that steps in dead layers contribute zero or partial energy.

- *Multi-site waveform identification*: waveforms are identified as single-site or multi-site. Currently this is done using a dt-heuristic method [65] developed by MAJORANA Collaborators Ren Cooper and David Radford at ORNL. The dt-heuristic method relies on a drift-time table generated for the detector and compares drift times of different interactions in the event, based on locations and energy deposits of the interactions, to determine whether the event is a multi-site event.

- *Nuclear recoil correction*: For nuclear recoils in germanium, a fraction of the energy is deposited as ionization energy that is recorded by the detector; the rest is lost as heat. To account for this loss, a quenching factor is applied by GAT's `GATMCEventEnergyCalculator` module according to Lindhard theory [66] using values measured in germanium [67].

The typical time to perform a MAGE run and generate a `MGOutputMCRun` ROOT file is a few to $\sim$ 100 times greater than the time required to process the file with GAT. A MAGE `MGOutputMCRun` ROOT file also typically occupies 10 to 100 times more disk space than the corresponding GAT output. Reprocessing a MAGE file with GAT requires fewer resources than repeating the MAGE simulation. MAGE might have been used to perform some of GAT's operations, e.g. apply dead layers and perform time windowing. However, performing these operations in GAT means that it is relatively quick to study the effects of different dead layer models, or change the time windowing parameters. Further post-processing, including convolution with function to describe energy resolution and preamplifier effects, are described in Chapter 7. A summary of GAT settings and results for all MAGE/GEANT4 results used in the MALBEK background model appears in Table H.3.

The sample MAGE/GEANT4 Tier 0 results of MALBEK response to ^{68}Ge decays in the germanium crystal were processed with GAT. The energy spectrum of Tier 1 GAT-processed results appears in Figure 5.1. The `GATAnalysisEvent` data member `fTotalEnergy` was used to make the spectrum of GAT results. Each count in the histogram is one entry in the GAT output `TTree`. A summary of MAGE/GEANT4 Tier 0 and Tier 1 results from the example runs is listed in Table 5.3.

5.10 Performing MAGE runs on computing clusters

MAGE/GEANT4 simulations of MALBEK response to expected backgrounds were performed on the Parallel Distributed Systems Facility (PDSF) at the National Energy Research Scientific Computing Center (NERSC) and on the CENPA-Rocks cluster at CENPA.

A set of Python scripts were developed to submit jobs to the computing clusters. Each run is submitted as a single job. The scripts generate MAGE macros that define the physics

Table 5.3: Summary of MAGE and GAT results for example MALBEK simulations performed on the CENPA-Rocks cluster.

MAGE/GEANT4 Run Parameters		
Primary particle	^{68}Ge	^{40}K
Number of GEANT4 events	1×10^5	5×10^6
Confinement volume for decays	Ge crystal	Teflon insulator
Tier 0: MAGE/GEANT4 `MGOutputMCRun` Results		
ROOT file size [MB]	194	35
Number of `TTree` entries	100023	29758
Processing time [minutes:seconds]	2:52	63:41
Tier 1: GAT `GATMGTMCEventToAnalysisEvent` Results		
ROOT file size [MB]	14	2.4
Number of `TTree` entries	180302	25786
Processing time [minutes:seconds]	0:35	0:12

list, detector, decay type, number of events, and other parameters of the runs, and submit the MAGE runs to the cluster. An example of usage of these scripts appears in Appendix F for the example simulation of MALBEK response to ^{68}Ge in the crystal.

Chapter 6

MALBEK RESPONSE TO A BARIUM-133 SOURCE

6.1 Introduction

In this chapter, a dataset of MALBEK response to a ^{133}Ba source is presented. This dataset was collected with ORCA at KURF and contains the response of MALBEK to a well-understood input: radioactive decays from a point-like calibration source, where the position and activity of the source are known. A background dataset (collected without a source) is also presented. These data are compared to simulation results to characterize the germanium dead layer and validate simulation of MALBEK energy spectrum response. These three datasets will be referenced multiple times in this chapter. To keep things clear, here are titles and descriptions of the datasets:

ORCA/Struck ^{133}Ba (+ backgrounds): this is the response of MALBEK to a ^{133}Ba calibration source. This dataset was collected at KURF with ORCA using the Struck digitizer while MALBEK was unshielded. This dataset includes MALBEK response to the ^{133}Ba source and to background environmental radiation (^{40}K, ^{214}Bi, etc.) in the KURF experimental hall.

ORCA/Struck backgrounds: this is the response of MALBEK to background radiation at KURF. This dataset was collected with the ORCA/Struck DAQ while MALBEK was unshielded.

MaGe/Geant4 ^{133}Ba: this is the simulated response of MALBEK to decays of ^{133}Ba.

The MALBEK detector has a diffused lithium n^+ contact, covering most of the surface of the detector. The thickness of this dead layer was reported as approximately 1 mm by Mike Yocum of CANBERRA [41]. The implanted boron p^+ point contact is approximately 0.3 μm

thick. These contact dead layers are regions of weak electric field within the germanium crystal, from which charge is not completely collected. Germanium detector dead layers were introduced in Section 1.3. In the simplest approximation, the dead layers are treated as step-like: charge deposited by interactions within the active region of the detector is completely collected and charge deposited by interactions within the dead layer is not collected.

In reality, the dead layer is not as simple as the step-like approximation. More complex parameterizations of the dead layer typically include a truly dead region and a transition region. Charge deposited within the truly dead region is not collected and charge deposited in the transition region is partially collected. The total dead layer consists of the truly dead region and the transition dead region. The dead layer measurement in this chapter relies on a ratio of gamma peak areas. Since charge deposited in the transition dead layer is not completely collected, interactions in the transition dead layer contribute negligibly to full-energy gamma peaks. Therefore, the dead layer measurement in this chapter is a measurement of the total dead layer thickness.

Radiation entering the MALBEK crystal is attenuated by the dead layers, which affect the shape of the resulting energy spectrum. The thick n^+ contact covers a large fraction of the surface area of the MALBEK germanium crystal. The thickness of the dead layer must be well known to accurately model the energy spectrum of MALBEK response to radiation and to estimate the active volume of the detector.

A ^{133}Ba source is often used to study the dead layer of a germanium detector. The decay of ^{133}Ba proceeds by electron capture to the stable isotope ^{133}Cs. The half life of this decay is 10.5 years and the Q-value is 517.5 keV. Gammas of up to 383.8 keV are emitted in the decay, along with conversion electrons and x-rays.

To study the thick n^+ germanium dead layer, a ratio of areas of the 81-keV and 356-keV ^{133}Ba gamma peaks was calculated from the ORCA/Struck ^{133}Ba dataset. Low-energy gammas are attenuated more strongly than high-energy gammas, so this ratio of peak intensities can be used to determine the dead layer thickness. This method has been used by GERDA [68] and MAJORANA Collaborators. MAGE/GEANT4 was used to simulate MALBEK response to the ^{133}Ba source. The Tier 0 simulation results were processed with GAT to apply different dead layer thicknesses, and a peak ratio was calculated for each set of

GAT-processed MAGE/GEANT4 Tier 1 results. The total dead layer thickness was determined from the value that best reproduced the ratio found from the ORCA data. The following sections describe the data collection and calculation of the dead layer thickness.

Simulated detector response may disagree with actual detector response for many reasons including inaccurate modeling of the geometry in MAGE, incomplete understanding of the behavior of the MALBEK detector readout electronics, and incorrect simulation of particle interactions by GEANT4. In this chapter, sources of discrepancies between simulated energy spectra and energy spectra collected at KURF with ORCA are quantified and used to estimate the uncertainty in the dead layer thickness measurement. These estimates of discrepancy are discussed in some detail so that they may be used in later chapters to describe uncertainties in other simulated energy spectra. The active mass of the detector is also estimated in this chapter.

6.2 Data collected with ORCA DAQ at KURF

In August 2011, MALBEK was removed from its shielding at KURF so that source spectra could be collected. To remove MALBEK, polyethylene surrounding the lead shield was first unstacked. A frame supporting the LN dewar, detector, and ancient lead was then lowered from the modern lead shielding and moved out from under the modern lead shield. Finally, the ancient lead surrounding the cryostat was removed. A background energy spectrum was collected in this unshielded configuration. The background dataset is summarized in Table 6.1 and the peaks are identified in Table C.4.

After the background dataset was collected, an uncollimated ^{133}Ba source was positioned 25 cm above the top face of the MALBEK cryostat, on axis with the detector, in the configuration recommended in IEEE Standard 325-1996 [69]. The source activity and run conditions are summarized in Table 6.2. Peaks in the energy spectrum were identified and fit with the unbinned maximum likelihood method described in Chapter 2. The results of peak fitting are listed in Table C.5. The ^{133}Ba and background energy spectra are shown in Figure 6.1.

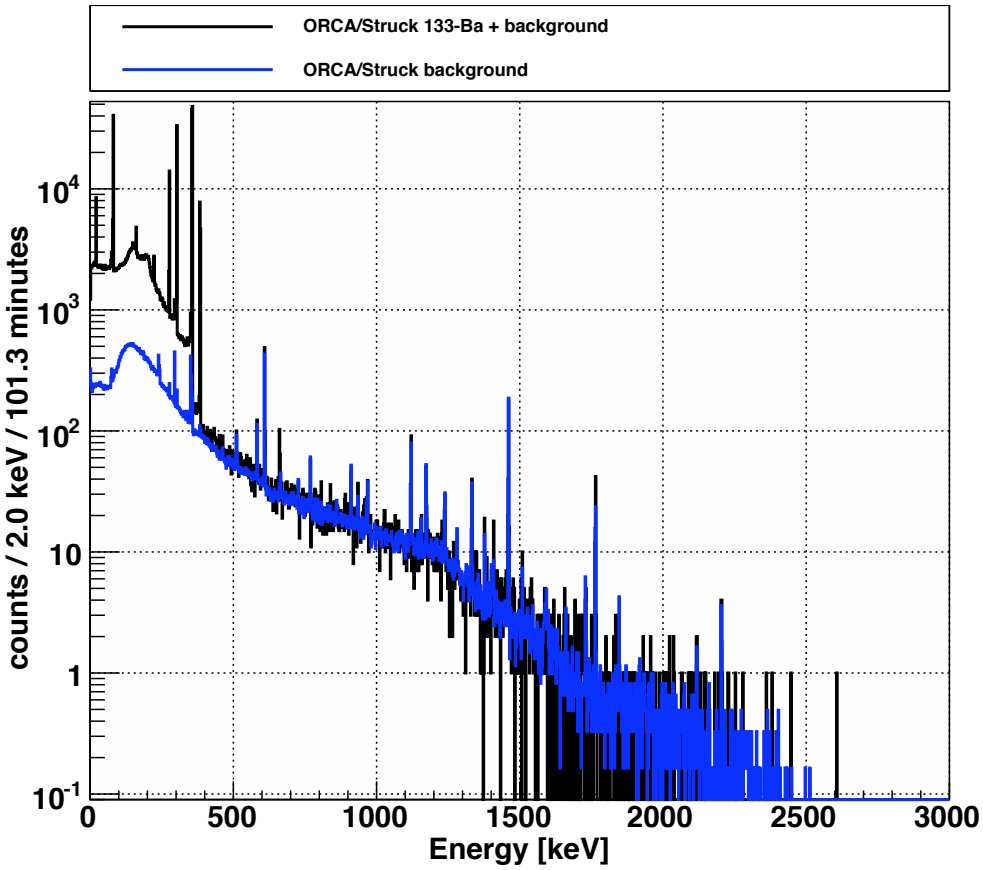

Figure 6.1: MALBEK response to a ^{133}Ba source and backgrounds at KURF. These spectra were collected from MALBEK at KURF using ORCA and the Struck digitizer. MALBEK was unshielded while the data were collected. The combined rise-time cut described in Chapter 2 was applied.

Table 6.1: Summary of ORCA/Struck unshielded background data collected at KURF.

Parameter	**Value**
Measurement date	August 16–17, 2011
ORCA run numbers	11853–11876
Duration of each run	30 minutes
Run time	800.8 minutes
Live time	617.7 minutes
Count rate above 5 keV	13.5 Hz
Pulser frequency	0.1 Hz
Pulser amplitude	100 mV (35.7 keV)
Energy resolution parameter c_0	118.9 ± 0.5 eV
Energy resolution parameter c_1	0.113 ± 0.003

6.3 Simulation of MALBEK response to barium-133

The MAGE `MJGeometryKURFBEGeDetectorInShield` geometry model was modified to match the setup at KURF during the unshielded source and background runs. The polyethylene shielding was removed from the model. The detector was placed inside the trailer, beside the lead shield, to match position measurements made at KURF in August 2011. Modeling the setup accurately ensures that any gamma scattering from the lead shield or trailer can be reproduced correctly in the simulation. MAGE/GEANT4 was used to simulate MALBEK response to 6.7×10^8 decays of ^{133}Ba emitted 25 cm from the cryostat endcap. The ^{133}Ba calibration source was approximated as a point source. This approximation is appropriate because the 133-Ba in the source is 3 mm in diameter, which is point-like at a distance of 25 cm. GAT processing of the Tier 0 results was performed with various n^+ dead layer thicknesses; each thickness produced a separate MAGE/GEANT4 Tier 1 result. An example energy spectrum of simulated MALBEK response to ^{133}Ba is shown in Figure 6.2 for an n^+

Table 6.2: Summary of ORCA/Struck ^{133}Ba data collected at KURF. The source activity was reported as 40.44 kBq ± 3.0% on September 1, 2008. Using the ^{133}Ba half life of 10.6 years, the activity at the time of the measurement is calculated to be 33.28 ± 1.00 kBq.

Parameter	**Value**
Measurement date	August 16, 2011
ORCA run numbers	11881–11903
Duration of each run	10 minutes
Run time	115.2 minutes
Live time	103.3 minutes
Count rate above 5 keV	100.6 Hz
Pulser frequency	1 Hz
Pulser amplitude	60 mV (21.5 keV)
Source activity	33.28 ± 1.00 kBq
Source-to-cryostat distance	25.0 cm
Energy resolution parameter c_0	120.5 ± 1.5 eV
Energy resolution parameter c_1	0.1053 ± 0.0005

dead layer thickness of 1.0 mm.

Florian Fraenkle, a MAJORANA collaborator, created software to validate MAGE/GEANT4 against published data. This code is included as part of MAGE. The simulated energies and intensities of radiation produced in many decays are compared to published values. The interactions of α, β, and γ particles in copper, germanium, and lead are also validated.

Results from the validation software related to gamma energies and intensities from ^{133}Ba decay are presented in Table 6.3. All simulated gamma energies are correct within 0.01 keV. GEANT4 under-produces gammas, with the exception of the 81-keV line. Gamma intensities are within 5% of published values, except the 79.6-keV line. Deviations from

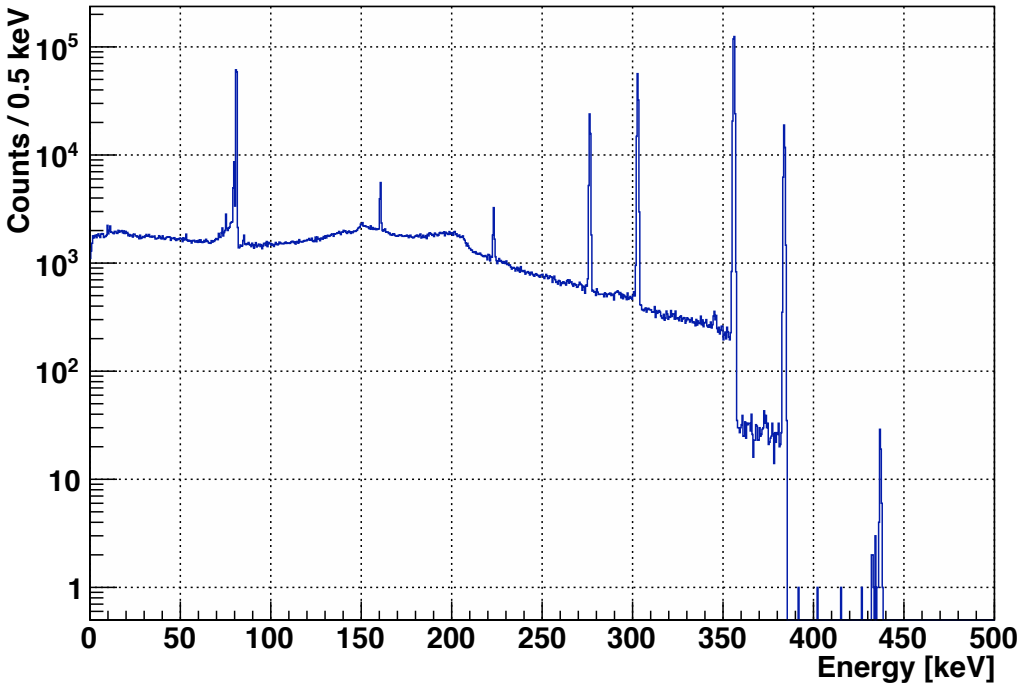

Figure 6.2: Simulated MALBEK response to a ^{133}Ba source. A 1.0-mm dead layer was applied. There are 1.5 $\times$ 10^6 counts in the spectrum; 6.7 $\times$ 10^8 decays of ^{133}Ba were simulated. The spectrum was convolved with a Gaussian function to match the energy resolution of the ORCA data listed in Table 6.2. The preamplifier efficiency curve was also applied to the data.

published gamma intensities will be considered when peak ratios are calculated from MAGE/GEANT4 results.

GEANT4.9.3.p01 includes two sets of data files that are used to determine radiation emitted in nuclear decays [4]. The data files in the RadioactiveDecay3.2 package describe the decays of a parent nucleus to excited states of a daughter nucleus. The energy levels of the daughter nucleus and the probability for the decay to populate each level are contained in the file. The PhotonEvaporation2.0 data files include nuclear de-excitation data, including gamma branching ratios for de-excitation from each energy level in a nucleus. The RadioactiveDecay and PhotonEvaporation packages are based on data from the Evaluated Nuclear Structure Data File (ENSDF), which is maintained by the National Nuclear Data Center. The most recent ENSDF data for ^{133}Ba decay is available in the Nuclear Data Sheets for A=133 [70]. There are some discrepancies in transition probabilities between the most recent ENSDF data and the RadioactiveDecay3.2 data files. There are also discrepancies in branching ratios between the ENSDF data and the PhotonEvaporation2.0 data files. GEANT4.9.3.p01, which was used in this dissertation work, was released in 2010, while the most recent ENSDF data for ^{133}Ba decay was updated in 2011. The GEANT4 data files may be based on outdated ENSDF data. A GEANT4 bug report was submitted about this issue [71].

The 81-keV and 356-keV gammas emitted in ^{133}Ba decay have a small positive angular correlation when they are emitted in coincidence [72]. GEANT4 does not simulate angular correlations of gammas. If the angular correlation between the 81-keV and 356-keV gammas had a significant effect on the energy spectrum, a sum peak would appear at 437 keV in the ^{133}Ba dataset. No such peak is visible, so the lack of angular correlation in the MAGE/GEANT4 results should not affect the dead layer measurement.

6.4 Dead layer measurement

A ratio, R_{ORCA}, of areas of the 81-keV and 356-keV ^{133}Ba gamma peaks was calculated from the ORCA/Struck ^{133}Ba dataset:

Table 6.3: Gamma energies and intensities from ^{133}Ba decay in simulation and literature. Literature values are from Nuclear Data Sheets for A = 133 [70]. Simulation values are from F.M. Fraenkle's MAGE validation software for GEANT4 version 9.3.p01 [73]. One million decays of ^{133}Ba were simulated to produce the results. Energies are in keV. Intensities are per 100 decays. Uncertainties are 68% C.L. statistical.

Literature		**MAGE/GEANT4**		**Comparison**	
E_{lit}	I_{lit}	E_{sim}	I_{sim}	$E_{sim} - E_{lit}$	$(I_{sim}/I_{lit}) - 1$ [%]
53.16	2.14 ± 0.03	53.16	2.08 ± 0.01	0.00	-2.8 ± 1.6
79.61	2.65 ± 0.05	79.61	2.41 ± 0.02	0.00	-9.0 ± 1.8
81.00	32.95 ± 0.33	81.00	33.30 ± 0.06	0.00	1.1 ± 1.0
160.61	0.64 ± 0.01	160.61	0.62 ± 0.01	0.00	-2.8 ± 1.5
223.24	0.45 ± 0.00	223.24	0.44 ± 0.01	0.00	-3.3 ± 1.6
276.40	7.16 ± 0.05	276.40	6.83 ± 0.03	0.00	-4.6 ± 0.7
302.85	18.34 ± 0.06	302.85	18.00 ± 0.04	0.00	-1.8 ± 0.4
356.01	62.05 ± 0.19	356.02	59.80 ± 0.08	0.01	-3.6 ± 0.3
383.85	8.94 ± 0.06	383.86	8.78 ± 0.03	0.01	-1.8 ± 0.8

$$R_{ORCA} = \frac{N_{81}}{N_{356}} \tag{6.1}$$

$$= \frac{36,557.1 \pm 197.8}{91,801.3 \pm 304.3} \tag{6.2}$$

$$= 0.3982 \pm 0.0025 \tag{6.3}$$

where N_{81} is the number of counts in the 81-keV peak and N_{356} is the number of counts in

the 356-keV peak. Results from the fits are shown in Figures 6.3 and 6.4. The combined rise time cut described in Chapter 2 had been applied to the dataset. Regions of the energy spectrum were fit with the unbinned maximum likelihood approach described in Chapter 2 to determine the number of counts in the gamma peaks. When determining the number of counts in the 81-keV peak, the 79.6-keV and 81.0-keV ^{133}Ba peaks were each fit with Gaussian functions, and the continuum below the peaks was fit with a linear polynomial. A step function was included on the low-energy side of the 81-keV peak, because this step improved the value of χ^2 per degree of freedom by more than 1.0. A step function was not used on the 79.6-keV peak because it did not significantly improve the fit. When determining the number of counts in the 356-keV peak, the 351.9-keV ^{241}Pb and 356.0-keV ^{133}Ba peaks were fit with Gaussian functions, and the continuum below the peaks was fit with a linear polynomial. A step function was included on the low-energy side of the 356-keV peak. The uncertainties listed in the number of counts are those reported by the fitter.

After convolving the simulated energy spectrum with a Gaussian resolution function and the preamplifier efficiency curve, the areas of the 81-keV and 356-keV peaks in MAGE/GEANT4 Tier 1 results were found with the same maximum likelihood fitting code used for the ORCA data. In Table 6.3, the MAGE validation software showed that GEANT4 produces incorrect gamma intensities in ^{133}Ba decay. The peak ratio from the MAGE/GEANT4 results must be corrected for this discrepancy. Expressions for the number of counts in a peak in the MALBEK energy spectrum and for the ratio of counts in two peaks are formulated below. These expressions will be used to show how the peak ratio measured from simulation should be corrected for gamma intensity. These expressions will also be used in the next section to determine uncertainty in the dead layer measurement from various sources.

The number of gammas of energy E emitted in a ^{133}Ba decay that contribute to a full-energy peak in the MALBEK energy spectrum is given by the product:

$$N_E = N_{decays} \times I_E \times \epsilon_{solid\ angle} \times \epsilon_{atten.}(E) \times \epsilon_{dep.}(E) \times \epsilon_{preamp}(E) \tag{6.4}$$

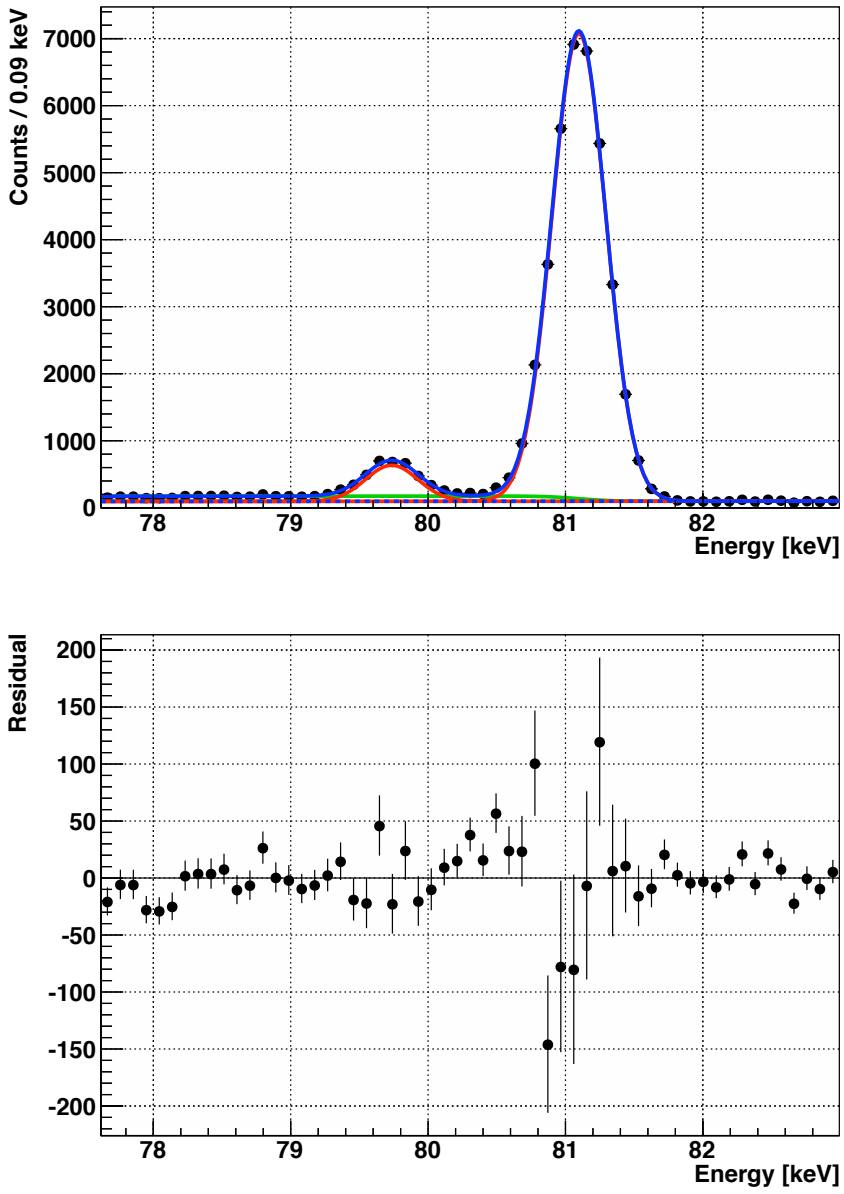

Figure 6.3: Fit of the 79.6-keV and 81.0-keV peaks in the ORCA/Struck ^{133}Ba dataset. In the top panel, the ORCA/Struck data points are shown in black, the fit result is blue, the Gaussian contributions to the fit function are red, and the step function contribution to the fit is green. Fit residuals are shown in the bottom panel. This fit has a χ^2 value of 87.8 and 47 degrees of freedom. This is a reduced χ^2 of 1.87 and a P-value of 0.0003.

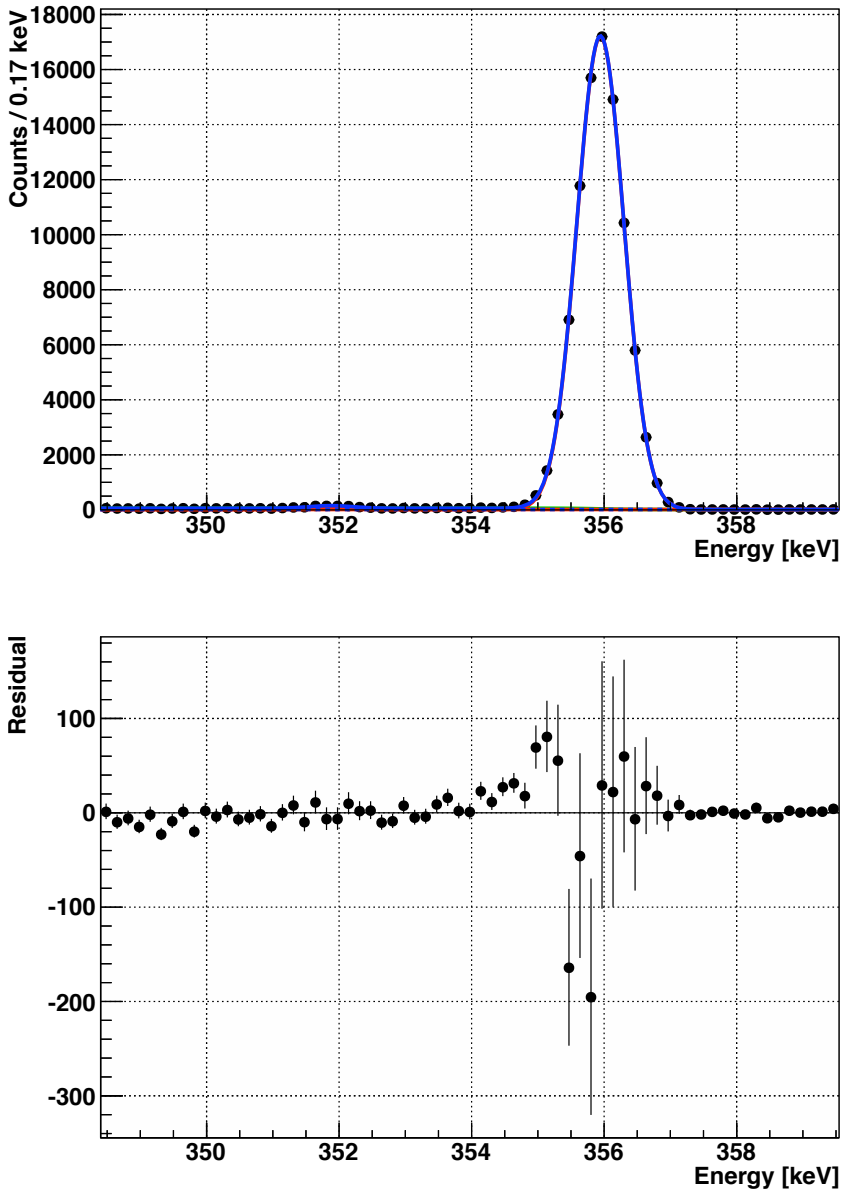

Figure 6.4: Fit of the 352-keV ^{214}Pb and 356-keV ^{133}Ba peaks in the ORCA/Struck ^{133}Ba dataset. In the top panel, the ORCA/Struck data points are shown in black and the fit result is blue. Fit residuals are shown in the bottom panel. This fit has a χ^2 value of 93.5 and 57 degrees of freedom. This is a reduced χ^2 of 1.64 and a P-value of 0.002.

where the following factors contribute to the number of counts in the full energy peak, N_E:

N_{decays} is the number of ^{133}Ba decays in the time period of interest.

I_E is the number of gammas of energy E produced per decay.

$\epsilon_{solid\ angle}$ is the geometric efficiency for a gamma to hit the detector. This efficiency depends on the solid angle subtended by the detector.

$\epsilon_{atten.}(E)$ is the attenuation of gammas of energy E by material between the source and active detector region. Gammas between MALBEK and the source are attenuated by air, copper, Teflon, and the germanium dead layer.

$\epsilon_{dep.}(E)$ is the efficiency for a gamma of energy E in the active detector region to deposit its full energy. This value depends on the dimensions of the active volume of the detector and the cross sections for gamma and electron interaction.

$\epsilon_{preamp}(E)$ is the energy-dependent efficiency due to the pulsed-reset preamplifier, which depends on the reset energy of the preamplifier and the leakage current of the detector.

The ratio of ^{133}Ba peak counts can be expressed in terms of Equation 6.4:

$$R = \frac{N_{81}}{N_{356}} \tag{6.5}$$

$$R = \frac{I_{81}}{I_{356}} \frac{\epsilon_{atten.}(E = 81\ keV)}{\epsilon_{atten.}(E = 356\ keV)} \frac{\epsilon_{dep.}(E = 81\ keV)}{\epsilon_{dep}(E = 356\ keV)} \frac{\epsilon_{preamp}(E = 81\ keV)}{\epsilon_{preamp}(E = 356\ keV)} \tag{6.6}$$

$$R = I_{rel.} \times \epsilon_{rel.\ atten.} \times \epsilon_{rel.\ dep.} \times \epsilon_{rel.\ preamp} \tag{6.7}$$

where the subscripts *rel.* indicate relative values: the value at 81 keV divided by the value at 356 keV. The factors N_{decays} and $\epsilon_{solid\ angle}$ cancel since they do not depend on energy.

In the Nuclear Data Sheets, the intensity of the 81-keV peak relative to the 356-keV peak is quoted as $53.10 \pm 0.50\%$ [70]. The results of the MAGE validation software, in Table 6.3, indicate that the relative intensity simulated by GEANT4 is $55.69 \pm 0.12\%$. To make a higher-statistics measurement of the relative intensity produced by GEANT4, a dedicated set of simulations were performed and 2.2×10^7 decays of ^{133}Ba were simulated. The relative intensity of the 81-keV and 356-keV peaks in the simulation was found to be $55.75 \pm 0.03\%$.

A ratio $R_{sim.}$ was calculated from the MAGE/GEANT4 results for each dead layer thickness. According to Equation 6.7, this ratio should be corrected for the gamma intensity as follows:

$$R_{sim.} = \left(\frac{N_{81}}{N_{356}}\right)\left(\frac{I_{rel.\ lit.}}{I_{rel.\ sim}}\right) \tag{6.8}$$

where $I_{rel.\ lit}$ is the published intensity of the 81-keV peak relative to the 356-keV peak and $I_{rel.\ sim}$ is the relative intensity produced by GEANT4. Example peak fits are shown in Figures 6.5 and 6.6 for the 0.9-mm dead layer.

The peak ratios from the ORCA ^{133}Ba dataset and from the MAGE/GEANT4 ^{133}Ba dataset are plotted in Figure 6.7. The ORCA ratio from Equation 6.1 is plotted as the violet horizontal dashed line. The uncertainty reported by the fitter is shown by the width of the violet hatched band. The ratio calculated from each MAGE/GEANT4 Tier 1 dataset is plotted as a black point in Figure 6.7. The ratios from MAGE/GEANT4 were fit with a quadratic curve, which appears in red in Figure 6.7. The data are well-described by the curve; the fit has a χ^2 value of 1.11 and 18 degrees of freedom. The best fit value of the dead layer thickness was calculated from the intersection of the ORCA ratio and the quadratic curve. This value is shown in the figure as a blue vertical line. Uncertainties in the ORCA and MAGE/GEANT4 ratios were combined in quadrature and propagated into the measured dead layer value using the equation of the quadratic curve. The resulting uncertainty in the measured dead layer is shown with the blue hatched box. The measured dead layer thickness is 0.933 ± 0.018 mm, where only statistical uncertainties due to fitting have been considered. Additional systematic uncertainties contribute to the measurement

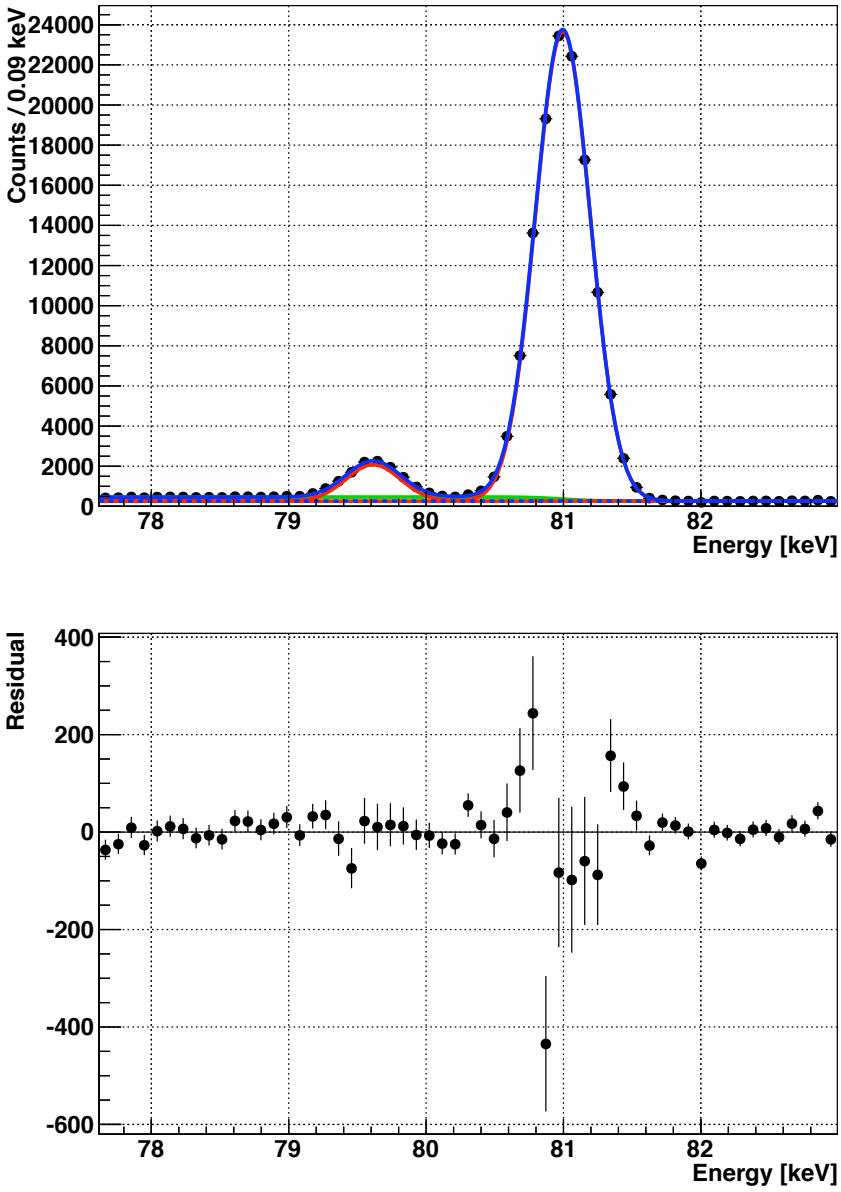

Figure 6.5: Fit of the 79.6-keV and 81.0-keV peaks in the MAGE/GEANT4 ^{133}Ba dataset. In the top panel, the MAGE/GEANT4 data points are shown in black, the fit result is blue, the Gaussian contributions to the fit function are red, and the step function contribution to the fit is green. Fit residuals are shown in the bottom panel. This fit has a reduced χ^2 value of 1.61 and a P-value of 0.005. An 0.9-mm dead layer was applied to the MAGE/GEANT4 results.

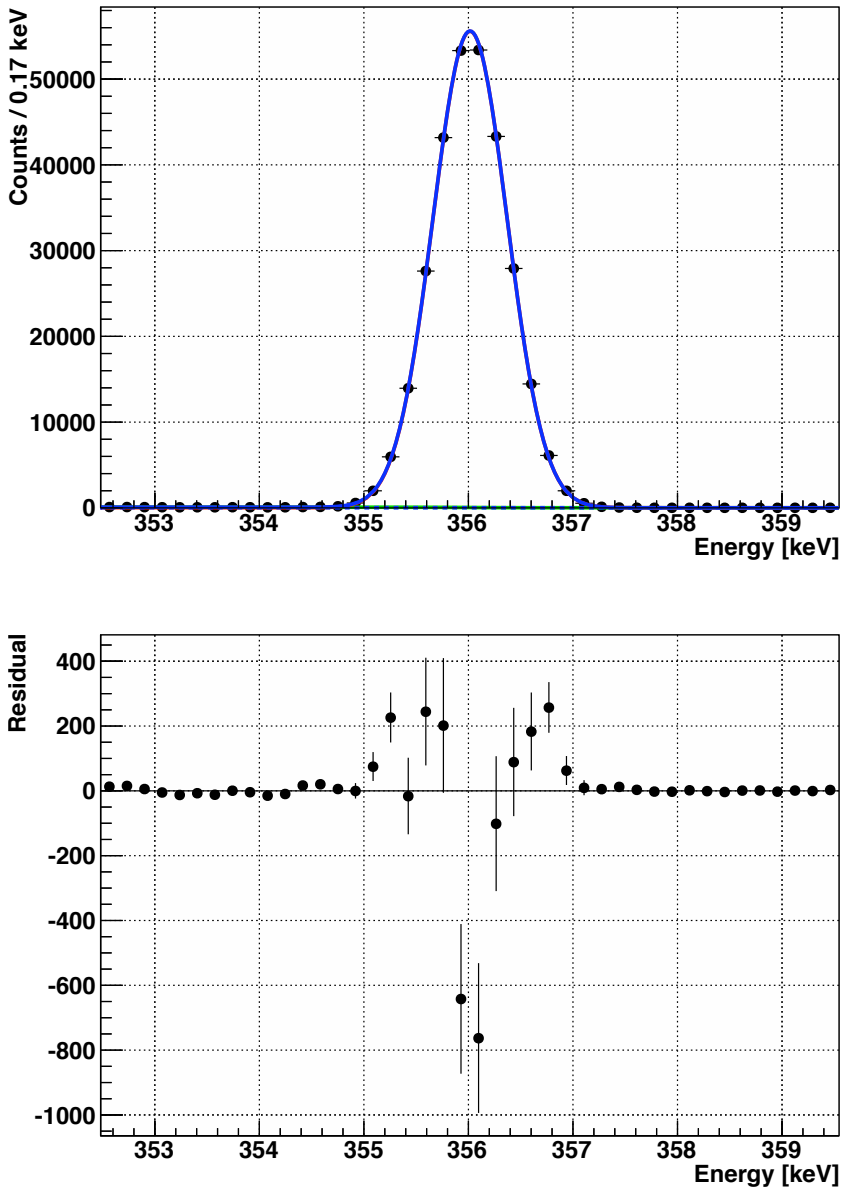

Figure 6.6: Fit of the 356-keV ^{133}Ba peak in the MAGE/GEANT4 ^{133}Ba dataset. In the top panel, the MAGE/GEANT4 data points are shown in black and the fit result is blue. Fit residuals are shown in the bottom panel. This fit has a reduced χ^2 of 1.19 and a P-value of 0.201. An 0.9-mm dead layer was applied to the MAGE/GEANT4 results.

and are described below. When these uncertainties are taken into account, the measured dead layer thickness is:

$$0.933 \pm 0.018 \text{ stat.} \pm 0.092 \text{ sys. mm.}$$

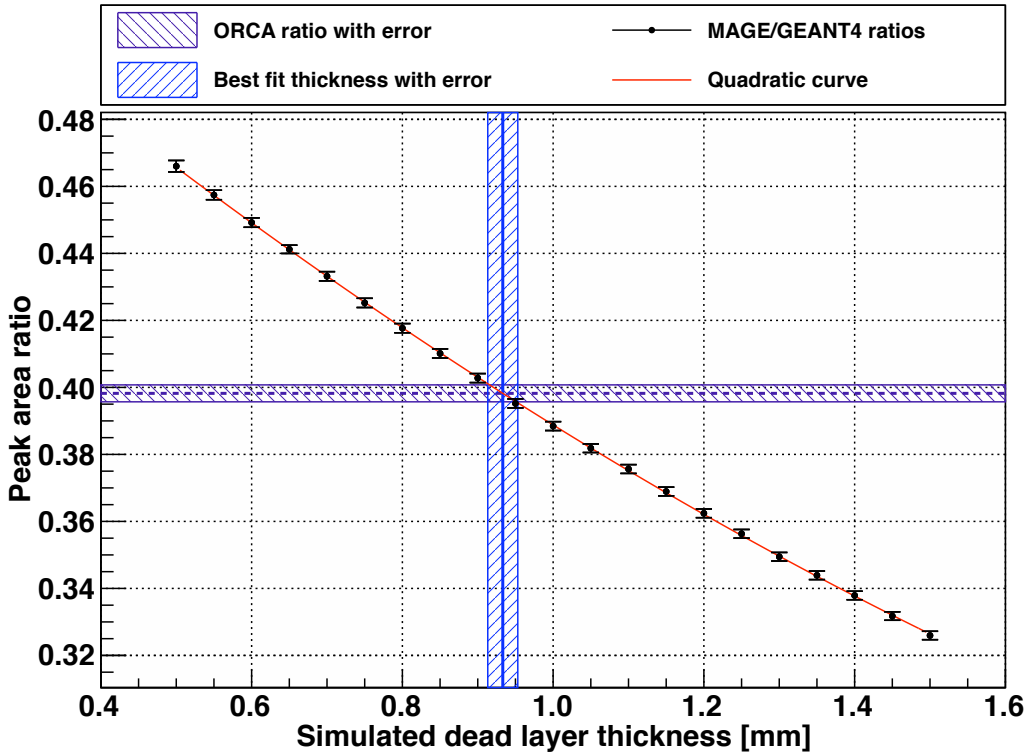

Figure 6.7: Dead layer measurement with ^{133}Ba. The best fit dead layer thickness is 0.933 mm. Uncertainties due to peak fitting are shown. Total uncertainties contributing to the MAGE/GEANT4 results are listed in Table 6.4 and explained in the text.

6.5 Sources of uncertainty in the dead layer measurement

In addition to the uncertainties in peak areas described above, several sources of systematic uncertainty contribute to the dead layer measurement. In this section, the uncertainty in the dead layer due to each factor in R_{sim}, according to equation 6.7, are calculated. Additional

uncertainty in the value of R_{ORCA} is also considered. Contributions to uncertainty in the dead layer are listed in Table 6.4. The contents of the table are described below.

Table 6.4: Uncertainties contributing to total dead layer thickness, measured with a ratio of ^{133}Ba peaks. Uncertainties in peak ratios are determined from the peak fitter. The other uncertainties are described in the text. The total uncertainties were calculated by adding contributions in quadrature.

Statistical uncertainty	
Ratio of peaks in ORCA/Struck data (R_{ORCA})	0.018 mm
Ratio of peaks in MAGE/GEANT4 results (R_{sim})	0.003 mm
Total statistical uncertainty	0.018 mm

Systematic uncertainty	
Gamma intensities from literature [70] ($I_{rel.\ sim.}$)	0.026 mm
Gamma intensities from MAGE/GEANT4 ($I_{rel.\ sim.}$)	0.001 mm
Cryostat component dimensions ($\epsilon_{rel.\ atten.}$)	0.057 mm
Energy deposition efficiency ($\epsilon_{rel.\ dep.}$)	0.068 mm
Preamplifier efficiency ($\epsilon_{rel.\ preamp}$)	0.002 mm
Systematic uncertainty in peak fitting	0.020 mm
Total systematic uncertainty	0.092 mm

6.5.1 Uncertainty in attenuating materials

Air and various components in the detector separate the ^{133}Ba source from the MALBEK active volume. The efficiency $\epsilon_{atten.}$ describes the attenuation of ^{133}Ba gammas by these

materials: air, copper, Teflon, and germanium. This efficiency depends on gamma energy and is the product of five efficiencies, one for traversing each layer of material:

$$\epsilon_{atten.}(E) = \epsilon_{air}(E) \times \epsilon_{Cu\ endcap}(E) \times \epsilon_{Cu\ lid}(E) \times \epsilon_{Teflon\ sheets}(E) \times \epsilon_{Ge\ DL}(E) \quad (6.9)$$

Attenuation within the source is neglected. The source is small and low mass, so attenuation within the source is believed to be small compared to attenuation within the cryostat components.

In principle, the uncertainty in the dead layer measurement due to $\epsilon_{atten.}$ can be determined by varying each factor in Equation 6.9 within its uncertainty, then performing the dead layer thickness measurement and determining the resulting change in dead layer thickness. For $\epsilon_{atten.}$ this would require modification of the MAGE MALBEK model and regeneration of the high-statistics ^{133}Ba simulations. Due to practical limitations on time and disk space, uncertainty in the dead layer due to $\epsilon_{atten.}$ will be calculated analytically.

The fractional uncertainty in $R_{sim.}$ can be expressed in terms of the fractional uncertainties in each term in Equation 6.7:

$$\frac{\sigma_{R_{sim.}}}{R_{sim.}} = \sqrt{\left(\frac{\sigma_{I_{rel.}}}{I_{rel.}}\right)^2 + \left(\frac{\sigma_{\epsilon_{rel.\ atten.}}}{\epsilon_{rel.\ atten.}}\right)^2 + \left(\frac{\sigma_{\epsilon_{rel.\ dep.}}}{\epsilon_{rel.\ dep.}}\right)^2 + \left(\frac{\sigma_{\epsilon_{rel.\ preamp}}}{\epsilon_{rel.\ preamp}}\right)^2} \quad (6.10)$$

The resulting uncertainty in the dead layer thickness can be determined from the equation of the quadratic curve describing R_{sim} as a function of dead layer thickness.

Each of the efficiencies in Equation 6.9 can be determined from the attenuation equation, which describes a beam of mono-energetic photons incident on a surface with intensity I_0 and emerging from the surface with intensity I [74]:

$$\frac{I}{I_0} = \exp\left[-\left(\frac{\mu}{\rho}\right)\rho t\right] \quad (6.11)$$

where ρ is the material density, t is the thickness, and the quantity μ/ρ is the mass attenuation coefficient, which is available from several evaluated data libraries.

The mass attenuation coefficient varies with energy and is related to the total photon cross section:

$$\frac{\mu}{\rho} = \frac{\sigma_{total}}{uA} \tag{6.12}$$

where σ_{total} is the total photon cross section per atom, u is the atomic mass unit, and A is the atomic mass of the target element. Photon interaction cross sections in GEANT4 have been validated extensively by the GEANT4 Collaboration [75], so uncertainty in photon intensity is believed to result from uncertainties in the dimensions of geometry models.

The fractional change in I due to uncertainty in t, σ_t, is:

$$\frac{I\left(t \pm \sigma_t\right) - I(t)}{I(t)} = \frac{\exp\left[-\mu\left(t \pm \sigma_t\right)\right] - \exp\left[-\mu t\right]}{\exp\left[-\mu t\right]} \tag{6.13}$$

$$= \exp\left[-\mu\left(\pm\sigma_t\right)\right] - 1 \tag{6.14}$$

$$= \frac{I(\pm\sigma_t)}{I_0} - 1 \tag{6.15}$$

Gammas from the ^{133}Ba source are emitted isotropically. For the ^{133}Ba source at a distance of 25.5 cm from the 30-mm-radius MALBEK germanium crystal (25.0 cm from the front face of the cryostat), gammas that traverse the front face of the cryostat and enter the germanium crystal will have an angle of incidence between 0 and 6.8 degrees. This corresponds to a solid angle of 0.014π. The gammas at the largest angles of incidence travel through an additional 0.7% thickness of material before reaching the crystal. This tiny difference in the material thickness is negligible in the uncertainty calculations, so a single thickness, t, is assumed for each component in Equation 6.13.

The thicknesses of the MALBEK copper endcap, copper lid, and Teflon sheets were measured at CANBERRA in October 2011, and each measurement was reported with 0.001 inch uncertainty [76]. In Figure 6.8, the quantity $1 - I/I_0$ is plotted for various materials, for a thickness of 0.001 inch. The figure shows how this small uncertainty in thickness produces a large uncertainty in the intensity of the ^{133}Ba gamma peaks. If the copper lid in the MAGE model of the MALBEK cryostat is just 0.001 inch thicker than reality, then the number of counts in the simulated 81-keV ^{133}Ba gamma peak will be reduced by $\sim 2\%$, while the number of counts in the 356-keV peak is reduced by only thickness $\sim 0.2\%$. This would reduce the measured dead layer thickness by 0.040 mm.

During the UNC trip to CANBERRA, it was found that a 0.001 inch layer of copper foil was wrapped around the outer diameter of the MALBEK crystal, with a small tab that extended around the high-voltage contact [58]. This foil is not included in the MAGE model. The foil is not between the ^{133}Ba source and the Ge crystal, so the ^{133}Ba spectrum is not affected, but other spectra may be. Superinsulation was also discovered inside the cryostat, wrapped around the copper cup and lid, and extending along other parts inside of the copper endcap. The superinsulation serves as an IR shield to improve the thermal performance of the cryostat. This superinsulation is believed to be aluminized Mylar, and it is not included in the MAGE model. Based on the mass and approximate dimensions of the superinsulation [58], this superinsulation could contribute up to 0.006 inches of aluminum around the top and sides of the copper cup, and up to 0.040 inches of aluminum around the lower portion of the copper cup. Only the $\sim$ 0.006 inches of aluminum on the top of the copper lid would affect the ^{133}Ba spectrum. The effect would be on the order of 1 part in 10^3, so it is neglected here.

6.5.2 Uncertainty in energy deposition in the active volume

The relative efficiency for energy deposits in the active volume ($\epsilon_{rel.\ dep.}$) depends on the dimensions of the active volume of the detector and the cross sections for gamma and electron interaction. Interaction cross sections have been validated by the GEANT4 Collaboration, so uncertainty in $\epsilon_{rel.\ dep.}$ will be estimated from uncertainty in the geometry of the crystal.

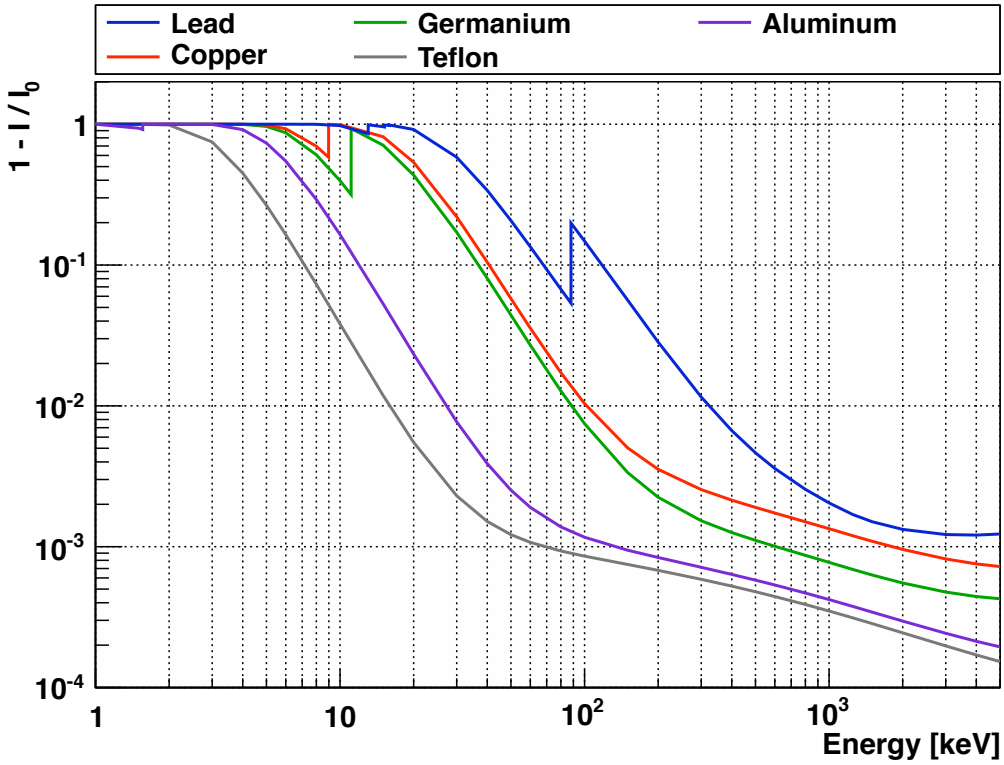

Figure 6.8: Photon attenuation in various materials. The quantity $1 - I/I_0$ represents the fraction of photon intensity that is lost by traversing 0.001 inch (0.025 mm) of material. Intensities were calculated using Equation 6.11 and the values published by NIST [74]. This plot shows how small uncertainties in dimensions of components near a germanium detector lead to large uncertainties in gamma peak intensities. After traversing a copper part with thickness known to 0.001 inch, the intensity of a 100-keV gamma can only be known to within about 1%; if the uncertainty in the thickness is 0.010 inch, the intensity can only be known to about 10%. Typically, the dimensions of machined parts are specified with 0.003-inch to 0.010-inch tolerances.

CANBERRA reported the length of the MALBEK germanium crystal as 30 mm [38], [39]. No uncertainty estimate was reported with this value. We will estimate an uncertainty of 1 mm (0.04 inches). To estimate the effect of this uncertainty, the MAGE/GEANT4 results presented in Section 6.3 were reprocessed with GAT, assuming the crystal was 1 mm shorter than in the MAGE model. A measurement of the dead layer was made from this set of MAGE/GEANT4 results: 1.001 $\pm$ 0.020 mm. This is a nominal increase of 0.068 mm in the dead layer thickness; this is the largest uncertainty contributing to the totals in Table 6.4.

Uncertainty in the germanium crystal diameter does not affect the ^{133}Ba peak ratio, since the 81-keV and 356-keV gamma efficiencies are equally affected by the diameter, but the absolute normalization of the energy spectrum is affected. The diameter of the MALBEK crystal is specified as 2.385 inch (60.6 mm) in a purchase request [38]. The diameter of the crystal was also measured as 2.396 inches during the lead shim removal trip [58]. So the crystal would not be damaged by the calipers, it was measured while wrapped in copper foil. The foil thickness was measured as 0.001 inch, so the crystal diameter was measured as approximately 2.394 inch. Given the inexact nature of the measurement through the foil, the uncertainty in the crystal diameter is less than 0.009 inch.

6.5.3 Uncertainty in preamplifier efficiency

Using Equation 4.13, and values of the time between resets (T_{reset} = 39.0 $\pm$ 0.5 ms) and reset energy (E_{reset} = 2682 $\pm$ 11 keV) measured from the ^{133}Ba dataset, the uncertainty in the dead layer due to $\epsilon_{rel.preamp}$ is calculated to be 0.002 mm.

6.5.4 Uncertainty in the ORCA 356-keV peak

Some ^{133}Ba peaks are visible in the ORCA/Struck background dataset. In particular, a statistically significant 356-keV ^{133}Ba peak is present. The origin of this peak is not clear. The 33-kBq calibration source used for the ^{133}Ba dataset was removed from the MALBEK trailer during collection of the background dataset, but the source was still in the experimental hall and it may have contributed to the background energy spectrum. Also, a 36-kBq ^{133}Ba calibration source was in a nearby trailer at KURF during data taking. The

356-keV peak in the background dataset may be due to either one of these sources or both sources may have contributed – it's not possible to tell.

If some counts in the 356-keV peak of the ORCA/Struck background dataset are due to the 36-kBq source in the nearby trailer, then this is a problem for the dead layer measurement. The 36-kBq ^{133}Ba source would also contribute counts to the 356-keV peak of the ORCA/Struck ^{133}Ba dataset, and the 356-keV to 81-keV peak ratio would be affected by these spurious counts. Fortunately, the count rate in 356-keV peak of the background dataset (0.029 ± 0.001 Hz) is very small compared to the count rate in the 356-keV peak of the ^{133}Ba dataset (15.110 ± 0.050 Hz). To account for the possibility of a spurious 356-keV ^{133}Ba contribution to the ORCA/Struck ^{133}Ba energy spectrum, a systematic uncertainty of 0.029 Hz (0.2%) in the area of the 356-keV peak is considered when the peak ratio R_{ORCA} is calculated. This contributes 0.005 mm to the uncertainty in the dead layer thickness.

6.5.5 Systematic uncertainty in peak fitting

To estimate the systematic error associated with peak fitting, the dead layer measurement was repeated with modifications to the fitting procedure. The modifications that were tested include using a different energy range surrounding the peaks, neglecting the low-energy step, and using a binned maximum likelihood fit. Based on these tests, the systematic uncertainty in the dead layer due to fitter is approximately 0.020 mm.

6.6 Calculation of active detector mass

The MALBEK germanium crystal consists of an active detector region, a thick n^+ dead layer, and a point-contact p^+ dead layer. Now that the n^+ dead layer thickness has been measured, the active volume and active mass of the crystal can be estimated. Using the crystal dimensions described in Section 6.5.2 and provided by CANBERRA, the total volume of the crystal is 85.6 ± 3.0 cm^3. The density of germanium is 5.32 g/cm^3, so this corresponds to a total mass of 455.5 ± 15.8 g. This agrees with an estimate of nominal detector mass provided by CANBERRA, 465 g [38]. The active volume of the crystal can be estimated from the total volume and dead layer volumes. The active volume is 75.9 ± 2.9 cm^3. The active mass is 404.2 ± 15.5 g.

6.7 Comparison of energy spectra

Now that a measurement of the MALBEK dead layer has been made, the simulated energy spectra of MALBEK response to ^{133}Ba can be compared to the energy spectrum collected from MALBEK with the ORCA DAQ. The ^{133}Ba dataset collected at KURF contains the response of MALBEK to the ^{133}Ba source and also to backgrounds at KURF. The MAGE/GEANT4 ^{133}Ba results only contain the response of MALBEK to the ^{133}Ba source, so the ORCA/Struck energy spectrum of MALBEK response to unshielded backgrounds at KURF will be added to the MAGE/GEANT4 energy spectrum of MALBEK response to ^{133}Ba, and this combined spectrum will be compared to the ORCA/Struck ^{133}Ba energy spectrum. The following steps were taken to make the combined energy spectrum:

1. The MAGE/GEANT4 Tier 0 ^{133}Ba results were processed with GAT to apply a p^+ point-contact dead layer with 0.3-μm thickness and an n^+ dead layer with the thickness measured in this chapter: 0.933 mm. The surface between the n^+ and p^+ contacts was assumed to have a dead layer of zero thickness.

2. The resulting MAGE/GEANT4 Tier 1 energy spectrum was convolved with a Gaussian energy resolution function described by the parameters in Table 6.2 and with the preamp efficiency curve. A histogram of this energy spectrum was created.

3. The simulated energy spectrum is the result of 6.7×10^8 decays of ^{133}Ba. At the time of the ^{133}Ba measurements at KURF, the activity of ^{133}Ba source was 33.28 kBq; therefore the simulation corresponds to 335.5 minutes of livetime. The histogram of the simulated energy spectrum was normalized by this livetime.

4. An energy-spectrum histogram was generated from the ORCA/Struck dataset of unshielded MALBEK response to backgrounds at KURF, after the combined rise-time cut. This histogram was normalized by the background dataset livetime of 617.7 minutes and was added to the simulated energy spectrum histogram.

The combined energy spectrum and its components are shown in Figure 6.9. The ORCA/Struck ^{133}Ba dataset is also plotted in the figure. The ^{133}Ba peaks and Compton features in the energy spectrum are well reproduced by the simulation. There is a pulser peak at 21.5 keV in the ^{133}Ba dataset collected with ORCA that does not appear in the simulation.

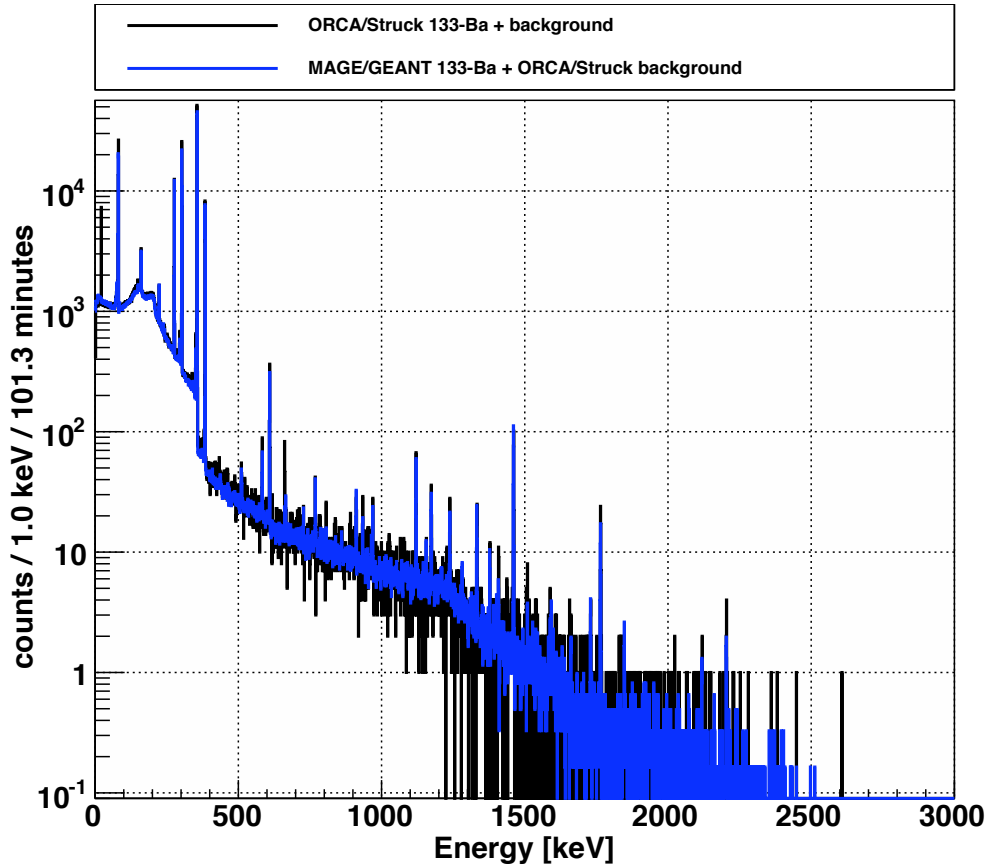

Figure 6.9: Simulated and measured energy spectra of MALBEK response to a ^{133}Ba source. The simulated response of MALBEK to the ^{133}Ba source has been added to the background energy spectrum measured at KURF, as described in the text.

The highest energy counts present in the energy spectrum of simulated response to ^{133}Ba decay are at 437 keV, caused by coincidence summing of gammas. To compare the simulated and measured energy spectra, two energy regions will be considered: below 440 keV, where

the response is dominated by ^{133}Ba, and above 440 keV, where ^{133}Ba does not contribute. The data collected at KURF has a low-energy threshold of approximately 2 keV. Only data above 5 keV are considered to avoid this threshold.

Studies of HPGe detector response to gamma sources have achieved agreement on the order of a few percent between GEANT4 simulation and experiment [7], [77], and one study reported 1% agreement of photopeak efficiencies between 36 and 1460 keV [78]. Good agreement can generally be achieved by tuning the dead layers and dimensions of the germanium crystal.

Table 6.5 lists the integral count rates in the MALBEK spectra. The energy spectrum including simulated ^{133}Ba response has a lower integral count rate than the ^{133}Ba spectrum collected with ORCA/Struck: between 5 and 3000 keV the rate is low by 2.9 ± 0.1 Hz (3.2%). In the region between 5 and 440 keV, where the ^{133}Ba source is the dominant contribution, the spectrum of MAGE/GEANT4 ^{133}Ba response is low by 2.7 ± 0.1 Hz (3.1%). This agreement is reasonable since GEANT4 under-produces most gammas emitted in ^{133}Ba decay by a few percent and the activity of the ^{133}Ba source is known to 3%.

Table 6.5: Integral count rates in simulated and measured ^{133}Ba spectra. Uncertainties are statistical. When calculating the rate between 5 and 440 keV, the region between 20 and 23 keV was excluded; the ORCA/Struck ^{133}Ba dataset has a pulser peak at 21.3 keV and no timing information is available for vetoing this peak.

Energy Region	**MAGE/GEANT4 ^{133}Ba + ORCA/Struck bkgd. [Hz]**	**ORCA/Struck ^{133}Ba (+ bkgd.) [Hz]**	**Difference [Hz]**
5–3000 keV	86.8 ± 0.1	89.7 ± 0.1	-2.9 ± 0.1
5–440 keV	84.8 ± 0.1	87.5 ± 0.1	-2.7 ± 0.1
440–3000 keV	2.00 ± 0.01	2.14 ± 0.02	-0.14 ± 0.02

6.8 Conclusions

In this chapter, a ratio of counts in two ^{133}Ba gamma peaks was measured from an energy spectrum of MALBEK response to a ^{133}Ba source at KURF. Simulated energy spectra of MALBEK response to ^{133}Ba were generated for various n^+ germanium dead layer thicknesses. The MALBEK dead layer was measured by comparing the peak ratio from the energy spectrum collected at KURF to the simulation results. The dead layer thickness is 0.933 ± 0.018 stat. ± 0.092 sys. mm. This dead layer thickness is the sum of truly dead and transition dead layers. This value agrees with the approximate thickness of 1 mm provided by Mike Yocum of CANBERRA. When statistical and systematic uncertainties are combined in quadrature, the measured MALBEK dead layer is 0.933 ± 0.094 mm. The 10% uncertainty in this measurement is comparable to the precision of another measurement of BEGe dead layer thickness made by GERDA Collaborators [68]. Using the dead layer measurement, information provided by CANBERRA, and dimensions measured by UNC Collaborators, the active mass of the germanium crystal was calculated to be 404.2 ± 15.5 g.

After the dead layer was measured, MaGe/Geant4 ^{133}Ba simulation results were processed to apply the measured dead layer thickness. An energy spectrum of the simulation results was added to a background energy spectrum collected from MALBEK with the ORCA/Struck DAQ at KURF. This combined spectrum was compared to a spectrum of MALBEK response to ^{133}Ba collected with the DAQ at KURF. The simulated energy spectrum was normalized to its effective livetime, given the activity of the source at KURF. Using this normalization, the integral count rates in the two energy spectra agree within 3.2% across the full range of the energy spectrum from 5 to 3000 keV. This discrepancy is on the order of the uncertainty in the ^{133}Ba source activity and known errors in Geant4 gamma production. The dead layer measured in this chapter will be applied to the simulations of MALBEK response presented in the rest of this dissertation.

Chapter 7

PREDICTION OF MALBEK BACKGROUNDS

7.1 Introduction

Carefully fabricated from low-background materials, located deep underground at KURF, and shielded by lead and polyethylene, MALBEK is a very low background detector. However, radioactive backgrounds do manage to deposit energy in the detector at a small rate of less than 10 mHz above 5 keV during Dataset I. The Dataset I energy spectrum is the response of MALBEK to many different sources of background, primarily gamma rays from radioactive decays in components near the detector. This chapter will describe how a background model of the Dataset I energy spectrum was constructed.

The background model contains the simulated energy-spectrum response of MALBEK to known backgrounds at KURF. The first step in creating the model was to form a list of expected backgrounds, based on energy spectra observed in other low-background germanium detector experiments and tabulated in the MAJORANA Background Summary Document [79]. The list contains contaminants such as ^{238}U, ^{232}Th, ^{40}K, and ^{68}Ge. The response of MALBEK to each background was simulated with MAGE/GEANT4. From each simulation, an energy spectrum was produced to represent the efficiency for the background to deposit a given amount of energy in the detector.

MAGE/GEANT4 simulations do not include a description of the preamplifier or the detector's energy resolution, so MAGE/GEANT4 energy spectra must be convolved with functions describing the energy resolution and the energy-dependent efficiency of the preamplifier. After the convolutions, each MAGE/GEANT4 energy spectrum represents the efficiency for a background to produce a count in the energy spectrum of detector response.

To estimate the magnitude of a background's contribution to the total energy spectrum, information about the expected rate of radioactive decays of the background and the DAQ livetime are needed. For some background contributions, information about the history of

exposure of cryostat components to cosmic rays is also needed. Each MaGe/Geant4 energy spectrum is scaled to the appropriate magnitude to represent the predicted contribution of the background to the Dataset I energy spectrum.

All scaled MaGe/Geant4 energy spectra are added to produce a total predicted energy spectrum. This is the spectrum one would expect to observe during Dataset I data taking, based on known backgrounds, simulation results, radiopurity data, and other information about the detector and DAQ. The Dataset I background model consists of the predicted energy spectrum and all information used to construct it.

In this chapter, the Dataset I background model is presented. The predicted energy spectrum produced from the model is compared to the ORCA/Struck Dataset I energy spectrum. Then, in a fit to the ORCA/Struck Dataset I energy spectrum, the scaling of the MaGe/Geant4 contributions are allowed to float. The results of the fit are analyzed and conclusions are drawn about our understanding of the Dataset I energy spectrum.

Datasets II and III were blinded until Dataset I analysis was complete. These datasets are described in the following chapters.

7.2 The background-modeling software

The MALBEK background model is constructed using the MJBackgroundModel code, which is part of GAT. MJBackgroundModel is a set of python classes and scripts that are used to predict the energy-spectrum response of a detector to backgrounds expected during an experiment.

The following terms will be used to describe how the background model is assembled:

Component a physical part of the MALBEK apparatus, e.g. the Teflon insulator called `connectorInsulatorPhysical0` in the MaGe model.

Material the substance from which a component is fabricated, e.g. Teflon.

Contaminant a radioactive isotope of interest, e.g. ^{40}K.

Material assay data information about radioactive contamination of a material, e.g. the intrinsic amount of ^{40}K in Teflon, in units of Bq/kg, or the cosmogenic production rate of ^{68}Ge in natural germanium at sea level, in atoms/kg/day.

Contribution the energy spectrum response of MALBEK to a contaminant from a component, e.g. ^{40}K from the Teflon insulator. The background model is the sum of many contributions.

Each of these terms is represented by a Python class in the MJBackgroundModel code.

In the background model, contaminants associated with a component are assumed to be either *primordial* (long-lived and intrinsic to the material) or *cosmogenic* (relatively short-lived and appearing due to exposure to cosmic rays). Anthropogenic contaminants are not considered in this analysis. The distribution of a contaminant within a component is assumed to be *bulk* (distributed uniformly throughout the volume of a component) or *surface* (distributed uniformly over the component's surface). Primordial contaminants may be in the bulk of a component (due to intrinsic contaminantion) or on its surface (due to handling or radon plate-out), while cosmogenic contaminants are assumed to occur only within the bulk. Based on these definitions, material assay data may describe three types of contamination: bulk primordial, surface primordial, and bulk cosmogenic.

The following types of contamination are considered in the model: bulk primordial contamination of components in the cryostat, shielding, and rock walls with ^{40}K, ^{232}Th, and ^{238}U; bulk cosmogenic contamination of the germanium crystal and copper cryostat parts; surface contamination of components inside and outside of the cryostat with long-lived radon daughters; a continuous flux of high-energy muons, producing neutrons and other spallation products.

To build a model of the MALBEK background energy spectrum, MJBackgroundModel takes the following as input:

An ORCA/Struck shielded background dataset this contains the response of MALBEK to backgrounds at KURF. The ORCA/Struck energy spectrum of MALBEK

response contained in the dataset *is not* a direct input used to determine the energy spectrum predicted by the background model – only the associated information about livetime, energy resolution, and preamplifier settings are. The ORCA/Struck spectrum *is* used when drawing plots to compare it to the predicted spectrum.

MAGE/GEANT4 results this set of MAGE/GEANT4 Tier 1 results contains the simulated response of MALBEK to each background of interest. Information about the mass and material of all components in the geometry model is also included.

Radiopurity information material assay data describing the types and amounts of contamination expected in each material. The cosmogenic exposure history of components is also provided.

The components in the MALBEK geometry model are listed in Table I.1 with their masses and materials. The masses were determined by GEANT4. Some material information was input manually into the model to allow flexibility. For example, the lead patches, called `patchOnePhysical` and `patchTwoPhysical`, are modeled from the ancient lead material defined in MAGE (Lead-Ain). The name of their material was manually entered as Lead-Patch to allow separate specification of material assay data for the patches. Radiopurity information for each material is tabulated in Appendix J. A problem with importance sampling of energy spectra was discovered during unblinding of Dataset II. This issue is described in Section 8.2. As a result of this problem, energy spectra from the rock walls at KURF or the polyethylene shielding were not used in the MALBEK background model.

As an example of a single contribution to the background model, the predicted response of MALBEK to the background from ^{40}K in the Teflon insulator `connectorInsulator-Physical0` during Dataset I is shown in Figure 7.1. The simulation of MALBEK's response to decays of ^{40}K from the Teflon insulator was discussed as an example in Chapter 5.2. This background will be used as an example again in this chapter.

The total energy-spectrum prediction for Dataset I is shown in black in Figure 7.2. The total energy spectrum is the sum of 739 background contributions, which were produced from 9057 MAGE runs simulating MALBEK response to contamination in 55 components.

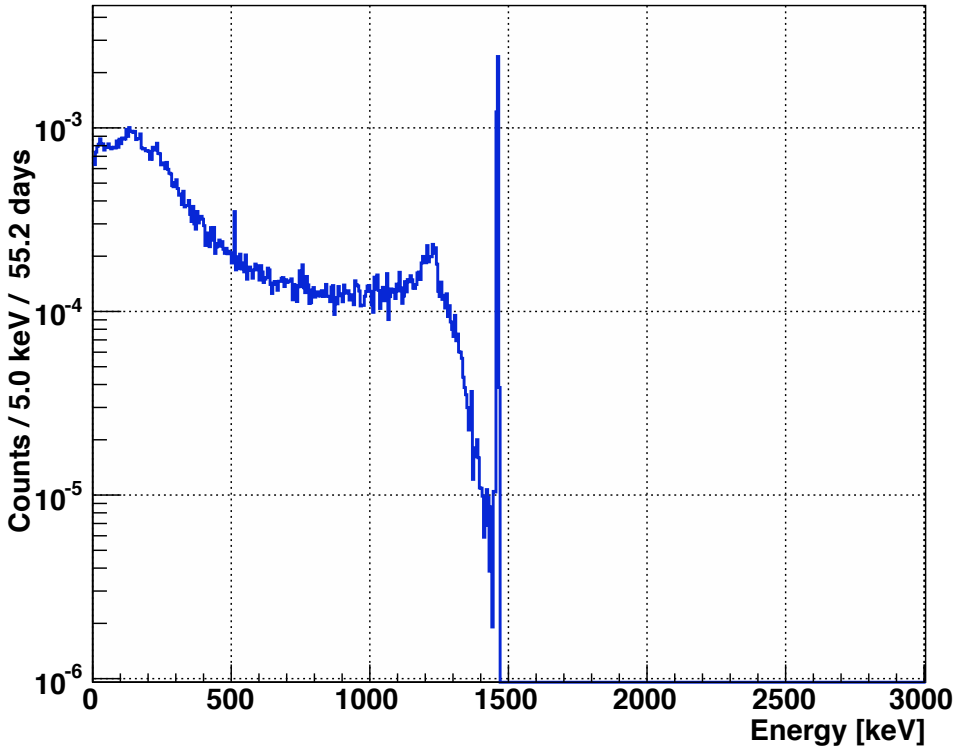

Figure 7.1: Predicted contribution of ^{40}K in the Teflon component `connectorInsulator-Physical0` to the Dataset I energy spectrum during 55.21 days of livetime.

The sum of all contributions from each contaminant are also shown in the figure, i.e. the contribution from ^{40}K in `connectorInsulatorPhysical0` has been added to all other ^{40}K contributions to form the ^{40}K energy spectrum. In Figure 7.3, the energy spectrum predicted with MJBackgroundModel is compared to the ORCA/Struck Dataset I spectrum. The prediction captures many of the peaks in the ORCA/Struck spectrum and the continua are in reasonable agreement throughout the spectrum. The prediction is based on the simulation results, radiopurity information, information about the Dataset I livetime, and preamplifier characteristics – the predicted spectrum was not scaled to match the ORCA/Struck spectrum. The predicted spectrum and the ORCA/Struck spectrum will be compared quantitatively later in this chapter. The prediction of each background contribution is described next.

7.3 Contributions to the background model

As mentioned earlier, the spectral shape of each contribution to the background model is determined by convolving a simulated spectrum of detector response with the energy resolution of the detector and the preamplifier efficiency. The absolute normalization of the contribution is determined by material assay data, information about DAQ livetime, and information about cosmogenic exposure of components. In this section, equations will be presented to describe the energy-spectrum contributions of arbitrary backgrounds.

For decays of a radioactive contaminant from a component, the contribution to the differential energy spectrum of detector response is:

$$\frac{\partial N^{ij}}{\partial E} = \int R^{ij}(t)\,\epsilon^{ij}(E,t)\,\mathrm{d}t \tag{7.1}$$

where the superscripts i and j label the contaminant and component, respectively, $R^{ij}(t)$ is the activity of contaminant decays originating from the component, $\epsilon^{ij}(E,t)$ is the energy- and time-dependent efficiency for a decay to create a count at energy E, and the integral is over t, the run time of the experiment.

The efficiency $\epsilon^{ij}(E,t)$ is a product:

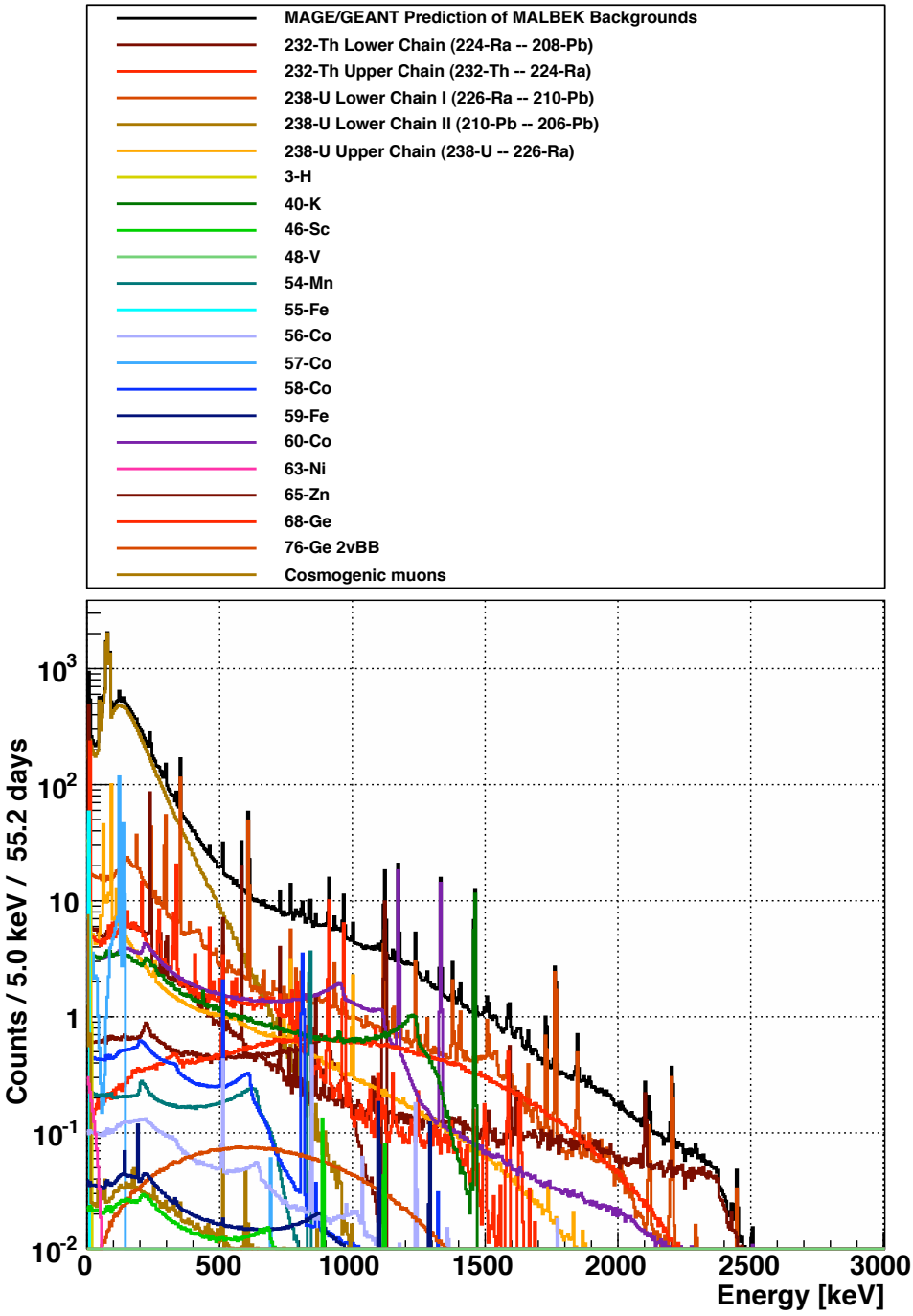

Figure 7.2: Predicted Dataset I energy spectrum.

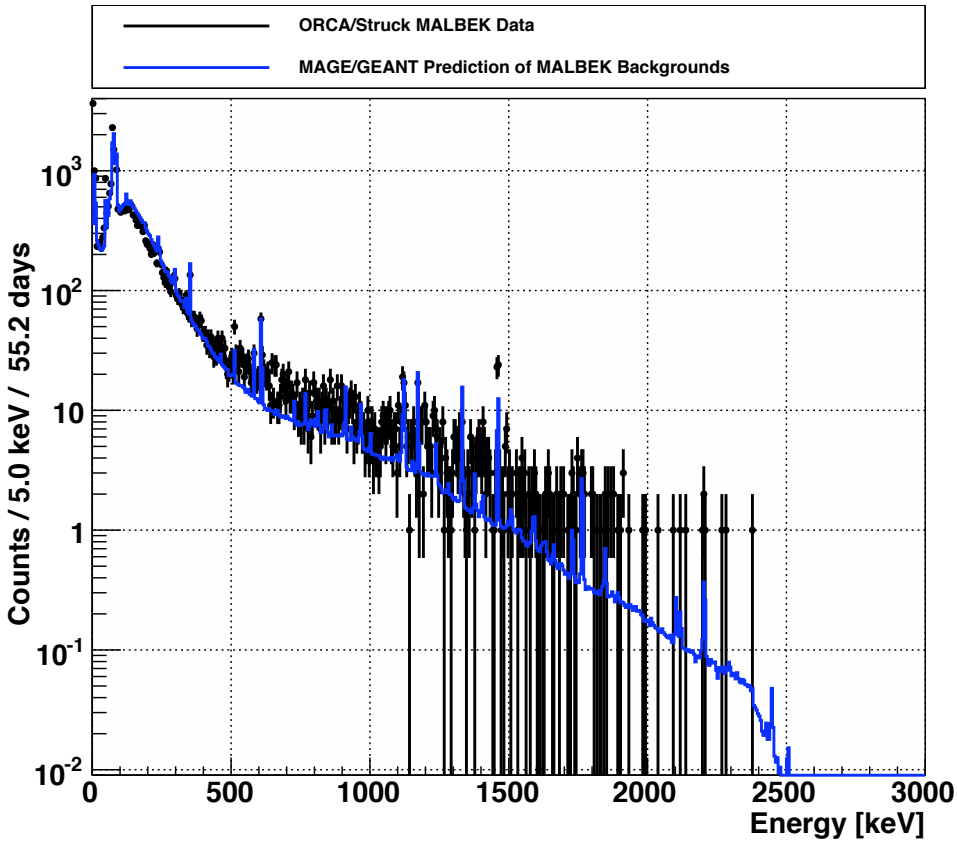

Figure 7.3: Comparison of Dataset I energy spectrum to background model prediction.

$$\epsilon^{ij}(E,t) = \epsilon_{\text{livetime}}(t) \times \epsilon^{ij}_{\text{detection}}(E) \times \epsilon_{\text{preamp}}(E,t) \tag{7.2}$$

where $\epsilon_{\text{livetime}}(t)$ is an efficiency representing the DAQ livetime, $\epsilon^{ij}_{\text{detection}}(E)$ is the efficiency for a decay to deposit energy in the detector, and $\epsilon_{\text{preamp}}(E,t)$ is the efficiency related to the preamplifier. These efficiencies have been described in earlier chapters. The DAQ live time is measured with a pulser, as described in Chapter 4.5. The efficiency for a decay to deposit energy in the detector is determined from Monte Carlo simulation and was discussed in Chapter 6.4. The preamplifier efficiency depends on the detector leakage current and is described by Equation 4.13.

For a bulk contaminant, the activity $R^{ij}(t)$ is:

$$R^{ij}(t) = A^{ij}(t)_{\text{bulk}}\, m^j \tag{7.3}$$

where $A^{ij}(t)_{\text{bulk}}$ is the specific activity of the material, in units of decays per mass per time, and m^j is the mass of the component. For a long-lived primordial contaminant like ^{40}K, with a half life of 1.2×10^9 years, the activity $A^{ij}(t)_{\text{bulk}}$ can be assumed constant. Substituting Equations 4.13 , 7.2, and 7.3 into Equation 7.14, the contribution from such a bulk primordial contaminant is:

$$\frac{\partial N^{ij}}{\partial E} = \int R^{ij}(t)\, \epsilon^{ij}(E,t)\, \mathrm{d}t \tag{7.4}$$

$$= R^{ij}\, \epsilon^{ij}_{\text{detection}}(E)\, \epsilon_{\text{preamp}}(E) \int \epsilon_{\text{livetime}}(t)\, \mathrm{d}t \tag{7.5}$$

$$= R^{ij}\, \epsilon^{ij}_{\text{detection}}(E)\, \epsilon_{\text{preamp}}(E)\, T_{\text{live}} \tag{7.6}$$

$$= \begin{cases} A^{ij}_{\text{bulk}}\, m^j\, \epsilon^{ij}_{\text{detection}}(E) \left(1 - \frac{E}{E_{\text{max}}}\right) T_{\text{live}} & \text{for } E \leq E_{\text{max}} \\ 0 & \text{for } E > E_{\text{max}} \end{cases} \tag{7.7}$$

where the integral evaluates to T_{live}, the livetime of the experiment. Here Equation 4.13 is used for $\epsilon_{\text{preamp}}(E)$ and E_{max} is assumed to be constant in time.

The quantity $A^{ij}_{\text{bulk}}\, m^j\, T_{\text{live}}$ is the number of contaminant decays expected during the livetime of the experiment. If this number of expected decays is labeled N^{ij}_{decays}, then Equation 7.7 can be rewritten:

$$\frac{\partial N^{ij}}{\partial E} = \begin{cases} N^{ij}_{\text{decays}}\, \epsilon^{ij}_{\text{detection}}(E)\, \left(1 - \frac{E}{E_{\text{max}}}\right) & \text{for } E \leq E_{\text{max}} \\ 0 & \text{for } E > E_{\text{max}} \end{cases} \tag{7.8}$$

This equation applies for decays of any bulk or surface contaminant, as long as the time-dependence of the preamplifier efficiency, $\epsilon_{\text{preamp}}(E, t)$, can be neglected. This formulation is useful because the energy-spectrum contribution from an arbitrary background is broken down into three simple factors. The first, N^{ij}_{decays}, can be calculated analytically for each contribution from material assay data, information about livetime, and cosmogenic exposure. For these types of contamination:

$$N^{ij}_{\text{decays}} = \begin{cases} A^{ij}_{\text{bulk}}\, m^j\, T_{\text{live}} & \text{for bulk primordial contamination} \\ A^{ij}_{\text{surf}}\, a^j\, T_{\text{live}} & \text{for surface primordial contamination} \\ N^{ij}_{\text{atoms}} \int \exp(-t/\tau^i)\, \mathrm{d}t & \text{for cosmogenic activation} \end{cases} \tag{7.9}$$

where a^j is the surface area of component j, N^{ij}_{atoms} is the number of contaminant i atoms in component j at the start of the experiment, and τ^i is the lifetime of contaminant i. The quantity N^{ij}_{atoms} depends on the history of activation and cooldown of the component. In the simplest case, a component may be activated on the earth's surface for a time, then moved underground, where activation effectively stops and the contaminant decays away before and during the experiment:

$$N_{\text{atoms}}^{ij} = P^{ij}\, m^{j}\, \tau^{i}\, \left[1 - \exp(-T_{\text{activation}}/\tau^{i})\right] \exp(-T_{\text{cooldown}}/\tau^{i}) \tag{7.10}$$

where P^{ij} is the rate of cosmogenic production of the contaminant in the component, $T_{\text{activation}}$ is the duration of the component's activation, and T_{cooldown} is the duration of cooldown before the start of the experiment. The value of P^{ij} is altitude dependent. In this analysis, sea-level activation rates were used.

The predicted bulk primordial background contribution due to ^{40}K in `connectorInsulatorPhysical0` can be calculated from the three terms in Equation 7.8. The first term is simple to calculate. During Dataset I, the number of ^{40}K decays in `connectorInsulatorPhysical0` is:

$$N_{\text{decays}}^{^{40}\text{K in ins.}} = A_{\text{bulk}}^{^{40}\text{K in ins.}}\, m^{\text{ins.}}\, T_{\text{live}} \tag{7.11}$$

$$= (8.00 \times 10^{-2}\ \text{Bq/kg})(6.13 \times 10^{-5}\ \text{kg})(55.21\ \text{days}) \left(\frac{8.64 \times 10^{4}\ \text{s}}{\text{day}}\right) \tag{7.12}$$

$$= 23.4\ \text{decays} \tag{7.13}$$

where the mass was reported by GEANT4 and is listed in Table I.1, the activity of Teflon was taken from the ILIAS database [53] and is listed in Table J.17, and the livetime of Dataset I was measured with a pulser. The second term, $\epsilon_{\text{detection}}^{ij}(E)$, is estimated from Monte-Carlo simulations using MAGE. Earlier, Figure 5.2 showed the simulated energy-spectrum response of MALBEK to 5×10^{6} decays of ^{40}K from `connectorInsulatorPhysical0`. At each binned energy in Figure 5.2, the value of $\epsilon_{\text{detection}}^{ij}(E)$ can be estimated by dividing the number of counts in the bin by the number of simulated decays (5×10^{6}). This will produce an energy spectrum like Figure 5.2, but where the y-axis has been re-scaled. Finally, the post-preamplifier energy spectrum of MALBEK response is estimated by convolving the scaled energy spectrum by the preamplifier efficiency. The resulting predicted contribution to the Dataset I energy spectrum is shown in Figure 7.1. Integrated over all energies, this

background contributes 0.11 counts to the Dataset I energy spectrum. This is a negligible contribution compared to the 2.96×10^4 counts observed above 5 keV in Dataset I.

7.3.1 Radiopurity data

To predict the MALBEK background spectrum, MAGE/GEANT4 results must be combined with information about material radiopurity. Material radiopurity data were collected from multiple references and appear in Appendix J. Only a few of the MALBEK materials were assayed directly, including the modern and ancient lead. For other materials, typical values from the literature were used. Upper limits were reported as results of some radiopurity measurements. For these measurements the upper limit was used as the activity of the material. Assay results were averaged if multiple measurements were available for the same material.

For many materials the available radiopurity data were incomplete. Material samples are often screened with germanium detectors, which are sensitive to gamma peaks. Gamma assay typically provides activities of ^{234}Th, ^{214}Pb, and ^{214}Bi in the ^{238}U chain, and to ^{228}Ac, ^{212}Pb, and ^{208}Tl from the ^{232}Th chain. These measurements do not constrain activities of other isotopes in the decay chain that may be out of secular equilibrium with the gamma emitters.

As described in Chapter 5.6, the ^{232}Th and ^{238}U decay chains are simulated in multiple steps. The steps are then reassembled into sections that are expected to be in equlibrium, based on half lives of the involved isotopes. The ^{232}Th chain is simulated in four steps and reassembled into two sections, the upper and lower parts of the chain, which may be in disequilibrium. The ^{232}Th steps and sections are shown in Figure 5.7 and listed in Table 5.1. The ^{238}U chain is simulated in ten steps and reassembled into three sections: the upper chain, lower chain I, and lower chain II. The ^{238}U steps and sections are shown in Figure 5.8 and tabulated in Table 5.2.

For the ^{232}Th chain, if a gamma assay measurement of ^{228}Ac activity was available for a material, this activity was used for steps 1 through 3 of the ^{232}Th decay chain. Measurements of ^{212}Pb and ^{208}Tl activity were used to determine the activity of step 4 of the ^{232}Th

decay chain. Secular equilibrium was assumed if activities were only available from one step in the decay chain.

In the ^{238}U chain, if gamma assay results for ^{234}Th were available for a material, this activity was used for steps 1 through 5 of the ^{238}U decay chain. Gamma assay results for ^{214}Pb and ^{214}Bi were used for steps 6 through 9. If ^{210}Pb activity was available it was used for steps 7 through 9. If activities were only available for one step in the decay chain, the sections were assumed to be in secular equilibrium.

7.3.2 Cosmic-ray muons at KURF

Cosmic-ray muons are a special class of background, distinct from the bulk and surface distributions of other backgrounds. The MAGE generator `MGGeneratorCosmicRayMuons` was used to simulate the distributions of muons in angle and energy. The generator was written by Luciano Pandola and used the angular and energy distributions reported by Lipari and Stanev [80]. In the simulation, μ^+ and μ^- tracks are fired through a circle surrounding the detector, 20 m in radius. The tracks are distributed throughout the area of the circle. Parallel volumes and importance sampling of muons were used during MAGE simulations of MALBEK response to muons.

The flux of muons at KURF was determined from a depth-dependent expression for a flat overburden:

$$I_\mu(h) = A\exp(-h/0.285) + B\exp(-h/0.698) \tag{7.14}$$

Where h is the depth, A and B are constants, and I_μ is the muon flux, in cm^{-2}s^{-1}. The coefficients $A = 67.97 \times 10^{-6}$ and $B = 2.071 \times 10^{-6}$ were determined by Mei and Hime [81]. For KURF, at a depth of 1400 mwe, a flux of 7.79×10^{-7} cm^{-2}s^{-1} is predicted.

7.4 Results of the background model prediction for Dataset I

The energy-spectrum prediction for Dataset I was shown earlier in this chapter, in Figure 7.2. The results in the region from 5 to 3000 keV are also listed in Table 7.1. At lower energies, between 5 and 500 keV, the results are shown in Figure 7.4 and listed in Table 7.2.

Above 5 keV, the Dataset I energy spectrum contains 2.96×10^4 counts. In the same energy range, the background model predicts 3.56×10^4 counts. This is an overprediction of 5.93×10^3 counts, or 20%. This is reasonable agreement considering that there was no direct assay of most of the MALBEK components – the background model is based on typical radiopurities of materials, as found in the literature and from MAJORANA material assay results.

The majority of counts predicted by the background model are due to the ^{238}U Lower Chain II (^{210}Pb and its progeny), shown in Table 7.3 and Figure 7.5. This spectrum is dominated by the contribution from the lead patches.

A summary of the GEANT4 software environment used for the simulations appears in Table H.1. Information about MAGE settings and results appears in Table H.2.

The accuracy of the Dataset I background energy spectrum prediction depends on the MAGE/GEANT4 simulation of detector response, the description of the detector's energy resolution and preamplifier effects, and the input radiopurity values. In Section 7.5, the normalization of the contributions to the Dataset I energy spectrum prediction will be allowed to float in a fit to the ORCA/Struck energy spectrum. After the fit and its results are described, the results of the background model are discussed in Section 7.6.

7.4.1 Notes about lead patches

As described in Section 2.4, an early version of the MALBEK background model was presented at the Low Energy Spectrum workshop in August of 2010. This version did not contain full Monte-Carlo statistics, but it did contain contributions from components in the cryostat, including the tin, lead patches, and brass parts. The specific activity of ^{210}Pb in the lead patches was set to 0.013 Bq/kg, based on a measurement at Pacific Northwest National Lab (PNNL) that reported an upper limit on ^{210}Po at this level [56]. The PNNL

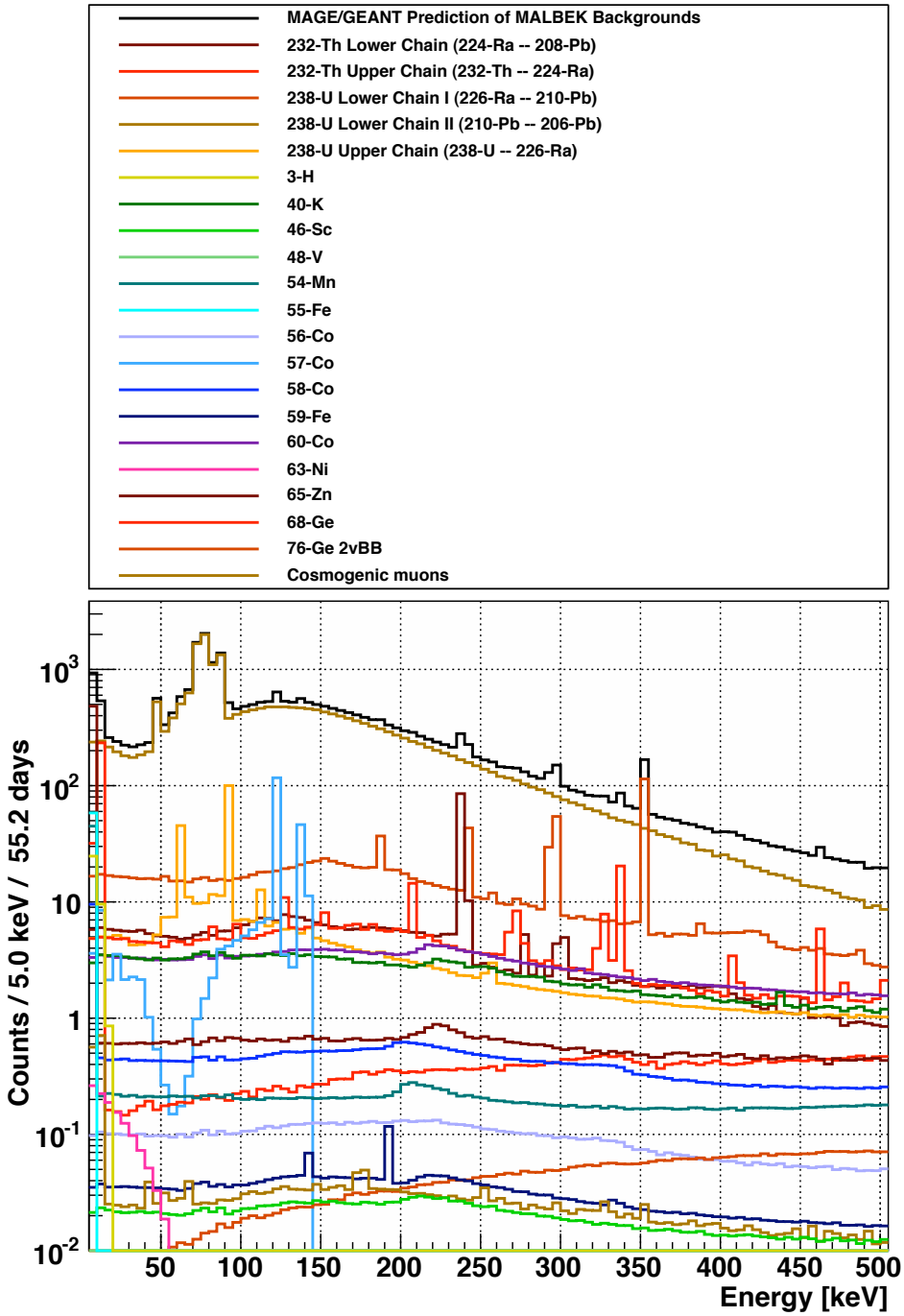

Figure 7.4: Energy spectrum of MAGE/GEANT4 Prediction of MALBEK Backgrounds. Sum of all contributions is shown in black.

Table 7.1: Integral counts in the predicted Dataset I energy spectrum above 5 keV. Counts are per 55.21 days of livetime. Uncertainties are statistical.

Contribution	**Counts**
232-Th Lower Chain (224-Ra – 208-Pb)	$(5.64 \pm 0.01) \times 10^2$
232-Th Upper Chain (232-Th – 224-Ra)	$(5.43 \pm 0.01) \times 10^2$
238-U Lower Chain I (226-Ra – 210-Pb)	$(1.71 \pm 0.00) \times 10^3$
238-U Lower Chain II (210-Pb – 206-Pb)	$(2.34 \pm 0.00) \times 10^4$
238-U Upper Chain (238-U – 226-Ra)	$(5.54 \pm 0.00) \times 10^2$
3-H	$(3.52 \pm 0.00) \times 10^1$
40-K	$(3.86 \pm 0.01) \times 10^2$
46-Sc	$(3.27 \pm 0.00) \times 10^0$
48-V	$(5.29 \pm 0.01) \times 10^{-4}$
54-Mn	$(7.87 \pm 0.00) \times 10^1$
55-Fe	$(5.83 \pm 0.01) \times 10^1$
56-Co	$(1.47 \pm 0.00) \times 10^1$
57-Co	$(2.50 \pm 0.00) \times 10^2$
58-Co	$(6.85 \pm 0.00) \times 10^1$
59-Fe	$(5.32 \pm 0.00) \times 10^0$
60-Co	$(5.20 \pm 0.00) \times 10^2$
63-Ni	$(1.24 \pm 0.00) \times 10^0$
65-Zn	$(6.05 \pm 0.01) \times 10^2$
68-Ge	$(4.25 \pm 0.00) \times 10^2$
76-Ge 2vBB	$(1.26 \pm 0.00) \times 10^1$
Cosmogenic muons	$(5.25 \pm 0.01) \times 10^0$
Total	$(2.93 \pm 0.00) \times 10^4$

Table 7.2: Integral counts in the predicted Dataset I energy spectrum between 5 and 500 keV. Counts are per 55.21 days of livetime. Uncertainties are statistical.

Contribution	**Counts**
232-Th Lower Chain (224-Ra – 208-Pb)	$(4.66 \pm 0.01) \times 10^2$
232-Th Upper Chain (232-Th – 224-Ra)	$(4.16 \pm 0.01) \times 10^2$
238-U Lower Chain I (226-Ra – 210-Pb)	$(1.37 \pm 0.00) \times 10^3$
238-U Lower Chain II (210-Pb – 206-Pb)	$(2.33 \pm 0.00) \times 10^4$
238-U Upper Chain (238-U – 226-Ra)	$(4.67 \pm 0.00) \times 10^2$
3-H	$(3.52 \pm 0.00) \times 10^1$
40-K	$(2.42 \pm 0.00) \times 10^2$
46-Sc	$(1.98 \pm 0.00) \times 10^0$
48-V	$(3.40 \pm 0.01) \times 10^{-4}$
54-Mn	$(6.40 \pm 0.00) \times 10^1$
55-Fe	$(5.83 \pm 0.01) \times 10^1$
56-Co	$(9.24 \pm 0.01) \times 10^0$
57-Co	$(2.50 \pm 0.00) \times 10^2$
58-Co	$(4.97 \pm 0.00) \times 10^1$
59-Fe	$(3.17 \pm 0.00) \times 10^0$
60-Co	$(2.85 \pm 0.00) \times 10^2$
63-Ni	$(1.24 \pm 0.00) \times 10^0$
65-Zn	$(5.40 \pm 0.01) \times 10^2$
68-Ge	$(2.99 \pm 0.00) \times 10^2$
76-Ge 2vBB	$(4.07 \pm 0.01) \times 10^0$
Cosmogenic muons	$(3.68 \pm 0.01) \times 10^0$
Total	$(2.78 \pm 0.00) \times 10^4$

Table 7.3: Integral counts in the predicted Dataset I energy spectrum due to the ^{238}U Lower Chain II (210-Pb – 206-Pb). Counts are per 55.21 days of livetime. Uncertainties are statistical.

Contribution	**Counts**
238-U Lower Chain II (210-Pb – 206-Pb) in Air	$(3.40 \pm 0.21) \times 10^{-6}$
238-U Lower Chain II (210-Pb – 206-Pb) in BerylliumCopper	$(2.44 \pm 0.00) \times 10^{1}$
238-U Lower Chain II (210-Pb – 206-Pb) in Brass	$(5.37 \pm 0.01) \times 10^{1}$
238-U Lower Chain II (210-Pb – 206-Pb) in CopperOFHC	$(1.54 \pm 0.00) \times 10^{-2}$
238-U Lower Chain II (210-Pb – 206-Pb) in GermaniumNat	$(4.28 \pm 0.00) \times 10^{-2}$
238-U Lower Chain II (210-Pb – 206-Pb) in LeadAin	$(6.24 \pm 0.01) \times 10^{1}$
238-U Lower Chain II (210-Pb – 206-Pb) in LeadMod	$(6.14 \pm 0.05) \times 10^{1}$
238-U Lower Chain II (210-Pb – 206-Pb) in LeadPatch	$(2.32 \pm 0.00) \times 10^{4}$
238-U Lower Chain II (210-Pb – 206-Pb) in MoxtekFET	$(5.36 \pm 0.01) \times 10^{-5}$
238-U Lower Chain II (210-Pb – 206-Pb) in NickelSilver	$(4.61 \pm 0.01) \times 10^{-1}$
238-U Lower Chain II (210-Pb – 206-Pb) in Resistor	$(1.02 \pm 0.00) \times 10^{1}$
238-U Lower Chain II (210-Pb – 206-Pb) in RnExposureInCryostat	$(5.20 \pm 0.01) \times 10^{-1}$
238-U Lower Chain II (210-Pb – 206-Pb) in RnExposureOutsideCryostat	$(1.95 \pm 0.07) \times 10^{-2}$
238-U Lower Chain II (210-Pb – 206-Pb) in StainlessSteel304	$(3.87 \pm 0.06) \times 10^{-1}$
238-U Lower Chain II (210-Pb – 206-Pb) in Teflon	$(2.63 \pm 0.00) \times 10^{0}$
238-U Lower Chain II (210-Pb – 206-Pb) in Tin	$(1.41 \pm 0.00) \times 10^{1}$
238-U Lower Chain II (210-Pb – 206-Pb) in Zeolite	$(1.26 \pm 0.33) \times 10^{-1}$
Total	$(2.34 \pm 0.00) \times 10^{4}$

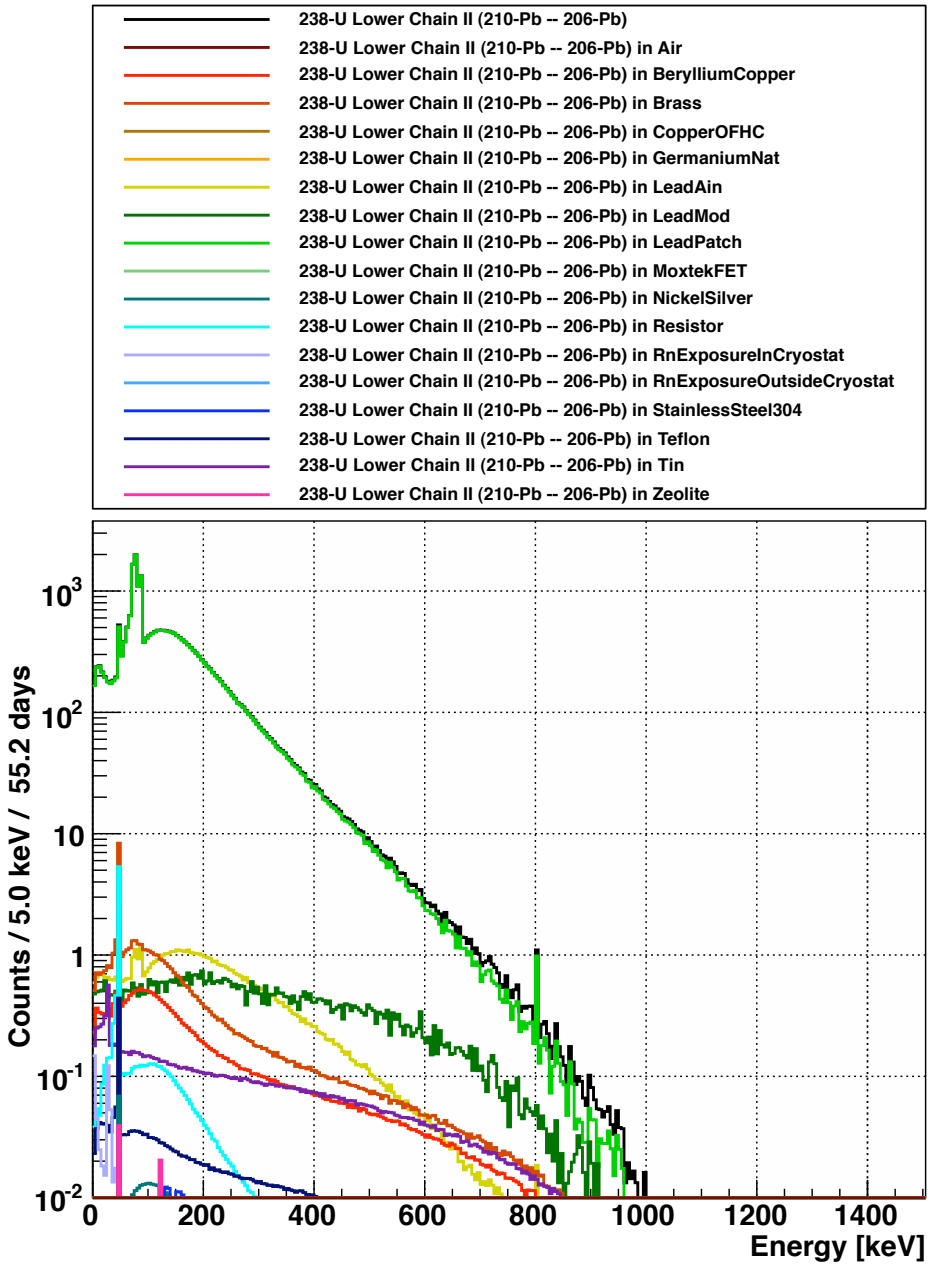

Figure 7.5: Energy spectrum of ^{238}U Lower Chain II (210-Pb – 206-Pb). The sum of all contributions is shown in black. All spectra in this plot were generated from MAGE/GEANT4 results for the MALBEK background model.

measurement was performed on a 100-g sample of ancient lead from stock used to make lead foil designated for use in MALBEK. The ancient lead that forms the inner layer of MALBEK's shielding is from this same stock.

The background model significantly under-predicted the integral count rate of the energy spectrum measured with MALBEK at KURF. At the workshop, after looking at the comparison of the background model to the energy spectrum measured at KURF, Juan Collar suggested changing the background model to include 100 Bq/kg of ^{210}Pb in the lead patches, to test the idea that the lead patches might be made of modern lead instead of ancient lead. This value gave reasonable agreement between the energy spectrum predicted with the background model and the spectrum measured at KURF. Figure 7.6 shows a comparison between the background model prediction and 18.5 days of shielded ORCA/Struck data that were available at the time of the workshop. The plots were produced on the day of the workshop. In the top panel, the background model includes 0.013 Bq/kg of ^{210}Pb in the lead patches. In the bottom panel, the background model contains 100 Bq/kg of ^{210}Pb in the patches. In the bottom panel, the background model gives a reasonable approximation of the shape of the bremsstrahlung continuum, the 46.5 keV peak, and Pb x-ray peaks. This early work with the MALBEK background model, followed by higher-statistics improvements [82], helped convince MALBEK collaborators to remove the lead patches from the cryostat [58]. Figure 7.7 shows results from the current background model, where the contributions from the lead patches and other possible sources of ^{210}Pb contamination have been varied to see whether they could account for the high count rate.

At the time of the workshop, the detector dead layer had not yet been measured and the reset energy of the preamplifier had not been calculated precisely, so a peak at 2615 keV appears in the background model energy spectrum.

The suggested value of 100 Bq/kg for ^{210}Pb in the lead patches has been used in the background model energy-spectrum prediction shown throughout this chapter, as documented in Table J.9. Figure 7.8 shows what the current version of the background model would look like if the lead patches were assumed to be made of ancient lead, with ^{210}Pb specific activity of 0.013 Bq/kg. This can be compared to Figure 7.3, where the value of 100 Bq/kg is used.

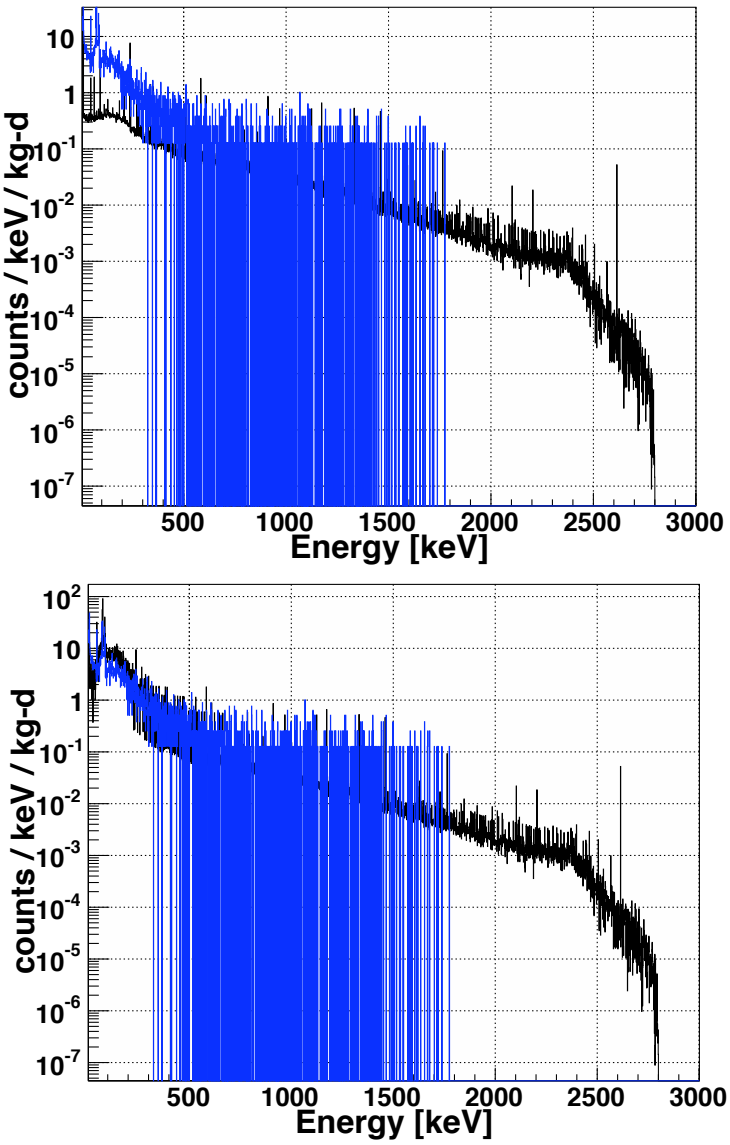

Figure 7.6: The MALBEK background model energy spectrum as of August 2010. The background model (black) is compared to 18.5 days of ORCA/Struck data collected with MALBEK at KURF in shielding (blue). This was the status of the background model as of August 26th, 2010. In the top panel, the lead patches have a ^{210}Pb specific activity of 0.013 Bq/kg, consistent with a measurement of ancient lead at PNNL [56]. In the bottom panel, the lead patches have a ^{210}Pb specific activity of 100 Bq/kg, on the recommendation of Juan Collar.

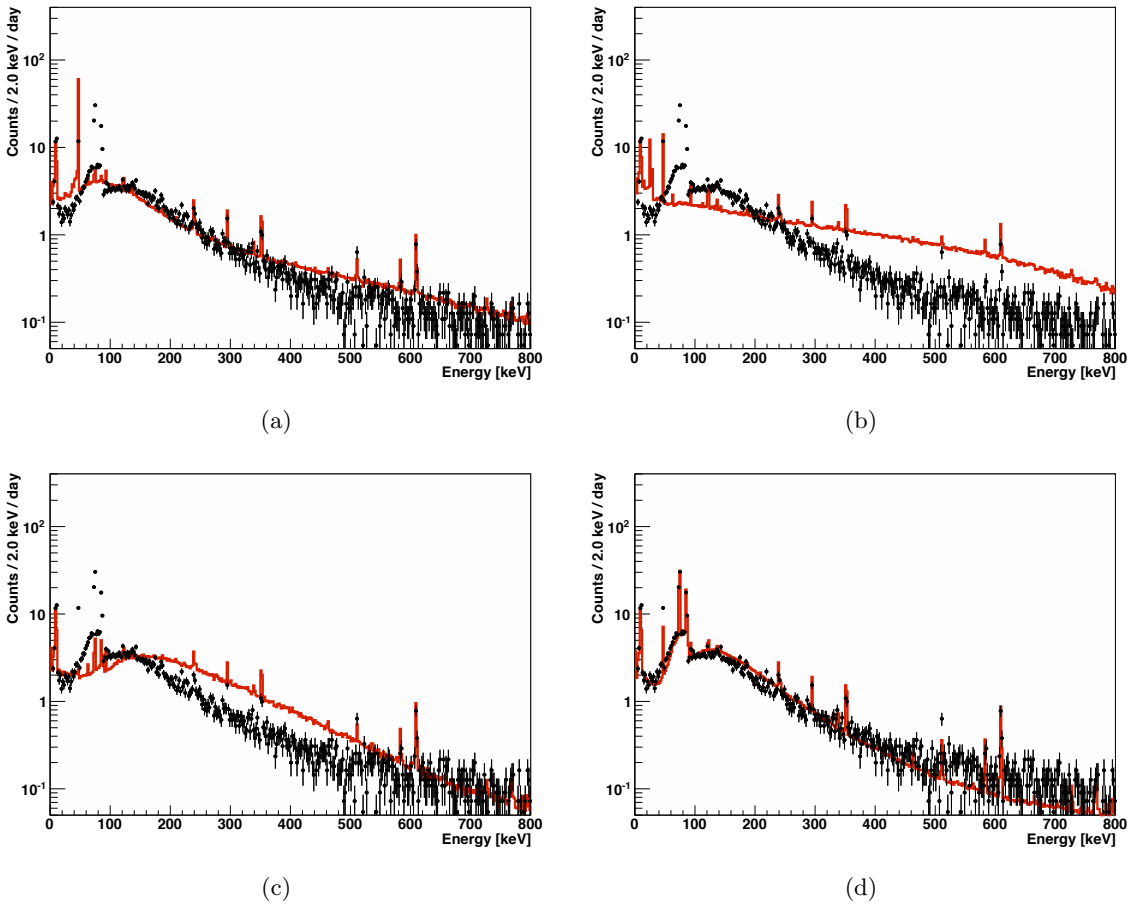

Figure 7.7: Comparison of background model energy spectra to Dataset I, where the normalization of selected background model contributions has been varied. In each plot, the normalization of a contribution to the background model was increased to match the total number of counts above 5 keV. This is shown for the contributions from ^{210}Pb in the brass components (a), tin solder (b), ancient lead shielding (c), and lead patches (d).

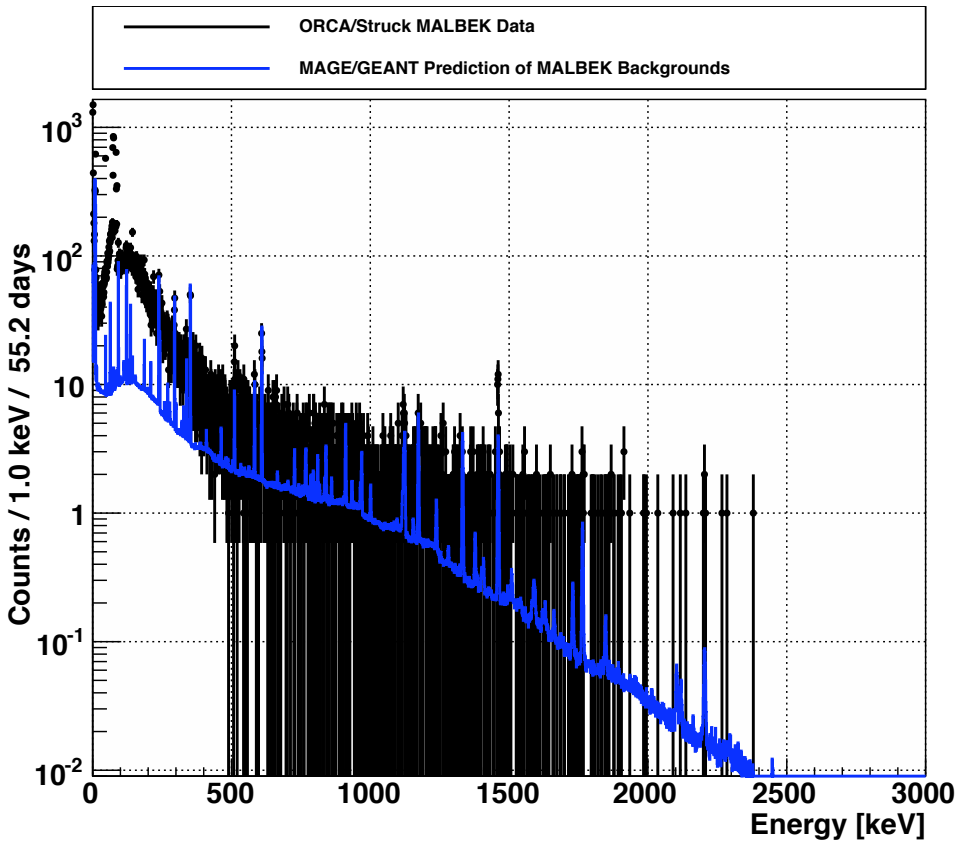

Figure 7.8: Comparison of Dataset I energy spectrum to background model prediction, where activity of ^{210}Pb in lead patches is consistent with ancient lead.

7.5 Results from fit of background model to ORCA/Struck Dataset I

After the predicted energy spectrum was produced, a fit was performed to allow the normalization of the simulated background contributions to vary. This section will describe the fit and present results for Dataset I.

The MALBEK background model consists of 739 energy-spectrum contributions. Each contribution represents the response of MALBEK to a contaminant in a component. To reduce the number of simulated energy spectra involved in the fit, the contributions were grouped by contaminant and material. The spectra in each group were added to produce one spectrum. For example, the energy spectra due to ^{40}K in all Teflon components were added to produce one total spectrum due to ^{40}K in Teflon. Grouping the contributions in this way reduced the number of energy spectra used in the fit from 739 to 84. Each of these composite energy spectra, identified by a material and contaminant, is used as a binned probability distribution function (PDF) in the fit. The PDFs are shown in Appendix L.1. Each binned PDF is subject to the normalization condition:

$$\sum_{l} f_{k\,l} = 1 \tag{7.15}$$

where the index k labels the PDF and the index l identifies a bin in the fit region. The PDFs have 10-keV bins and the fit was performed in the region from 10 to 2000 keV. The fit region was chosen to avoid the low-energy threshold of approximately 2 keV, and to minimize uncertainty in the preamplifier efficiency, which increases with increasing energy. One potential PDF, for ^{55}Fe, a cosmogenic contaminant in the germanium crystal, was omitted because it did not contain any counts in the fit region.

The PDFs were fit to the Dataset I energy spectrum using the RooFit [83] toolkit for ROOT. An extended binned maximum likelihood fit was performed using the ROOT implementation of the MINUIT [84] minimization package and the MIGRAD algorithm.

The function minimized by MINUIT is the negative log likelihood (NLL) [85]:

$$-\log L = \sum_k \hat{\mu}_k - \sum_l n_l \log \left[\sum_k \hat{\mu}_k f_{k\,l} \right] \tag{7.16}$$

where $\hat{\mu}_k$ is the estimated number of counts due to PDF k and n_l is the number of counts in bin l of the ORCA/Struck energy spectrum.

The parameter $\hat{\mu}_k$ was allowed to vary in the fit. As initial conditions of the fit, all of the $\hat{\mu}_k$ were set to the same value: one part in 84 of the total number of counts in the fit region of the ORCA/Struck energy spectrum. Each $\hat{\mu}_k$ was constrained to be greater than or equal to zero so that the log likelihood was well defined. MINUIT does not allow one-sided parameter constraints – a lower limit cannot be specified for a parameter without also specifying an upper limit [84]. For this reason, an upper limit was specified for each parameter – each PDF was constrained from contributing more than 1.5 times the integral number of counts observed in the fit region of the ORCA spectrum.

The use of parameter limits may introduce bias into the fit results. For the fit performed here, the fit parameters are not expected to reach the upper limit, but they may reach the lower limit of zero. Some PDFs may not contribute any counts to the fit region, but the fitter must report their contribution as a value greater than or equal to zero. This small bias is not concerning for this fit.

Uncertainties in the $\hat{\mu}_k$ estimates were calculated with the MINOS algorithm [84]. MINOS determines the change in parameter $\hat{\mu}_k$ required to produce an increase of 0.5 above the minimum value of the NLL – this is reported as the parameter's error. This is achieved by varying parameter $\hat{\mu}_k$, then minimizing the NLL with respect to all other parameters. The errors reported by MINOS are generally asymmetric and account for parameter correlations and non linearities.

The total number of counts estimated by the fitter in bin l is $\hat{v}_l$:

$$\hat{v}_l = \hat{\mu}_k \sum_k f_{k\,l} \tag{7.17}$$

Results of the fit are shown in Figure 7.9. A detailed view of the region below 500 keV is shown in Figure 7.10. The fit has χ^2 of 132.81 and 115 degrees of freedom, for a P-value of 0.12. In the figures, the fit result defined by Equation 7.17 is plotted and compared to the ORCA/Struck energy spectrum. The residual and pull are plotted and defined as follows:

$$\text{residual} = n_l - \hat{v}_l \tag{7.18}$$

$$\text{pull} = \frac{n_l - \hat{v}_l}{\sigma_{n_l}} \tag{7.19}$$

where n_l is the number of counts observed in bin l of the ORCA/Struck energy spectrum, σ_{n_l} is the Poisson uncertainty in this number, and $\hat{v}_l$ is the number of counts in bin l in the fit result.

The full fit results are listed in Table L.1. The subset of 15 spectra that were found by the fitter to contribute more than 100 counts to the fit region are shown in Figure 7.11 and listed in Table 7.4. The fit region is shown in more detail in Appendix L.3.

Figure 7.12 shows a comparison between the fit results and the predicted number of counts. For some contributions, the predicted integral number of counts was very small but the integral number of counts reported by the fitter are much larger. The predicted values were taken from typical values in the literature, and were not directly measured from components or materials used in MALBEK. Better agreement with the predicted values would be expected for an experiment like the DEMONSTRATOR, where detailed material assay data is available.

In Table 7.4, the number of counts due to the patches is estimated by the fitter to be $91.6^{+1.2}_{0.0}$% of the predicted number of counts. In the prediction of the background energy

spectrum, the specific activity of the lead patches was estimated as 100 Bq/kg, so the results of the fit imply that the activity of the lead patches is $91.6^{+1.2}_{0.0}$ Bq/kg.

The ^{238}U Lower Chain II from the lead patches is found by the fitter to contribute the vast majority of counts: 2.8×10^4 of 2.9×10^4 counts above 10 keV. This is consistent with our expectation of contamination in these patches. Although Datasets II and III are blinded in this analysis, it is known that the count rate in the low-energy channel decreased after the lead patches were removed in October 2011.

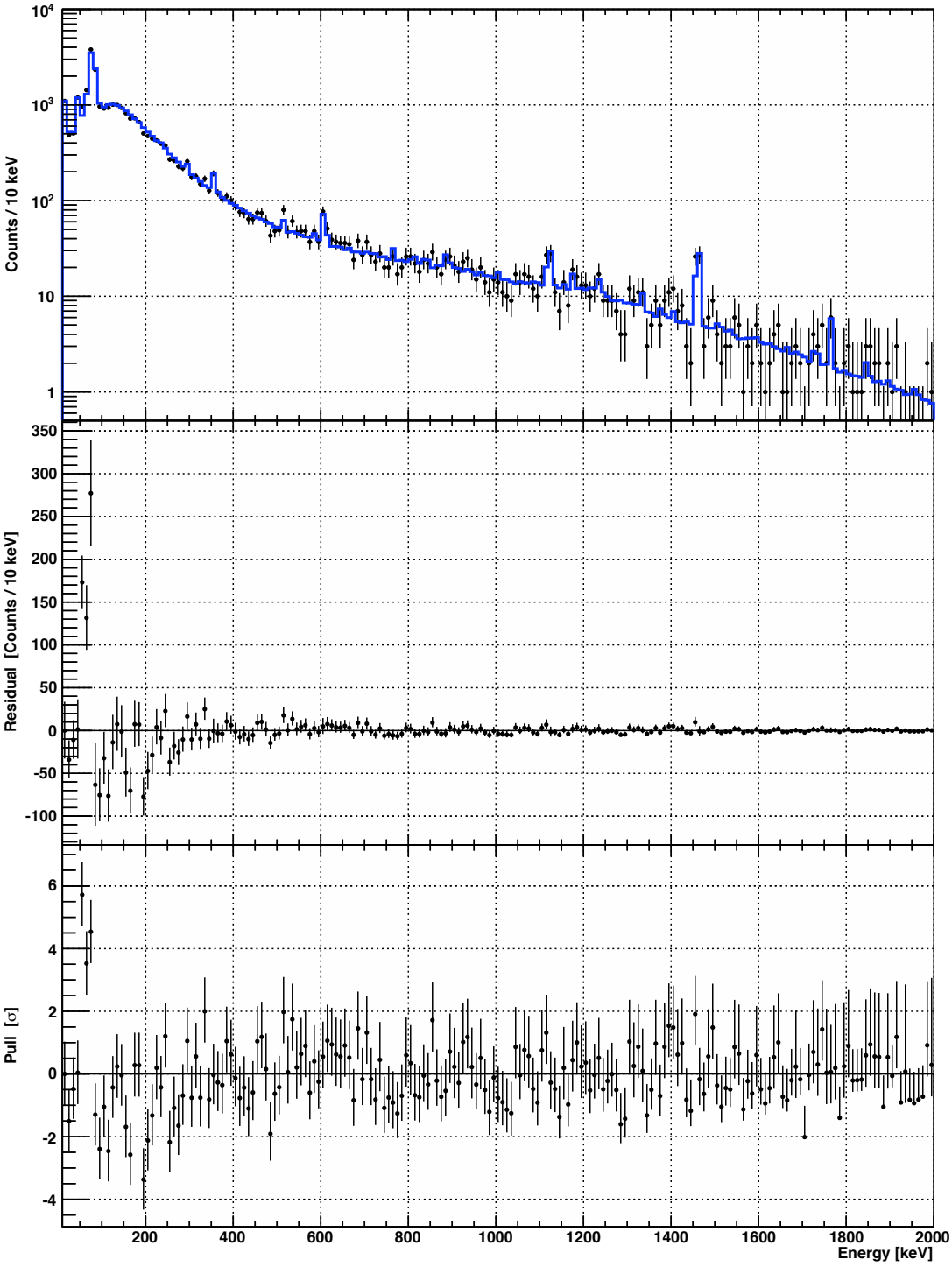

Figure 7.9: Results of background model fit to the Dataset I energy spectrum. The fit gives χ^2 of 132.81 per 115 degrees of freedom, for a P-value of 0.12.

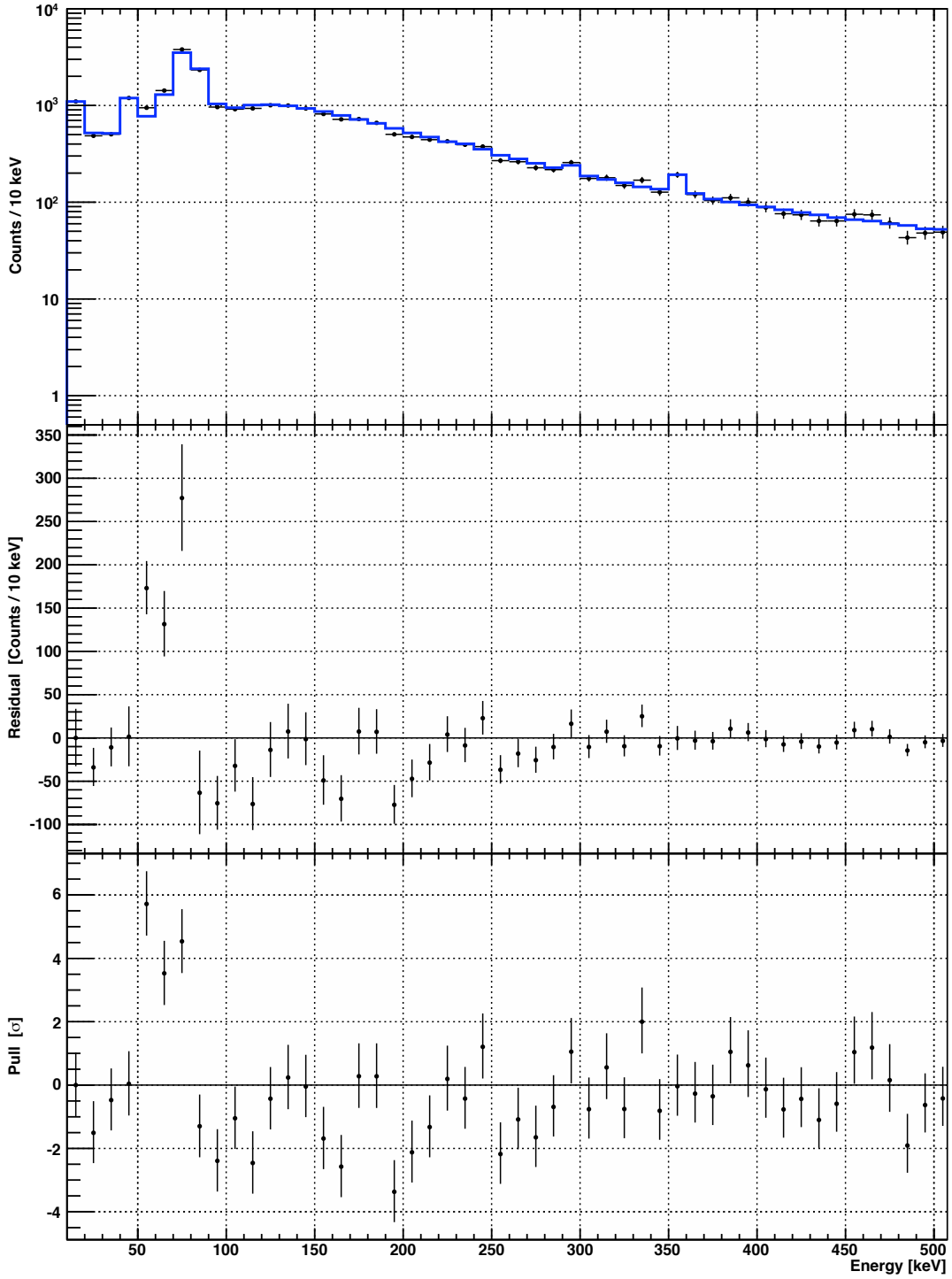

Figure 7.10: Results of background model fit to Dataset I, shown for energies below 500 keV.

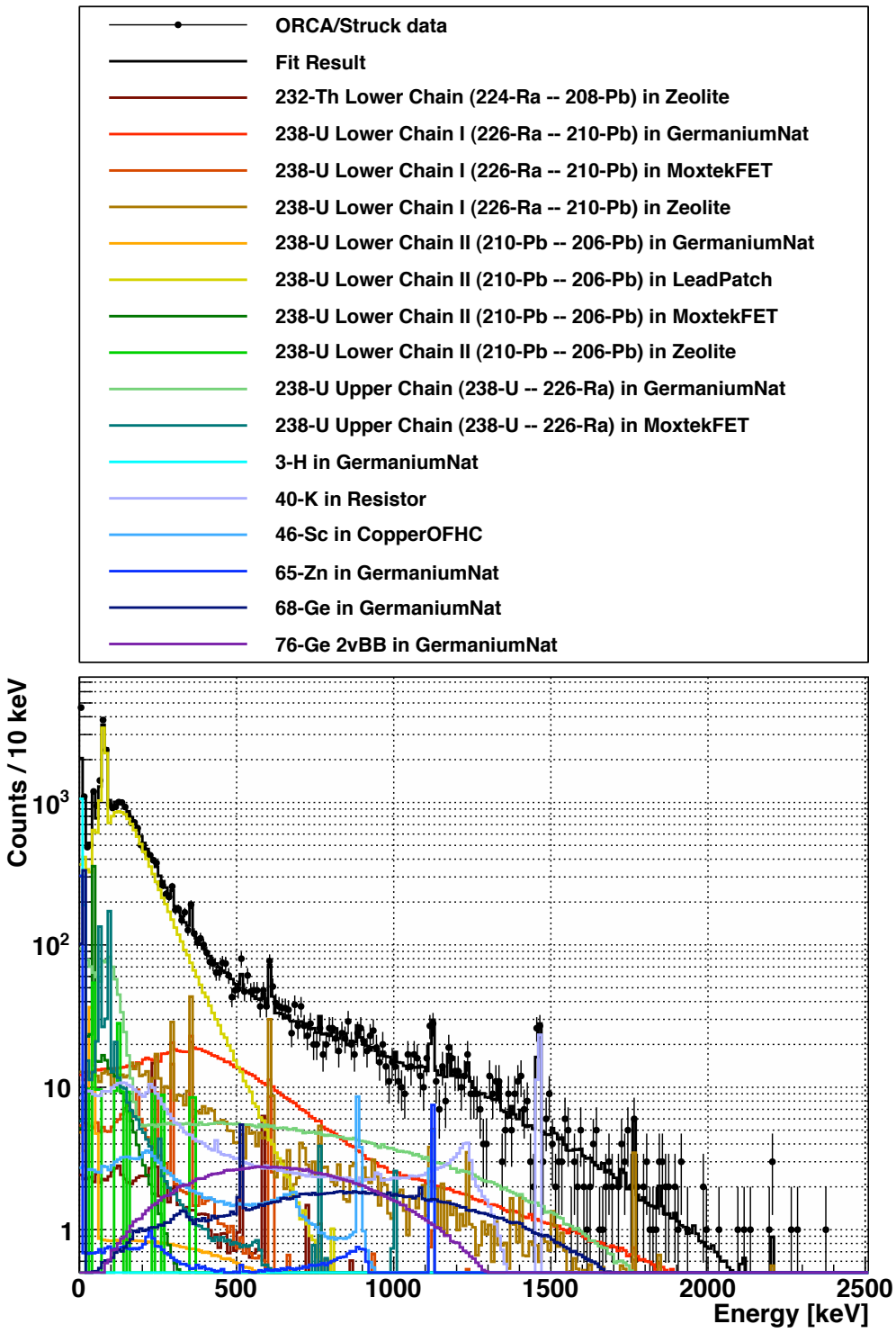

Figure 7.11: Significant contributions to background model fit of the Dataset I energy spectrum. The 15 PDFs found by the fitter to contribute more than 100 counts are shown.

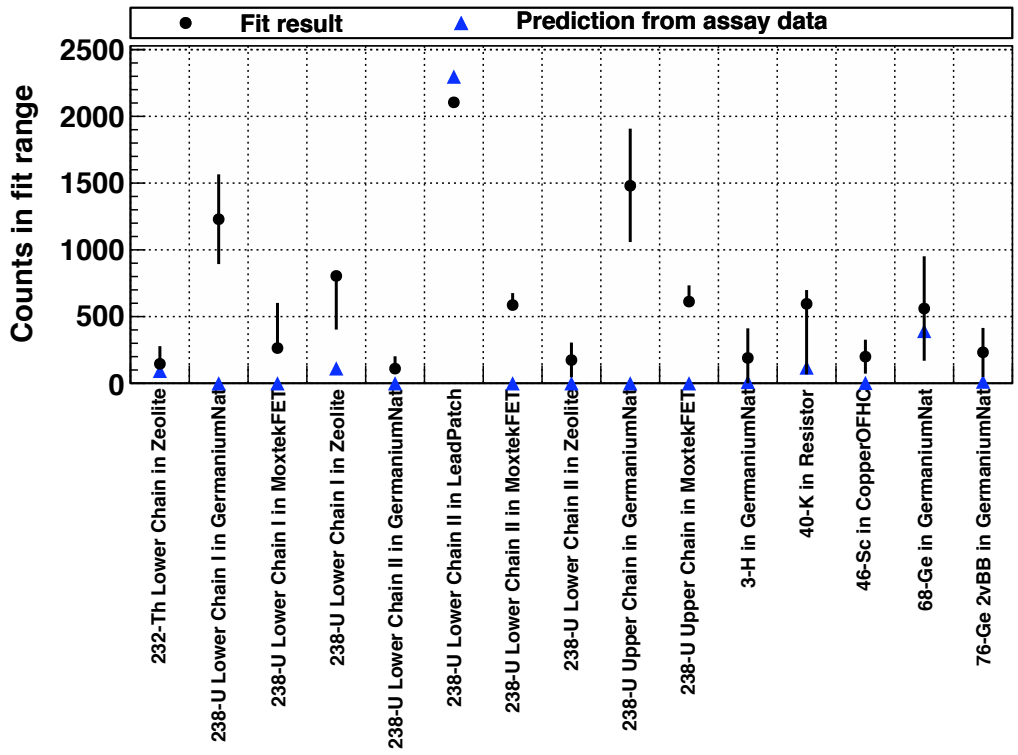

Figure 7.12: Numbers of counts found from fit of background model to the Dataset I energy spectrum. The values and uncertainties for the ^{238}U Lower Chain II in the lead patches were divided by 10 so that all data points can be shown on the same scale. The 15 PDFs found by the fitter to contribute more than 100 counts are shown.

Table 7.4: Selected results from fit of background model to Dataset I energy spectrum. The fit was performed in the region from 10 to 2000 keV, using 10-keV bins. The first column of the table is an index used to identify the fit components. The third column is the number of counts expected from the predicted background energy spectrum. Spectra that were found by the fitter to contribute more than 100 counts are listed.

	Description	**Prediction**	**Fit Result**
9	232-Th LC in Zeolite	9.32×10^{1}	$\left(1.46\ ^{+1.32}_{-0.00}\right) \times 10^{2}$
24	238-U LC I in GermaniumNat	3.56×10^{-2}	$\left(1.23\ ^{+0.34}_{-0.34}\right) \times 10^{3}$
25	238-U LC I in MoxtekFET	2.88×10^{-3}	$\left(2.64\ ^{+3.38}_{-0.00}\right) \times 10^{2}$
30	238-U LC I in Zeolite	1.12×10^{2}	$\left(8.05\ ^{+0.00}_{-4.02}\right) \times 10^{2}$
35	238-U LC II in GermaniumNat	4.20×10^{-2}	$\left(1.10\ ^{+0.92}_{-0.00}\right) \times 10^{2}$
38	238-U LC II in LeadPatch	2.30×10^{4}	$\left(2.10\ ^{+0.03}_{-0.00}\right) \times 10^{4}$
39	238-U LC II in MoxtekFET	5.33×10^{-5}	$\left(5.86\ ^{+0.90}_{-0.00}\right) \times 10^{2}$
47	238-U LC II in Zeolite	1.26×10^{-1}	$\left(1.74\ ^{+1.31}_{-1.29}\right) \times 10^{2}$
51	238-U UC in GermaniumNat	3.75×10^{-2}	$\left(1.48\ ^{+0.43}_{-0.42}\right) \times 10^{3}$
52	238-U UC in MoxtekFET	2.57×10^{-4}	$\left(6.12\ ^{+1.22}_{-0.00}\right) \times 10^{2}$
58	3-H in GermaniumNat	1.04×10^{1}	$\left(1.90\ ^{+2.22}_{-2.22}\right) \times 10^{2}$
61	40-K in Resistor	1.18×10^{2}	$\left(5.96\ ^{+1.03}_{-5.29}\right) \times 10^{2}$
65	46-Sc in CopperOFHC	3.24×10^{0}	$\left(2.00\ ^{+1.27}_{-1.27}\right) \times 10^{2}$
81	68-Ge in GermaniumNat	3.92×10^{2}	$\left(5.60\ ^{+3.91}_{-3.91}\right) \times 10^{2}$
82	76-Ge 2vBB in GermaniumNat	1.26×10^{1}	$\left(2.32\ ^{+1.83}_{-1.84}\right) \times 10^{2}$

7.6 Discussion of results

The MALBEK background model gives a good description of the Dataset I energy spectrum. When the normalization of contributions is fixed by material radiopurity information, the energy spectra measured and KURF and predicted by the background model agree within 20% for the integral count rate above 5 keV. When the normalization of contribution is allowed to float in a fit, the result has χ^2 of 132.81 per 115 degrees of freedom, for a P-value of 0.12.

Background model results for two other datasets, blinded during analysis of Dataset I, will be presented later in this dissertation. This section will describe some implications and limitations of modeling the MALBEK background energy spectrum, especially as they will apply to Datasets II and III.

Dataset II is a continuation of Dataset I – data collected just after the end of Dataset I. Dataset III is a very different set of data – collected soon after the lead patches were removed and the detector was brought to the surface, where the germanium crystal and copper components were exposed to cosmic rays. Since the lead patches account for 90% of the predicted Dataset I energy spectrum, agreement between the Dataset I and II energy spectra will be dominated by the accuracy of the simulated response of MALBEK to ^{210}Pb in the lead patches. The Dataset III energy spectrum is most likely composed of a larger variety of energy-spectrum contributions, and will be a more rigorous test of the background model.

The shape of each simulated energy-spectrum contribution to the background model depends on several factors described by Equations 7.2 and 6.4. These will be summarized here, with notes about possible effects on the background model.

- The energy spectrum of radiation emitted by each source and the interactions of radiation in matter are described by GEANT4. Chapter 6 described accounts of GEANT4's performance in the literature and an ongoing MAJORANA effort to validate GEANT4. Section 7.6.1, below, presents information about GEANT4's performance for isotopes of interest in the Dataset I energy spectrum.

- The MAGE/GEANT4 geometry model determines the solid angle each source of contamination subtends on the detector and the geometry of attenuating materials between the source and detector. The model was created based on technical drawings and information provided by CANBERRA and Juan Collar, as described in Chapter 5. Any discrepancies between the actual and modeled geometries could affect the solid angles and attenuation, as shown in Figure 6.8.

- The outer n^+ germanium detector dead layer has been measured to within 11% in Chapter 6. The nominal value of the dead layer thickness, 0.933 mm, was applied with GAT to the MAGE/GEANT4 results. These GAT results are used to construct the energy spectrum PDFs used in the fit. Any discrepancy between the estimated thickness and the actual thickness could affect the shape of the energy spectra, and would have a larger effect on low-energy radiation, as shown in Figure 6.8. The agreement between the simulated and measured ^{210}Pb spectra is a good test of the dead layer thickness, since the shape of the bremsstrahlung continuum and relative intensity of the Pb x-rays and gamma would be distorted by an error in the dead layer.

- The effect of the preamplifier on the energy spectrum was characterized in Chapter 4. The uncertainty in the efficiency increases with increasing energy.

- The energy calibration and description of the energy resolution as a function of energy were measured from the Dataset I energy spectrum and applied to the simulation results. Any errors in these measurements could create discrepancies between the measured spectrum and the PDFs.

7.6.1 Notes about GEANT4.9.3.p01

To simulate the MALBEK background energy spectrum, GEANT4 must describe the interactions of many particles with matter: gammas, electrons, neutrons, muons, alphas, and others. These interactions must be accurate over a wide range of energies – from a few keV to a few MeV. Decays of unstable nuclei must emit radiation with the correct energies

and branching ratios. To accomplish this, the GEANT4 software package must simulate a wide variety of particle interactions. Even if the underlying physics is described correctly, GEANT4 still relies on many parameters measured experimentally: interaction cross sections, energies of atomic and nuclear states and the intensities with which they are populated in decays, lifetimes of unstable nuclei, and internal conversion coefficients, to name a few.

GEANT4 gives a good description of many physics processes [75]. There are some known shortcomings of GEANT4, many of which are documented in publications, on the GEANT4 website, and in bug reports. GEANT4 is under active development. New GEANT4 versions are released regularly that feature improvements, and the GEANT4 data files that contain input parameters measured from experiment are updated regularly. Below, some issues with the GEANT4 version used in this work, 4.9.3.p01, that affect the simulation of the MALBEK background energy spectrum are described.

Cobalt-57 is produced in germanium by cosmogenic activation. It decays by electron capture to ^{57}Fe with a half life of 271.7 days. The decay typically populates a 136.5-keV energy level of ^{57}Fe. In 10.7% of decays, a 122.0-keV gamma is emitted from this level; in 85.6% of decays a 136.5-keV gamma is emitted. Within a detector, the 136.5 keV of energy released in the decay typically sums with 7.1 keV of atomic de-excitation energy to produce a peak in the energy spectrum at 143.6 keV [86] [87]. Gammas from decays in the dead layer of the detector may reach the active volume, where the energy of the gamma with be recorded but the atomic de-excitation energy will be lost. Peaks at 122.0, 136.5, and 143.6 keV are visible in energy spectra collected from neutron-activated germanium detectors, and the peak at 143.6 keV is the most intense, typically by an order of magnitude. The 143.6-keV peak is visible in the MALBEK Dataset I energy spectrum, but no other ^{57}Co peaks are present at statistically significant levels. However, in MAGE/GEANT4 simulation, the energy spectrum ^{57}Co decay is not correctly reproduced, as shown in Figure 7.13. In the figure, the highest-intensity peak is at 136.5 keV.

The ^{57}Co discrepancy is apparent in the MAGE Validation Report [73]. A 6.4-keV x-ray from the ^{57}Fe nucleus is emitted in 17.60 ± 0.04% of simulated decays, while the published value (for both kα1 and kα2) is 49.5% [33]. The kβ1 and kβ3 x-rays of 7.1 keV are emitted in 1.9 ± 0.4% of simulated decays, compared to the published value of 5.9% [33]. The

underproduction of these x-rays contributes to the reduced intensity of the 143.6 keV peak in the simulated energy spectrum.

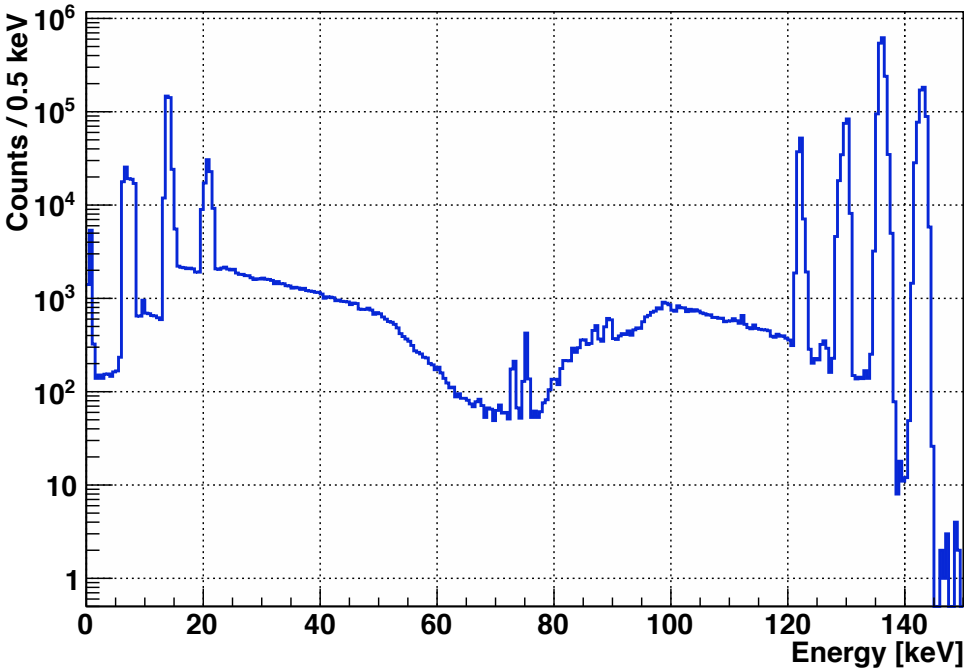

Figure 7.13: Response of MALBEK to 3.4×10^6 decays of ^{57}Co, simulated with MAGE/GEANT4. The MAGE results have been processed with GAT to apply the MALBEK dead layer. The spectrum has been convolved with the energy resolution of Dataset I. Branching ratios of 6.4- and 7.1-keV x-rays are not reproduced correctly in the simulation.

The decays of many isotopes were simulated to create the MALBEK background model. The branching ratios produced by GEANT4 for the 15 significant peaks in Dataset I listed in Table C.1 are compared to published values in Table 7.5. The GEANT4 branching ratios are in good agreement with published values for the majority of the peaks. Branching ratios for the betas emitted in ^{68}Ge and ^{210}Bi decay are listed in Table 7.6 and agree well with published values.

The 46.5-keV gamma emitted in the decay of ^{210}Pb is under-produced by about 7%, while the 1.1-MeV beta emitted in ^{210}Bi decay is produced with the correct branching ratio. Decays of ^{210}Pb are simulated in equilibrium with ^{210}Bi as part of the ^{238}U Lower Chain II, and these two isotopes contribute to the spectrum of MALBEK response to contamination in the lead patches. Because of the discrepancy between GEANT4 and the literature for the branching ratio of the 46.5-keV peak, each PDF describing MALBEK's response to the ^{238}U Lower Chain II is expected to be slightly incorrect.

In the electron capture decay of ^{68}Ge, 10.36 keV of atomic de-excitation energy is emitted as x-rays and Auger electrons in 86.25% of decays. In GEANT4 simulations of this decay, 1.3 keV of this energy was often carried by the ^{68}Ga nucleus. This energy of 1.3 keV is much larger than the expected recoil energy. When MAGE/GEANT4 results were processed with GAT, nuclear quenching was applied, and only 0.2 keV of the 1.3 keV of recoil energy was detected as ionization energy. This produced a peak at 9.3 keV, comparable in intensity to the peak at 10.36 keV. To mitigate this issue, a modified version of GAT was used to process the ^{68}Ge results, where nuclear quenching was disabled.

The response of an underground germanium detector to cosmic rays depends on many physics processes. High-energy muons interact in the detector, shielding, and rock of the experimental hall. These muons may deposit energy directly in the detector, or they may produce neutrons or spallation products that can deposit energy in the detector. Neutrons and gammas from inelastic neutron interactions are a particular concern for low-background experiments. GEANT4 has known issues with neutron production and interactions, including issues with neutron production and propogation [89]. Other documented issues relevant for germanium detectors include problems with recoil energies assigned to germanium isotopes involved in neutron interactions, Doppler broadening of photon peaks, and the production of gammas due to neutron interactions [90].

A GEANT4 bug in the track weights of particles produced in radioactive decay affected the spectra of MALBEK response to cosmic-ray muons, which were generated using importance sampling, with event biasing of neutrons [91]. Due to the bug, unstable isotopes produced by biased neutrons with track weight w are assigned a weight of 1.0 instead of the correct weight, w. This affects the weights of gammas and other radiation produced by

Table 7.5: Comparison of GEANT4.9.3.p01 peak intensities and published values. Intensities are per decay of the listed isotope. Energies are in keV. GEANT4 intensities were determined from MAGE/GEANT4 studies and are listed with one-sigma statistical uncertainties. The ^{65}Zn and ^{68}Ge peaks are due to atomic relaxation; the energies of these lines are from Bearden and Burr [62]. The intensity of the ^{68}Ge peak is from Schönfeld et al. [61]. See the additional notes in the text about ^{68}Ge and GEANT4. The intensity of the ^{65}Zn peak was calculated from Bé et al. [88]. Other intensities and energies are from the National Nuclear Data Center [33].

		Intensity [%]	
Isotope	**Energy**	**Literature**	**GEANT4**
^{65}Zn	8.98	86.98 ± 0.18	87.02 ± 0.07
^{68}Ge	10.36	86.25 ± 0.22	86.53 ± 0.05
^{210}Pb	46.54	4.25 ± 0.04	3.95 ± 0.01
^{212}Pb	238.63	43.60 ± 0.50	42.74 ± 0.05
^{214}Pb	295.22	18.42 ± 0.04	18.79 ± 0.03
^{214}Pb	351.93	35.60 ± 0.07	36.80 ± 0.04
^{208}Tl	510.77	22.60 ± 0.20	22.82 ± 0.02
^{208}Tl	583.19	85.00 ± 0.30	84.94 ± 0.04
^{214}Bi	609.32	45.49 ± 0.16	46.40 ± 0.04
^{40}K	1460.82	10.66 ± 0.18	10.55 ± 0.02

Table 7.6: Comparison of GEANT4.9.3.p01 beta intensities and published values. Intensities are per decay of the listed isotope. Endpoint energies are in keV. GEANT4 intensities were determined from MAGE/GEANT4 studies and are listed with one-sigma statistical uncertainties. Intensities and energies are from the National Nuclear Data Center [33].

			Intensity [%]	
Isotope	**Energy**		**Literature**	**GEANT4**
^{68}Ga	821.7	β^+	1.19 ± 0.01	1.22 ± 0.01
	1899.1	β^+	87.72 ± 0.09	87.91 ± 0.09
^{210}Bi	1162.1	β^-	100.0 ± 0.00	100.0 ± 0.10

muon-induced neutrons. To correct for this issue, GAT was modified while processing MAGE/GEANT4 muon results – tracks in the detector with weight 1.0 were assigned a weight of 2^{-33}, which is the weight neutrons have in the MALBEK simulation once they reach the detector and inner shielding.

GEANT4 does not simulate angular correlations of gammas emitted in decays. Angular correlations may affect the spectrum of detector response to decays of ^{60}Co and ^{214}Bi. Efforts to include angular correlations in GEANT4 are ongoing [92].

7.7 Plan for analysis of blinded data

The following tasks were completed in preparation for analysis of the blinded data:

- Procedures and software for producing energy spectra from data collected with MALBEK using the high-energy channel from the ORCA/Struck DAQ were developed, as described in Chapter 4. This includes the implementation of timing cuts and a rise-time cut that is valid across the energy spectrum.

- The energy-dependent efficiency of the preamplifier was measured and uncertainty was quantified in Section 4.8.

- A process for identifying peaks and calibrating the energy spectrum was chosen and tested, as described in Chapter 4.

- The energy resolution of the detector is understood as a function of energy for multiple datasets, as described in Section 4.7.3.

- The detector dead layer was measured with a ^{133}Ba source, as described in Chapter 6. With this dead layer, the integral count rate of detector response above 5 keV agrees within 5% between simulation and measurement of response to ^{133}Ba.

- The sources of all peaks in the Dataset I energy spectrum were identified in Table C.1. The background model includes all of the listed isotopes.

- The MALBEK background model was shown to provide a good description of the Dataset I energy spectrum. The predicted energy spectrum, based on material assay data, is a good description of the Dataset I energy spectrum – gamma peaks and spectral shapes are reproduced by the model. When the normalization of PDFs contributing to the background model spectrum is allowed to float in a fit, the background model is in good agreement with the Dataset I energy spectrum – the fit gives χ^2 of 132.81 per 115 degrees of freedom, for a P-value of 0.12.

After these criteria were met, Datasets II and III were unblinded and analyzed. At the time of unblinding, the planned sequence of analysis was the following:

1. Process the ORCA data files through all tiers, according to the process described in Chapter 4.

2. Calibrate the energy spectrum of each dataset using peaks in the background spectrum. As described in Section 4.7.2, this is done using using 5-σ significant peaks. The source datasets described in this dissertation, e.g. ^{133}Ba, are used for detector characterization but not energy calibration.

3. Characterize the energy resolution of each dataset according to Section 4.7.3.

4. Predict the background energy spectrum of each dataset using the MALBEK background model as described in this chapter, including the livetime, energy resolution, preamplifier, and cosmogenic exposure parameters appropriate for the dataset. The radiopurity information used for the Dataset I energy-spectrum prediction will be used for energy-spectrum predictions of Datasets II and III, except the specific activity of ^{210}Pb in the lead patches, which will be set to 91.6 Bq/kg for Dataset II (as determined from the fit of Dataaset I). The contribution of the patches will be omitted from Dataset III, since the patches were removed from the cryostat before Dataset III was collected.

5. Fit the background model to the energy spectrum of each dataset, using the procedure and PDFs described in this chapter. The energy spectrum fit of the Dataset II will provide a second measurement of the ^{210}Pb activity in the patches.

6. If evidence of additional backgrounds is present in the datasets, simulate MALBEK's response to these backgrounds and add them to the background model.

To ensure that statistical uncertainties in the PDF shapes were minimized, a goal of at least 10^5 counts in each PDF was established. At the time of unblinding, Monte Carlo runs

were ongoing to increase statistics in seven PDFs: the ^{232}Th Upper Chain in rock, the ^{238}U Upper Chain in rock, the ^{238}U Lower Chain I in air and rock, and the ^{238}U Lower Chain II in modern lead, stainless steel, and the radon-exposed surfaces outside the cryostat.

In the following chapters, the MALBEK background model is compared to energy spectra from Datasets II and III.

7.8 Conclusions

In this chapter, the process for building a background model of a MALBEK energy spectrum was described. A predicted energy spectrum was presented for Dataset I, where the normalization of each contribution was based on material assay data, cosmogenic exposure history of the components, and live time. The predicted spectrum reproduced many peaks, spectral shapes, and continuum levels in the Dataset I energy spectrum. The integral number of counts above 5 keV was reproduced within 20% by the prediction. The majority of counts are due to ^{210}Pb contamination in the lead patches near the detector.

Normalization of the contributions were then allowed to float in an extended binned maximum likelihood fit. The fit result was in good agreement with the Dataset I energy spectrum, with χ^2 of 132.81 per 115 degrees of freedom, for a P-value of 0.12. A specific activity of $91.6^{+1.2}_{0.0}$ Bq/kg ^{210}Pb in the lead patches was determined from the fit.

In the next chapter, the MALBEK background model is compared to energy spectra from Datasets II and III. Dataset II is similar to Dataset I, but contains more statistics. Dataset III was collected after the lead patches were removed. Dataset III will be an interesting test of the background model because the dominant background contribution due to the lead patches will be removed.

Chapter 8

DATASET II BACKGROUND MODEL

8.1 Introduction

Dataset II consists of MALBEK ORCA runs 7513–11831, collected between January and August 2011. The lead patches were still in the cryostat during these runs, as in Dataset I. Energy spectra from the two datasets are compared in Figure 8.1. Peaks are labeled in Table C.2.

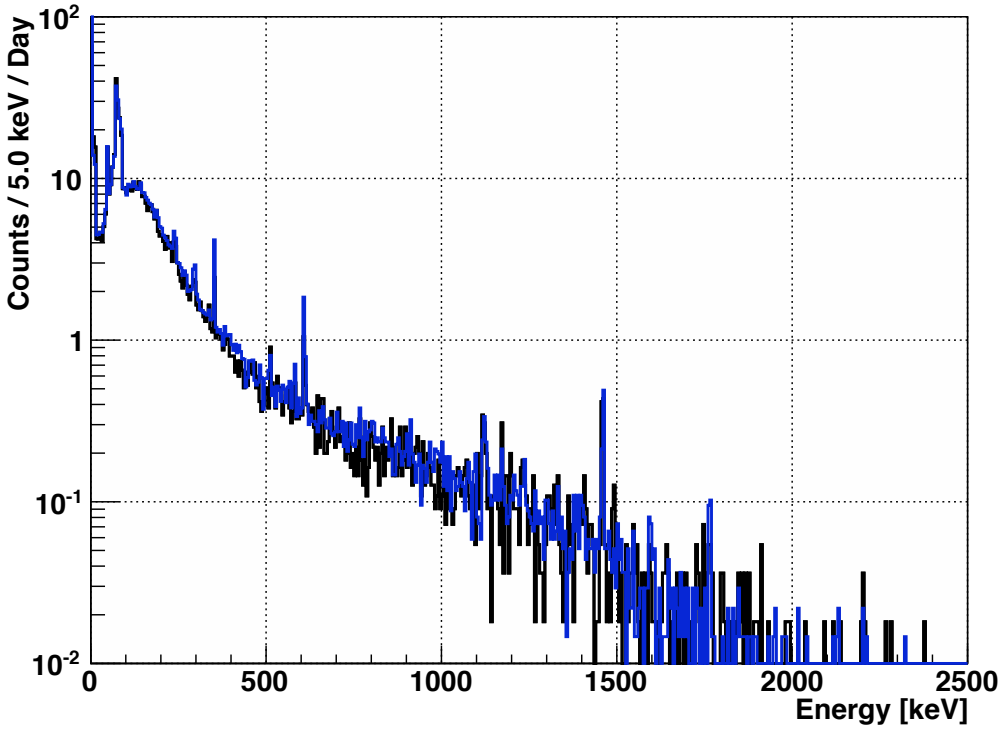

Figure 8.1: Comparison of ORCA/Struck Datasets I and II energy spectra. The energy spectrum from Dataset II (blue) is overlaid on the spectrum from Dataset I (black). The spectra are shown after timing cuts and the combined slow pulse cut.

Figure 8.2 shows the two energy spectra at low energies. The 8.98-keV and the 10.37-keV peak are due to decays of ^{65}Zn and ^{68}Ge, respectively, which were produced by cosmogenic activation of the germanium crystal while MALBEK was on the earth's surface. At the beginning of Dataset II, MALBEK had been underground at KURF for one year and eight days, and some of the cosmogenic activation products decayed away.

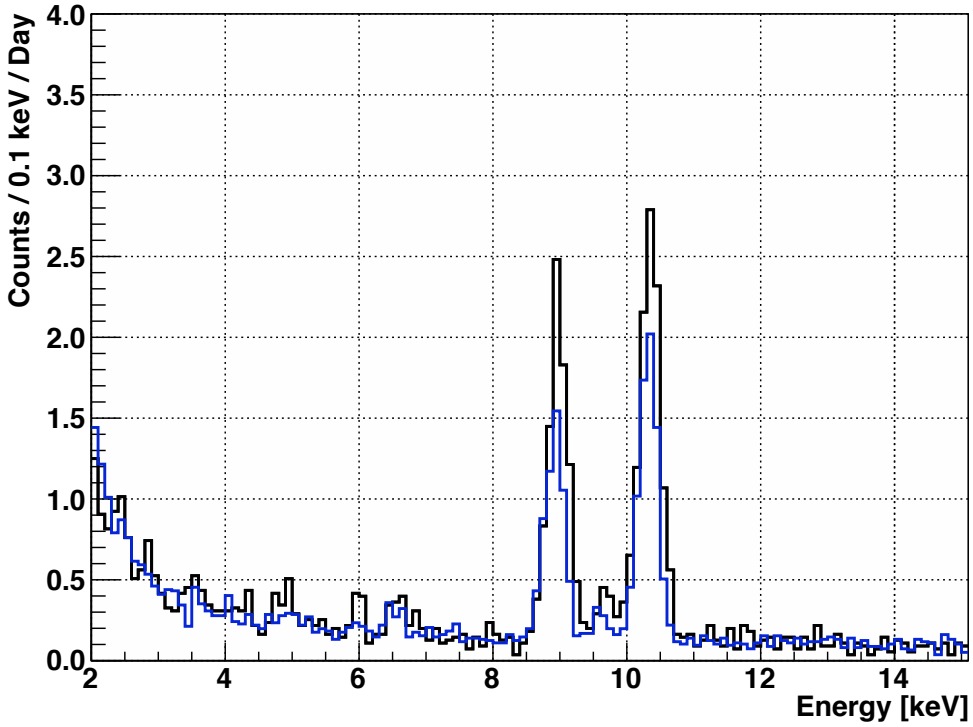

Figure 8.2: Comparison of ORCA/Struck Datasets I and II energy spectra at low energies. The energy spectrum from Dataset II (blue) is overlaid on the spectrum from Dataset I (black). The spectra are shown after timing cuts and the combined slow pulse cut. In MALBEK's unamplified (high-energy) channel, the slow-pulse cut breaks down for energies below approximately 5 keV, which contributes to the rise at low energy.

8.2 Notes about unblinding

Dataset II was unblinded in October 2012. The following changes were made to the dataset generation process described in Section 4.5 to address issues affecting Dataset II:

- The set of runs from which Dataset II was constructed included measurements of calibration sources. To eliminate these, a run was skipped if it contained more than 100 counts above 5 keV in the unamplified energy channel after the pulser veto.

- In some Dataset II runs, counts from the pulser were detected in the pulser channel of the Struck card, but not in the unamplified ionization energy channel. This was due to issues with the digitizer while DAQ software was under development. The number of pulser counts in the unamplified channel is used to calculate livetime. To avoid these runs, a run was eliminated from the dataset if it did not have any counts coincident in time with the pulser.

As a result of unblinding Dataset II, a bug was discovered in the MJBM code. The livetime efficiency had been applied to the number of initial contaminant atoms from cosmogenic activation, and not the number of expected decays due to arbitrary contamination. In Dataset I, the livetime efficiency is 81.9%. This efficiency includes deadtime due to cuts of events related to the pulser and preamplifier resets, but also deadtime due to power outages and other breaks in data taking. In Dataset II, the livetime efficiency is 65.7%. The increase in deadtime is due to gaps in data taking due to issues with the DAQ. The MJBM bug first became apparent because the activity of ^{210}Pb measured from Dataset I did not agree with Dataset II.

Correcting this bug changed the Pb patch activity measured in Dataset I from 74.8 ± 0.5 Bq/kg to the current value of $91.6^{+1.2}_{0.0}$ Bq/kg. Initially, a value of 60.3 ± 0.5 was measured for DSII; correcting the bug produced the current value of $92.9^{+0.7}_{-0.8}$ Bq/kg.

Based on additional reading of published and MAJORANA-internal information, two contaminants were added to the MALBEK background model: ^{40}K in Copper per an EXO paper [93] and notes on the MAJORANA Background Model Wiki page [94], and ^{40}K in KURF rock per a measurement at KURF [36].

An issue with importance-sampled MAGE/GEANT4 spectra was discovered. Some of the simulated spectra in which gammas were biased were dominated by many counts originating from the same few initial events. The issue was discovered during an ongoing study of the simulated spectra, and was unrelated to the unblinding. This issue affected spectra of decays in the rock and zeolite. A gamma emitted by a decay had a small chance of entering the MALBEK shielding in the space between the cold finger and lead. Once in this space, the gamma track would be doubled at the boundaries of the parallel volumes shown in Figure 5.9 and split into a new event. The many gamma tracks produced by this process would deposit energy in the detector, producing many correlated counts in the simulated energy spectrum. To eliminate this issue, the zeolite simulations were reproduced without importance sampling. The rock sampling volume was divided into two regions: one section below the shielding and the remainder of the volume. Importance sampling was used when simulating decays in the main sampling volume, but not in the small area under the shield. Unfortunately, these simulations of MALBEK response to decays from the rock were not completed in time for this analysis, and are not included in this work – simulations of decays from volumes outside the shield are not included in analysis of Datasets I, II, and III.

8.3 Background model results

The background model prediction for Dataset II is shown in Figure 8.3. This energy spectrum is based on the run start and stop time and the energy resolution of Dataset II, as listed in Table A.1, the material radiopurity information listed in Appendix J, and the cosmogenic exposure history of the cryostat. The activity of ^{210}Pb in the lead patches measured from Dataset I, $91.6^{+1.2}_{0.0}$ Bq/kg, was used. In Figure 8.4, the prediction is compared to the Dataset II spectrum measured at KURF. The two spectra are in good agreement at low energies, where the lead patches are the dominant contribution, but the continua diverge above a few hundered keV, where other backgrounds are significant.

The simulated spectra were fit to the Dataset II energy spectrum, and the results are shown in Figure 8.5. At energies below 500 keV, the fit results are shown in Figure 8.6. Significant contributions to the Dataset II fit results are shown in Figure 8.7 and Figure 8.8. These contributions are also documented in Table 8.1. The full results of fitting are listed

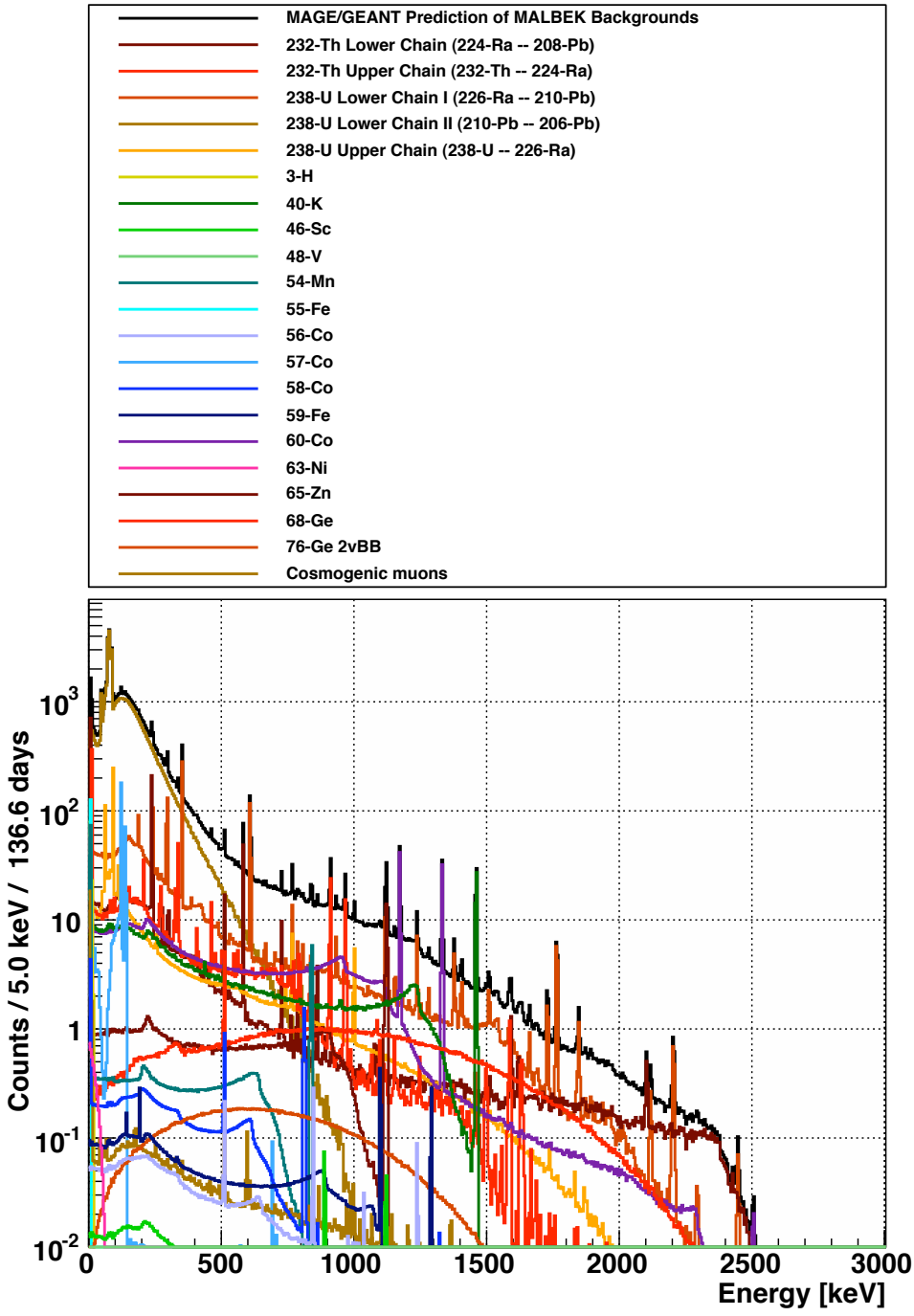

Figure 8.3: Predicted Dataset II energy spectrum. The activity of ^{210}Pb in the lead patches is 91.6 Bq/kg, based on the measurement from Dataset I.

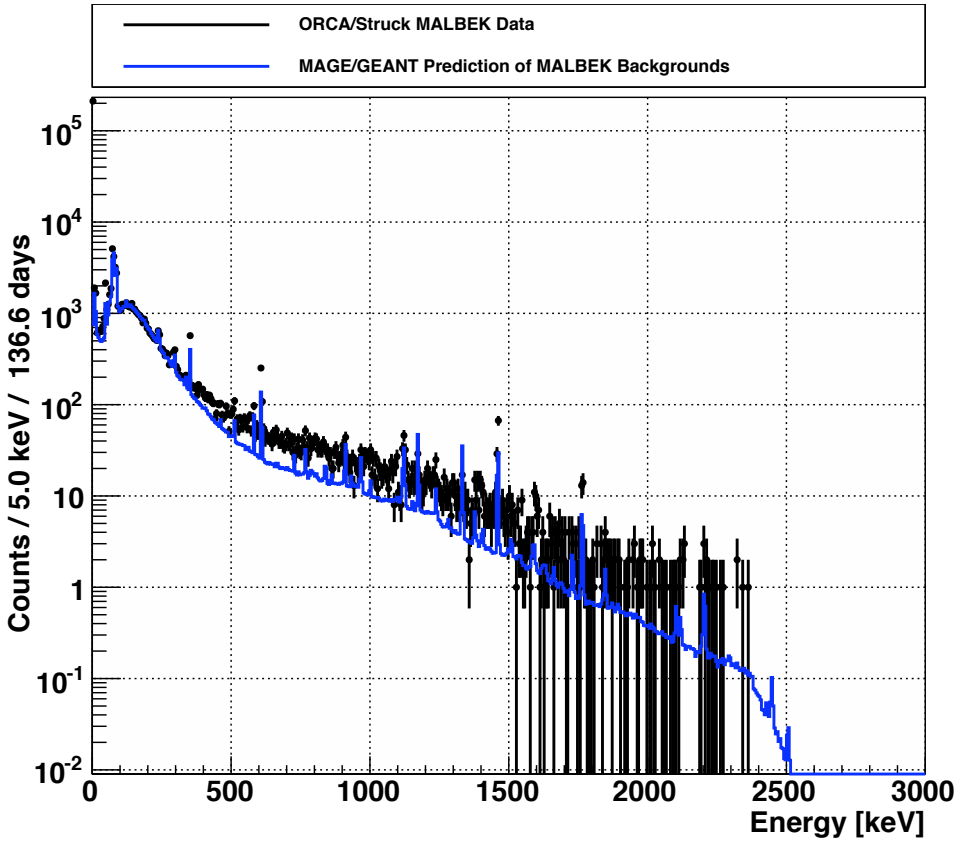

Figure 8.4: Comparison of Dataset II energy spectrum to background model prediction. The activity of ^{210}Pb in the lead patches is 91.6 Bq/kg, based on the measurement from Dataset I.

in Table L.3. Correlations between fit parameters are shown in Figure L.35 and listed in Table L.4. The fit has χ^2 of 186.15 per 115 degrees of freedom, for a P-value of 3.00E-05. The fit gives poor agreement, mostly due to discrepancies below 200 keV. At these energies, the shape of the spectrum is due primarily to the contamination in the lead patches. As discussed in Section 7.6.1, GEANT4 under-produces the 46.5-keV gamma from ^{210}Pb decay, so the simulated energy spectrum is expected to be slightly inaccurate. At low energies, the effect of the dead layer is also more important, and a small discrepancy between the dead layer measurement and the actual thickness of the dead layer could affect the shape of the energy spectrum.

Figure 8.9 shows some measured and simulated energy spectra that are useful for understanding the Dataset II fit results. Datasets I and II were added to produce a single high-statistics background spectrum measured before the lead patches were removed; this combined spectrum is shown in black. Dataset III, collected after the patches were removed, is shown in red. Dataset III is presented in detail in Chapter 9. The differences between the black and red spectra are primarily due to the contribution of the lead patches. In blue, the simulated spectrum of MALBEK response to ^{210}Pb in the lead patches has been added to the Dataset III spectrum. The normalization of the simulated spectrum is determined by the ^{210}Pb activity used in the Dataset II background model, $92.9^{+0.7}_{-0.8}$ Bq/kg. The blue and black spectra show some discrepancies in the Pb peak intensities and in the bremsstrahlung continuum.

Table 8.2 quantifies the discrepancies in the peaks. In the table, R_{meas} was calculated from the black spectrum in Figure 8.9 and R_{sim} was calculated from the blue spectrum. For the Pb x-rays between 70 and 90 keV, the measured and simulated peak intensities are in good agreement, with the exception of the 87.3-keV peak. The Pb x-rays are induced in Pb by a high-energy beta emitted by ^{210}Bi, a ^{210}Pb daughter, so the intensities of the x-ray peaks depend on specifics of the lead patches and are difficult to predict. The intensity of the 46.5-keV peak is 44.8% lower in the simulation results than in the measured spectrum. This peak is under-produced in simulated ^{210}Pb decays, as shown earlier in Table 7.5, but the under-production is not enough the account for the 44.8% discrepancy.

The discrepancies in the 46.5-keV gamma peak and the bremsstrahlung continuum be-

Table 8.1: Selected results from fit of background model to Dataset II energy spectrum. The fit was performed in the region from 10 to 2000 keV, using 10-keV bins. The first column of the table is an index used to identify the fit components. The third column is the number of counts expected from the predicted background energy spectrum. Spectra that were found by the fitter to contribute more than 100 counts are listed.

	Description	**Prediction**	**Fit Result**
0	232-Th LC in BerylliumCopper	1.89×10^{2}	$\left(2.19\ ^{+3.05}_{-0.00}\right) \times 10^{2}$
9	232-Th LC in Zeolite	2.30×10^{2}	$\left(6.38\ ^{+4.11}_{-4.16}\right) \times 10^{2}$
19	232-Th UC in Zeolite	2.01×10^{2}	$\left(4.55\ ^{+2.43}_{-0.00}\right) \times 10^{2}$
24	238-U LC I in GermaniumNat	8.80×10^{-2}	$\left(2.68\ ^{+0.48}_{-0.00}\right) \times 10^{3}$
25	238-U LC I in MoxtekFET	7.12×10^{-3}	$\left(2.53\ ^{+0.00}_{-1.82}\right) \times 10^{3}$
30	238-U LC I in Zeolite	2.76×10^{2}	$\left(3.52\ ^{+0.72}_{-0.71}\right) \times 10^{3}$
35	238-U LC II in GermaniumNat	1.04×10^{-1}	$\left(5.21\ ^{+1.38}_{-1.37}\right) \times 10^{2}$
38	238-U LC II in LeadPatch	5.18×10^{4}	$\left(5.27\ ^{+0.04}_{-0.04}\right) \times 10^{4}$
39	238-U LC II in MoxtekFET	1.32×10^{-4}	$\left(1.42\ ^{+0.15}_{-0.19}\right) \times 10^{3}$
47	238-U LC II in Zeolite	3.12×10^{-1}	$\left(5.05\ ^{+2.17}_{-2.15}\right) \times 10^{2}$
51	238-U UC in GermaniumNat	9.28×10^{-2}	$\left(2.82\ ^{+0.54}_{-0.53}\right) \times 10^{3}$
52	238-U UC in MoxtekFET	6.35×10^{-4}	$\left(1.31\ ^{+0.18}_{-0.18}\right) \times 10^{3}$
58	3-H in GermaniumNat	2.50×10^{1}	$\left(8.32\ ^{+0.54}_{-1.39}\right) \times 10^{2}$
61	40-K in Resistor	2.92×10^{2}	$\left(4.24\ ^{+6.67}_{-0.00}\right) \times 10^{2}$
64	40-K in Zeolite	1.08×10^{1}	$\left(9.38\ ^{+0.00}_{-6.68}\right) \times 10^{2}$
66	48-V in CopperOFHC	2.68×10^{-6}	$\left(1.93\ ^{+1.58}_{-1.51}\right) \times 10^{2}$
67	54-Mn in GermaniumNat	5.55×10^{1}	$\left(1.26\ ^{+0.65}_{-0.62}\right) \times 10^{2}$
71	58-Co in CopperOFHC	2.25×10^{1}	$\left(1.92\ ^{+1.26}_{-1.68}\right) \times 10^{2}$
78	60-Co in Teflon	4.43×10^{2}	$\left(2.09\ ^{+1.09}_{-0.00}\right) \times 10^{2}$
80	65-Zn in GermaniumNat	1.80×10^{2}	$\left(1.57\ ^{+0.80}_{-0.75}\right) \times 10^{2}$
82	76-Ge 2vBB in GermaniumNat	3.11×10^{1}	$\left(1.22\ ^{+0.34}_{-0.00}\right) \times 10^{3}$

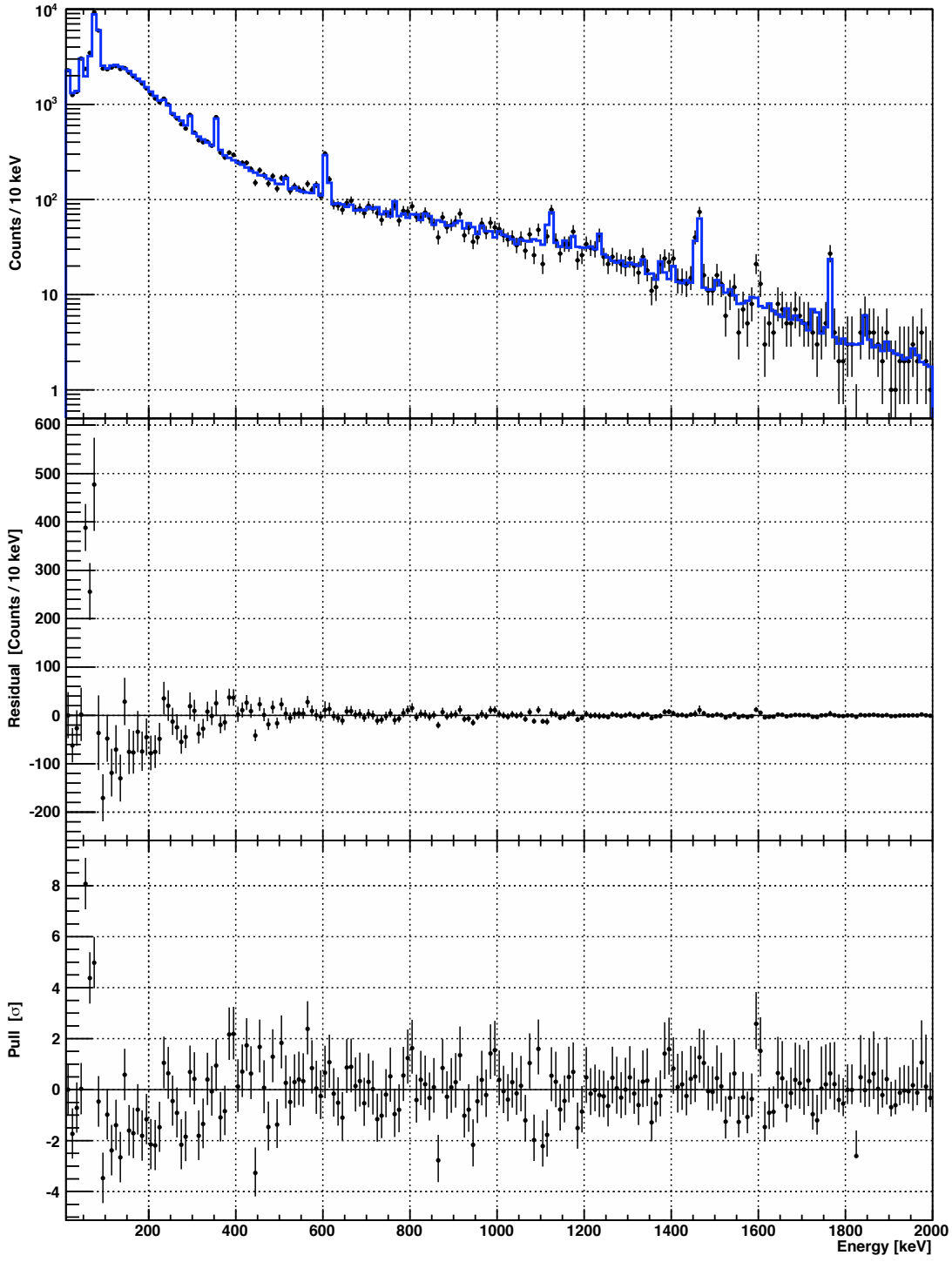

Figure 8.5: Results of background model fit to the Dataset II energy spectrum. The fit gives χ^2 of 186.15 per 115 degrees of freedom, for a P-value of 3.00E-05.

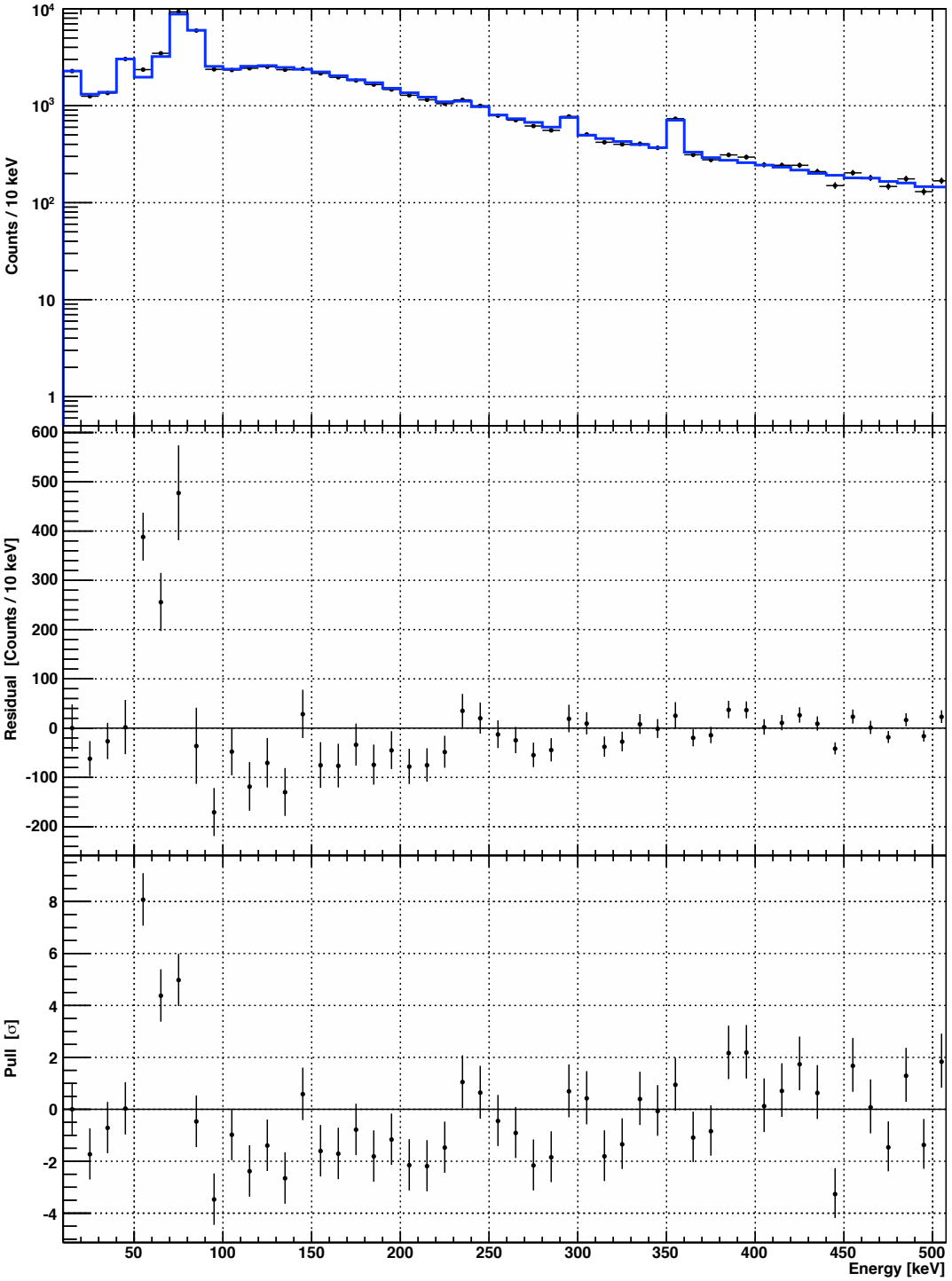

Figure 8.6: Results of background model fit to Dataset II, shown for energies below 500 keV.

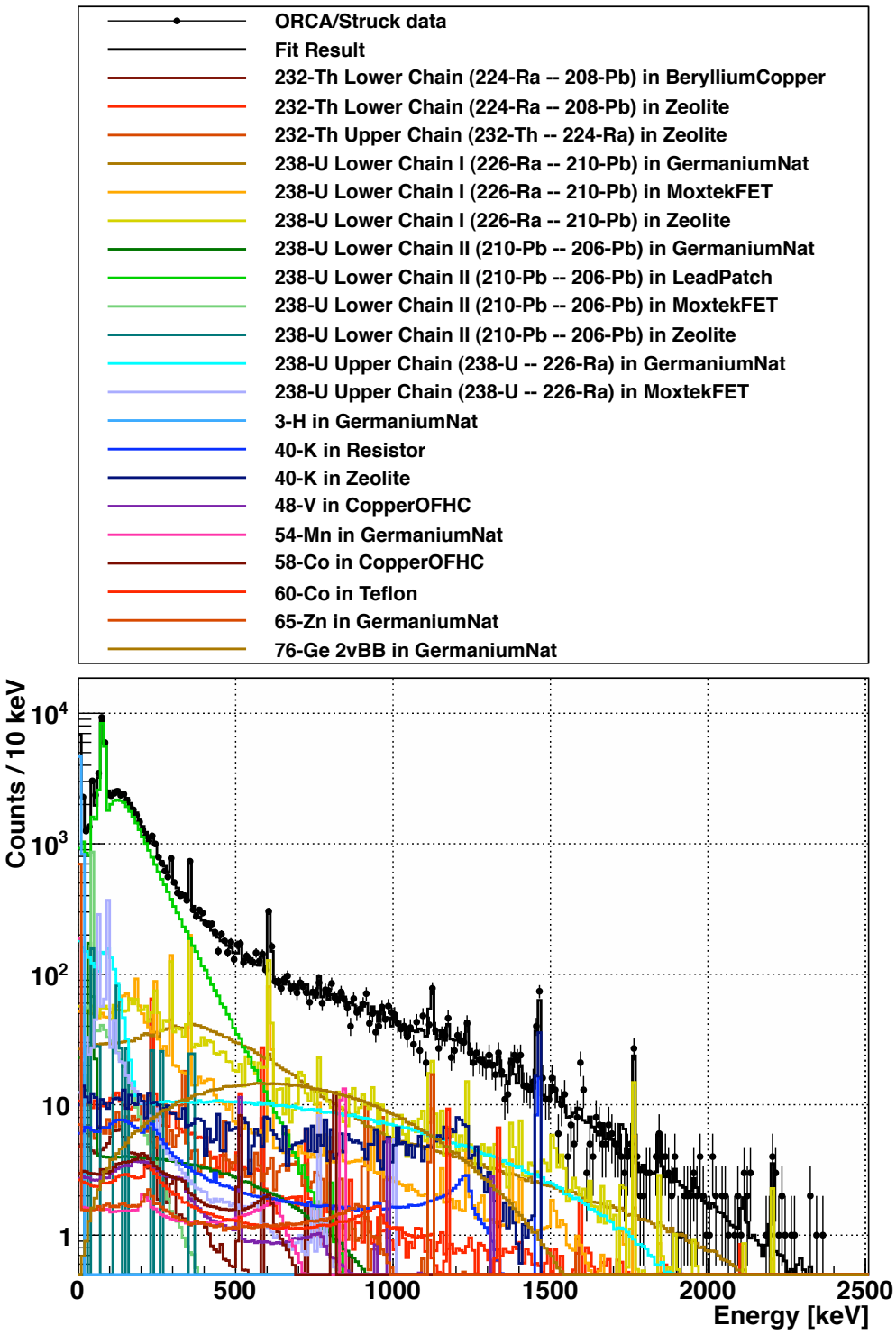

Figure 8.7: Significant contributions to background model fit of the Dataset II energy spectrum. The 21 PDFs found by the fitter to contribute more than 100 counts are shown.

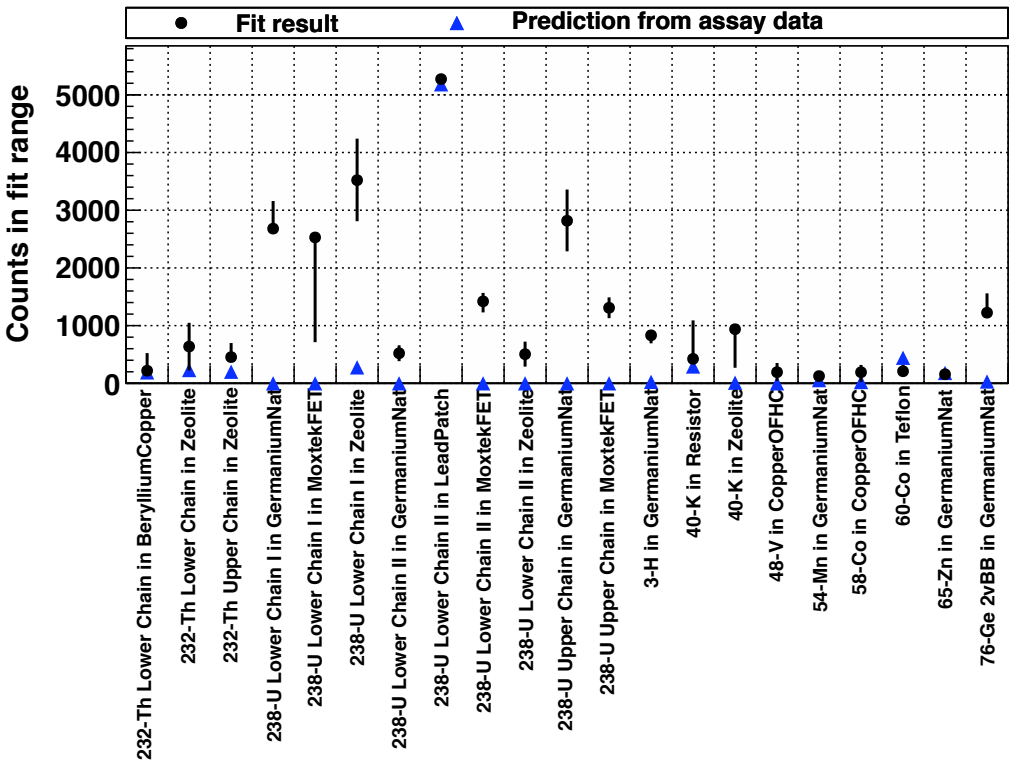

Figure 8.8: Numbers of counts found from fit of background model to the Dataset II energy spectrum. The values and uncertainties for the ^{238}U Lower Chain II in the lead patches were divided by 10 so that all data points can be shown on the same scale. The 21 PDFs found by the fitter to contribute more than 100 counts are shown.

tween simulated and measured spectra could be due to inaccuracies in the modeling of the geometry of the patches, e.g. self shielding within the patches could affect the spectrum if the patches are thicker in the model than in reality. The discrepancies might also be caused by inaccuracies in the thickness of the simulated dead layer – if the dead layer in the background model is thicker than in reality, this could explain the suppression of the 46.5-keV peak relative to the x-rays. It is hard to imagine inaccuracies in the geometry model that could affect the intensity of the 87.3-keV x-ray peak but not the 72 to 75-keV x-rays, so the low intenstity of the 87.3-keV x-ray may be the result of under-production by GEANT4. These discrepancies between the measured and simulated energy spectra of ^{210}Pb from the lead patches help to explain why the Dataset II background model fit has a poor goodness of fit.

Many of the fit results shown in Figure 8.8 and Table 8.1 do not agree with the predicted values. For most contributions, this is not very worrisome because materials in the MALBEK cryostat were not assayed directly. One result that is concerning is for $2\nu\beta\beta$ in ^{76}Ge. This is a well-measured value and the fit result over-predicts the rate by approximately four sigma. It is possible that the broad, smooth spectrum is filling in for a missing contribution in the model, such as a beta spectrum, or that the number of ^{76}Ge counts would change if a different dead layer thickness were applied.

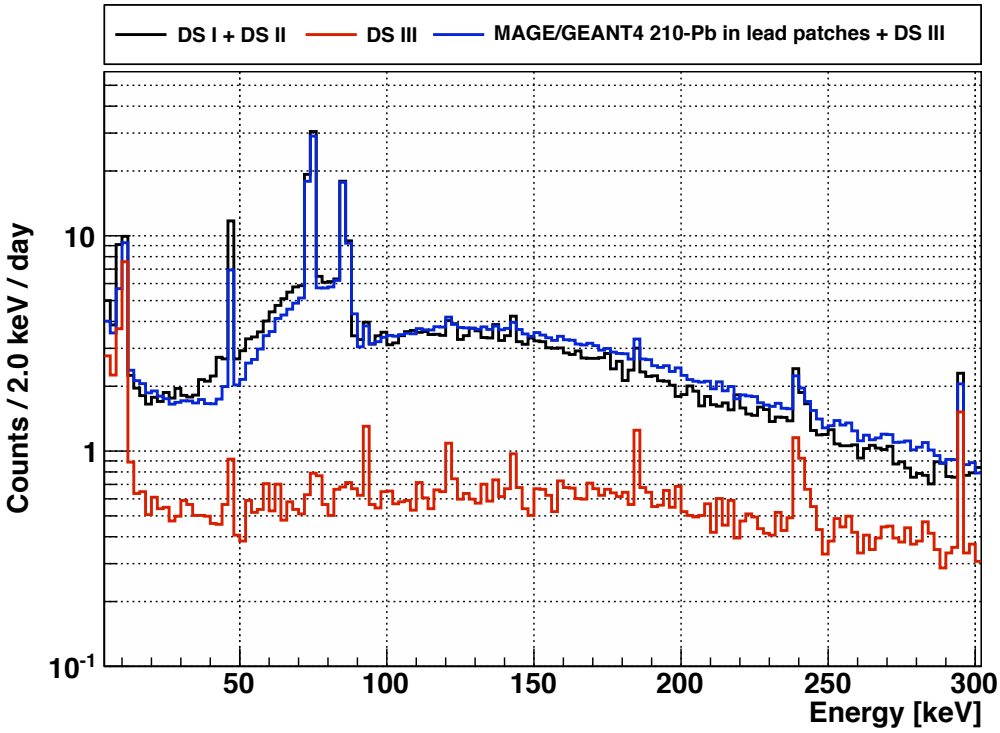

Figure 8.9: Comparison between simulated and measured energy spectra due to ^{210}Pb in the lead patches. The Datasets I and II energy spectra have been added to produce a high-statistics spectrum (black) measured while the lead patches were in place. The Dataset III spectrum (red) was measured after the lead patches were removed. The simulated spectrum of MALBEK response to ^{210}Pb in the patches has been added to the Dataset III spectrum (blue). The simulation results under-produce the intensity of the 46.5-keV ^{210}Pb gamma peak and show some discrepancies in the bremsstrahlung continuum.

Table 8.2: Peak intensities due to the lead patches, as measured at KURF and simulated with GEANT4. The first column contains published energies of Pb x-rays and the 46.5-keV ^{210}Pb gamma. The second column, R_{meas}, lists the count rate in each peak as measured in a combined spectrum from Datasets I and II. The third column, R_{sim}, contains the count rate predicted by the background model according to the ^{210}Pb activity in the lead patches calculated from Dataset I. R_{sim} also contains contributions from the Dataset III energy spectrum measured after the lead patches were removed. The contributions from Dataset III include any ^{210}Pb from sources other than the patches. The Dataset III contributions are small, so R_{sim} is dominated by the simulation results. In the final column, the difference is calculated between the measured and simulated count rates, $(R_{sim} - R_{meas})/R_{meas}$. For each peak listed, the count rate was found by integrating the region containing the peak and subtracting the count rate in regions of continuum surrounding the peak. Uncertainties are statistical. See the text for details.

E [keV]	**R_{meas} [cts/day]**	**R_{sim} [cts/day]**	**Diff. [%]**
46.54	9.0 ± 0.3	5.0 ± 0.1	-44.8 ± 3.0
72.81	13.1 ± 0.3	12.5 ± 0.1	-4.9 ± 2.7
74.97	24.3 ± 0.4	23.6 ± 0.1	-3.0 ± 1.8
84.45, 84.94	13.1 ± 0.3	13.1 ± 0.1	0.0 ± 2.6
87.30	3.9 ± 0.3	5.1 ± 0.1	28.9 ± 8.0

Chapter 9

DATASET III BACKGROUND MODEL

9.1 Introduction

The lead patches were removed on October 25, 2011. Dataset III begins with run 19019, on November 01, 2011, soon after the patches were removed, and ends with run 26122, in September 2012. There are 240.83 days of livetime. The Dataset III energy spectrum is compared to spectra from Datasets I and II in Figure 9.1. Prominent peaks in the energy spectrum are listed in Table C.3. One peak in the spectrum, near 344 keV, was not identified.

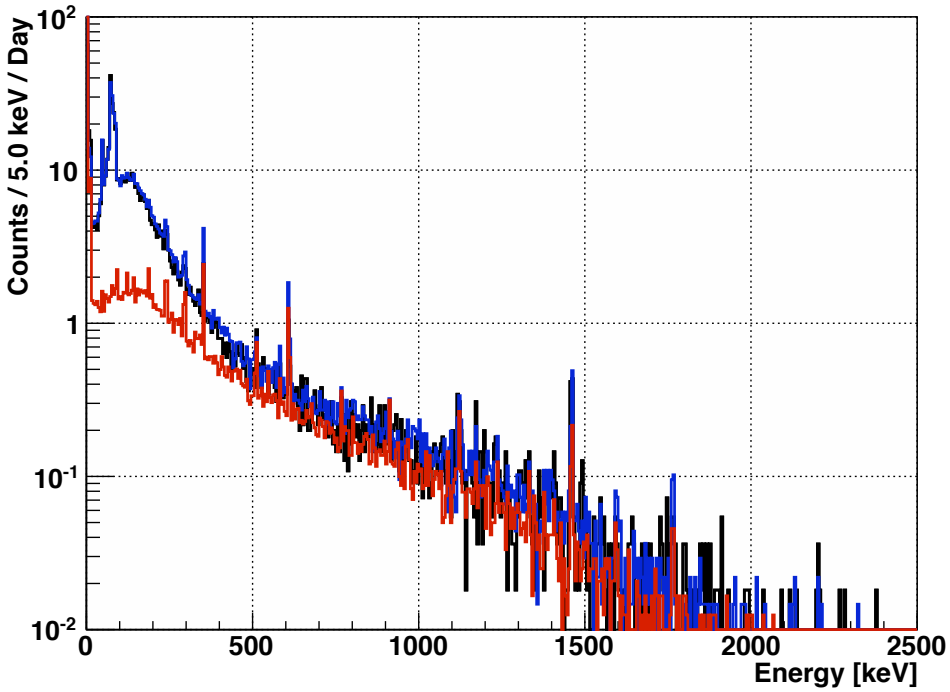

Figure 9.1: Comparison of ORCA/Struck Datasets I, II, and III energy spectra. The energy spectra from Dataset I (black), Dataset II (blue), and Dataset III (red) are shown after timing cuts and the combined slow pulse cut.

Figure 9.2 shows the energy spectra at low energies. The 8.98-keV, 9.66-keV, and 10.37-keV peaks are due to decays of ^{65}Zn, ^{68}Ga, and ^{68}Ge, respectively, which were produced by cosmogenic activation of the germanium crystal while MALBEK was on the earth's surface.

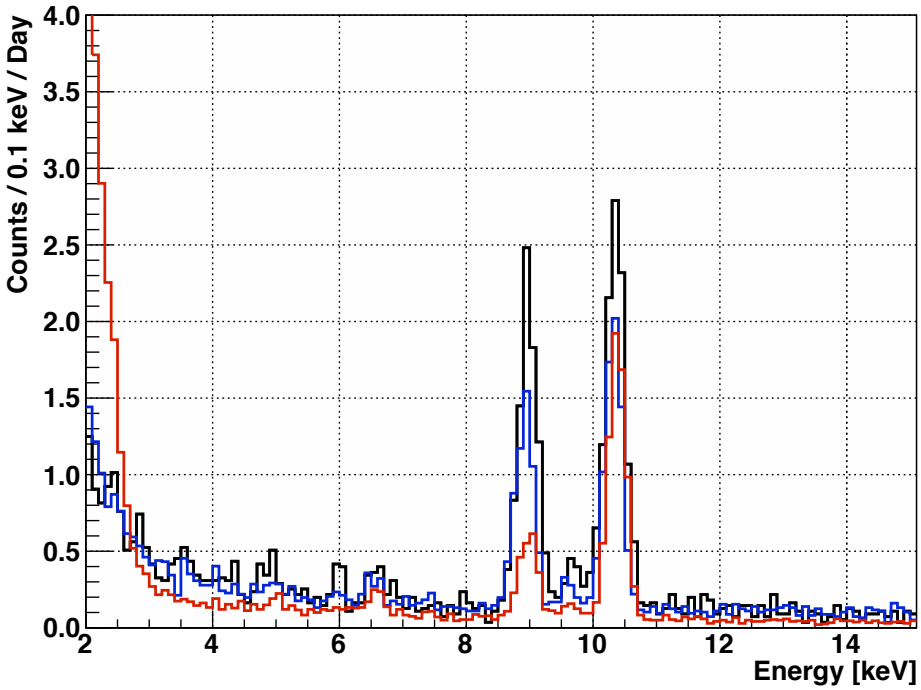

Figure 9.2: Comparison of ORCA/Struck Datasets I, II, and III energy spectra at low energies. The energy spectra from Dataset I (black), Dataset II (blue), and Dataset III (red) are shown after timing cuts and the combined slow pulse cut. In MALBEK's unamplified (high-energy) channel, the slow-pulse cut breaks down for energies below 5 keV, which contributes to the rise at low energy.

During the trip to CANBERRA, MALBEK was above ground for 2 days, 19 hours, and 30 minutes [58]. Dataset III data taking started within 5 days of the trip. During the time on the surface, cosmogenically activated isotopes were produced in the copper and germanium. Figure 9.3 shows the count rate in the 10.4-keV Ge x-ray peak as a function of time since the start of Dataset III. In Datasets I and II, MALBEK had been underground for more than 200 days by the time of data taking. This was long enough for relatively

short-lived cosmogenics to decay, including ^{69}Ge, with a half-life of 39.05 hours, and ^{71}Ge, with a half-life of 11.43 days. The isotopes ^{69}Ge and ^{71}Ge were not included in the Dataset I and II background models, but they are included in the Dataset III model. Cosmogenic production rates of 140 ^{69}Ge atoms/kg/day and 250 ^{71}Ge atoms/kg/day were used. These values were based on calculations by V. Guiseppe that used the TALYS nuclear reaction code [95].

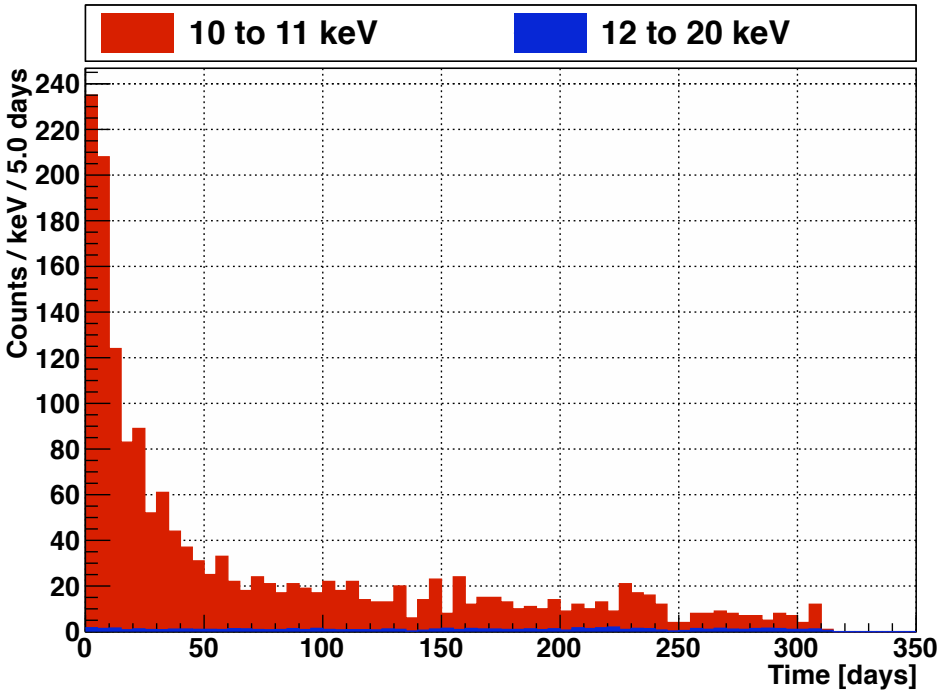

Figure 9.3: Count rate in the 10.4-keV Ge peak as a function of time. The rate in a 1-keV region surrounding the peak is compared to the rate per keV in an 8-keV continuum above the peak.

9.2 Neutrons at KURF

The thermal neutron flux at KURF can be measured using using a method proposed by Škoro et al. [96]. The method relies on the rate in the 139.7-keV ^{75m}Ge peak produced by neutron capture on ^{74}Ge to estimate the neutron flux:

$$\phi = \frac{980\, I_{139}}{(\epsilon^{\gamma}_{139} + 1.6)\ V} \tag{9.1}$$

where I_{139} is the measured count rate in the 139.7-keV peak, in counts per second, V is the volume of the detector, in cm^3, and ϵ^{γ}_{139} is given by:

$$\epsilon^{\gamma}_{139} = 1 - \frac{1 - \exp(-V^{1/3})}{V^{1/3}} \tag{9.2}$$

We can look for an excess of counts around 139.7-keV compared to the surrounding continuum. The energy resolution, $\sigma(E)$, at 139.7 keV is 0.26 keV for Dataset III. In the region within $\pm$ 3σ of 139.7 keV, there are 110 counts. In the two 3σ-wide regions immediately above and below this region, there are 128 counts. The signal and sideband regions are shown in Figure 9.4. Using the Feldman Cousins method [97], there is an upper limit of 5.87 counts (90% CL) in the signal region.

Using Equation 9.1, the 240.83-day livetime of Dataset III, and the crystal volume of 75.93 cm^3, we can set an upper limit on the thermal neutron flux within the MALBEK lead and polyethylene shielding:

$$\text{thermal neutron flux} < 3.98 \times 10^{-5}\text{cm}^{-2}\text{s}^{-1}(90\%\ \text{CL}) \tag{9.3}$$

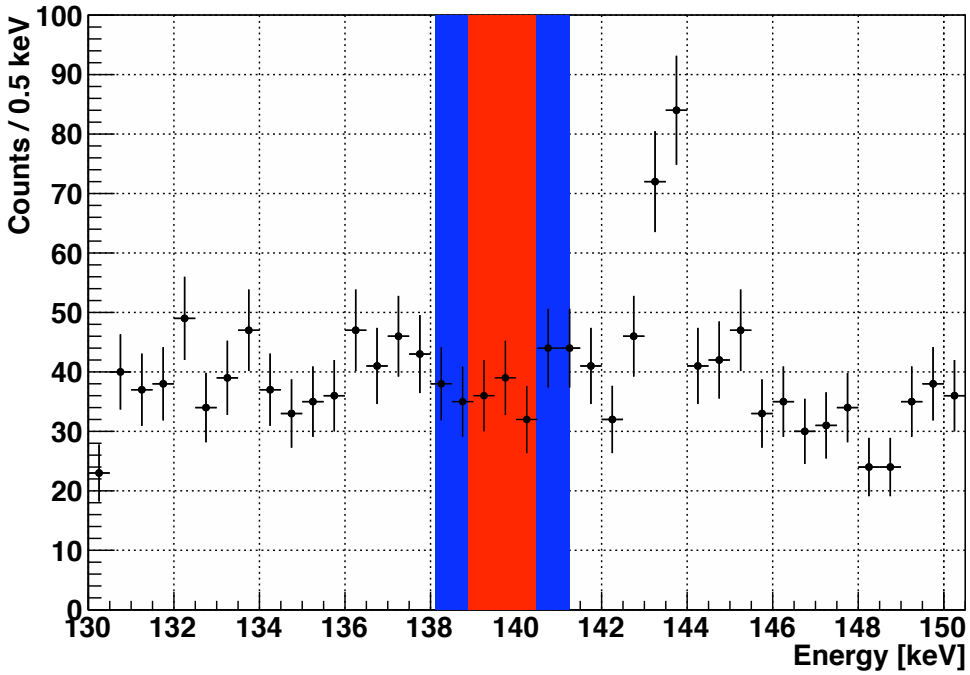

Figure 9.4: The region near the 139.7-keV ^{75m}Ge peak. Counts in the signal region (red) and sidebands (blue) were used to determine an upper limit on the neutron flux. Primordial ^{230}Th and cosmogenic ^{57}Co contribute to the peak at 143 keV.

9.3 Notes about unblinding

Dataset III was prepared according to the process described in Section 4.5, with the modifications discussed in Section 8.2. Cosmogenic contributions of ^{69}Ge and ^{71}Ge in the germanium were added.

9.4 Background model results

The background model prediction for Dataset III is shown in Figure 9.5. The predicted energy spectrum is based on the cosmogenic activation history, the run start and stop time, the energy resolution of Dataset III, as listed in Table A.1, and the radiopurity data in Appendix J. The prediction is compared to the measured Dataset III spectrum in Figure 9.6. The predicted spectrum under-predicts the measurement by 42%. This seems reasonable, given that the prediction is based on literature values of typical contamination in materials, and not on direct assay of the MALBEK components.

The contribution of each contaminant was then allowed to float in a fit; results are shown in Figure 9.7 for the entire fit region, between 10 and 2000 keV. In Figure 9.8, the results are shown in more detail in the region between 10 and 500 keV. The fit is in good agreement with the spectrum measured at KURF: χ^2 is 97.15 per 114 degrees of freedom, for a P-value of 0.87. Figure 9.9 shows the largest contributions to the fit result – those fit components that were found to contribute more than 200 counts to the fit region.

In Figure 9.10, the number of counts found by the fitter are compared to the number of counts predicted from material radiopurity information. The 23 spectra found to contribute more than 200 counts are shown. This information is also listed in Table 9.1. The full fit results are listed in Table L.5. As in the Dataset II result, the number of counts from $2\nu\beta\beta$ of ^{76}Ge is over-predicted. Correlations between fit parameters are shown in Figure L.36 and listed in Table L.6.

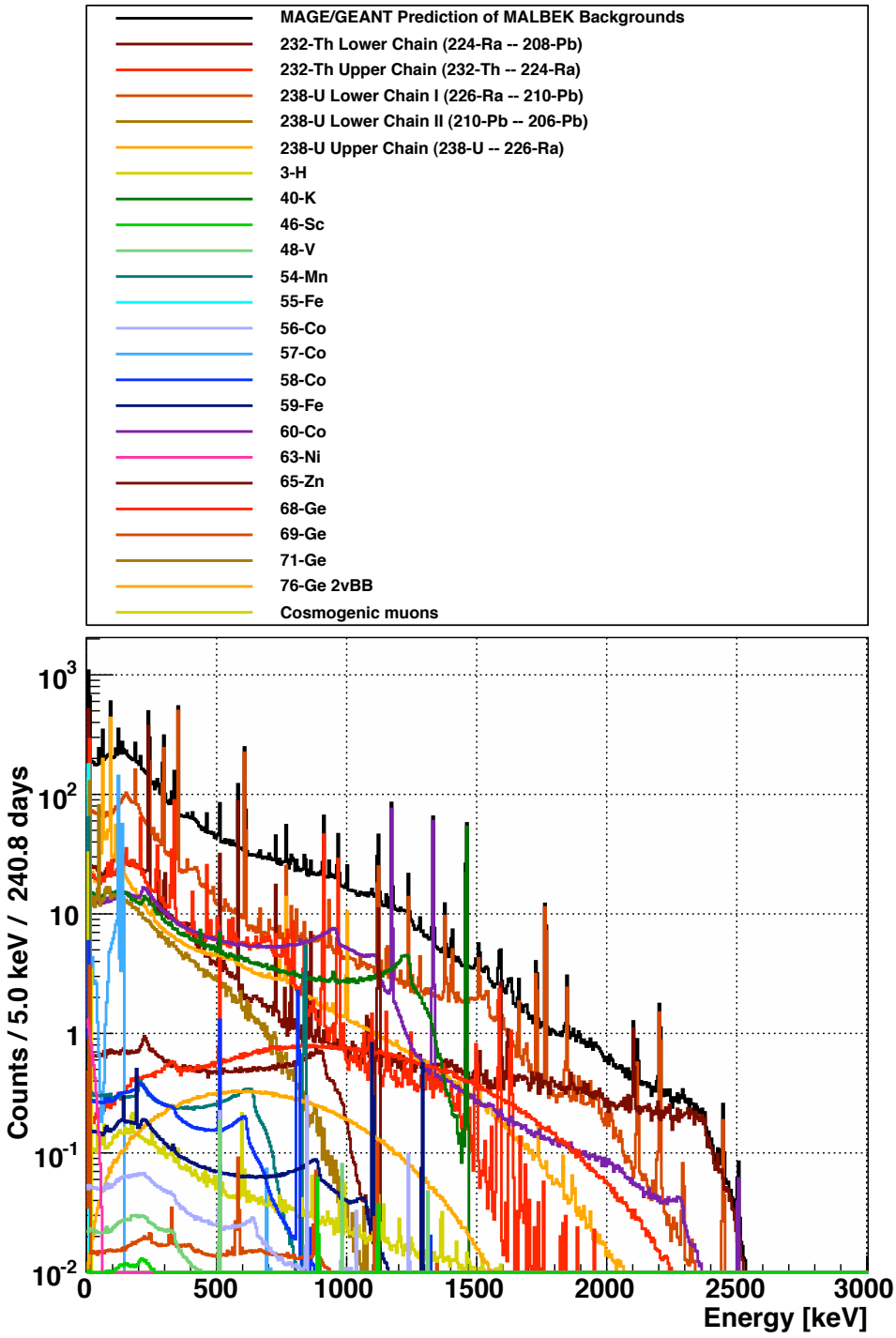

Figure 9.5: Predicted Dataset III energy spectrum.

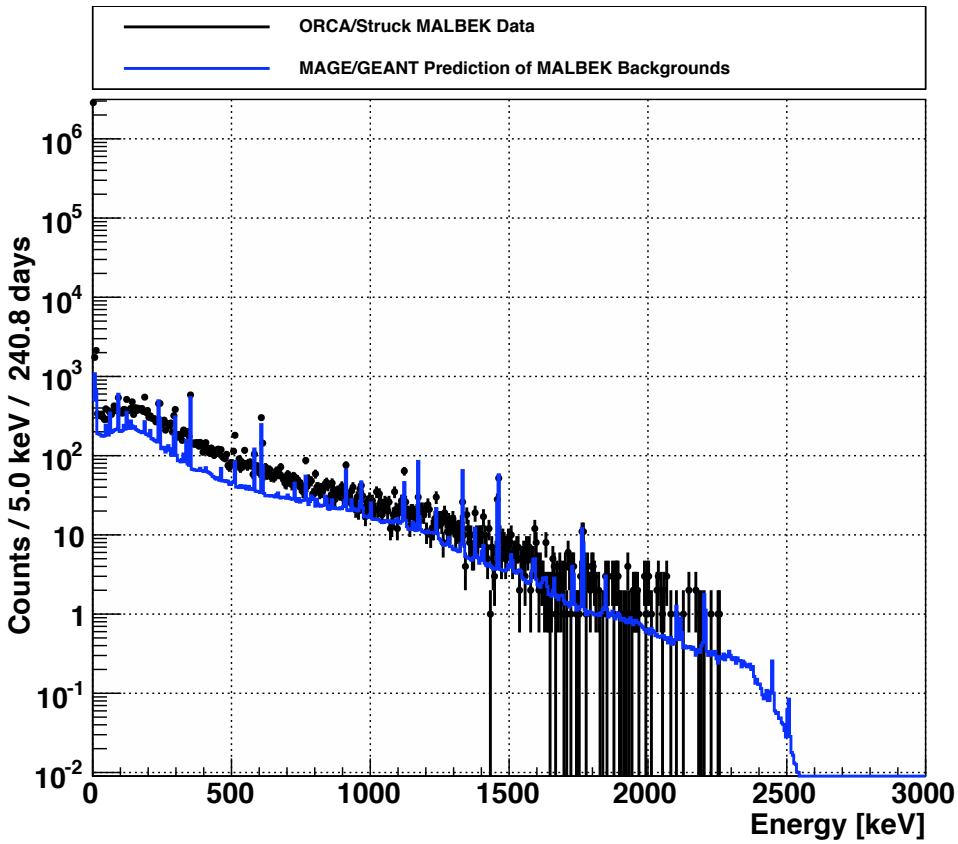

Figure 9.6: Comparison of measured Dataset III energy spectrum to the background model prediction based on material radiopurity data.

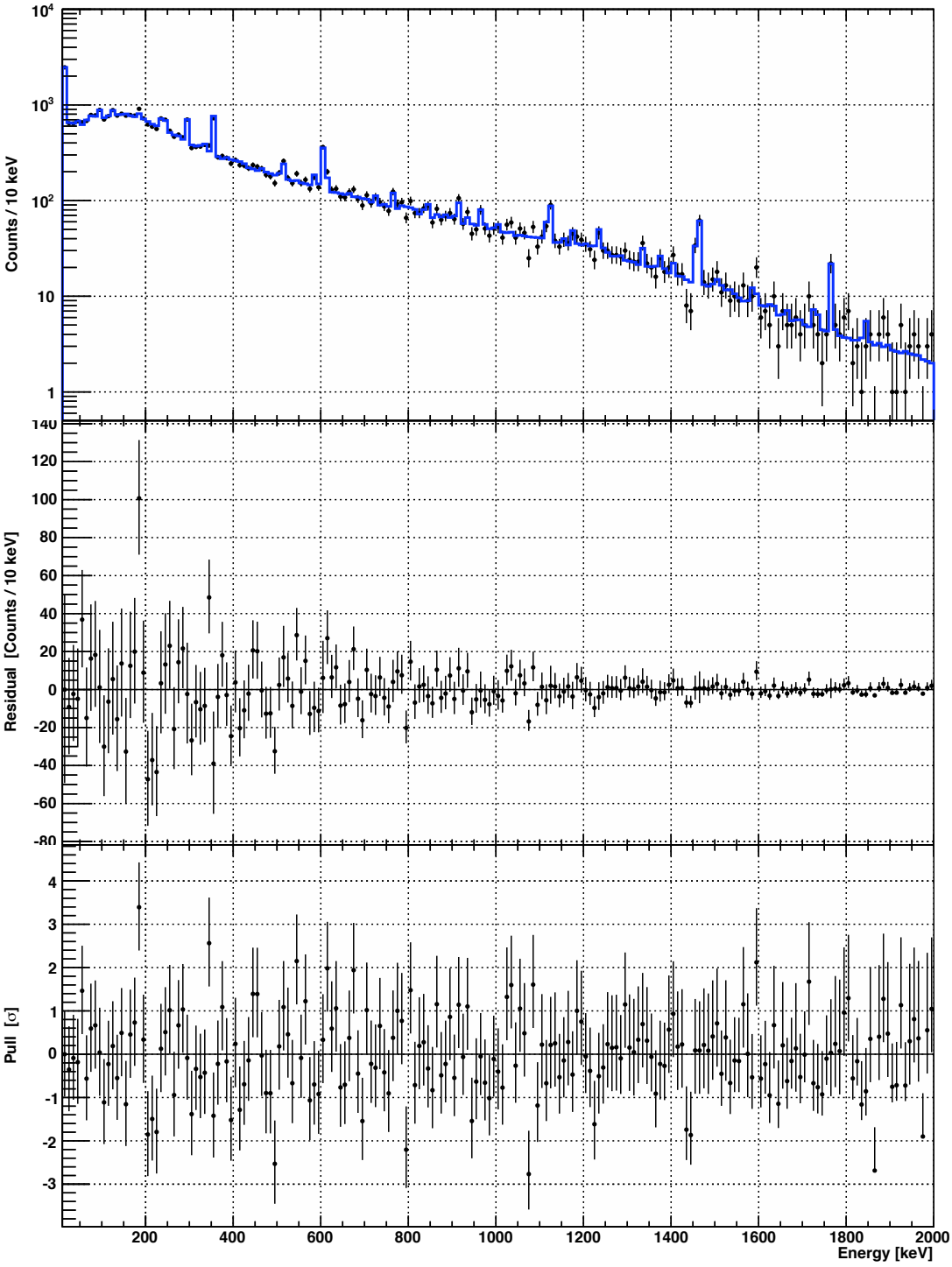

Figure 9.7: Results of background model fit to the Dataset III energy spectrum. The fit gives χ^2 of 97.15 per 114 degrees of freedom, for a P-value of 0.87.

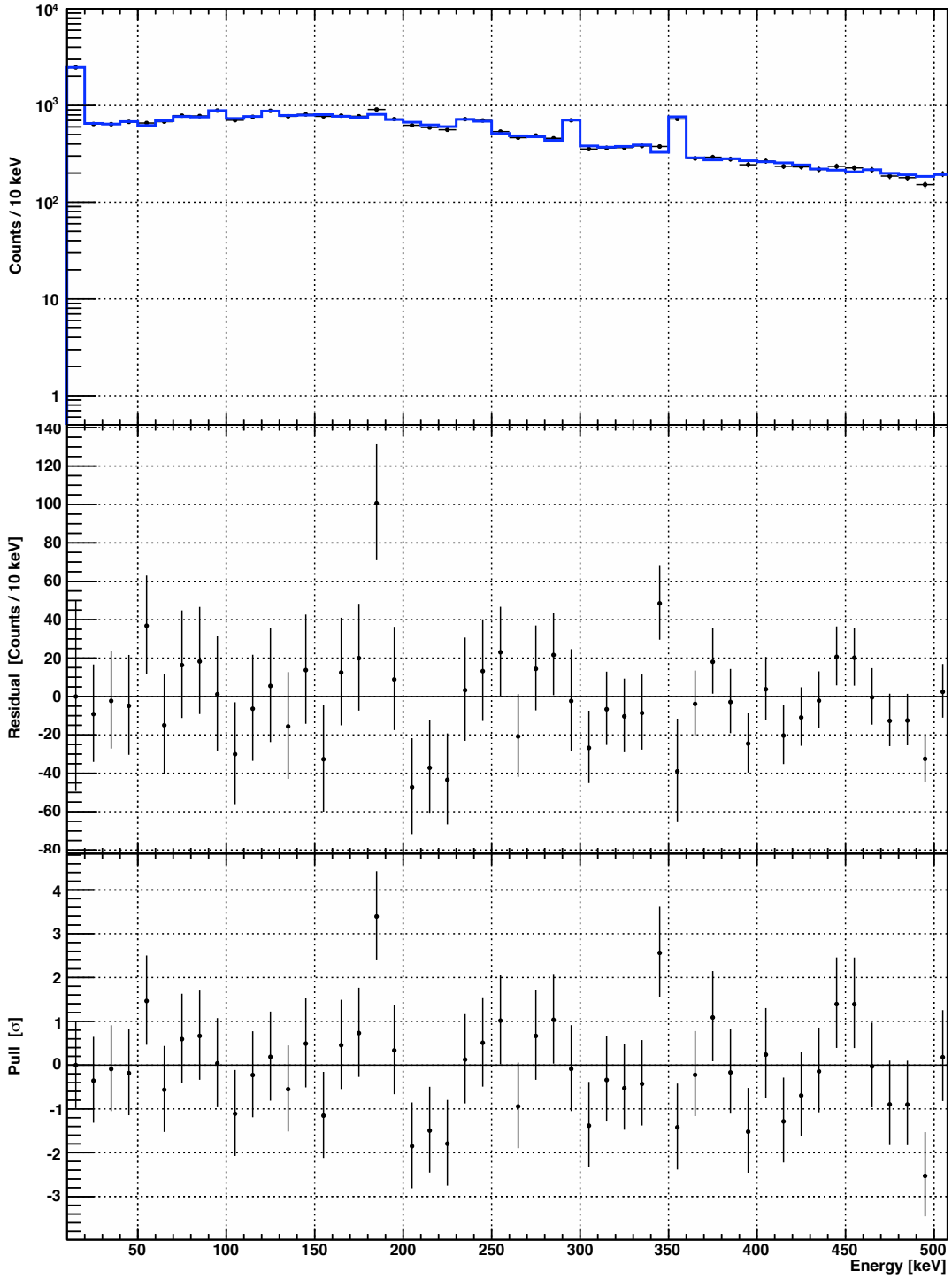

Figure 9.8: Results of background model fit to Dataset III, shown for energies below 500 keV.

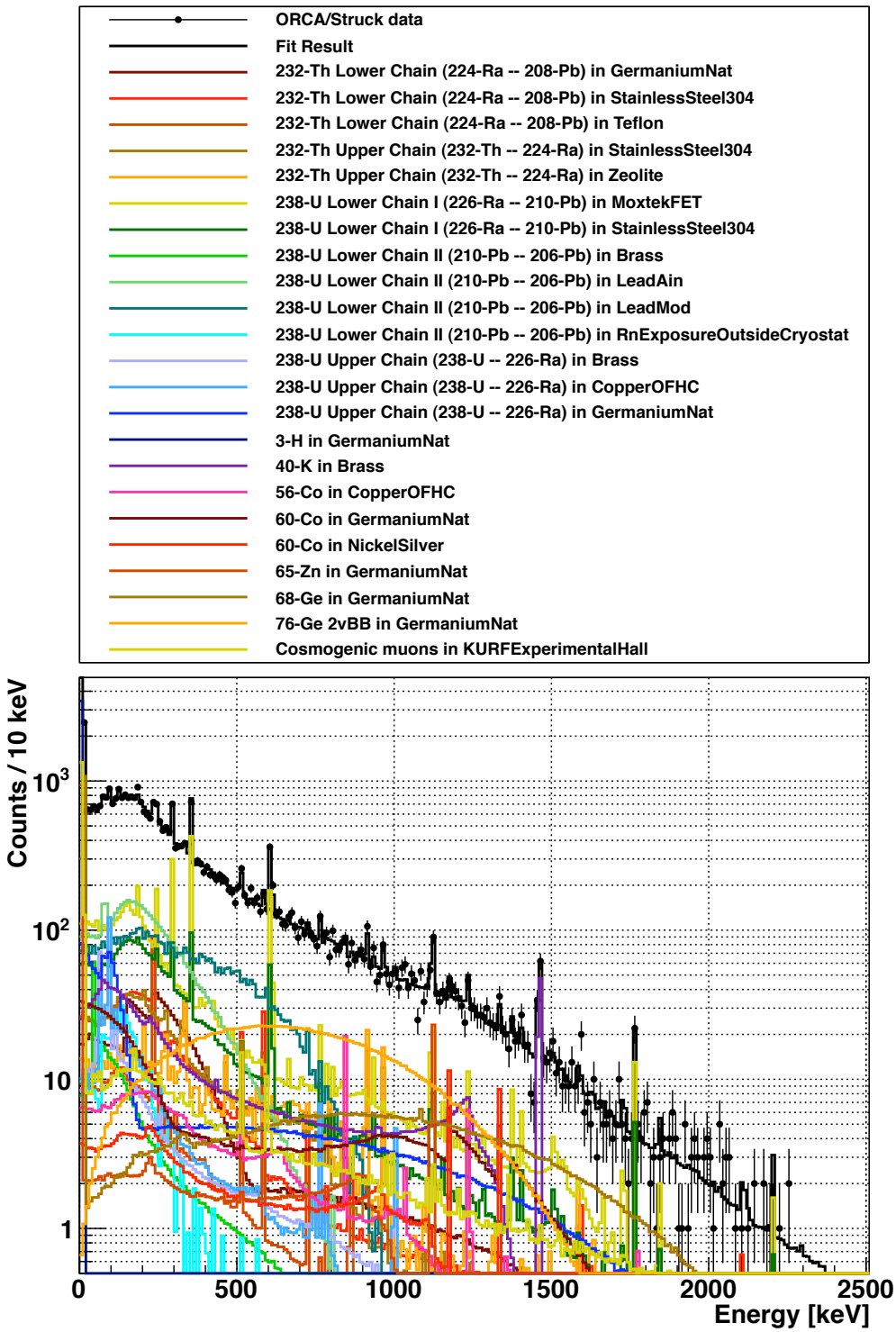

Figure 9.9: Significant contributions to background model fit of the Dataset III energy spectrum. The 23 PDFs found by the fitter to contribute more than 200 counts are shown.

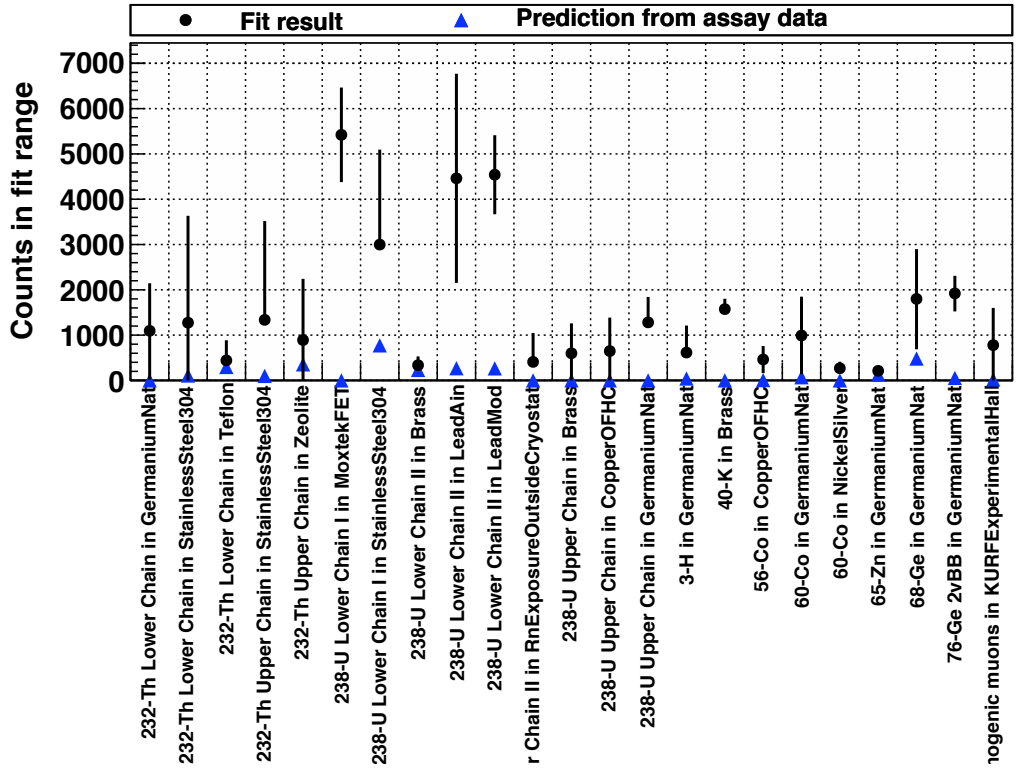

Figure 9.10: Numbers of counts found from fit of background model to the Dataset III energy spectrum. The 23 PDFs found by the fitter to contribute more than 200 counts are shown.

Table 9.1: Selected results from fit of background model to Dataset III energy spectrum. The fit was performed in the region from 10 to 2000 keV, using 10-keV bins. The first column of the table is an index used to identify the fit components. The third column is the number of counts expected from the predicted background energy spectrum. Spectra that were found by the fitter to contribute more than 200 counts are listed.

	Description	**Prediction**	**Fit Result**
3	232-Th LC in GermaniumNat	3.90×10^{-2}	$\left(1.10\ ^{+1.05}_{-1.07}\right) \times 10^{3}$
7	232-Th LC in StainlessSteel304	1.09×10^{2}	$\left(1.27\ ^{+2.36}_{-2.36}\right) \times 10^{3}$
8	232-Th LC in Teflon	2.97×10^{2}	$\left(4.42\ ^{+4.44}_{-0.00}\right) \times 10^{2}$
17	232-Th UC in StainlessSteel304	9.98×10^{1}	$\left(1.34\ ^{+2.18}_{-0.00}\right) \times 10^{3}$
19	232-Th UC in Zeolite	3.55×10^{2}	$\left(8.91\ ^{+13.51}_{-13.51}\right) \times 10^{2}$
25	238-U LC I in MoxtekFET	1.26×10^{-2}	$\left(5.42\ ^{+1.04}_{-1.04}\right) \times 10^{3}$
28	238-U LC I in StainlessSteel304	7.74×10^{2}	$\left(3.00\ ^{+2.10}_{-0.00}\right) \times 10^{3}$
33	238-U LC II in Brass	2.31×10^{2}	$\left(3.36\ ^{+1.94}_{-0.00}\right) \times 10^{2}$
36	238-U LC II in LeadAin	2.69×10^{2}	$\left(4.46\ ^{+2.31}_{-2.31}\right) \times 10^{3}$
37	238-U LC II in LeadMod	2.66×10^{2}	$\left(4.54\ ^{+0.87}_{-0.87}\right) \times 10^{3}$
42	238-U LC II in RnExposureOutsideCryostat	8.37×10^{-2}	$\left(4.09\ ^{+6.39}_{-0.00}\right) \times 10^{2}$
48	238-U UC in Brass	2.30×10^{0}	$\left(5.99\ ^{+6.60}_{-6.60}\right) \times 10^{2}$
49	238-U UC in CopperOFHC	4.72×10^{-1}	$\left(6.48\ ^{+7.38}_{-7.38}\right) \times 10^{2}$
50	238-U UC in GermaniumNat	1.64×10^{-1}	$\left(1.28\ ^{+0.56}_{-0.00}\right) \times 10^{3}$
57	3-H in GermaniumNat	4.21×10^{1}	$\left(6.15\ ^{+5.97}_{-0.00}\right) \times 10^{2}$
58	40-K in Brass	8.62×10^{-1}	$\left(1.57\ ^{+0.23}_{-0.00}\right) \times 10^{3}$
67	56-Co in CopperOFHC	7.45×10^{0}	$\left(4.62\ ^{+2.96}_{-3.00}\right) \times 10^{2}$
75	60-Co in GermaniumNat	7.00×10^{1}	$\left(9.91\ ^{+8.58}_{-8.53}\right) \times 10^{2}$
76	60-Co in NickelSilver	6.68×10^{-1}	$\left(2.69\ ^{+1.43}_{-0.00}\right) \times 10^{2}$
79	65-Zn in GermaniumNat	1.31×10^{2}	$\left(2.12\ ^{+0.00}_{-1.00}\right) \times 10^{2}$
80	68-Ge in GermaniumNat	4.83×10^{2}	$\left(1.80\ ^{+1.10}_{-1.11}\right) \times 10^{3}$
83	76-Ge 2vBB in GermaniumNat	5.51×10^{1}	$\left(1.92\ ^{+0.39}_{-0.40}\right) \times 10^{3}$
84	Cosmogenic muons in KURFExperimentalHall	2.04×10^{1}	$\left(7.79\ ^{+8.22}_{-8.22}\right) \times 10^{2}$

Chapter 10

IMPLICATIONS AND CONCLUSIONS

10.1 Introduction

MAJORANA has a background goal for the DEMONSTRATOR of less than three counts per tonne-year of exposure in an energy region of interest surrounding the $0\nu\beta\beta$ Q-value. This is approximately one-hundred times lower than background rates reported in earlier germanium detector experiments. Projections of the DEMONSTRATOR's sensitivity are based on a model of the background energy spectrum. The background model relies on assay of materials used in the experiment, the history of exposure of DEMONSTRATOR components to cosmogenic activation, and Monte Carlo simulations. MAJORANA collaborators operate a research and development detector, MALBEK, in a shielded clean underground environment in Virginia. Background studies with MALBEK can help to inform the DEMONSTRATOR background model.

This dissertation has described the construction of a background model for the MALBEK detector. Chapters 2 through 5 described the software and data processing used to produce measured energy spectra from KURF and to simulate MALBEK's response to backgrounds. Chapter 6 described measurement of the germanium crystal's n^+ dead layer and showed that energy spectra collected with MALBEK at KURF were well-reproduced by simulation results. Chapters 7 through 9 presented three shielded background energy spectra measured at KURF and compared these spectra to results of the background model. This work has shown that a background model based on Monte Carlo results and material radiopurity information can be used to explain a germanium detector background energy spectrum.

Energy spectra measured at KURF in 2010 indicated a source of ^{210}Pb contamination near the MALBEK detector. Results from the MALBEK background model helped to identify lead patches within the cryostat as the source of contamination. UNC collaborators brought MALBEK to CANBERRA in Meriden, Connecticut, where the cryostat was opened

and the lead patches were removed and replaced with Teflon. The background model was essential for identifying the unexpected contamination and for convincing collaborators to open the cryostat, which carried some risk for the detector. An energy spectrum collected after the CANBERRA trip confirmed that the patches were the source of contamination and showed that the detector was unharmed by opening the cryostat. Results from this analysis and implications for the MAJORANA DEMONSTRATOR are discussed in this chapter.

10.2 Summary of results

The history of MALBEK's cosmogenic exposure, time underground, and energy-spectrum measurements is shown in Figure 10.1. A total of 433 days of shielded background data were analyzed. The shielded background data were divided into Datasets I, II, and III, of 55, 137, and 241 days of livetime, respectively. Dataset I was an open dataset, used to develop the background modeling software and to identify the lead patches as the most likely source of contamination. Dataset II was collected after Dataset I and before removal of the lead patches; it contains higher statistics. Dataset III was collected after the patches were removed. Datasets II and III were blinded until analysis of Dataset I was finished.

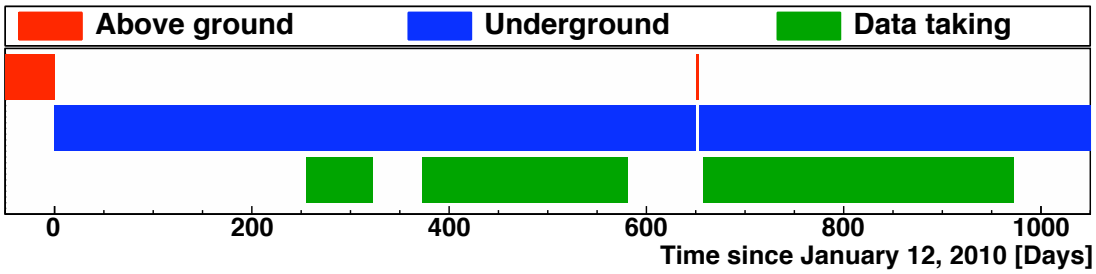

Figure 10.1: A timeline of MALBEK's history of activation and data taking. Day zero is January 12, 2010, when MALBEK was first taken underground at KURF. For the purpose of this plot, only 50 days of activation are shown before day zero. The actual exposure was much longer. The short duration of activation around day 650 is the trip to CANBERRA. The three instances of data taking represent Datasets I, II, and III.

Before removal of the lead patches, the background model predicted the integral count rate between 5 and 3000 keV within 20% of the measured rate. The background model is compared to Datasets I and II in Figures 7.3 and 8.4, respectively. The normalization of the background model prediction was largely based on radiopurity data found in the literature, but the activity of the lead patches was an estimate based on the observed energy spectrum. The normalization of the background model components was then allowed to fluctuate in a fit. The fit confirmed that the patches were the source of ^{210}Pb contamination. The fit of the Dataset I spectrum determined the activity of the patches to be $91.6^{+1.2}_{0.0}$ Bq/kg; the Dataset II fit produced a consistent activity of $92.9^{+0.7}_{-0.8}$ Bq/kg. The Dataset I fit was good, with χ^2 of 132.81 per 115, a P-value of 0.12. The Dataset II had a poor goodness of fit: χ^2 of 186.15 per 115, a P-value of 3.00E-05. Uncertainty in the dead layer and issues with GEANT4, described in Section 7.6.1 and later in this chapter, may have contributed to the poor Dataset II goodness of fit.

The unblinding of Dataset II revealed some software and hardware issues, which are described in Section 8.2. As a result, more stringent cuts were developed for generating datasets, and a minor bug was corrected in the background modeling software.

After the lead patches were removed, the background model spectrum predicted the integral count rate between 5 and 3000 keV within 42% of the measured rate, as shown in Figure 9.6. This agreement is reasonable given that the predicted spectrum was largely based on radiopurity data found in the literature for typical materials. When the normalization of the background model contributions were allowed to float in a fit to the measured energy spectrum, the goodness of fit was good: χ^2 of 97.15 per 114, a P-value of 0.87. These results should be interpreted cautiously, however, because the number of counts attributed to $2\nu\beta\beta$ of ^{76}Ge by the fitter was significantly larger than the known value. Issues affecting this result are discussed in the following sections.

The MALBEK background model was useful for identifying the lead patches as the source of ^{210}Pb contamination. If an unexpected source of contamination is discovered in the DEMONSTRATOR, it may be possible to pinpoint the responsible component with techniques similar to those used for MALBEK. After determining the isotope(s) responsible for the contamination, it would be necessary to identify components of the DEMONSTRATOR

that could be contaminated. Simulations of DEMONSTRATOR response to contamination of each component should be performed. It may be sufficient to compare the simulated energy spectra to the measured energy spectrum – relative peak heights and features of the spectra may identify the responsible component. Fits of the spectrum may also be performed, as described in Section 7.5.

10.3 Lessons learned from MALBEK data taking

While collecting data from MALBEK, we encountered several issues with the detector and data acquisition system. Information about our experiences may be useful for the MAJORANA DEMONSTRATOR and other experiments. The issues are summarized in Table 10.1 and described in detail below.

10.3.1 Slow pulses

Slow, energy-degraded pulses have been observed in germanium detectors for many years. Recent studies have highlighted the importance of understanding these waveforms, especially for dark matter germanium experiments. This is an active area of research for MAJORANA and GERDA. Slow pulses were observed throughout the MALBEK energy spectrum, as shown in Figures 4.14, 10.2, 10.3, and Table 10.2.

Section 4.6 described a cut to remove slow pulses from the energy spectrum. This cut combined two measures of the rise time: one that worked well for mitigating electronics noise at low energies and one that avoided misidentifying fast multi-site events at high energies. This analysis of MALBEK data considered the energy spectrum between 5 keV and approximately 3 MeV. For the DEMONSTRATOR, it will be important to understand the energy spectrum at higher energies, including the 8 and 9 MeV alphas from the ^{232}Th and ^{238}U chains. It may be necessary to develop new methods for identifying slow pulses across this energy region.

The slow pulse cut used in this analysis was shown to produce ^{133}Ba and ^{60}Co energy spectra that were well-described by Monte Carlo simulation results. For the DEMONSTRATOR, it would be useful to study slow pulse identification using other sources, possibly ^{208}Tl and ^{214}Bi, to establish performance of a slow-pulse cut at high energies and for backgrounds

Table 10.1: Issues encountered during MALBEK data taking. Estimates of effects on the energy spectrum are given.

Issue	**Effect**
Slow pulses	Contributions to energy-spectrum continuum at all energies, affecting 8–20% of counts between 5 keV and 3 MeV for measured spectra
Uncertainty in dead layer thickness	Uncertainty in background spectral shapes and intensities, e.g. 15% uncertainty in flux of 50-keV gammas through the n^+ dead layer
Digitizer non-linearities	Peak offsets of up to 0.3 keV
Various digitizer issues	Duplicate waveforms, down time of the data acquisition system
Degradation of energy resolution	Broadening of gamma peaks by a factor of two at 1.5 MeV in energy spectra collected over long time spans
Reset preamplifier	Energy-spectrum cutoff at 2.7 MeV; decreasing efficiency with increasing energy, including less than 25% efficiency above 2 MeV; associated 5% dead time

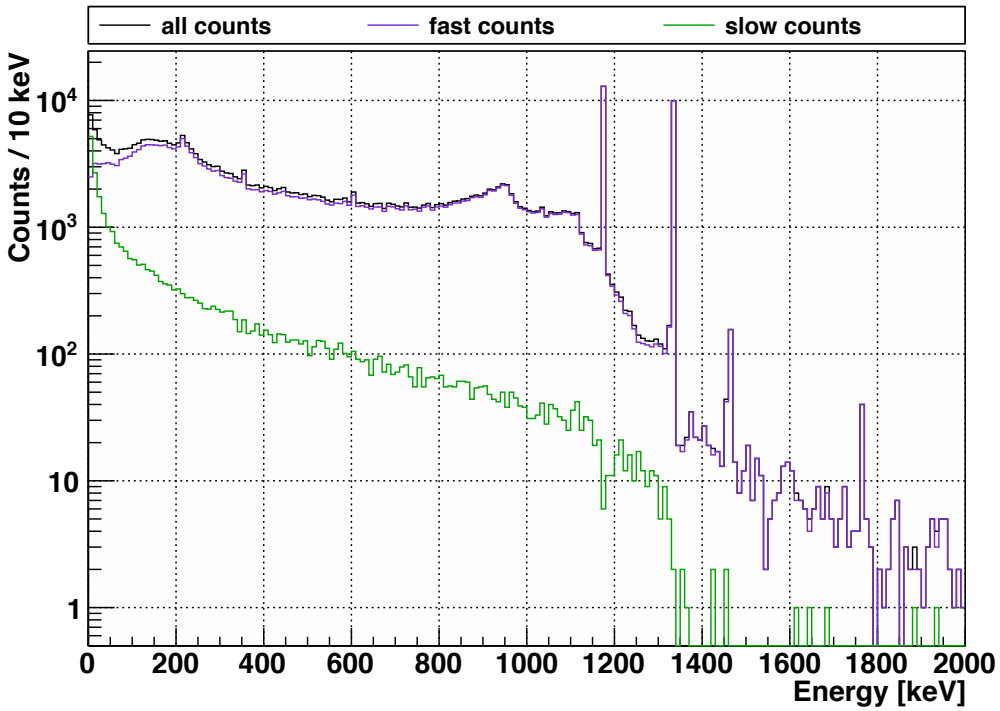

Figure 10.2: The distribution of slow and fast pulses in a ^{60}Co spectrum measured at KURF. Above 5 keV, $8.98 \pm 0.05\%$ of counts are slow pulses. In the region above 1 MeV, which is dominated by the 1172 and 1333-keV ^{60}Co peaks, only $1.57 \pm 0.06\%$ of counts are slow.

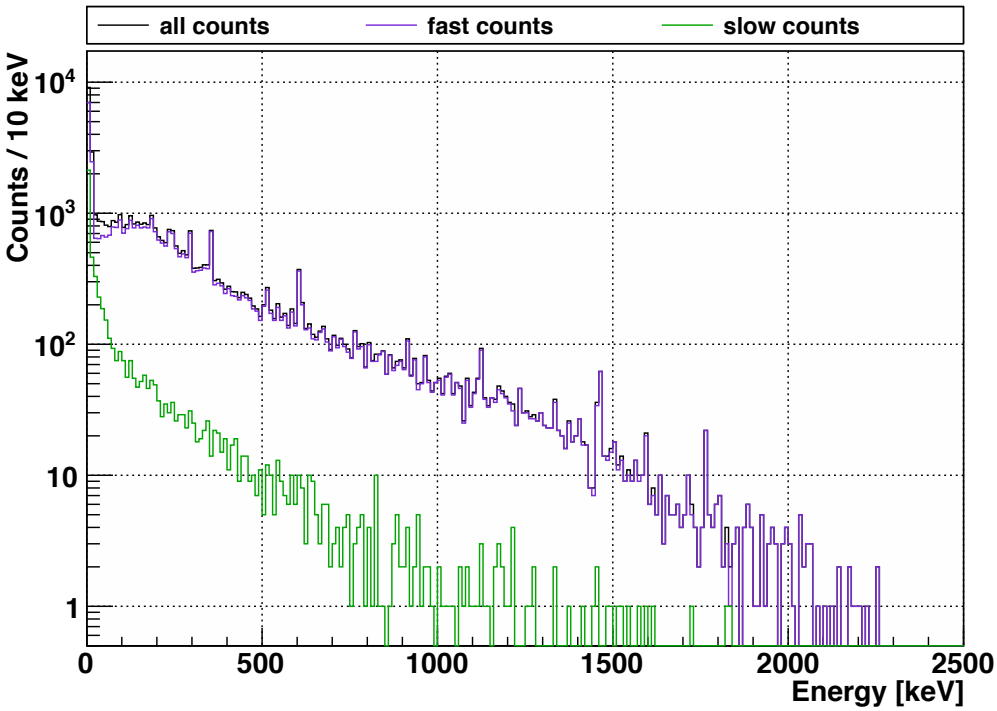

Figure 10.3: The distribution of slow and fast pulses in the Dataset III energy spectrum. Above 5 keV $9.08 \pm 0.15\%$ of counts are slow pulses; $2.63 \pm 0.36\%$ of counts above 1 MeV are slow.

Table 10.2: The contribution of slow pulses to the energy spectrum of various datasets. The percentage of counts that are slow in three regions of the energy spectra are listed. The slow pulse cut described in Section 4.6 was used to identify slow pulses.

Dataset	**5–3000 keV**	**5–1000 keV**	**1000–3000 keV**
Unshielded backgrounds	8.59 ± 0.04	8.86 ± 0.04	2.00 ± 0.11
^{133}Ba source	9.18 ± 0.04	9.21 ± 0.04	2.34 ± 0.28
^{60}Co source	8.98 ± 0.05	10.32 ± 0.06	1.57 ± 0.06
Dataset I	19.64 ± 0.23	19.97 ± 0.23	2.95 ± 0.64
Dataset II	19.28 ± 0.14	19.62 ± 0.15	2.15 ± 0.34
Dataset III	9.08 ± 0.15	9.42 ± 0.16	2.63 ± 0.36

of interest. It would also be useful to characterize the efficiency of a slow-pulse identification algorithm using pulses with known rise times and amplitudes. If a variety of rise times and amplitudes are used, it should be possible to perform a detailed characterization of the efficiency of a cut for accepting fast pulses and rejecting slow pulses. This could help to understand whether any energy-spectrum distortion might result from a slow-pulse cut.

10.3.2 Uncertainty in dead layer thickness

The MALBEK dead layer was measured as 0.933 ± 0.094 using a ^{133}Ba source. The precision of this measurement was limited by uncertainties in the length of the MALBEK germanium crystal and thickness of the copper cup and end cap. The 11% uncertainty in the dead layer thickness does not have much effect on high-energy gammas entering the germanium crystal, but it does a significant effect on low-energy gammas and other radiation that are attenuated by the dead layer. Due to the uncertainty in the dead layer thickness, the intensity of a 50-keV gamma can only be determined to within 15%. It is important that MAJORANA understand the entire DEMONSTRATOR energy spectrum to identify ^{68}Ge

decays and perform a low-energy WIMP dark matter search. Making precise measurements of the dimensions and dead layers of the DEMONSTRATOR crystals *before* they are in the copper cryostats is critical.

The thickness of dead layers on the MALBEK point contact and the surface surrounding the point contact were not characterized in this analysis because they were shielded from calibration sources by many copper parts. Dead layers on these surfaces would affect the energy spectra produced by backgrounds in the region of the front-end electronics. The DEMONSTRATOR germanium crystals will be characterized in dedicated test cryostats before being deployed into the DEMONSTRATOR. During detector characterization, it would be useful to measure dead layer thickness at several points on the germanium crystals. It may be useful to insert calibration sources into the test cryostats, to minimize the amount of material between the source and germanium crystals. Such studies have been performed previously by MAJORANA Collaborators, as described by R. A. Johnson [98].

A good understanding of the slow pulse cut and of the germanium dead layers are needed to obtain agreement between measured energy spectra and simulation results. Active investigation of germanium crystal dead layers is ongoing within MAJORANA and GERDA and is leading to better understanding of effects of the dead layers.

10.3.3 The Struck SIS3302 digitizer

The calibration of MALBEK energy spectra was complicated by non-linearities in the Struck digitizer, described in Section 4.7.2. These non-linearities caused peak offsets of up to 0.3 keV at some energies. The offsets in peak centroids make peak identification more difficult and could contribute to discrepancies between measured and simulated energy spectra. Efforts by MAJORANA Collaborators are underway to understand and mitigate these issues.

Early efforts for MALBEK data taking were complicated by issues with the digitizer, including duplicated waveforms and issues with digitizer dead time. Ongoing development of the data acquisition software continues to improve the digitizer's performance. The 0.1 Hz periodic pulser was invaluable for identifying affected runs and for studying changes in the detector over time.

10.3.4 Degradation of energy resolution

The energy resolution of a germanium detector is often described by Equation 4.5, which includes the effects of electronics noise and the Fano factor. The ^{133}Ba and ^{60}Co datasets collected over short time spans are well-described by this equation, as described in Section 4.7.3 and shown in Figures 4.19 and 4.20. At high energies, above approximately 1 MeV, the effect of charge carrier statistics dominates and the width of observed peaks increases as the square root of the peak energy.

Energy spectra measured with MALBEK over periods of data-taking lasting several hours obtained better energy resolution than energy spectra measured over many days. For example, the energy resolution, σ, of a ^{40}K peak at 1461-keV was approximately 0.7 keV in the ^{133}Ba and ^{60}Co spectra. The same peak, when measured in Datasets I, II, and III, was approximately 1.5 keV wide, as shown in Figure 4.18. The energy resolution of these long-term datasets, listed in Table A.1, was best described by Equation 4.6, which includes a higher order term and is linear in energy at high energies.

Energy calibration of the shielded MALBEK datasets was performed using significant peaks in the background energy spectra, since periodic calibration data were not available. The degraded energy resolution observed in the long-term MALBEK spectra could be the result of calibration drift. With integral count rates above 5 keV on the order of a few mHz, and only a few tens of counts per hour-long run, it was difficult to track the drift of peaks in the energy spectrum.

The width of the $0\nu\beta\beta$ energy region of interest, approximately 4 keV, will be determined by the energy resolution of the DEMONSTRATOR. During operation of the DEMONSTRATOR, periodic energy calibration runs will be performed. This will prevent the calibration drift and degraded energy resolution observed during MALBEK data taking.

10.3.5 The MALBEK preamplifier

MALBEK's reset preamplifier, described in Section 4.8, imposed an energy-dependent efficiency on our energy spectra, made us insensitive to energy deposits greater than 2.7 MeV, and was responsible for a dead time of approximately 5%. Currently, the baseline de-

sign for the DEMONSTRATOR includes a resistive feedback preamplifier, which would avoid these complications. However, the natural-germanium BEGes were characterized while in cryostats with pulsed-reset preamplifiers, so it may be necessary to consider the effects of the preamplifiers on the characterization data.

10.4 Lessons learned from MALBEK background modeling

While simulating MALBEK response with MAGE/GEANT4 and modeling the background energy spectrum, issues with GEANT4, importance-sampled energy spectra, and fits of the background energy spectrum were encountered. These are discussed below.

10.4.1 Background model fits

The MALBEK background model has limited sensitivity to the contribution of $2\nu\beta\beta$ of ^{76}Ge in the energy spectrum, and the fit significantly over-predicts it. This is most noticeable in the analysis of Dataset III. The $2\nu\beta\beta$ spectrum may be filling in for a missing contribution to the energy spectrum. The missing contribution could be a broad, smooth continuum of highly attenuated gammas from outside the lead shielding, (since these energy spectra were not included in this analysis), a beta spectrum, or another contaminant. It is possible that the $2\nu\beta\beta$ spectrum is not filling in for a missing contribution, but that the description of the MALBEK detector used in the simulation is slightly inaccurate. Inaccuracies in the simulated dead layer could result in distortion to the simulated energy spectra. This possibility is discussed in Section 8.3 for the case of ^{210}Pb contamination in the lead patches. In general, a simulated dead layer that is thinner than the actual dead layer would allow more low-energy gammas from outside the crystal to reach the active volume; this could distort the intensity of low-energy gamma peaks relative to higher-energy gamma peaks. The relative intensities of gammas, betas, and alphas reaching the active volume could also be distorted by inaccuracies in the dead layer description. This could be especially important for contamination near crystal's signal contact, where incident radiation may be attenuated by the thin p^+ contact and the surface between the p^+ and n^+ contacts. It could also be the case that the MALBEK data simply does not have sufficient sensitivity to this spectral contribution.

If the number of counts due to $2\nu\beta\beta$ is constrained by the known rate, the fit results for each dataset change slightly. With the constraint, the contributions of the ^{238}U upper chain and lower chain I in the germanium crystal increase for Datasets I and II compared to the unconstrained fit. For Dataset III, the contribution from the ^{238}U lower chain II in the ancient lead shielding increases when $2\nu\beta\beta$ is constrained. The effect of this constraint on the goodness of fit for each dataset is shown in Table 10.3. There is a modest improvement in the Datasets II and III fits when the $2\nu\beta\beta$ contribution is allowed to float within the bounds described in Section 7.5, where each PDF may contribute between 0 and 1.5 times the integral number of counts in the fit region. The goodness-of-fit of Dataset II is poor in both cases, due to inaccuracy in the model of the energy spectrum from the lead patches, discussed in Section 8.3. The Dataset I fit is slightly worse when the $2\nu\beta\beta$ contribution is allowed to float. This is likely the result of performing a global minimization with a large number of free parameters. The results in Table 10.3 show that the fit is not very sensitive to the $2\nu\beta\beta$ contribution.

Table 10.3: Results from fitting with and without the ^{76}Ge $2\nu\beta\beta$ contribution constrained according to the known rate.

	With constraint		**Without constraint**	
Dataset	**χ^2/DOF**	**P-value**	**χ^2/DOF**	**P-value**
DS I	132.08 / 114	0.12	132.81 / 115	0.12
DS II	191.02 / 114	8.3×10^{-6}	186.15 / 115	3.0×10^{-5}
DS III	104.94 / 113	0.69	97.15 / 114	0.87

Given the issues encountered with the $2\nu\beta\beta$ results and the poor goodness-of-fit for Dataset II, it is important to use caution when interpreting fit results from the MALBEK background model. This work highlights the difficulties of fitting the background energy spectrum with many PDFs with unconstrained normalizations, particularly those

components to which the data has limited sensitivity. A more complete characterization of MALBEK's response, including measurements of the dead layer across all surfaces of the germanium crystal, would be ideal for better understanding the background energy spectrum and the difficulties encountered in fitting.

Based on these results, it is clear that MAJORANA will need to characterize the germanium crystals in the DEMONSTRATOR carefully and verify the simulation of their energy-spectrum response. Comprehensive characterization of the DEMONSTRATOR crystals is planned, and detailed studies of the detector dead layers is underway.

10.4.2 Description of peak shapes

To mimic the energy resolution of MALBEK, simulated energy spectra were convolved with a gaussian function. Some high-statistics peaks, including the pulser peak shown in Figure 4.16, are not well described by a gaussian peak plus a linear continuum. The non-gaussian shapes could be the result of calibration drift or pulse-processing parameters that are not optimal. Since the width of the DEMONSTRATOR's energy region of interest surrounding the $0\nu\beta\beta$ endpoint will be determined by the energy resolution at 2039 keV, it will be necessary to have a good understanding of peak shapes and energy resolution. Frequent energy calibration and extensive characterization of the DEMONSTRATOR will clarify these issues.

10.4.3 Issues with GEANT4

Several issues with GEANT4.9.3.p01, used in this work, affected simulations of MALBEK response. Problems with the simulation of ^{57}Co, ^{68}Ge, and ^{210}Pb decays were described in Section 7.6.1. A modification to post-processing with GAT was able to correct the ^{68}Ge issue.

Out-of-date data about gammas emitted in ^{133}Ba decay could have affected the dead layer measurement, as described in Section 6.4. A correction factor applied during calculation of the dead layer thickness mitigated this problem.

Information from the MAGE/GEANT4 validation software was useful for identifying issues with simulated energy spectra. Ongoing work with this validation package will be useful for cataloging and correcting discrepancies between GEANT4 and measured values.

10.4.4 Importance sampling of Monte Carlo events

Importance sampling of gammas, introduced in Section 5.7, was used while simulating decays originating from the KURF rock and other materials outside the MALBEK shielding. After the unblinding of Dataset II, as described in Section 8.2, these spectra were discovered to consist primarily of correlated events arising from a few initial decays. Although the energy spectra of detector response contained many counts, the counts were highly correlated and the spectral shapes were not a good description of the underlying distribution. Because of these problems, energy spectra from radioactive decays in the rock were not used in this analysis. For the DEMONSTRATOR simulation campaign, it might be useful to employ event biasing based on the direction of particle momentum.

10.5 Conclusions

This dissertation presented three low-background energy spectra collected with the MALBEK detector in a shielded underground environment. A model of the background energy spectrum, based on material radiopurity information, Monte Carlo simulation results of detector response, and cosmogenic exposure was used to understand the shielded MALBEK background energy spectra. The MALBEK background model was used to help identify contaminated material with the detector cryostat, which was successfully removed, reducing the background count rate significantly.

A similar background model has been constructed for the DEMONSTRATOR by other members of the MAJORANA Collaboration. The accuracy of the DEMONSTRATOR background model is expected to exceed the model shown here, since MAJORANA Collaborators will precisely measure the dimensions of the germanium crystals, material assay results will be available for the materials used in the DEMONSTRATOR, and several characterization studies are planned for the germanium array.

The DEMONSTRATOR will begin taking data in 2013. It will be exciting to see results from the DEMONSTRATOR after all of the careful preparation by MAJORANA.

BIBLIOGRAPHY

[1] "CLHEP – A Class Library for High Energy Physics." http://proj-clhep.web.cern.ch/proj-clhep/.

[2] **MAJORANA** Collaboration, "Germanium Analysis Toolkit (GAT)." http://mjwiki.npl.washington.edu/bin/view/Majorana/GermaniumAnalysisToolkit. MAJORANA Collaboration internal document.

[3] J. Allison *et al.*, "GEANT4 Developments and Applications," *Nuclear Science, IEEE Transactions on* **53** no. 1, (2006) 270–278.

[4] S. Agostinelli *et al.*, "GEANT4–A Simulation Toolkit," *Nuclear Instruments and Methods in Physics Research Section A: Accelerators, Spectrometers, Detectors and Associated Equipment* **506** no. 3, (2003) 250 – 303.

[5] **GERDA** Collaboration, I. Abt *et al.*, "GERDA: The GERmanium Detector Array for the search of neutrinoless $\beta\beta$ decays of ^{76}Ge at LNGS," 2004. http://www.mpi-hd.mpg.de/gerda/reportsLNGS/proposal_21sept.pdf. Proposal to the LNGS P38/04.

[6] J. Detwiler, R. Henning, R. Johnson, and M. Marino, "A Generic Surface Sampler for Monte Carlo Simulations," *Nuclear Science, IEEE Transactions on* **55** no. 4, (2008) 2329 –2333, arXiv:0802.2960 [nucl-ex].

[7] M. Boswell, Y.-D. Chan, J. Detwiler, P. Finnerty, R. Henning, V. Gehman, R. Johnson, D. Jordan, K. Kazkaz, M. Knapp, K. Kroninger, D. Lenz, L. Leviner, J. Liu, X. Liu, S. MacMullin, M. Marino, A. Mokhtarani, L. Pandola, A. Schubert, J. Schubert, C. Tomei, and O. Volynets, "MAGE–A GEANT4-Based Monte Carlo Application Framework for Low-Background Germanium Experiments," *Nuclear Science, IEEE Transactions on* **58** no. 3, (2011) 1212 –1220, arXiv:1011.3827 [nucl-ex].

[8] M. Agostini, J. A. Detwiler, P. Finnerty, K. Kröninger, D. Lenz, J. Liu, M. G. Marino, R. Martin, K. D. Nguyen, L. Pandola, A. G. Schubert, O. Volynets, and P. Zavarise, "The MGDO software library for data analysis in Ge neutrinoless double-beta decay experiments," *Journal of Physics Conference Series* **375** no. 4, (July, 2012) 042027, arXiv:1111.7260 [physics.data-an].

[9] M. Howe, G. Cox, P. Harvey, F. McGirt, K. Rielage, J. Wilkerson, and J. Wouters, "Sudbury neutrino observatory neutral current detector acquisition software overview," *Nuclear Science, IEEE Transactions on* **51** no. 3, (2004) 878 – 883. http://orca.physics.unc.edu.

[10] I. Antcheva *et al.*, "ROOT – A C++ framework for petabyte data storage, statistical analysis and visualization," *Computer Physics Communications* **180** no. 12, (2009) 2499 – 2512. 40 YEARS OF CPC: A celebratory issue focused on quality software for high performance, grid and novel computing architectures.

[11] C. Loizides, "Tree Analysis Modules for ROOT." https://code.google.com/p/tree-ana-mod/.

[12] F. Boehm and P. Vogel, *Physics of Massive Neutrinos*. Cambridge University Press, 1992.

[13] A. S. Barabash, "Precise half-life values for two-neutrino double-β decay," *Phys. Rev.* **C81** (2010) 035501, arXiv:1003.1005 [nucl-ex].

[14] **Particle Data Group** Collaboration, J. Beringer *et al.*, "Review of Particle Physics," *Phys. Rev. D* **86** (Jul, 2012) 010001. http://pdg.lbl.gov.

[15] H. Klapdor-Kleingrothaus, A. Dietz, L. Baudis, G. Heusser, I. Krivosheina, *et al.*, "Latest results from the Heidelberg-Moscow double beta decay experiment," *Eur.Phys.J.* **A12** (2001) 147–154, arXiv:hep-ph/0103062 [hep-ph].

[16] **IGEX** Collaboration, C. Aalseth *et al.*, "The IGEX Ge-76 neutrinoless double beta decay experiment: Prospects for next generation experiments," *Phys.Rev.* **D65** (2002) 092007, arXiv:hep-ex/0202026 [hep-ex].

[17] H. V. Klapdor-Kleingrothaus and I. V. Krivosheina, "The evidence for the observation of $0\nu\beta\beta$ decay: the identification of $0\nu\beta\beta$ events from the full spectra," *Modern Physics Letters A* **21** no. 20, (2006) 1547–1566.

[18] **EXO** Collaboration, M. Auger *et al.*, "Search for Neutrinoless Double-Beta Decay in ^{136}Xe with EXO-200," *Phys.Rev.Lett.* **109** (2012) 032505, arXiv:1205.5608 [hep-ex].

[19] **KamLAND-Zen** Collaboration, A. Gando *et al.*, "Limit on Neutrinoless $\beta\beta$ Decay of Xe-136 from the First Phase of KamLAND-Zen and Comparison with the Positive Claim in Ge-76," arXiv:1211.3863 [hep-ex].

[20] **MAJORANA** Collaboration, P. Finnerty *et al.*, "The MAJORANA DEMONSTRATOR: Progress towards showing the feasibility of a tonne-scale ^{76}Ge neutrinoless double-beta decay experiment," arXiv:1210.2678 [nucl-ex].

[21] I. Phillips, D.G., E. Aguayo, I. Avignone, F.T., H. Back, A. Barabash, *et al.*, "The MAJORANA experiment: an ultra-low background search for neutrinoless double-beta decay," *J. Phys. Conf. Ser.* **381** (2012) 012044, arXiv:1111.5578 [nucl-ex].

[22] **MAJORANA** Collaboration, A. Schubert *et al.*, "The MAJORANA DEMONSTRATOR: A Search for Neutrinoless Double-beta Decay of Germanium-76," *AIP Conf.Proc.* **1441** (2012) 480–482, arXiv:1109.1567 [nucl-ex].

[23] J. Suhonen and O. Civitarese, "Weak-interaction and nuclear-structure aspects of nuclear double beta decay," *Physics Reports* **300** no. 34, (1998) 123 – 214.

[24] F. Simkovic, A. Faessler, H. Muther, V. Rodin, and M. Stauf, "The 0 nu bb-decay nuclear matrix elements with self-consistent short-range correlations," *Phys.Rev.* **C79** (2009) 055501, arXiv:0902.0331 [nucl-th].

[25] J. Detwiler, "MJD $0\nu\beta\beta$ Decay Sensitivity Calculations," 2011. https://mjdoc.npl.washington.edu/record/1458. MAJORANA Technical Report M-TECHDOCPHYS-2011-043.

[26] G. F. Knoll, *Radiation detection and measurement*. John Wiley & Sons, Inc., Hoboken, NJ, USA, 3rd ed., 2000.

[27] P. Luke, F. Goulding, N. Madden, and R. Pehl, "Low capacitance large volume shaped-field germanium detector," *Nuclear Science, IEEE Transactions on* **36** no. 1, (Feb, 1989) 926 –930.

[28] P. S. Barbeau, J. I. Collar, and O. Tench, "Large-mass ultralow noise germanium detectors: performance and applications in neutrino and astroparticle physics," *Journal of Cosmology and Astroparticle Physics* **2007** no. 09, (2007) 009. http://stacks.iop.org/1475-7516/2007/i=09/a=009.

[29] M. G. Marino, *Dark Matter Physics with P-type Point-contact Germanium Detectors: Extending the Physics Reach of the MAJORANA Experiment*. PhD thesis, The University of Washington, 2010.

[30] **CoGeNT collaboration** Collaboration, C. Aalseth *et al.*, "Results from a Search for Light-Mass Dark Matter with a P-type Point Contact Germanium Detector," *Phys.Rev.Lett.* **106** (2011) 131301, arXiv:1002.4703 [astro-ph.CO].

[31] **MAJORANA** Collaboration, E. Aguayo *et al.*, "Characteristics of Signals Originating Near the Lithium-Diffused N+ Contact of High Purity Germanium P-Type Point Contact Detectors," arXiv:1207.6716 [physics.ins-det].

[32] G. Heusser, "Background in ionizing radiation detection – illustrated by Ge-spectrometry," in *Proceedings of the International Summer School on Low-Level Measurements of Radioactivity in the Environment: Techniques and Applications, Huelva, Spain, 1993*, M. García-León and R. García-Teonorio, eds., pp. 69–112. World Scientific, Singapore, 1994.

[33] National Nuclear Data Center. http://www.nndc.bnl.gov/nudat2/. Information extracted from the NuDat 2.6 database.

[34] J. Detwiler, S. R. Elliott, D. Radford, D. Steele, and J. Wilkerson, "The MAJORANA DEMONSTRATOR Background Criteria for Critical Decision 4," 2012. https://mjdoc.npl.washington.edu/record/1591. MAJORANA Technical Report M-TECHDOCPHYS-20112-047.

[35] **MAJORANA** Collaboration, C. Aalseth *et al.*, "Astroparticle physics with a customized low-background broad energy Germanium detector," *Nuclear Instruments and Methods in Physics Research Section A: Accelerators, Spectrometers, Detectors and Associated Equipment* **652** no. 1, (2011) 692 – 695, arXiv:1007.3231 [nucl-ex]. Symposium on Radiation Measurements and Applications (SORMA) XII 2010.

[36] P. Finnerty, S. MacMullin, H. Back, R. Henning, A. Long, K. Macon, J. Strain, R. Lindstrom, and R. Vogelaar, "Low-background gamma counting at the Kimballton Underground Research Facility," *Nuclear Instruments and Methods in Physics Research Section A: Accelerators, Spectrometers, Detectors and Associated Equipment* **642** no. 1, (2011) 65 – 69, arXiv:1007.0015 [nucl-ex].

[37] CANBERRA. http://www.canberra.com.

[38] UNC, "Purchase Request," 2009. http://mjwiki.npl.washington.edu/pub/Majorana/UncMalbek/mj_canberra_bege.pdf. MAJORANA Collaboration internal document.

[39] CANBERRA, *Detector Specification and Performance Data*, 2009. http://mjwiki.npl.washington.edu/pub/Majorana/UncMalbek/MALBEK_Detector_Manual.pdf. MAJORANA Collaboration internal document.

[40] M. Yocum. Private correspondence, July, 2010.

[41] M. Yocum. Private correspondence, 2010.

[42] G. Swift, "MALBEK Detector Shield Full Assembly," 2009. http://mjwiki.npl.washington.edu/pub/Majorana/UncMalbek/ShieldShopDrawings.pdf. Technical drawing, MAJORANA Collaboration internal.

[43] G. Giovanetti, P. Finnerty, R. Henning, M. Howe, M. Marino, J. Strain, and J. Wilkerson, "Development of a data acquisition system for the MALBEK Low-Background BEGe detector," *Nuclear Science Symposium Conference Record (NSS/MIC), 2010 IEEE* (2010) 1282 –1284.

[44] M. A. Howe, M. G. Marino, and J. F. Wilkerson, "Integration of embedded single board computers into an object-oriented software bus DAQ application," in *Nuclear Science Symposium Conference Record, 2008. NSS '08. IEEE*, pp. 3562 –3567. Oct., 2008.

[45] P. Finnerty, "Astroparticle and Nuclear Physics with a Customized Low-Background Broad Energy Germanium Detector." Presentation at aps april meeting 2010, February, 2010. Abstract ID: BAPS.2010.APR.Y10.4.

[46] P. Finnerty, "Astroparticle Physics with Prototype Broad Energy Germanium Detectors." Preliminary oral exam, April, 2010.

[47] P. Finnerty, G. Giovanetti, R. Henning, M. Marino, A. Schubert, and J. Wilkerson, "MALBEK Update," June, 2010. Presentation at MAJORANA Collaboration Meeting.

[48] C. Aalseth, P. Barbeau, J. Colaresi, J. Collar, J. Diaz Leon, *et al.*, "Search for an Annual Modulation in a P-type Point Contact Germanium Dark Matter Detector," *Phys.Rev.Lett.* **107** (2011) 141301, arXiv:1106.0650 [astro-ph.CO].

[49] **CoGeNT** Collaboration, C. Aalseth *et al.*, "CoGeNT: A Search for Low-Mass Dark Matter using p-type Point Contact Germanium Detectors," arXiv:1208.5737 [astro-ph.CO].

[50] J. I. Collar. Private correspondence, February, 2010.

[51] M. Yocum. Private correspondence, February, 2010.

[52] R. Henning. Private correspondence, March, 2010.

[53] **ILIAS** Collaboration, "The ILIAS database on radiopurity of materials." http://radiopurity.in2p3.fr, 2010.

[54] J. I. Collar. Private correspondence, March, 2010.

[55] "Mill-Max Mfg. Corp: Connector pins & interconnect solutions," 2012. http://www.mill-max.com.

[56] J. Collar. Private correspondence, February, 2010. PNNL measurement.

[57] J. I. Collar. Private correspondence, March, 2010.

[58] P. Finnerty, G. K. Giovanetti, R. Henning, and J. F. Wilkerson, "MALBEK Lead Shim Removal," November, 2011. https://mjdoc.npl.washington.edu/record/1532. MAJORANA Technical Report M-TECHDOCPHYS-2012-140.

[59] J. Roth, J. H. Primbsch, and R. P. Lin, "Segmentation and Pulse Shape Discrimination Techniques for Rejecting Background in Germanium Detectors," *Nuclear Science, IEEE Transactions on* **31** no. 1, (Feb., 1984) 367 –371.

[60] P. Finnerty. Private correspondence, September, 2011.

[61] E. Schönfeld, U. Schötzig, E. Günther, and H. Schrader, "Standardization and decay data of 68Ge/68Ga," *Applied Radiation and Isotopes* **45** no. 9, (1994) 955 – 961.

[62] J. A. BEARDEN and A. F. BURR, "Reevaluation of X-Ray Atomic Energy Levels," *Rev. Mod. Phys.* **39** (Jan, 1967) 125–142. http://link.aps.org/doi/10.1103/RevModPhys.39.125.

[63] S. Chu, L. L.P. Ekström, and R. Firestone, "WWW Table of Radioactive Isotopes,". http://nucleardata.nuclear.lu.se/nucleardata/toi/. Database version 2/28/1999.

[64] M. Dressel, "Geometrical importance sampling in Geant4: from design to verification," Tech. Rep. CERN-OPEN-2003-048, CERN, Geneva, Sep, 2003. http://cdsweb.cern.ch/record/642987.

[65] R. Cooper and D. Radford, "A PSA Heuristic Code," 2009. https://mjdoc.npl.washington.edu/record/1060. MAJORANA Technical Report M-TECHDOCPHYS-2009-010.

[66] J. Lindhard and M. Scharff, "Energy Dissipation by Ions in the kev Region," *Phys. Rev.* **124** (1961) 128–130.

[67] P. S. Barbeau, *Neutrino and astroparticle physics with P-type point contact high purity germanium detectors*. PhD thesis, The University of Chicago, 2009.

[68] M. Agostini, E. Bellotti, R. Brugnera, C. M. Cattadori, A. D'Andragora, A. di Vacri, A. Garfagnini, M. Laubenstein, L. Pandola, and C. A. Ur, "Characterization of a broad energy germanium detector and application to neutrinoless double beta decay search in ^{76}Ge," *Journal of Instrumentation* **6** (Apr., 2011) 4005P, arXiv:1012.5200 [physics.ins-det].

[69] "IEEE Standard Test Procedures for Germanium Gamma-Ray Detectors," *IEEE Std 325-1996* (1997) .

[70] Y. Khazov, A. Rodionov, and F. Kondev, "Nuclear Data Sheets for A = 133," *Nuclear Data Sheets* **112** no. 4, (2011) 855 – 1113.

[71] "GEANT4 Problem 1340 - Incorrect gamma branching ratios in 133-Ba decay," July, 2012. http://bugzilla-geant4.kek.jp/show_bug.cgi?id=1340.

[72] A. P. Arya, "Gamma-Gamma Directional Correlations in Cs^{133}," *Phys. Rev.* **122** (Apr, 1961) 549–555.

[73] A. G. Schubert, "GEANT4.9.3.p01 MAGE Validation Report," 2012. https://mjdoc.npl.washington.edu/record/1571. MAJORANA Technical Report M-TECHDOCPHYS-2012-063.

[74] J. Hubbell and S. Seltzer, "NIST: X-Ray Mass Attenuation Coefficients," 2011. http://www.nist.gov/pml/data/xraycoef/index.cfm.

[75] G. Cirrone, G. Cuttone, F. D. Rosa, L. Pandola, F. Romano, and Q. Zhang, "Validation of the GEANT4 electromagnetic photon cross-sections for elements and compounds," *Nuclear Instruments and Methods in Physics Research Section A: Accelerators, Spectrometers, Detectors and Associated Equipment* **618** no. 13, (2010) 315 – 322.

[76] P. Finnerty. Private correspondence, April, 2012.

[77] I. Abt, A. Caldwell, K. Kröninger, J. Liu, X. Liu, and B. Majorovits, "Identification of photons in double beta-decay experiments using segmented germanium detectors – Studies with a GERDA phase II prototype detector," *Nuclear Instruments and Methods in Physics Research A* **583** (Dec., 2007) 332–340, arXiv:nucl-ex/0701005.

[78] S. Hurtado, M. García-León, and R. García-Tenorio, "GEANT4 code for simulation of a germanium gamma-ray detector and its application to efficiency calibration," *Nuclear Instruments and Methods in Physics Research Section A: Accelerators, Spectrometers, Detectors and Associated Equipment* **518** no. 3, (2004) 764 – 774.

[79] **MAJORANA** Collaboration, H. Back *et al.*, "MAJORANA Background Summary Document v0.3." https://mjdoc.npl.washington.edu/record/437, 2008. MAJORANA technical report M-TECHDOCPHYS-2008-003.

[80] P. Lipari and T. Stanev, "Propagation of multi-TeV muons," *Phys. Rev. D* **44** (Dec, 1991) 3543–3554. http://link.aps.org/doi/10.1103/PhysRevD.44.3543.

[81] D.-M. Mei and A. Hime, "Muon-induced background study for underground laboratories," *Phys. Rev. D* **73** (Mar, 2006) 053004. http://link.aps.org/doi/10.1103/PhysRevD.73.053004.

[82] A. Schubert, "Modeling the DEMONSTRATOR background energy spectrum." Presentation at mj simulations and analysis preliminary design review, February, 2011.

[83] **ROOT** Collaboration, "RooFit." http://root.cern.ch/drupal/content/roofit.

[84] F. James, "CERN Program Library Long Writeup D506: MINUIT." wwwasdoc.web.cern.ch/wwwasdoc/minuit/minmain.html.

[85] G. Cowan, *Statistical Data Analysis*. Oxford Science Publications. Oxford University Press, USA, 1998.

[86] S. Elliott and V. Guiseppe, February, 2011. Private correspondence.

[87] V. Guiseppe, S. Elliott, V. Gehman, R. Johnson, B. LaRoque, S. Mashnik, and D. Steele, "Ge activation work: neutron activation of nat-Ge and enr-Ge at LANSCE," 2009. Presentation at MJ Collaboration Meeting, December 2009.

[88] M.-M. Bé *et al.*, "Vol. 3 – A=3 to 244," *Monagraphie BIPM-5 Table of Radionuclides* (2006) .

[89] M. Marino, J. Detwiler, R. Henning, R. Johnson, A. Schubert, and J. Wilkerson, "Validation of spallation neutron production and propagation within Geant4," *Nuclear Instruments and Methods in Physics Research Section A: Accelerators, Spectrometers, Detectors and Associated Equipment* **582** (2007) 611–620, arXiv:0708.0848 [nucl-ex].

[90] I. Abt, A. Caldwell, K. Kroninger, J. Liu, X. Liu, *et al.*, "Neutron interactions as seen by a segmented germanium detector," *Eur.Phys.J.* **A36** (2008) 139–149, arXiv:0711.2255 [nucl-ex].

[91] "GEANT4 Problem 1273: Secondary track weighting is now grossly wrong." http://bugzilla-geant4.kek.jp/show_bug.cgi?id=1273.

[92] J. A. Detwiler. Private correspondence, September, 2011.

[93] D. Leonard *et al.*, "Systematic study of trace radioactive impurities in candidate construction materials for EXO-200," *Nuclear Instruments and Methods in Physics Research Section A: Accelerators, Spectrometers, Detectors and Associated Equipment* **591** no. 3, (2008) 490 – 509, arXiv:0709.4524 [physics.ins-det].

[94] **MAJORANA** Collaboration, "MAJORANA Twiki: Background Model Simulations." http://mjwiki.npl.washington.edu/bin/view/Majorana/BackgroundModelSimulations. MAJORANA Collaboration internal document.

[95] V. Guiseppe. Private correspondence, December, 2012.

[96] G. Škoro, I. Aničin, A. Kukoč, D. Krmpotić, P. Adžić, R. Vukanović, and M. Župančić, "Environmental neutrons as seen by a germanium gamma-ray spectrometer," *Nuclear Instruments and Methods in Physics Research Section A: Accelerators, Spectrometers, Detectors and Associated Equipment* **316** no. 23, (1992) 333 – 336.

[97] G. J. Feldman and R. D. Cousins, "Unified approach to the classical statistical analysis of small signals," *Phys. Rev. D* **57** (Apr, 1998) 3873–3889. http://link.aps.org/doi/10.1103/PhysRevD.57.3873.

[98] R. A. Johnson, *Alpha backgrounds and their implications for neutrinoless double-beta decay experiments using HPGE detectors*. PhD thesis, The University of Washington, 2010.

[99] J. Detwiler, "DEMONSTRATOR Background Calculations Spreadsheet." https://mjdoc.npl.washington.edu/record/1259, 2010. MAJORANA technical report M-TECHDOCPHYS-2010-024.

[100] G. Heusser, M. Laubenstein, and H. Neder, "Low-level germanium gamma-ray spectrometry at the μBq/kg level and future developments towards higher sensitivity," in *Radionuclides in the Environment Int. Conf. On Isotopes in Env. Studies*, P. Povinec and J. Sanchez-Cabeza, eds., vol. 8 of *Radioactivity in the Environment*, pp. 495 – 510. Elsevier, 2006.

[101] J. Detwiler, "Backgrounds from Bulk U and Th in Ge Detectors." https://mjdoc.npl.washington.edu/record/446, 2008. MAJORANA technical report M-TECHDOCPHYS-2008-006.

[102] D.-M. Mei. Private correspondence, July, 2008.

[103] S. R. Elliott *et al.*, "Fast-Neutron Activation of Long-Lived Isotopes in Enriched Ge," *Phys. Rev.* **C82** (2010) 054610, arXiv:0912.3748 [nucl-ex].

[104] J. Strain, "Radioactivity Analysis of Sullivan Lead Bricks." https://mjdoc.npl.washington.edu/record/1280, 2010. MAJORANA technical report M-TECHDOCPHYS-2010-027.

[105] J. Loach, "ICP-MS Measurements at Chernogolovka - FET dies, Cr, Wire, Cables and Tin." https://mjdoc.npl.washington.edu/record/1260, 2010. MAJORANA technical report M-TECHDOCDET-2010-095.

[106] R. Henning. Private correspondence, April, 2011.

Appendix A

SHIELDED BACKGROUND DATA COLLECTED AT KURF

Table A.1: Summary of ORCA/Struck data from the MALBEK detector. These datasets were collected at KURF while MALBEK was shielded. The Tier 1–3 data sizes contain calibration data that was not included in the Tier 4 datasets.

	Data Sets		
Parameter	**I**	**II**	**III**
Start date	24 Sep 2010	20 Jan 2011	01 Nov 2011
Stop date	30 Nov 2010	16 Aug 2011	10 Sep 2012
ORCA run numbers	4723–6290	7513–11831	19019–26122
Run time [days]	67.41	207.97	314.35
Live time (after cuts) [days]	55.21	136.58	240.83
Count rate above 5 keV (after cuts) [mHz]	7.73	7.93	1.96
Energy res. par. c_0 [eV]	153.8 ± 0.2	126.0 ± 0.1	119.2 ± 0.1
Energy res. par. c_1	0.079 ± 0.014	0.122 ± 0.008	0.094 ± 0.017
Energy res. par. c_2 [10^{-7}]	13.3 ± 3.4	15.2 ± 2.0	8.1 ± 1.5
Tier 0 data (ORCA output) [GB]	115	301	393
Tier 1 data (MJOR output) [GB]	107	267	387
Tier 2 data (GAT output) [GB]	23	81	94
Tier 3 data (GAT output) [MB]	554	3,174	5,793
Tier 4 data (GAT output) [MB]	249	799	3,441

Table A.2: Summary of timing cuts applied to MALBEK ORCA/Struck data from the unamplified ionization energy channel. These cuts were applied to generate Tier 3 data from Tier 2 data, and are described in Section 4.4.1. Cuts are applied cumulatively in the order listed. The count rates are integral rates above 5 keV.

		Veto	**Approx.**	**Dead time [%]**			**Rate after cut [mHz]**		
Cut	**Description**	**Duration**	**Frequency**	**DSI**	**DSII**	**DSIII**	**DSI**	**DSII**	**DSIII**
1	Run edges	$\sim$ 10 s	per run	0.28	0.28	0.28	110.59	110.55	102.99
2	Inhibit coincident	2 ms	25 Hz	4.77	5.22	4.07	108.00	108.02	102.05
3	Long inhibit intervals	$\geq$ 60 ms	intermittent	4×10^{-4}	4×10^{-4}	1×10^{-3}	107.92	107.94	101.98
4	Long pulser intervals	$\geq$ 10 s	intermittent	0.32	0.02	0.03	107.73	107.93	101.96
5	Pulser coincident	2 μs	0.1 Hz	2×10^{-5}	2×10^{-5}	2×10^{-5}	7.73	7.93	1.96
			Total dead time [%]:	5.37	5.52	4.11			

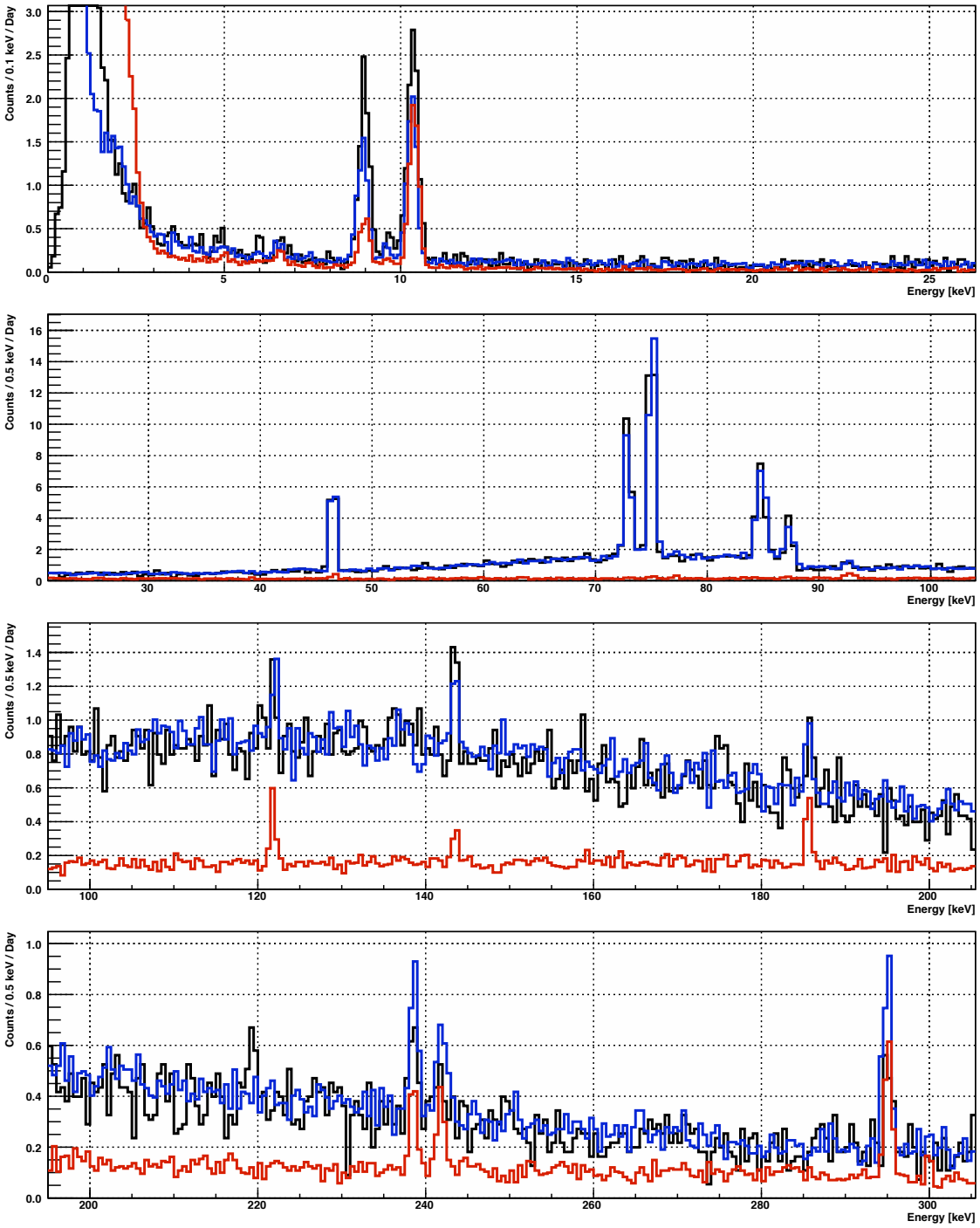

Figure A.1: The MALBEK shielded energy spectrum. The energy spectra from Dataset I (black), Dataset II (blue) and Dataset III (red) are shown. Timing cuts, the combined rise-time cut, and the pulser veto have been applied.

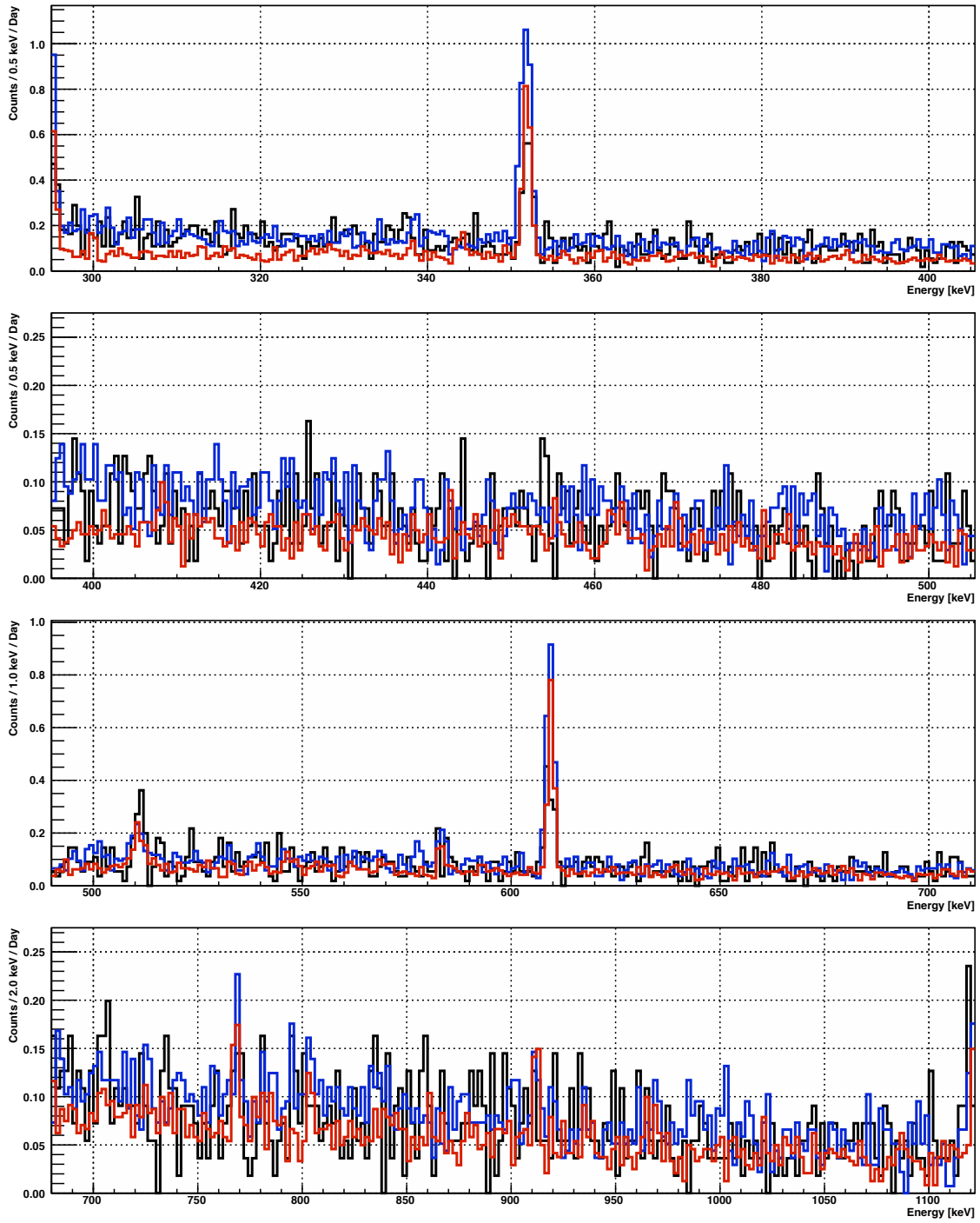

Figure A.2: The MALBEK shielded energy spectrum, continued. The energy spectra from Dataset I (black), Dataset II (blue) and Dataset III (red) are shown. Timing cuts, the combined rise-time cut, and the pulser veto have been applied.

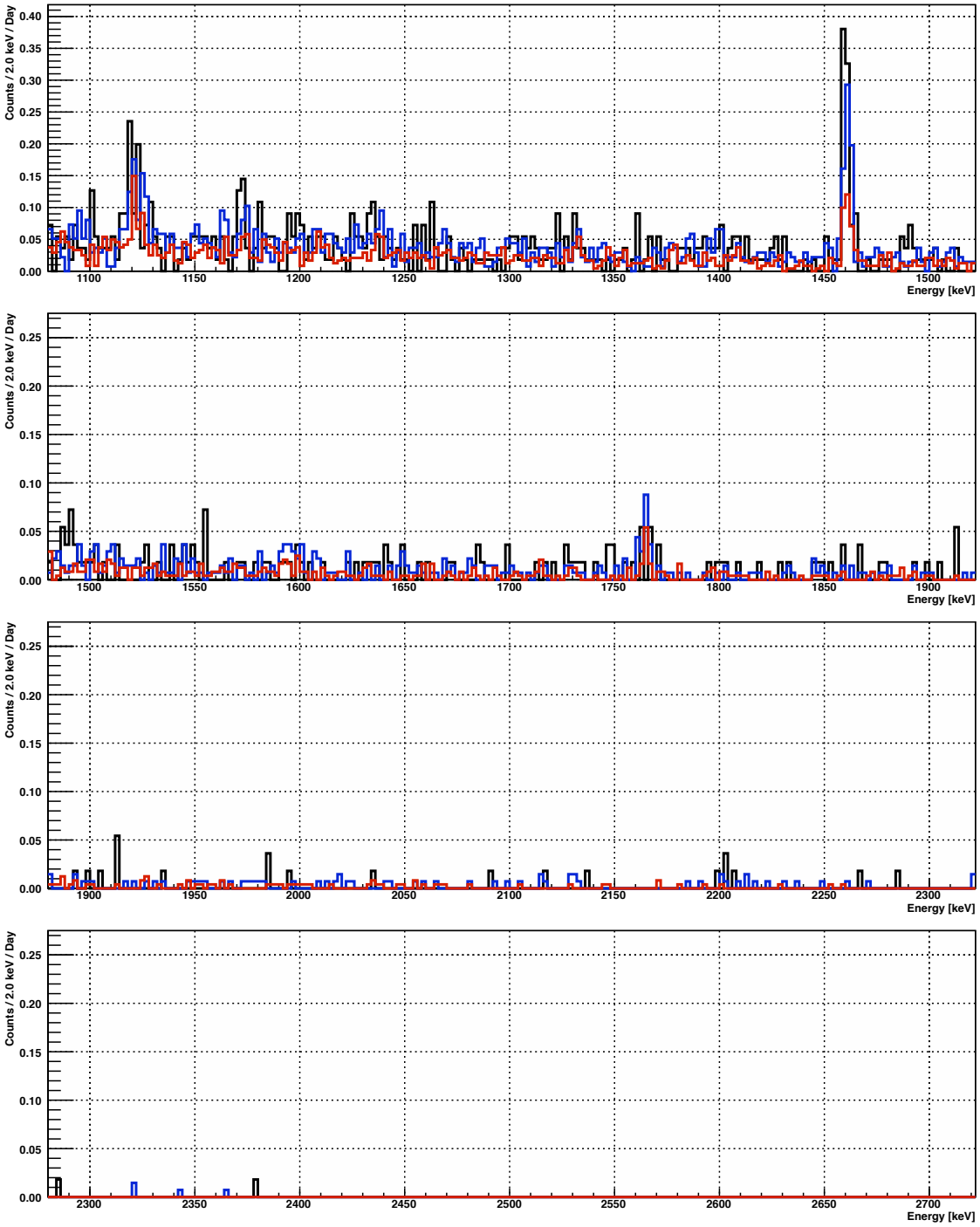

Figure A.3: The MALBEK shielded energy spectrum, continued. The energy spectra from Dataset I (black), Dataset II (blue) and Dataset III (red) are shown. Timing cuts, the combined rise-time cut, and the pulser veto have been applied.

Appendix B

PEAK SCANNING

After the combined rise-time cut has been applied, a dataset is scanned for possible peaks. The scanning is performed with a simple counting method that is intended to identify statistically significant peaks in an objective way. The scanning is performed by a Python script, `scan_for_peaks.py`. This script marches over the energy spectrum in steps of 100 eV. At each energy, E_i, the following procedure is performed:

1. The energy resolution, σ, is estimated at energy E_i. This energy resolution is calculated using Equation 4.5, assuming an electronics noise of 154 eV and a Fano factor of 0.12, which are reasonable estimates for data collected with MALBEK.

2. A signal region is defined to include the energy region around E_i. This is the region between $E_i - 4\sigma$ and $E_i + 4\sigma$. The number of counts, N_S, in this region is calculated.

3. The number of counts, N_{B1}, in the sideband below the signal region is calculated. This is the region between $E_i - 8\sigma$ and $E_i - 4\sigma$.

4. The number of counts, N_{B2}, in the sideband above the signal region is calculated. This is the region between $E_i + 4\sigma$ and $E_i + 8\sigma$.

5. The number of counts in the sidebands is calculated from $N_B = N_{B1} + N_{B2}$. The statistical uncertainty in this number of counts is given by $\sqrt{N_B}$.

6. The number of excess counts in the signal region is calculated from $N_S - N_B$. A ratio is calculated to compare the excess counts to the statistical uncertainty in the sideband counts: $R = (N_S - N_B)/\sqrt{N_B}$.

7. If the ratio R is greater than 3.0, the energy E_i is reported as the location of a possible peak. If R remains above 3.0 for multiple sequential steps, the energy corresponding to the maximum value of R is reported as the location of a possible peak.

In Figure B.1, this process is shown near the 46.5 keV ^{210}Pb peak in Dataset I. Signal and sideband regions are shown in the top panel of the figure for $E_i = 46.5$ keV. The bottom panel shows the value of R calculated at each E_i.

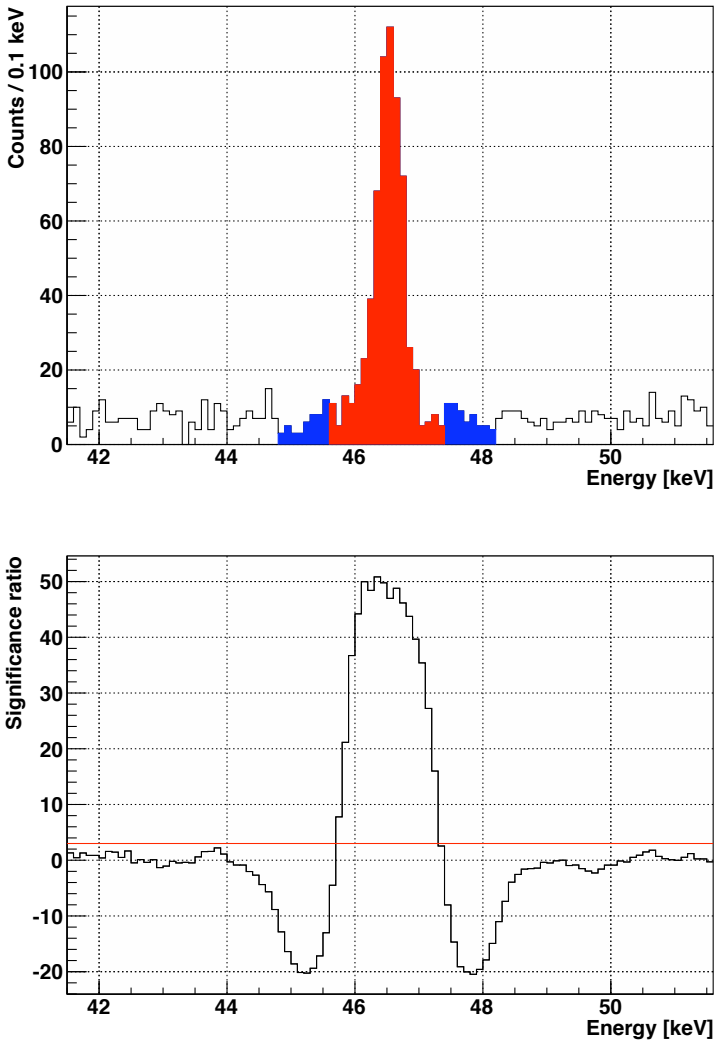

Figure B.1: An example of peak scanning near the 46.5-keV ^{210}Pb peak. This scan was performed on the Dataset I energy spectrum after the combined rise-time cut was applied. Peak scanning is described in the text. In the top panel, the energy spectrum is shown. The central signal band (red) and side bands (blue) are shown for an energy of 46.5 keV. In the bottom panel, the ratio R is shown as a function of energy. The significance threshold, 3.0, is shown in red.

Appendix C

IDENTIFIED PEAKS

For the energy spectra listed below, peaks were found using the algorithm described in Appendix B. Peaks were fit with the unbinned maximum likelihood method described in Section 4.7.1. Published energies are from NuDat [33].

Table C.1: Peaks in the Dataset I energy spectrum.

Peak	**Energy [keV]**	**Centroid [keV]**	**Sigma [eV]**	**Count Rate [μHz]**	**χ^2 / DOF**	**P-value**
^{65}Zn[1]	8.98	8.97 ± 0.01	144.1 ± 7.2	90.5 ± 4.8		
^{68}Ga	9.66	9.71 ± 0.05	178.5 ± 62.3	13.7 ± 3.7	35.2 / 49 (0.72)	0.930
^{68}Ge[1]	10.37	10.35 ± 0.01	149.6 ± 7.8	114.0 ± 5.7		
pulser	-	35.43 ± 0.00	153.8 ± 0.2	100000.2 ± 0.0	663.9 / 36 (18.44)	1.4E-116
^{210}Pb[1]	46.54	46.51 ± 0.01	188.6 ± 9.0	104.5 ± 5.2	39.8 / 36 (1.11)	0.303
Pb K$_{\alpha 2}$[1]	72.81	72.86 ± 0.01	234.3 ± 9.7	157.9 ± 6.9	64.4 / 54 (1.19)	0.157
Pb K$_{\alpha 1}$[1]	74.97	74.99 ± 0.01	220.3 ± 6.5	273.1 ± 8.5		
Pb K$_{\beta 3}$, Pb K$_{\beta 1}$	84.45, 84.94	84.77 ± 0.02	370.1 ± 21.9	142.2 ± 7.9	65.2 / 54 (1.21)	0.141
Pb K$_{\beta 2}$	87.30	87.32 ± 0.02	283.1 ± 24.5	59.1 ± 5.0		
^{57}Co	122.06	121.78 ± 0.04	97.2 ± 31.0	5.8 ± 1.9	21.8 / 36 (0.61)	0.970
^{57}Co + atomic[1]	143.58	143.47 ± 0.07	270.0 ± 51.0	13.9 ± 0.2	18.5 / 36 (0.51)	0.993
^{212}Pb[1]	238.63	238.55 ± 0.12	356.9 ± 99.4	8.0 ± 0.2	26.2 / 36 (0.73)	0.886
^{214}Pb	295.22	295.17 ± 0.10	421.6 ± 81.3	9.6 ± 2.1	27.7 / 36 (0.77)	0.837
^{214}Pb[1]	351.93	351.97 ± 0.08	531.7 ± 57.1	16.7 ± 2.3	19.6 / 36 (0.54)	0.988
^{208}Tl + annih.	510.77, 511.00	511.07 ± 0.21	912.3 ± 151.9	7.8 ± 1.7	15.9 / 36 (0.44)	0.998
^{208}Tl	583.19	583.89 ± 0.56	1556.3 ± 480.1	3.8 ± 0.2	12.8 / 36 (0.36)	1.000
^{214}Bi[1]	609.32	609.16 ± 0.17	942.0 ± 136.5	11.2 ± 1.9	20.4 / 36 (0.57)	0.983
^{40}K[1]	1460.82	1460.14 ± 0.26	1395.2 ± 288.5	8.7 ± 1.5	11.1 / 36 (0.31)	1.000

[1]Used in energy calibration and fit of energy resolution function.

Table C.2: Peaks in the MALBEK Dataset II energy spectrum.

Peak	**Energy [keV]**	**Centroid [keV]**	**Sigma [eV]**	**Count Rate [μHz]**	**χ^2 / DOF**	**P-value**
^{65}Zn[1]	8.98	8.91 ± 0.01	143.5 ± 5.6	57.4 ± 2.5		
^{68}Ga	9.66	9.60 ± 0.02	106.8 ± 25.0	6.3 ± 1.3	32.3 / 52 (0.62)	0.985
^{68}Ge[1]	10.37	10.32 ± 0.01	135.0 ± 4.4	76.7 ± 2.8		
pulser	-	35.52 ± 0.00	126.0 ± 0.1	99993.6 ± 92.1	928.5 / 36 (25.79)	1.5E-171
^{210}Pb[1]	46.54	46.50 ± 0.01	190.5 ± 5.1	107.0 ± 3.3	33.6 / 36 (0.93)	0.585
Pb $K_{\alpha 2}$[1]	72.81	72.89 ± 0.01	224.2 ± 7.0	138.6 ± 4.2	55.0 / 54 (1.02)	0.437
Pb $K_{\alpha 1}$[1]	74.97	75.07 ± 0.00	228.4 ± 4.3	274.4 ± 5.5		
Pb $K_{\beta 3}$, $K_{\beta 1}$	84.45, 84.94	84.85 ± 0.01	375.1 ± 12.1	144.9 ± 4.9	96.0 / 54 (1.78)	3.8E-04
Pb $K_{\beta 2}$	87.30	87.35 ± 0.02	353.2 ± 25.1	54.2 ± 3.6		
^{234}Th	92.38, 92.80	92.62 ± 0.08	370.9 ± 62.9	11.0 ± 2.3	40.4 / 36 (1.12)	0.281
^{57}Co	122.06	122.10 ± 0.04	193.9 ± 43.9	8.3 ± 1.7	27.6 / 36 (0.77)	0.842
^{57}Co + atomic	143.58	143.57 ± 0.08	345.2 ± 78.7	10.1 ± 2.3	21.8 / 36 (0.61)	0.970
^{235}U, ^{226}Ra	185.72, 186.21	185.60 ± 0.07	356.3 ± 62.9	9.6 ± 0.1	31.3 / 36 (0.87)	0.691
^{212}Pb[1]	238.63	238.64 ± 0.05	419.5 ± 46.2	15.2 ± 0.1	38.6 / 50 (0.77)	0.880
^{214}Pb[1]	242.00	241.89 ± 0.10	550.6 ± 85.7	11.2 ± 0.1		
^{214}Pb[1]	295.22	294.96 ± 0.04	479.5 ± 34.2	21.7 ± 1.8	44.6 / 36 (1.24)	0.154
^{228}Ac	338.32	338.44 ± 0.13	355.1 ± 111.2	2.7 ± 0.9	35.2 / 36 (0.98)	0.505
^{214}Pb[1]	351.93	351.74 ± 0.03	580.2 ± 28.6	35.5 ± 2.0	30.9 / 36 (0.86)	0.708
^{208}Tl[1]	583.19	583.50 ± 0.17	683.1 ± 117.9	3.3 ± 0.1	32.3 / 36 (0.90)	0.646
^{214}Bi[1]	609.32	609.32 ± 0.06	867.5 ± 48.7	23.0 ± 1.5	32.1 / 36 (0.89)	0.655
^{228}Ac	964.77	969.31 ± 0.53	1121.7 ± 384.8	1.1 ± 0.1	16.9 / 36 (0.47)	0.997
^{214}Bi, ^{65}Zn + atomic	1120.29, 1124.52	1122.02 ± 0.71	3565.2 ± 640.8	5.8 ± 1.3	24.9 / 36 (0.69)	0.918
^{40}K[1]	1460.82	1461.02 ± 0.21	1647.3 ± 178.3	7.1 ± 0.9	25.2 / 36 (0.70)	0.911
^{214}Bi	1764.49	1764.50 ± 0.42	1827.5 ± 292.1	2.0 ± 0.4	16.8 / 36 (0.47)	0.997

Table C.3: Peaks in the MALBEK Dataset III energy spectrum. Peaks were fit with the unbinned maximum likelihood method. The peak near 344 keV has not been identified.

Peak	**Energy [keV]**	**Centroid [keV]**	**Sigma [eV]**	**Count Rate [μHz]**	**χ^2 / DOF**	**P-value**
^{65}Zn[1]	8.98	8.98 ± 0.01	142.7 ± 7.5	23.6 ± 1.3		
^{68}Ga	9.66	9.66 ± 0.03	139.4 ± 33.9	3.7 ± 0.8	43.3 / 54 (0.80)	0.851
^{68}Ge[1]	10.37	10.38 ± 0.00	131.7 ± 2.9	74.6 ± 2.0		
^{210}Pb[1]	46.54	46.63 ± 0.03	162.0 ± 25.0	4.1 ± 0.6	23.2 / 36 (0.65)	0.950
^{234}U, ^{72}Ge(n, γ)	53.20, 53.53	53.91 ± 0.03	72.6 ± 18.9	1.0 ± 0.0	23.5 / 36 (0.65)	0.947
^{234}Th[1]	63.29	63.47 ± 0.06	224.3 ± 44.3	2.2 ± 0.0	31.2 / 36 (0.87)	0.694
Bi $K_{\alpha 2}$	74.81	75.06 ± 0.06	222.9 ± 54.2	2.3 ± 0.6	39.3 / 59 (0.67)	0.977
Bi $K_{\alpha 1}$	77.11	77.23 ± 0.06	222.9 ± 50.6	2.8 ± 0.6		
^{234}Th	92.38, 92.80	92.76 ± 0.07	441.7 ± 51.5	9.0 ± 1.3	23.2 / 36 (0.64)	0.951
^{57}Co[1]	122.06	121.81 ± 0.03	286.5 ± 32.4	8.5 ± 0.9	34.4 / 36 (0.96)	0.545
^{57}Co + atomic	143.58	143.53 ± 0.06	306.5 ± 66.0	4.0 ± 0.8	25.9 / 36 (0.72)	0.894
^{235}U, ^{226}Ra	185.72, 186.21	185.60 ± 0.04	332.5 ± 33.8	8.8 ± 0.9	21.7 / 36 (0.60)	0.971
^{212}Pb[1]	238.63	238.52 ± 0.03	303.5 ± 33.1	7.9 ± 0.8	27.3 / 54 (0.51)	0.999
^{214}Pb[1]	242.00	241.82 ± 0.04	338.4 ± 41.1	7.3 ± 0.8		
^{214}Pb[1]	295.22	295.12 ± 0.03	408.2 ± 29.7	13.8 ± 1.0	12.2 / 36 (0.34)	1.000
?	-	344.07 ± 0.08	381.7 ± 72.6	2.8 ± 0.6	22.4 / 36 (0.62)	0.962
^{214}Pb[1]	351.93	351.89 ± 0.03	443.0 ± 21.5	20.8 ± 0.0	26.8 / 36 (0.74)	0.867
^{208}Tl + annih.	510.77, 511.00	510.88 ± 0.19	1209.8 ± 189.0	5.1 ± 0.0	25.6 / 36 (0.71)	0.900
^{208}Tl[1]	583.19	583.18 ± 0.13	620.3 ± 99.9	2.7 ± 0.5	18.3 / 36 (0.51)	0.994
^{214}Bi[1]	609.32	609.58 ± 0.05	703.5 ± 40.2	15.6 ± 1.0	17.4 / 36 (0.48)	0.996
^{214}Bi[1]	768.36	768.36 ± 0.23	1113.3 ± 190.3	2.6 ± 0.0	14.6 / 36 (0.40)	0.999
^{210}Po	803.10	803.61 ± 0.35	1042.1 ± 280.6	1.3 ± 0.4	13.0 / 36 (0.36)	1.000
^{228}Ac	911.20	911.80 ± 0.22	1024.9 ± 183.3	2.3 ± 0.5	13.2 / 36 (0.37)	1.000
^{214}Bi, ^{65}Zn + atomic	1120.29, 1124.52	1122.03 ± 0.52	2171.4 ± 487.9	2.5 ± 0.6	25.3 / 36 (0.70)	0.910

[1]Used in energy calibration and fit of energy resolution function.

Table C.3: continued

Peak	**Energy** [**keV**]	**Centroid** [**keV**]	**Sigma** [**eV**]	**Count Rate** [μ**Hz**]	χ^2 **/ DOF**	**P-value**
^{40}K[1]	1460.82	1461.08 ± 0.28	1887.1 ± 244.5	3.3 ± 0.5	12.7 / 36 (0.35)	1.000
^{214}Bi	1764.49	1765.35 ± 0.20	674.1 ± 157.8	0.7 ± 0.2	9.4 / 36 (0.26)	1.000

[1]Used in energy calibration and fit of energy resolution function.

Table C.4: Peaks in spectrum of unshielded MALBEK response to backgrounds.

Peak	Energy [keV]	Centroid [keV]		Sigma [eV]		Count Rate [mHz]		χ^2	/ DOF	P-value
pulser	-	35.73	± 0.00	118.9	± 0.5	1002.6	± 5.3	34.7	/ 36 (0.96)	0.532
Pb $K_{\alpha 2}$[1]	72.81	73.05	± 0.03	185.2	± 32.4	6.6	± 1.0	52.1	/ 57 (0.91)	0.661
Pb $K_{\alpha 1}$[1]	74.97	75.22	± 0.02	229.4	± 19.9	14.9	± 1.2			
Pb $K_{\beta 3}$, Pb $K_{\beta 1}$	84.45, 84.94	85.08	± 0.04	208.6	± 36.9	5.4	± 1.0	27.5	/ 36 (0.76)	0.845
^{212}Pb[1]	238.63	238.71	± 0.02	265.4	± 16.3	22.7	± 1.3	48.4	/ 57 (0.85)	0.784
^{214}Pb[1]	242.00	241.99	± 0.02	314.4	± 30.6	19.8	± 1.5			
^{133}Ba + ^{208}Tl	276.40, 277.37	276.67	± 0.09	582.2	± 86.9	10.0	± 1.6	26.4	/ 36 (0.73)	0.878
^{214}Pb[1]	295.22	295.19	± 0.01	326.2	± 10.6	46.5	± 1.5	40.6	/ 36 (1.13)	0.274
^{133}Ba[1]	302.85	302.80	± 0.04	291.3	± 43.2	8.0	± 1.0	30.7	/ 36 (0.85)	0.719
^{228}Ac[1]	338.32	338.09	± 0.05	267.4	± 53.5	4.5	± 0.8	31.8	/ 36 (0.88)	0.668
^{214}Pb[1]	351.93	351.89	± 0.01	349.2	± 7.0	78.9	± 1.7	47.9	/ 58 (0.83)	0.824
^{133}Ba[1]	356.01	355.96	± 0.01	335.4	± 13.9	28.8	± 1.2			
^{133}Ba[1]	383.85	383.96	± 0.05	260.1	± 43.0	4.3	± 0.7	45.0	/ 36 (1.25)	0.145
^{208}Tl + annih.	510.77, 511.00	510.74	± 0.13	1048.8	± 134.7	10.2	± 1.5	27.9	/ 36 (0.78)	0.829
^{208}Tl[1]	583.19	583.19	± 0.03	470.3	± 27.4	12.8	± 0.0	25.4	/ 36 (0.70)	0.907
^{214}Bi[1]	609.32	609.33	± 0.01	461.8	± 8.6	70.4	± 1.5	34.1	/ 36 (0.95)	0.561
^{137}Cs[1]	661.66	661.78	± 0.10	448.7	± 88.8	2.5	± 0.5	39.1	/ 51 (0.77)	0.889
^{214}Bi[1]	665.45	665.55	± 0.05	271.1	± 44.4	2.6	± 0.4			
^{212}Bi[1]	727.33	727.32	± 0.09	426.6	± 64.3	2.7	± 0.0	40.5	/ 36 (1.13)	0.277
^{214}Bi[1]	768.36	768.53	± 0.06	511.4	± 61.8	6.3	± 0.7	38.3	/ 36 (1.06)	0.364
^{228}Ac[1]	911.20	911.34	± 0.05	542.8	± 44.2	6.9	± 0.6	17.9	/ 36 (0.50)	0.995
^{214}Bi[1]	934.06	934.18	± 0.09	619.5	± 81.2	3.8	± 0.5	35.3	/ 36 (0.98)	0.503
^{214}Bi[1]	1120.29	1120.42	± 0.03	609.8	± 28.7	14.5	± 0.0	25.3	/ 36 (0.70)	0.909
^{214}Bi	1155.21	1155.45	± 0.10	434.1	± 85.1	1.7	± 0.3	19.5	/ 36 (0.54)	0.989
^{60}Co[1]	1173.23	1173.32	± 0.05	628.5	± 44.7	8.3	± 0.6	27.8	/ 36 (0.77)	0.836
^{214}Bi[1]	1238.12	1238.26	± 0.08	804.4	± 72.3	5.6	± 0.0	28.5	/ 36 (0.79)	0.809

Table C.4: continued

Peak	Energy [keV]	Centroid [keV]		Sigma [eV]		Count Rate [mHz]		χ^2	/ DOF	P-value
^{60}Co[1]	1332.49	1332.57	± 0.06	803.5	± 55.7	7.2	± 0.0	16.3	/ 36 (0.45)	0.998
^{214}Bi[1]	1377.67	1377.76	± 0.08	616.7	± 77.3	2.6	± 0.0	26.6	/ 36 (0.74)	0.874
^{214}Bi	1407.99	1407.95	± 0.14	585.1	± 125.0	1.3	± 0.3	31.4	/ 36 (0.87)	0.687
^{40}K[1]	1460.82	1460.73	± 0.02	745.2	± 15.7	38.3	± 0.0	22.5	/ 36 (0.63)	0.961
^{214}Bi	1509.21	1509.00	± 0.11	421.6	± 138.0	0.9	± 0.2	14.3	/ 36 (0.40)	1.000
^{214}Bi[1]	1729.60	1729.46	± 0.15	811.1	± 133.9	1.2	± 0.2	17.0	/ 36 (0.47)	0.997
^{214}Bi[1]	1764.49	1764.22	± 0.06	884.8	± 46.6	6.5	± 0.4	15.6	/ 36 (0.43)	0.999
^{214}Bi[1]	1847.43	1847.29	± 0.13	566.7	± 102.9	0.7	± 0.0	10.7	/ 36 (0.30)	1.000
^{214}Bi	2204.06	2203.35	± 0.00	995.7	± 0.0	0.8	± 0.0	5.7	/ 36 (0.16)	1.000

[1]Used in energy calibration and fit of energy resolution function.

Table C.5: Peaks in the energy spectrum of MALBEK response to ^{133}Ba. Peaks were fit with the unbinned maximum likelihood method.

Peak	Energy [keV]	Centroid [keV]		Sigma [eV]		Count Rate [mHz]		χ^2	/ DOF	P-value
pulser	-	21.32	± 0.00	120.5	± 1.5	1005.2	± 14.0	30.6	/ 36 (0.85)	0.721
Pb $K_{\alpha 2}$	72.81	72.85	± 0.05	202.2	± 33.9	32.7	± 6.6	68.2	/ 57 (1.20)	0.148
Pb $K_{\alpha 1}$[1]	74.97	75.06	± 0.03	211.5	± 30.5	53.4	± 7.9			
^{133}Ba[1,2]	79.61	79.74	± 0.01	192.0	± 5.1	451.8	± 0.2	88.5	/ 47 (1.88)	2.4E-04
^{133}Ba[1,2]	81.00	81.10	± 0.00	197.1	± 0.9	6018.0	± 0.2			
^{133}Ba[1]	160.61	160.56	± 0.01	238.3	± 8.8	302.2	± 11.0	34.7	/ 36 (0.97)	0.528
^{133}Ba[1]	223.24	223.17	± 0.01	282.7	± 14.2	180.7	± 8.8	22.5	/ 36 (0.63)	0.961
^{212}Pb	238.63	238.79	± 0.07	289.2	± 48.1	28.9	± 5.8	59.1	/ 57 (1.04)	0.399
^{214}Pb[1]	242.00	241.98	± 0.08	454.9	± 94.6	48.0	± 9.0			
^{133}Ba[1]	276.40	276.36	± 0.00	319.3	± 2.4	2335.8	± 20.5	31.4	/ 36 (0.87)	0.686
^{214}Pb[1]	295.22	295.18	± 0.03	286.6	± 26.5	58.9	± 5.6	36.4	/ 36 (1.01)	0.449
^{133}Ba[1]	302.85	302.74	± 0.00	330.8	± 1.5	5395.5	± 30.4	55.4	/ 36 (1.54)	0.021
^{214}Pb[1,2]	351.93	351.88	± 0.03	327.2	± 22.6	77.1	± 5.8	93.6	/ 57 (1.64)	1.6E-03
^{133}Ba[1,2]	356.01	355.94	± 0.00	354.5	± 0.9	15109.9	± 50.1			
^{133}Ba[1]	383.85	383.82	± 0.00	368.3	± 2.6	1990.2	± 18.3	37.9	/ 36 (1.05)	0.382
^{208}Tl[1]	583.19	583.35	± 0.06	359.9	± 65.2	12.3	± 2.0	22.5	/ 36 (0.63)	0.961
^{214}Bi[1]	609.32	609.41	± 0.02	475.9	± 19.3	82.4	± 4.0	39.0	/ 36 (1.08)	0.338
^{137}Cs[1]	661.66	661.83	± 0.06	492.7	± 58.5	17.9	± 2.1	27.5	/ 51 (0.54)	0.997
^{214}Bi[1]	768.36	768.60	± 0.10	-425.0	± 91.9	6.2	± 0.2	22.3	/ 36 (0.62)	0.964
^{228}Ac	911.20	911.83	± 0.11	454.2	± 85.7	5.6	± 1.3	14.0	/ 36 (0.39)	1.000
^{214}Bi	934.06	934.33	± 0.51	-121.5	± 9761.5	2.2	± 0.0	20.5	/ 36 (0.57)	0.983
^{60}Co[1]	1173.23	1173.78	± 0.12	607.9	± 111.7	8.4	± 1.5	15.1	/ 36 (0.42)	0.999
^{214}Bi	1238.12	1238.47	± 0.09	346.2	± 67.9	4.3	± 1.0	12.9	/ 36 (0.36)	1.000
^{60}Co	1332.49	1333.22	± 0.13	577.0	± 160.9	6.3	± 1.3	10.6	/ 36 (0.29)	1.000
^{214}Bi	1377.67	1377.91	± 0.16	615.9	± 140.4	3.7	± 0.9	10.7	/ 36 (0.30)	1.000

Table C.5: continued

Peak	Energy [keV]	Centroid [keV]		Sigma [eV]		Count Rate [mHz]		χ^2	/ DOF	P-value
^{40}K[1]	1460.82	1461.15	± 0.05	662.1	± 39.1	33.2	± 2.4	9.0	/ 36 (0.25)	1.000
^{214}Bi	1764.49	1764.47	± 1.58	1460.7	± 1945.7	9.9	± 0.1	15.2	/ 36 (0.42)	0.999

[1]Used in energy calibration and fit of energy resolution function.

[2]Erfc step function used in fit.

Appendix D

MGDO CLASSES FOR ENCAPSULATION OF MONTE CARLO RESULTS

Table D.1: Selected data members of MGDO's `MGTMCRun` class, which encapsulates run-level information about a Monte-Carlo simulation.

Data Type	**Data Member**	**Description**
uint64_t	fRunID	an identification number for the run
uint64_t	fNEvents	the number of events simulated
map <string, int>	fSensitiveVolumeIDs	map of geometry volume names to sensitive volume IDs
bool	fWriteAllSteps	whether all steps were written
bool	fKillAlphas	whether alpha tracks were killed
bool	fKillBetas	whether beta tracks were killed
bool	fKillGammas	whether gamma tracks were killed
bool	fKillNeutrons	whether neutrons were killed
bool	fStopNuclei	stop nuclei outside sensitive volumes, but don't kill them
bool	fUseTimeWindow	whether events were time windowed
double	fTimeWindow	duration of time window
bool	fUseImportanceSampling	whether geometry importance sampling was used
int32_t	fBiasedParticleID	particle ID of the biased particle
bool	fUseImportanceProcessWindow	whether tracks created by importance sampling were windo
bool	fUseParallelWorld	whether parallel geometry was used
uint32_t	fAmax	maximum atomic number of nuclei allowed to decay
uint32_t	fAmin	minimum atomic number of nuclei allowed to decay
uint32_t	fZmax	maximum proton number of nuclei allowed to decay
uint32_t	fZmin	minimum proton number of nuclei allowed to decay
string	fMaGeRevision	MAGE svn revision
string	fMaGeTag	MAGE svn tag
string	fMGDORevision	MGDO svn revision
string	fMGDOTag	MGDO svn tag
string	fGeantVersion	GEANT4 release version
string	fCLHEPVersion	CLHEP release version
string	fROOTVersion	ROOT release version

Table D.2: Data members of MGDO's `MGTMCEventHeader` class, which encapsulates event-level Monte-Carlo information.

Data Type	**Data Member**	**Description**
uint64_t	fEventID	identification number for the event
string	fRandGenStatefEventID	state of random number generator
double	fTotalEnergy	total energy deposited in detectors
map <int, double>	fEnergyOfDetectorID	map of sensitive detector IDs to the energy deposited in each detector

Table D.3: Selected data members of MGDO's `MGTMCEventSteps` class, which encapsulates information about steps in a Monte-Carlo event.

Data Type	**Data Member**	**Description**
uint64_t	fEventID	identification number of the event
int	fNSteps	number of steps
TClonesArray	fSteps	ROOT-based array of `MGTMCStepData` objects

Table D.4: Selected data members of MGDO's `MGTMCStepData` class, which encapsulates information about a Monte-Carlo step.

Data Type	**Data Member**	**Description**
bool	fIsPreStep	whether this information describes the beginning or end of a step
int	fParticleID	type of particle
int	fTrackID	ID number for the particle's track
int	fParentTrackID	ID of the track that created this particle
string	fProcessName	the interaction that produced these conditions
string	fPhysVolName	name of the volume containing the particle
int	fSensVolID	ID of the volume containing the particle
double	fT	time since the start of the event
double	fT	offset time, used if the event is time-windowed
double	fEdep	energy deposited in the step
double	fKineticEnergy	kinetic energy of the particle
double	fStepLength	length of the step
double	fTotalTrackLength	length of the particle's track
double	f[X, Y, Z]	x, y, and z coordinates relative to a global coordinate system
double	fLocal[X, Y, Z]	x, y, and z coordinates relative to the origin of the volume containing the particle
double	fP[x, y, z]	x, y, and z components of the momentum
int	fStepNumber	the number of the step in the track
double	fTrackWeight	track weight, for importance sampling

Appendix E

GAT CLASSES FOR ENCAPSULATION OF ORCA AND MONTE-CARLO RESULTS

Table E.1: Data members of GAT's `GATAnalysisEvent` class, which encapsulates information about an ORCA or Monte Carlo event.

Data Type	**Data Member**	**Description**
`ULong64_t`	`fRunID`	run identification number
`ULong64_t`	`fEventID`	event identification number
`double`	`fRunStartTime`	run start time
`double`	`fTotalEnergy`	total energy deposited in Ge detector(s)
`double`	`fTotalVetoEnergy`	total energy deposited in muon veto
`UInt_t`	`fNWaveforms`	number of waveforms in this event
`vector`	`fAnalysisEventDataVector`	vector of `GATAnalysisEventData`, one element per waveform
`string`	`fGATRevision`	GAT SVN revision number
`string`	`fGATTag`	GAT SVN tag
`string`	`fMGDORevision`	MGDO SVN revision number
`string`	`fMGDOTag`	MGDO SVN tag
`string`	`fCLHEPVersion`	CLHEP version information
`string`	`fROOTVersion`	ROOT version information

Table E.2: Data members of GAT's `GATAnalysisEventData` class, which encapsulates information about energy deposited in one detector in an event.

Data Type	**Data Member**	**Description**
`UInt_t`	`fID`	electronics channel ID (crate, card, channel)
`ULong64_t`	`fWaveformID`	detector ID
`ULong64_t`	`fWaveformIndex`	index of ith waveform in a run
`double`	`fTime`	time stamp
`double`	`fEnergy`	energy deposited
`double`	`fIsMultiSite`	multi-site analysis result
`double`	`fIsSstc`	single-site time correlation analysis result
`double`	`fIsSlow`	slowness

Appendix F

AN EXAMPLE OF MAGE JOB SUBMISSION

An example of command-line usage appears below, for a run to simulate response of the MALBEK detector to 100,000 decays of ^{68}Ge uniformly distributed in the bulk of the germanium crystal volume. This job was run on the CENPA-Rocks cluster.

```
$ python submitBulkProdJob.py
  usage: submitBulkProdJob.py [-r run id] [-d detector] [A] [Z]
      [volume] [number of events] [kill alphas & stop nuclei] [Amin]
      [Zmin] [Amax] [Zmax]
    - flags are optional --  default detector is BEGe-KURF-InShield,
      default run id is 17649
    - kill alphas & stop nuclei is optional, can be 0 or 1, default
      is 0 (False)
    - nucleus bounds (Amin, Zmin, Amax, Zmax) are optional.  If any
      bounds are set, all must be set.  If any bounds are set, stop
      nucleus must be set to 0 or 1.  Nucleus bounds specify isotopes
      that *will* decay.

$ python submitBulkProdJob.py 68 32 ActiveCrystal0CrystalColumn0 100000
```

The Python scripts store MAGE/GEANT4 output from the jobs in an organized directory structure on disk, in a directory defined by the environment variable `MAGERESULTS`: A ROOT file, a MAGE macro, a shell script for job submission, a file of standard output, and a file of standard error are produced by the Python code and are saved for each run. The MAGE macro produced by the command above appears in Appendix G. Other scripts handle the submission of cosmic ray simulations and steps in decay chains as described in Section 5.6.

```
$MAGERESULTS/[detector]/[decay type]/[volume]/[contaminant]
```

In the example of ^{68}Ge decays above, results were saved in the following location:

```
$MAGERESULTS/BEGe-KURF-InShield/bulk/ActiveCrystal0CrystalColumn0/A68_Z32
```

Appendix G

A MaGe MACRO

This sample MaGe macro was produced on the CENPA-Rocks cluster using the script `submitBulkProdJob.py`. Arguments to `submitBulkProdJob.py` specified the simulation of MALBEK response to 100000 decays of ^{68}Ge uniformly distributed in the volume of the germanium crystal.

```
# auto generated by runBulkProdJob.py
# on 2012-02-06 13:24:16.267727

/MG/manager/mglog routine
/MG/eventaction/reportingfrequency 10000
/MG/manager/seedWithUUID
/MG/processes/realm BBdecay
/MG/processes/lowenergy true

/MG/geometry/detector BEGe-KURF-InShield
/MG/geometry/WorldMaterial Vacuum
/MG/eventaction/rootschema MCRun

/MG/eventaction/rootfilename /SCRATCH/alexis/MaGeResults/openFiles/
    BEGeKURFInShield_bulk_A68_Z32_in_ActiveCrystal0CrystalColumn0_1000_17649.root
/MG/io/MCRun/SetSensitiveIDLabelScheme classic

/MG/io/MCRun/setRunID 17649

/MG/io/MCRun/useTimeWindow true
/MG/io/MCRun/setTimeWindow 86400 second

/run/initialize
/MG/generator/select RDMiso
/gun/energy 0 eV
```

```
/grdm/ion 68 32 0

/MG/generator/confine volume
/MG/generator/volume ActiveCrystal0CrystalColumn0

/run/beamOn 100000
```

The following command could be added before `/run/beamOn` to specify nuclei that are allowed to decay in the simulation:

```
/grdm/nucleusLimits [Amin] [Amax] [Zmin] [Zmax]
```

where A_{min}, A_{max}, Z_{min}, and Z_{max} specify mass numbers and proton numbers of isotopes that are allowed to decay. This command is used to split the ^{232}Th and ^{238}U decay chains into steps as described in Section5.6.

The following command can be added before `/run/initialize` to turn on parallel worlds:

```
/MG/geometry/useParallelWorld true
```

The following command can be added after `/run/initialize` to perform geometry importance sampling of gammas:

```
/MG/geometry/EventBias/useImportanceSampling true
/MG/geometry/EventBias/setBiasedParticle gamma
/MG/geometry/EventBias/initializeVarRed
```

The following command can be used before `/run/initialize` to window importance-sampled events:

```
/MG/io/MCRun/useImportanceSamplingWindow
```

Importance-sampling windowing should not be used together with time windowing.

Appendix H

SOFTWARE VERSION INFORMATION

Table H.1: GEANT4 version information.

Package Description	**Version**
CLHEP	2.0.4.7
GEANT4	4.9.3.p01
GEANT4 Data Files	
Neutron data with thermal cross sections	G4NDL 3.13
Low-energy electromagnetic processes	G4EMLOW 6.9
Photon evaporation	PhotonEvaporation 2.0
Radioactive decay hadronic processes	RadioactiveDecay 3.2
Nuclear shell effects in INCL/ABLA hadronic model	G4ABLA 3.0
Measured optical surface reflectance	RealSurface 1.0

Table H.2: Summary of MAGE Tier 0 settings and results.

Parameter	**Value**
MAGE SVN version	trunk $\leq$5785
MGDO SVN version	trunk $\leq$5785
Number of ROOT output files	12910
Total size of output files	646 GB
Approximate run time	5×10^4 CPU hours

Table H.3: Summary of GAT-processed MAGE Tier 1 settings and results.

Parameter	**Value**
GAT SVN version	trunk $\leq$5785
MGDO SVN version	trunk $\leq$5785
Number of ROOT output files	12910
Total size of output files	36 GB

Appendix I

COMPONENTS IN THE MaGe/Geant4 MALBEK MODEL

Table I.1: Components in MaGe/Geant4 geometry model. Table generated by *MJBMDbInfo.ComponentsStore*.

Component	**Material**	**Mass [kg]**	**Reference**
ActiveCrystal0CrystalColumn0	Germanium-Nat	4.55E-01	Geant4
centerContactSolderPhysical	Tin	7.36E-06	Geant4
compressionSpringLogical	StainlessSteel304	1.28E-04	Geant4
connectorInsulatorPhysical0	Teflon	6.12E-05	Geant4
connectorInsulatorPhysical1	Teflon	6.12E-05	Geant4
connectorInsulatorPhysical2	Teflon	6.12E-05	Geant4
connectorInsulatorPhysical3	Teflon	6.12E-05	Geant4
connectorInsulatorPhysical4	Teflon	6.12E-05	Geant4
connectorInsulatorPhysical5	Teflon	6.12E-05	Geant4
copperCupPhysical	Copper-OFHC	1.49E-01	Geant4
copperLidPhysical	Copper-OFHC	8.95E-02	Geant4
cryostatNeckAndFlangePhysical	StainlessSteel304	8.25E-01	Geant4
detectorSpacerPhysical	Copper-OFHC	1.52E-02	Geant4
ebDHPin0	Brass	7.45E-05	Geant4
ebDHPin1	Brass	7.45E-05	Geant4
ebDHPin2	Brass	7.45E-05	Geant4
ebDHPin3	Brass	7.45E-05	Geant4

Table I.1: continued

Component	**Material**	**Mass [kg]**	**Reference**
ebDHPin4	Brass	7.45E-05	GEANT4
ebDHPin5	Brass	7.45E-05	GEANT4
electronicsBasePhysical	Copper-OFHC	1.89E-01	GEANT4
endCapLogical	Copper-OFHC	5.35E-01	GEANT4
fDHPinInReceptaclePhysical1	Brass	1.27E-04	GEANT4
fDHPinInReceptaclePhysical2	Brass	1.27E-04	GEANT4
fDHPinInReceptaclePhysical3	Brass	1.27E-04	GEANT4
fDHPinInReceptaclePhysical4	Brass	1.27E-04	GEANT4
fDHPinPhysical	Brass	7.41E-05	GEANT4
fFETPhysical	MoxtekFET	1.16E-06	GEANT4[1]
fHeaterResistorPhysical	Resistor	9.18E-06	GEANT4[1]
fInjectorResistorPhysical	Resistor	9.18E-06	GEANT4[1]
fetBlockPhysical	Copper-OFHC	2.41E-02	GEANT4
fetSolderPhysical	Tin	3.86E-06	GEANT4
hvContactExtensionPhysical	Teflon	9.75E-04	GEANT4
hvPogoBarrelPhysical	NickelSilver	1.13E-03	GEANT4
hvPogoPlungerPhysical	BerylliumCopper	1.08E-04	GEANT4
hvSolderPhysical	Tin	2.33E-06	GEANT4
innerAinLeadPhysical	Lead-Ain	4.10E+01	GEANT4
leadShield	Lead-Mod	1.89E+03	GEANT4
leadShieldSampling	Lead-Mod	5.56E+01	GEANT4
millMaxReceptaclePhysical	Brass	5.47E-05	GEANT4
outsideTestPhysical	Air	2.61E+03	GEANT4
patchOnePhysical	Lead-Patch	2.49E-03	GEANT4[1]
patchTwoPhysical	Lead-Patch	1.88E-03	GEANT4[1]
pentaPlugPhysical	Teflon	2.50E-04	GEANT4

Table I.1: continued

Component	**Material**	**Mass [kg]**	**Reference**
pentaReceptaclePhysical	Teflon	6.59E-04	GEANT4
polySpiderPhysical	Teflon	5.46E-02	GEANT4
rdcColdFingerPhysical	Copper-OFHC	1.05E+00	GEANT4
rockPhysical	Rock	4.35E+08	GEANT4
rockSampling	Rock	3.29E+05	GEANT4
smallRockSampling	Rock	4.15E+03	GEANT4
spiderTrestlePhysical	Copper-OFHC	1.40E-01	GEANT4
supportPostPhysical0	Teflon	2.05E-04	GEANT4
teflonCupPhysical	Teflon	1.78E-02	GEANT4
teflonDiskPhysical	Teflon	3.75E-03	GEANT4
threadedCollarPhysical	Copper-OFHC	3.62E-02	GEANT4
trailerAirSpace	Air	1.57E+01	GEANT4
trailerAirSpaceSampling	Air	5.78E-02	GEANT4
trailerPhysical	StainlessSteel304	6.22E+02	GEANT4
zeolitePhysical	Zeolite	7.50E-02	Mass entered by hand

[1]Material name entered by hand.

Table I.2: Surfaces in MaGe/Geant4 geometry model. Table generated by *MJBMDbInfo.-ComponentsStore*.

Component	**Material**	**Surf. Area [cm^2]**	**Reference**
cosmic	KURF-Experimental-Hall	1.26E+09	calc from GSS
surfacesInsideCryostat	Rn-Exposure-In-Cryostat	8.86E+03	calc from GSS
surfacesOutsideCryostat	Rn-Exposure-Outside-Cryostat	1.06E+04	calc from GSS

Appendix J

RADIOPURITY DATA FOR THE MALBEK BACKGROUND MODEL

Table J.1: Radiopurity information for Air. Table generated by *MJBMDbInfo.ComponentsStore*.

Contaminant	**Activity/ Production Rate**	**Reference**
^{226}Ra to ^{222}Rn (^{238}U step 5)	8.61E-01 μBq/kg	MAJORANA BSD [79]
^{222}Rn to ^{210}Tl or ^{210}Pb (^{238}U step 6)	8.61E-01 μBq/kg	MAJORANA BSD [79]
^{210}Tl to ^{210}Pb (^{238}U step 6a)	1.81E-04 μBq/kg	MAJORANA BSD [79]
^{210}Pb to ^{210}Bi or ^{206}Pb (^{238}U step 7)	8.61E-01 μBq/kg	MAJORANA BSD [79]
^{210}Bi to ^{210}Po or ^{206}Pb (^{238}U step 8)	8.61E-01 μBq/kg	MAJORANA BSD [79]
^{210}Po to ^{206}Pb (^{238}U step 9)	8.61E-01 μBq/kg	MAJORANA BSD [79]

Table J.2: Radiopurity information for BerylliumCopper. Table generated by *MJBM-DbInfo.ComponentsStore*.

Contaminant	**Activity/ Production Rate**	**Reference**
^{232}Th to ^{228}Ra (^{232}Th step 1)	5.50E+05 μBq/kg	Edelweiss CuBe Foil Avg. – ILIAS [53]
^{228}Ra to ^{228}Th (^{232}Th step 2)	5.50E+05 μBq/kg	Edelweiss CuBe Foil Avg. – ILIAS [53]
^{228}Th to ^{224}Ra (^{232}Th step 3)	5.50E+05 μBq/kg	Edelweiss CuBe Foil Avg. – ILIAS [53]
^{224}Ra to ^{208}Pb (^{232}Th step 4)	5.50E+05 μBq/kg	Edelweiss CuBe Foil Avg. – ILIAS [53]
^{238}U to ^{234}Th (^{238}U step 1)	2.00E+07 μBq/kg	Edelweiss CuBe Foil Avg. – ILIAS [53]
^{234}Th to ^{234}U (^{238}U step 2)	2.00E+07 μBq/kg	Edelweiss CuBe Foil Avg. – ILIAS [53]
^{234}U to ^{230}Th (^{238}U step 3)	2.00E+07 μBq/kg	Edelweiss CuBe Foil Avg. – ILIAS [53]
^{230}Th to ^{226}Ra (^{238}U step 4)	2.00E+07 μBq/kg	Edelweiss CuBe Foil Avg. – ILIAS [53]
^{226}Ra to ^{222}Rn (^{238}U step 5)	5.00E+06 μBq/kg	Edelweiss CuBe Foil Avg. – ILIAS [53]
^{222}Rn to ^{210}Tl or ^{210}Pb (^{238}U step 6)	5.00E+06 μBq/kg	Edelweiss CuBe Foil Avg. – ILIAS [53]
^{210}Tl to ^{210}Pb (^{238}U step 6a)	1.05E+03 μBq/kg	Edelweiss CuBe Foil Avg. – ILIAS [53]
^{210}Pb to ^{210}Bi or ^{206}Pb (^{238}U step 7)	5.00E+06 μBq/kg	Edelweiss CuBe Foil Avg. – ILIAS [53]
^{210}Bi to ^{210}Po or ^{206}Pb (^{238}U step 8)	5.00E+06 μBq/kg	Edelweiss CuBe Foil Avg. – ILIAS [53]
^{210}Po to ^{206}Pb (^{238}U step 9)	5.00E+06 μBq/kg	Edelweiss CuBe Foil Avg. – ILIAS [53]

Table J.3: Radiopurity information for Brass. Table generated by *MJBMDbInfo.ComponentsStore*.

Contaminant	**Activity/ Production Rate**	**Reference**
^{232}Th to ^{228}Ra (^{232}Th step 1)	2.00E+03 μBq/kg	Brass rod, leadless – ILIAS [53]
^{228}Ra to ^{228}Th (^{232}Th step 2)	2.00E+03 μBq/kg	Brass rod, leadless – ILIAS [53]
^{228}Th to ^{224}Ra (^{232}Th step 3)	2.00E+03 μBq/kg	Brass rod, leadless – ILIAS [53]
^{224}Ra to ^{208}Pb (^{232}Th step 4)	5.56E+03 μBq/kg	Brass rod, leadless – ILIAS [53]
^{238}U to ^{234}Th (^{238}U step 1)	5.00E+03 μBq/kg	Brass rod, leadless – ILIAS [53]
^{234}Th to ^{234}U (^{238}U step 2)	5.00E+03 μBq/kg	Brass rod, leadless – ILIAS [53]
^{234}U to ^{230}Th (^{238}U step 3)	5.00E+03 μBq/kg	Brass rod, leadless – ILIAS [53]
^{230}Th to ^{226}Ra (^{238}U step 4)	5.00E+03 μBq/kg	Brass rod, leadless – ILIAS [53]
^{226}Ra to ^{222}Rn (^{238}U step 5)	5.00E+03 μBq/kg	Brass rod, leadless – ILIAS [53]
^{222}Rn to ^{210}Tl or ^{210}Pb (^{238}U step 6)	5.00E+03 μBq/kg	Brass rod, leadless – ILIAS [53]
^{210}Tl to ^{210}Pb (^{238}U step 6a)	1.05E+00 μBq/kg	Brass rod, leadless – ILIAS [53]
^{210}Pb to ^{210}Bi or ^{206}Pb (^{238}U step 7)	2.30E+06 μBq/kg	Brass rod, leadless – ILIAS [53]
^{210}Bi to ^{210}Po or ^{206}Pb (^{238}U step 8)	2.30E+06 μBq/kg	Brass rod, leadless – ILIAS [53]
^{210}Po to ^{206}Pb (^{238}U step 9)	2.30E+06 μBq/kg	Brass rod, leadless – ILIAS [53]
^{40}K	3.00E+03 μBq/kg	Brass rod, leadless – ILIAS [53]
^{60}Co	3.00E+03 μBq/kg	Brass rod, leadless – ILIAS [53]

Table J.4: Radiopurity information for Copper-OFHC. Table generated by *MJBMDbInfo.-ComponentsStore*.

Contaminant	Activity/ Production Rate	Reference
^{232}Th to ^{228}Ra (^{232}Th step 1)	9.00E-01 μBq/kg	DEMONSTRATOR Table [99]
^{228}Ra to ^{228}Th (^{232}Th step 2)	9.00E-01 μBq/kg	DEMONSTRATOR Table [99]
^{228}Th to ^{224}Ra (^{232}Th step 3)	9.00E-01 μBq/kg	DEMONSTRATOR Table [99]
^{224}Ra to ^{208}Pb (^{232}Th step 4)	9.00E-01 μBq/kg	DEMONSTRATOR Table [99]
^{238}U to ^{234}Th (^{238}U step 1)	3.00E+00 μBq/kg	DEMONSTRATOR Table [99]
^{234}Th to ^{234}U (^{238}U step 2)	3.00E+00 μBq/kg	DEMONSTRATOR Table [99]
^{234}U to ^{230}Th (^{238}U step 3)	3.00E+00 μBq/kg	DEMONSTRATOR Table [99]
^{230}Th to ^{226}Ra (^{238}U step 4)	3.00E+00 μBq/kg	DEMONSTRATOR Table [99]
^{226}Ra to ^{222}Rn (^{238}U step 5)	3.00E+00 μBq/kg	DEMONSTRATOR Table [99]
^{222}Rn to ^{210}Tl or ^{210}Pb (^{238}U step 6)	3.00E+00 μBq/kg	DEMONSTRATOR Table [99]
^{210}Tl to ^{210}Pb (^{238}U step 6a)	6.30E-04 μBq/kg	DEMONSTRATOR Table [99]
^{210}Pb to ^{210}Bi or ^{206}Pb (^{238}U step 7)	3.00E+00 μBq/kg	DEMONSTRATOR Table [99]
^{210}Bi to ^{210}Po or ^{206}Pb (^{238}U step 8)	3.00E+00 μBq/kg	DEMONSTRATOR Table [99]
^{210}Po to ^{206}Pb (^{238}U step 9)	3.00E+00 μBq/kg	DEMONSTRATOR Table [99]
^{40}K	1.24E+01 μBq/kg	EXO [93]
^{46}Sc	4.58E+00 atoms/kg/day	Heusser et al. [100]
^{48}V	9.50E+00 atoms/kg/day	Heusser et al. [100]
^{56}Co	1.99E+01 atoms/kg/day	Heusser et al. [100]
^{57}Co	1.56E+02 atoms/kg/day	Heusser et al. [100]
^{58}Co	1.43E+02 atoms/kg/day	Heusser et al. [100]
^{59}Fe	3.93E+01 atoms/kg/day	Heusser et al. [100]
^{60}Co	2.00E+02 atoms/kg/day	DEMONSTRATOR Table [99]

Table J.5: Radiopurity information for Germanium-Nat. Table generated by *MJBMDbInfo.-ComponentsStore*.

Contaminant	Activity/ Production Rate	Reference
^{232}Th to ^{228}Ra (^{232}Th step 1)	4.07E-03 μBq/kg	J. A. Detwiler [101]
^{228}Ra to ^{228}Th (^{232}Th step 2)	4.07E-03 μBq/kg	J. A. Detwiler [101]
^{228}Th to ^{224}Ra (^{232}Th step 3)	4.07E-03 μBq/kg	J. A. Detwiler [101]
^{224}Ra to ^{208}Pb (^{232}Th step 4)	4.07E-03 μBq/kg	J. A. Detwiler [101]
^{238}U to ^{234}Th (^{238}U step 1)	1.23E-02 μBq/kg	J. A. Detwiler [101]
^{234}Th to ^{234}U (^{238}U step 2)	1.23E-02 μBq/kg	J. A. Detwiler [101]
^{234}U to ^{230}Th (^{238}U step 3)	1.23E-02 μBq/kg	J. A. Detwiler [101]
^{230}Th to ^{226}Ra (^{238}U step 4)	1.23E-02 μBq/kg	J. A. Detwiler [101]
^{226}Ra to ^{222}Rn (^{238}U step 5)	1.23E-02 μBq/kg	J. A. Detwiler [101]
^{222}Rn to ^{210}Tl or ^{210}Pb (^{238}U step 6)	1.23E-02 μBq/kg	J. A. Detwiler [101]
^{210}Tl to ^{210}Pb (^{238}U step 6a)	2.59E-06 μBq/kg	J. A. Detwiler [101]
^{210}Pb to ^{210}Bi or ^{206}Pb (^{238}U step 7)	1.23E-02 μBq/kg	J. A. Detwiler [101]
^{210}Bi to ^{210}Po or ^{206}Pb (^{238}U step 8)	1.23E-02 μBq/kg	J. A. Detwiler [101]
^{210}Po to ^{206}Pb (^{238}U step 9)	1.23E-02 μBq/kg	J. A. Detwiler [101]
^{3}H	2.77E+01 atoms/kg/day	D.-M. Mei [102]
^{54}Mn	9.10E+00 atoms/kg/day	Avg. from Table I [103]
^{55}Fe	8.40E+00 atoms/kg/day	MAJORANA BSD – GENIUS [79]
^{57}Co	6.84E+00 atoms/kg/day	Avg. from Table I [103]
^{58}Co	1.61E+01 atoms/kg/day	MAJORANA BSD – GENIUS [79]
^{60}Co	5.00E+00 atoms/kg/day	DEMONSTRATOR Table [99]
^{63}Ni	4.60E+00 atoms/kg/day	MAJORANA BSD – GENIUS [79]
^{65}Zn	7.90E+01 atoms/kg/day	MAJORANA BSD – GENIUS [79]
^{68}Ge	3.00E+01 atoms/kg/day	DEMONSTRATOR Table [99]
^{76}Ge $2\nu\beta\beta$	9.03E+00 μBq/kg	A.S. Barabash [13]

Table J.6: Radiopurity information for KURF-Experimental-Hall. Table generated by *MJBMDbInfo.ComponentsStore*.

Contaminant	**Activity/ Production Rate**	**Reference**
Cosmogenic muons	7.79E-01 μBq/cm^2	D.-M. Mei and A. Hime [81]

Table J.7: Radiopurity information for Lead-Ain. Table generated by *MJBMDbInfo.ComponentsStore*.

Contaminant	**Activity/ Production Rate**	**Reference**
^{210}Pb to ^{210}Bi or ^{206}Pb (^{238}U step 7)	1.30E+04 μBq/kg	PNNL measurement [56]
^{210}Bi to ^{210}Po or ^{206}Pb (^{238}U step 8)	1.30E+04 μBq/kg	PNNL measurement [56]
^{210}Po to ^{206}Pb (^{238}U step 9)	1.30E+04 μBq/kg	PNNL measurement [56]

Table J.8: Radiopurity information for Lead-Mod. Table generated by *MJBMDbInfo.ComponentsStore*.

Contaminant	**Activity/ Production Rate**	**Reference**
^{210}Pb to ^{210}Bi or ^{206}Pb (^{238}U step 7)	2.50E+06 μBq/kg	KURF Assay [104]
^{210}Bi to ^{210}Po or ^{206}Pb (^{238}U step 8)	2.50E+06 μBq/kg	KURF Assay [104]
^{210}Po to ^{206}Pb (^{238}U step 9)	2.50E+06 μBq/kg	KURF Assay [104]

Table J.9: Radiopurity information for Lead-Patch. Table generated by *MJBMDbInfo.-ComponentsStore*.

Contaminant	**Activity/ Production Rate**	**Reference**
^{210}Pb to ^{210}Bi or ^{206}Pb (^{238}U step 7)	1.00E+08 μBq/kg	Modern Pb est., J. Collar
^{210}Bi to ^{210}Po or ^{206}Pb (^{238}U step 8)	1.00E+08 μBq/kg	Modern Pb est., J. Collar
^{210}Po to ^{206}Pb (^{238}U step 9)	1.00E+08 μBq/kg	Modern Pb est., J. Collar

Table J.10: Radiopurity information for MoxtekFET. Table generated by *MJBMDbInfo.ComponentsStore*.

Contaminant	Activity/ Production Rate	Reference
^{232}Th to ^{228}Ra (^{232}Th step 1)	7.68E+03 μBq/kg	JFET ICP-MS [105]
^{228}Ra to ^{228}Th (^{232}Th step 2)	7.68E+03 μBq/kg	JFET ICP-MS [105]
^{228}Th to ^{224}Ra (^{232}Th step 3)	7.68E+03 μBq/kg	JFET ICP-MS [105]
^{224}Ra to ^{208}Pb (^{232}Th step 4)	7.68E+03 μBq/kg	JFET ICP-MS [105]
^{238}U to ^{234}Th (^{238}U step 1)	1.74E+03 μBq/kg	JFET ICP-MS [105]
^{234}Th to ^{234}U (^{238}U step 2)	1.74E+03 μBq/kg	JFET ICP-MS [105]
^{234}U to ^{230}Th (^{238}U step 3)	1.74E+03 μBq/kg	JFET ICP-MS [105]
^{230}Th to ^{226}Ra (^{238}U step 4)	1.74E+03 μBq/kg	JFET ICP-MS [105]
^{226}Ra to ^{222}Rn (^{238}U step 5)	1.74E+03 μBq/kg	JFET ICP-MS [105]
^{222}Rn to ^{210}Tl or ^{210}Pb (^{238}U step 6)	1.74E+03 μBq/kg	JFET ICP-MS [105]
^{210}Tl to ^{210}Pb (^{238}U step 6a)	3.65E-01 μBq/kg	JFET ICP-MS [105]
^{210}Pb to ^{210}Bi or ^{206}Pb (^{238}U step 7)	1.74E+03 μBq/kg	JFET ICP-MS [105]
^{210}Bi to ^{210}Po or ^{206}Pb (^{238}U step 8)	1.74E+03 μBq/kg	JFET ICP-MS [105]
^{210}Po to ^{206}Pb (^{238}U step 9)	1.74E+03 μBq/kg	JFET ICP-MS [105]

Table J.11: Radiopurity information for NickelSilver. Table generated by *MJBMDbInfo.ComponentsStore*.

Contaminant	Activity/ Production Rate	Reference
^{232}Th to ^{228}Ra (^{232}Th step 1)	9.00E-01 μBq/kg	60% Cu [99], 20% Ni [53], 20% Zn
^{228}Ra to ^{228}Th (^{232}Th step 2)	9.00E-01 μBq/kg	60% Cu [99], 20% Ni [53], 20% Zn
^{228}Th to ^{224}Ra (^{232}Th step 3)	9.00E-01 μBq/kg	60% Cu [99], 20% Ni [53], 20% Zn
^{224}Ra to ^{208}Pb (^{232}Th step 4)	9.00E-01 μBq/kg	60% Cu [99], 20% Ni [53], 20% Zn
^{238}U to ^{234}Th (^{238}U step 1)	5.02E+02 μBq/kg	60% Cu [99], 20% Ni [53], 20% Zn
^{234}Th to ^{234}U (^{238}U step 2)	5.02E+02 μBq/kg	60% Cu [99], 20% Ni [53], 20% Zn
^{234}U to ^{230}Th (^{238}U step 3)	5.02E+02 μBq/kg	60% Cu [99], 20% Ni [53], 20% Zn
^{230}Th to ^{226}Ra (^{238}U step 4)	5.02E+02 μBq/kg	60% Cu [99], 20% Ni [53], 20% Zn
^{226}Ra to ^{222}Rn (^{238}U step 5)	5.02E+02 μBq/kg	60% Cu [99], 20% Ni [53], 20% Zn
^{222}Rn to ^{210}Tl or ^{210}Pb (^{238}U step 6)	5.02E+02 μBq/kg	60% Cu [99], 20% Ni [53], 20% Zn
^{210}Tl to ^{210}Pb (^{238}U step 6a)	1.05E-01 μBq/kg	60% Cu [99], 20% Ni [53], 20% Zn
^{210}Pb to ^{210}Bi or ^{206}Pb (^{238}U step 7)	6.50E+04 μBq/kg	60% Cu [99], 20% Ni [53], 20% Zn
^{210}Bi to ^{210}Po or ^{206}Pb (^{238}U step 8)	6.50E+04 μBq/kg	60% Cu [99], 20% Ni [53], 20% Zn
^{210}Po to ^{206}Pb (^{238}U step 9)	6.50E+04 μBq/kg	60% Cu [99], 20% Ni [53], 20% Zn
^{60}Co	1.20E+02 atoms/kg/day	OFHC DEMONSTRATOR Table [99]

Table J.12: Radiopurity information for Resistor. Table generated by *MJBMDbInfo.-ComponentsStore*.

Contaminant	Activity/ Production Rate	Reference
^{232}Th to ^{228}Ra (^{232}Th step 1)	2.85E+07 μBq/kg	Avg. from Eidelweiss – ILIAS [53]
^{228}Ra to ^{228}Th (^{232}Th step 2)	2.85E+07 μBq/kg	Avg. from Eidelweiss – ILIAS [53]
^{228}Th to ^{224}Ra (^{232}Th step 3)	2.85E+07 μBq/kg	Avg. from Eidelweiss – ILIAS [53]
^{224}Ra to ^{208}Pb (^{232}Th step 4)	2.34E+07 μBq/kg	Avg. from Eidelweiss – ILIAS [53]
^{238}U to ^{234}Th (^{238}U step 1)	1.07E+07 μBq/kg	Avg. from Eidelweiss – ILIAS [53]
^{234}Th to ^{234}U (^{238}U step 2)	1.07E+07 μBq/kg	Avg. from Eidelweiss – ILIAS [53]
^{234}U to ^{230}Th (^{238}U step 3)	1.07E+07 μBq/kg	Avg. from Eidelweiss – ILIAS [53]
^{230}Th to ^{226}Ra (^{238}U step 4)	1.07E+07 μBq/kg	Avg. from Eidelweiss – ILIAS [53]
^{226}Ra to ^{222}Rn (^{238}U step 5)	1.72E+07 μBq/kg	Avg. from Eidelweiss – ILIAS [53]
^{222}Rn to ^{210}Tl or ^{210}Pb (^{238}U step 6)	1.72E+07 μBq/kg	Avg. from Eidelweiss – ILIAS [53]
^{210}Tl to ^{210}Pb (^{238}U step 6a)	3.61E+03 μBq/kg	Avg. from Eidelweiss – ILIAS [53]
^{210}Pb to ^{210}Bi or ^{206}Pb (^{238}U step 7)	1.22E+08 μBq/kg	Avg. from Eidelweiss – ILIAS [53]
^{210}Bi to ^{210}Po or ^{206}Pb (^{238}U step 8)	1.22E+08 μBq/kg	Avg. from Eidelweiss – ILIAS [53]
^{210}Po to ^{206}Pb (^{238}U step 9)	1.22E+08 μBq/kg	Avg. from Eidelweiss – ILIAS [53]
^{40}K	1.60E+08 μBq/kg	Avg. from Eidelweiss – ILIAS [53]
^{60}Co	1.78E+06 μBq/kg	Avg. from Eidelweiss – ILIAS [53]

Table J.13: Radiopurity information for Rn-Exposure-In-Cryostat. Table generated by *MJBMDbInfo.ComponentsStore*.

Contaminant	**Activity/ Production Rate**	**Reference**
^{210}Pb to ^{210}Bi or ^{206}Pb (^{238}U step 7)	5.00E-03 μBq/cm^2	MAJORANA BSD [79]
^{210}Bi to ^{210}Po or ^{206}Pb (^{238}U step 8)	5.00E-03 μBq/cm^2	MAJORANA BSD [79]
^{210}Po to ^{206}Pb (^{238}U step 9)	5.00E-03 μBq/cm^2	MAJORANA BSD [79]

Table J.14: Radiopurity information for Rn-Exposure-Outside-Cryostat. Table generated by *MJBMDbInfo.ComponentsStore*.

Contaminant	**Activity/ Production Rate**	**Reference**
^{210}Pb to ^{210}Bi or ^{206}Pb (^{238}U step 7)	5.00E-03 μBq/cm^2	MAJORANA BSD [79]
^{210}Bi to ^{210}Po or ^{206}Pb (^{238}U step 8)	5.00E-03 μBq/cm^2	MAJORANA BSD [79]
^{210}Po to ^{206}Pb (^{238}U step 9)	5.00E-03 μBq/cm^2	MAJORANA BSD [79]

Table J.15: Radiopurity information for Rock. Table generated by *MJBMDbInfo.ComponentsStore*.

Contaminant	Activity/ Production Rate	Reference
^{232}Th to ^{228}Ra (^{232}Th step 1)	7.50E+05 μBq/kg	MPI Heidelberg [106]
^{228}Ra to ^{228}Th (^{232}Th step 2)	7.50E+05 μBq/kg	MPI Heidelberg [106]
^{228}Th to ^{224}Ra (^{232}Th step 3)	7.50E+05 μBq/kg	MPI Heidelberg [106]
^{224}Ra to ^{208}Pb (^{232}Th step 4)	7.50E+05 μBq/kg	MPI Heidelberg [106]
^{238}U to ^{234}Th (^{238}U step 1)	1.55E+06 μBq/kg	MPI Heidelberg [106]
^{234}Th to ^{234}U (^{238}U step 2)	1.55E+06 μBq/kg	MPI Heidelberg [106]
^{234}U to ^{230}Th (^{238}U step 3)	1.55E+06 μBq/kg	MPI Heidelberg [106]
^{230}Th to ^{226}Ra (^{238}U step 4)	1.55E+06 μBq/kg	MPI Heidelberg [106]
^{226}Ra to ^{222}Rn (^{238}U step 5)	1.55E+06 μBq/kg	MPI Heidelberg [106]
^{222}Rn to ^{210}Tl or ^{210}Pb (^{238}U step 6)	1.55E+06 μBq/kg	MPI Heidelberg [106]
^{210}Tl to ^{210}Pb (^{238}U step 6a)	3.26E+02 μBq/kg	MPI Heidelberg [106]
^{210}Pb to ^{210}Bi or ^{206}Pb (^{238}U step 7)	1.55E+06 μBq/kg	MPI Heidelberg [106]
^{210}Bi to ^{210}Po or ^{206}Pb (^{238}U step 8)	1.55E+06 μBq/kg	MPI Heidelberg [106]
^{210}Po to ^{206}Pb (^{238}U step 9)	1.55E+06 μBq/kg	MPI Heidelberg [106]
^{40}K	1.55E+07 μBq/kg	MPI Heidelberg [106]

Table J.16: Radiopurity information for StainlessSteel304. Table generated by *MJBM-DbInfo.ComponentsStore*.

Contaminant	Activity/ Production Rate	Reference
^{232}Th to ^{228}Ra (^{232}Th step 1)	1.60E+03 μBq/kg	SS 304L gamma assay avg. – ILIAS [53]
^{228}Ra to ^{228}Th (^{232}Th step 2)	1.60E+03 μBq/kg	SS 304L gamma assay avg. – ILIAS [53]
^{228}Th to ^{224}Ra (^{232}Th step 3)	1.60E+03 μBq/kg	SS 304L gamma assay avg. – ILIAS [53]
^{224}Ra to ^{208}Pb (^{232}Th step 4)	1.60E+03 μBq/kg	SS 304L gamma assay avg. – ILIAS [53]
^{238}U to ^{234}Th (^{238}U step 1)	7.41E+03 μBq/kg	SS 304L gamma assay avg. – ILIAS [53]
^{234}Th to ^{234}U (^{238}U step 2)	7.41E+03 μBq/kg	SS 304L gamma assay avg. – ILIAS [53]
^{234}U to ^{230}Th (^{238}U step 3)	7.41E+03 μBq/kg	SS 304L gamma assay avg. – ILIAS [53]
^{230}Th to ^{226}Ra (^{238}U step 4)	7.41E+03 μBq/kg	SS 304L gamma assay avg. – ILIAS [53]
^{226}Ra to ^{222}Rn (^{238}U step 5)	7.41E+03 μBq/kg	SS 304L gamma assay avg. – ILIAS [53]
^{222}Rn to ^{210}Tl or ^{210}Pb (^{238}U step 6)	7.41E+03 μBq/kg	SS 304L gamma assay avg. – ILIAS [53]
^{210}Tl to ^{210}Pb (^{238}U step 6a)	1.56E+00 μBq/kg	SS 304L gamma assay avg. – ILIAS [53]
^{210}Pb to ^{210}Bi or ^{206}Pb (^{238}U step 7)	7.41E+03 μBq/kg	SS 304L gamma assay avg. – ILIAS [53]
^{210}Bi to ^{210}Po or ^{206}Pb (^{238}U step 8)	7.41E+03 μBq/kg	SS 304L gamma assay avg. – ILIAS [53]
^{210}Po to ^{206}Pb (^{238}U step 9)	7.41E+03 μBq/kg	SS 304L gamma assay avg. – ILIAS [53]
^{40}K	4.00E+03 μBq/kg	SS 304L gamma assay avg. – ILIAS [53]
^{60}Co	5.82E+04 μBq/kg	SS 304L gamma assay avg. – ILIAS [53]

Table J.17: Radiopurity information for Teflon. Table generated by *MJBMDbInfo.-ComponentsStore*.

Contaminant	Activity/ Production Rate	Reference
^{232}Th to ^{228}Ra (^{232}Th step 1)	2.00E+03 μBq/kg	Edelweiss Physimeca – ILIAS [53]
^{228}Ra to ^{228}Th (^{232}Th step 2)	2.00E+03 μBq/kg	Edelweiss Physimeca – ILIAS [53]
^{228}Th to ^{224}Ra (^{232}Th step 3)	2.00E+03 μBq/kg	Edelweiss Physimeca – ILIAS [53]
^{224}Ra to ^{208}Pb (^{232}Th step 4)	2.00E+03 μBq/kg	Edelweiss Physimeca – ILIAS [53]
^{238}U to ^{234}Th (^{238}U step 1)	2.00E+04 μBq/kg	Edelweiss Physimeca – ILIAS [53]
^{234}Th to ^{234}U (^{238}U step 2)	2.00E+04 μBq/kg	Edelweiss Physimeca – ILIAS [53]
^{234}U to ^{230}Th (^{238}U step 3)	2.00E+04 μBq/kg	Edelweiss Physimeca – ILIAS [53]
^{230}Th to ^{226}Ra (^{238}U step 4)	2.00E+04 μBq/kg	Edelweiss Physimeca – ILIAS [53]
^{226}Ra to ^{222}Rn (^{238}U step 5)	2.00E+03 μBq/kg	Edelweiss Physimeca – ILIAS [53]
^{222}Rn to ^{210}Tl or ^{210}Pb (^{238}U step 6)	2.00E+03 μBq/kg	Edelweiss Physimeca – ILIAS [53]
^{210}Tl to ^{210}Pb (^{238}U step 6a)	4.20E-01 μBq/kg	Edelweiss Physimeca – ILIAS [53]
^{210}Pb to ^{210}Bi or ^{206}Pb (^{238}U step 7)	2.00E+03 μBq/kg	Edelweiss Physimeca – ILIAS [53]
^{210}Bi to ^{210}Po or ^{206}Pb (^{238}U step 8)	2.00E+03 μBq/kg	Edelweiss Physimeca – ILIAS [53]
^{210}Po to ^{206}Pb (^{238}U step 9)	2.00E+03 μBq/kg	Edelweiss Physimeca – ILIAS [53]
^{40}K	8.00E+04 μBq/kg	Edelweiss Physimeca – ILIAS [53]
^{60}Co	5.00E+03 μBq/kg	Edelweiss Physimeca – ILIAS [53]

Table J.18: Radiopurity information for Tin. Table generated by *MJBMDbInfo.ComponentsStore*.

Contaminant	**Activity/ Production Rate**	**Reference**
^{210}Pb to ^{210}Bi or ^{206}Pb (^{238}U step 7)	2.00E+06 μBq/kg	High Purity – ILIAS [53]
^{210}Bi to ^{210}Po or ^{206}Pb (^{238}U step 8)	2.00E+06 μBq/kg	High Purity – ILIAS [53]
^{210}Po to ^{206}Pb (^{238}U step 9)	2.00E+06 μBq/kg	High Purity – ILIAS [53]

Table J.19: Radiopurity information for Zeolite. Table generated by *MJBMDbInfo.-ComponentsStore*.

Contaminant	Activity/ Production Rate	Reference
^{232}Th to ^{228}Ra (^{232}Th step 1)	1.00E+07 μBq/kg	Finnerty et al. [36]
^{228}Ra to ^{228}Th (^{232}Th step 2)	1.00E+07 μBq/kg	Finnerty et al. [36]
^{228}Th to ^{224}Ra (^{232}Th step 3)	1.00E+07 μBq/kg	Finnerty et al. [36]
^{224}Ra to ^{208}Pb (^{232}Th step 4)	1.00E+07 μBq/kg	Finnerty et al. [36]
^{238}U to ^{234}Th (^{238}U step 1)	5.80E+06 μBq/kg	Finnerty et al. [36]
^{234}Th to ^{234}U (^{238}U step 2)	5.80E+06 μBq/kg	Finnerty et al. [36]
^{234}U to ^{230}Th (^{238}U step 3)	5.80E+06 μBq/kg	Finnerty et al. [36]
^{230}Th to ^{226}Ra (^{238}U step 4)	5.80E+06 μBq/kg	Finnerty et al. [36]
^{226}Ra to ^{222}Rn (^{238}U step 5)	8.20E+06 μBq/kg	Finnerty et al. [36]
^{222}Rn to ^{210}Tl or ^{210}Pb (^{238}U step 6)	8.20E+06 μBq/kg	Finnerty et al. [36]
^{210}Tl to ^{210}Pb (^{238}U step 6a)	1.72E+03 μBq/kg	Finnerty et al. [36]
^{210}Pb to ^{210}Bi or ^{206}Pb (^{238}U step 7)	8.20E+06 μBq/kg	Finnerty et al. [36]
^{210}Bi to ^{210}Po or ^{206}Pb (^{238}U step 8)	8.20E+06 μBq/kg	Finnerty et al. [36]
^{210}Po to ^{206}Pb (^{238}U step 9)	8.20E+06 μBq/kg	Finnerty et al. [36]
^{40}K	4.40E+06 μBq/kg	Finnerty et al. [36]

Appendix K

DECAY DATA

The following tables present information about selected radiation emitted in nuclear decays. The selection was made to aid in understanding the response of MALBEK to each contaminant.

Table K.1: Selected radiation emitted in decays of interest. Intensities are per 100 decays of the parent isotope. Energies are in keV. For β spectra, the endpoint energy is listed. Stable isotopes are bolded. Data are from NuDat [33].

Contaminant	Half Life	Type	Energy	Intensity
$^{3}_{1}$H $\rightarrow$ $^{\mathbf{3}}_{\mathbf{2}}$**He**	12.3 y	β^-	18.6	100.0
$^{40}_{19}$K $\rightarrow$ $^{\mathbf{40}}_{\mathbf{20}}$**Ca** (89.3%)	1.2×10^9 y	β^-	1311.1	89.1
$^{40}_{19}$K $\rightarrow$ $^{\mathbf{40}}_{\mathbf{18}}$**Ar** (10.7%)		γ	1460.8	10.7
$^{46}_{21}$Sc $\rightarrow$ $^{\mathbf{46}}_{\mathbf{22}}$**Ti**	83.8 d	γ	889.3	100.0
		γ	1120.5	100.0
$^{48}_{23}$V $\rightarrow$ $^{\mathbf{48}}_{\mathbf{22}}$**Ti**	16.0 d	β^+	694.6	49.9
		γ	983.5	100.0
		γ	1312.1	100.0
$^{54}_{25}$Mn $\rightarrow$ $^{\mathbf{54}}_{\mathbf{24}}$**Ca**	312.1 d	γ	834.8	100.0
$^{55}_{26}$Fe $\rightarrow$ $^{\mathbf{55}}_{\mathbf{25}}$**Mn**	2.7 y	Auger L	0.6	139.9
		Auger K	5.2	60.2
		$XR_{K\alpha 1,\ K\alpha 2}$	5.9	24.4
		$XR_{K\beta 1,\ K\beta 3}$	6.5	2.9

Table K.1: continued

Contaminant	Half Life	Type	Energy	Intensity
$^{56}_{27}\mathrm{Co} \rightarrow \mathbf{^{56}_{26}Fe}$	77.2 d	γ	1238.3	66.5
		γ	846.8	99.9
		γ	1037.8	14.1
		β^+	1458.9	18.4
		γ	1771.4	15.4
		γ	2034.8	7.8
		γ	2598.5	17.0
$^{57}_{27}\mathrm{Co} \rightarrow \mathbf{^{57}_{26}Fe}$	271.7 d	γ	122.1	85.6
		γ	136.5	10.7
		γ	692.4	0.1
$^{58}_{27}\mathrm{Co} \rightarrow \mathbf{^{58}_{26}Fe}$	70.9 d	β^+	474.8	14.9
		γ	810.8	99.5
		γ	864.0	0.7
		γ	1674.7	0.5
$^{59}_{26}\mathrm{Fe} \rightarrow \mathbf{^{59}_{27}Co}$	44.5 d	γ	1099.2	56.5
		γ	1291.6	43.2
$^{60}_{27}\mathrm{Co} \rightarrow \mathbf{^{60}_{28}Ni}$	5.3 y	γ	1173.2	99.9
		γ	1332.5	100.0
$^{63}_{28}\mathrm{Ni} \rightarrow \mathbf{^{63}_{29}Cu}$	101.2 y	β^-	66.9	100.0
$^{65}_{30}\mathrm{Zn} \rightarrow \mathbf{^{65}_{29}Cu}$	243.9 d	β^+	330.1	1.4
		γ	1115.5	50.0

Table K.1: continued

Contaminant	**Half Life**	**Type**	**Energy**	**Intensity**
$^{68}_{32}$Ge → $^{68}_{31}$Ga	271.0 d	Auger L	1.1	121.9
		Auger K	8.0	41.8
		XR_L	1.1	1.5
		$XR_{\alpha 2}$	9.2	13.1
		$XR_{\alpha 1}$	9.3	25.8
		$XR_{K\beta 1,\ K\beta 3}$	10.3	4.8
$^{68}_{31}$Ga → $^{\mathbf{68}}_{\mathbf{30}}$**Zn**	67.7 m	annih.	511.0	177.8
		γ	1077.3	3.2
		β^+	1899.1	87.7
$^{68}_{32}$Ge → $^{\mathbf{76}}_{\mathbf{34}}$**Se**	1.5×10^{21} y	$2\beta^-$	2039	100.0

Table K.2: Selected radiation emitted from isotopes in the ^{232}Th chain. Intensities are per 100 decays of the parent isotope. Energies are in keV. For β spectra, the endpoint energy is listed. Data are from NuDat [33].

Step	**Contaminant**	**Half Life**		**Energy**	**I**
UC 1	$^{232}_{90}\mathrm{Th} \rightarrow {}^{228}_{88}\mathrm{Ra}$	1.4×10^{10} y	α	3947.2	21.7
			α	4012.3	78.2
UC 2	$^{228}_{88}\mathrm{Ra} \rightarrow {}^{228}_{89}\mathrm{Ac}$	5.8 y	γ	13.5	1.6
			β^-	39.2	40.0
			β^-	39.6	10.0
UC 2	$^{228}_{89}\mathrm{Ac} \rightarrow {}^{228}_{90}\mathrm{Th}$	6.2 h	γ	129.1	2.4
			γ	209.3	3.9
			γ	270.3	3.5
			γ	328.0	3.0
			γ	338.3	11.3
			γ	463.0	4.4
			γ	794.9	4.3
			γ	911.2	25.8
			γ	964.8	5.0
			γ	969.0	15.8
			β^-	1158.0	29.9
			γ	1588.2	3.2
			β^-	1731.0	11.7
			β^-	2069.0	8.0
UC 3	$^{228}_{90}\mathrm{Th} \rightarrow {}^{224}_{88}\mathrm{Ra}$	1.9 y	γ	84.4	1.2
			α	5423.2	72.2
			α	5340.4	27.2

Table K.2: continued

Step		Contaminant	Half Life		Energy	I
LC	4	$^{224}_{88}\mathrm{Ra} \rightarrow {}^{220}_{86}\mathrm{Rn}$	3.7 d	γ	241.0	4.1
				α	5685.4	94.2
				α	5448.6	5.1
LC	4	$^{220}_{86}\mathrm{Rn} \rightarrow {}^{216}_{84}\mathrm{Po}$	55.6 s	γ	549.7	0.1
				α	6288.1	99.9
LC	4	$^{216}_{84}\mathrm{Po} \rightarrow {}^{212}_{82}\mathrm{Pb}$	0.1 s	α	6778.3	100.0
LC	4	$^{212}_{82}\mathrm{Pb} \rightarrow {}^{212}_{83}\mathrm{Bi}$	10.6 h	γ	238.6	43.6
				γ	300.1	3.3
				β^-	331.3	83.1
				β^-	569.9	11.9
LC	4	$^{212}_{83}\mathrm{Bi} \rightarrow {}^{212}_{84}\mathrm{Po}$ (64.1%) $^{212}_{83}\mathrm{Bi} \rightarrow {}^{208}_{81}\mathrm{Tl}$ (35.9%)	60.6 m	γ	727.3	6.7
				β^-	2252.1	55.4
				α	6050.8	25.1
				α	6089.9	9.8
LC	4	$^{212}_{84}\mathrm{Po} \rightarrow {}^{208}_{82}\mathrm{Pb}$	0.3 μs	α	8784.9	100.0
LC	4	$^{208}_{81}\mathrm{Tl} \rightarrow \mathbf{{}^{208}_{82}Pb}$	3.1 m	$\mathrm{XR}_{K\alpha 2}$	72.8	2.0
				$\mathrm{XR}_{K\alpha 1}$	75.0	3.4
				γ	277.4	6.6
				γ	510.8	22.6
				γ	583.2	85.0
				γ	860.6	12.5
				γ	2614.5	99.8

Table K.3: Selected radiation emitted from isotopes in the ^{238}U chain. Intensities are per 100 decays of the parent isotope. Energies are in keV. For β spectra, the endpoint energy is listed. Data are from NuDat [33].

Step		Contaminant	Half Life		Energy	I
UC	1	$^{238}_{92}\mathrm{U} \rightarrow {}^{234}_{90}\mathrm{Th}$	4.5×10^9 y	α	4151.0	21.0
				α	4198.0	79.0
UC	2	$^{234}_{90}\mathrm{Th} \rightarrow {}^{234\mathrm{m}}_{91}\mathrm{Pa}$	24.1 d	γ	63.3	3.7
				γ	92.4	2.1
				γ	92.8	2.1
				β^-	107.0	14.0
				β^-	199.0	78.0
UC	2	$^{234\mathrm{m}}_{91}\mathrm{Pa} \rightarrow {}^{234}_{92}\mathrm{U}$ (99.8%) $^{234\mathrm{m}}_{91}\mathrm{Pa} \rightarrow {}^{234}_{91}\mathrm{Pa}$ (0.2%)	1.2 m	β^-	1224.0	1.0
				β^-	2269.0	97.6
UC	3	$^{234}_{92}\mathrm{U} \rightarrow {}^{230}_{90}\mathrm{Th}$	2.5×10^5 y	α	4722.4	28.4
				α	4774.6	71.4
UC	4	$^{230}_{90}\mathrm{Th} \rightarrow {}^{226}_{88}\mathrm{Ra}$	7.5×10^4 y	α	4620.5	23.4
				α	4687.0	76.3
LC I	5	$^{226}_{88}\mathrm{Ra} \rightarrow {}^{222}_{86}\mathrm{Rn}$	1.6×10^3 y	α	4784.3	93.8
				γ	186.2	3.6
LC I	6	$^{222}_{86}\mathrm{Rn} \rightarrow {}^{218}_{84}\mathrm{Po}$	3.8 d	α	5489.5	99.9
LC I	6	$^{218}_{84}\mathrm{Po} \rightarrow {}^{214}_{82}\mathrm{Pb}$ (100.0%) $^{218}_{84}\mathrm{Po} \rightarrow {}^{218}_{85}\mathrm{At}$ (< 0.1%)	3.1 m	α	6002.3	100.0

Table K.3: continued

Step		**Contaminant**	**Half Life**		**Energy**	**I**
LC I	6	$^{214}_{82}$Pb → $^{214}_{83}$Bi	26.8 m	γ	242.0	7.3
				γ	295.2	18.4
				γ	351.9	35.6
LC I	6	$^{214}_{83}$Bi → $^{214}_{84}$Po (99.98%) $^{214}_{83}$Bi → $^{210}_{81}$Tl (0.02%)	19.9 m	γ	609.3	45.5
				γ	768.4	4.9
				γ	934.1	3.1
				γ	1120.3	14.9
				γ	1238.1	5.8
				γ	1377.7	4.0
				γ	1408.0	2.4
				γ	1509.2	2.1
				γ	1729.6	2.9
				γ	1764.5	15.3
				γ	1847.4	2.0
				γ	2204.1	4.9
LC I	6	$^{214}_{84}$Po → $^{210}_{82}$Pb	0.2 ms	α	7686.8	100.0
LC II	7	$^{210}_{82}$Pb → $^{210}_{83}$Bi (100.0%) $^{210}_{82}$Pb → $^{206}_{80}$Hg (1.9×10^{-6}%)	22.2 y	XR_L	10.8	23.6
				γ	46.5	4.3
LC II	8	$^{210}_{83}$Bi → $^{210}_{84}$Po (100.0%) $^{210}_{83}$Bi → $^{206}_{81}$Tl (1.3×10^{-5}%)	5.0 d	β^-	1162.1	100.0
LC II	9	$^{210}_{84}$Po → $\mathbf{^{206}_{82}Pb}$	138.4 d	α	5304.3	100.0
				γ	803.1	1E-3

Appendix L

RESULTS OF BACKGROUND MODEL FITS

L.1 Energy spectrum PDFs included in the fit

PDFs used in the fit are shown in Figures L.1–L.28. The PDF shapes are shown in blue; statistical errors are in red.

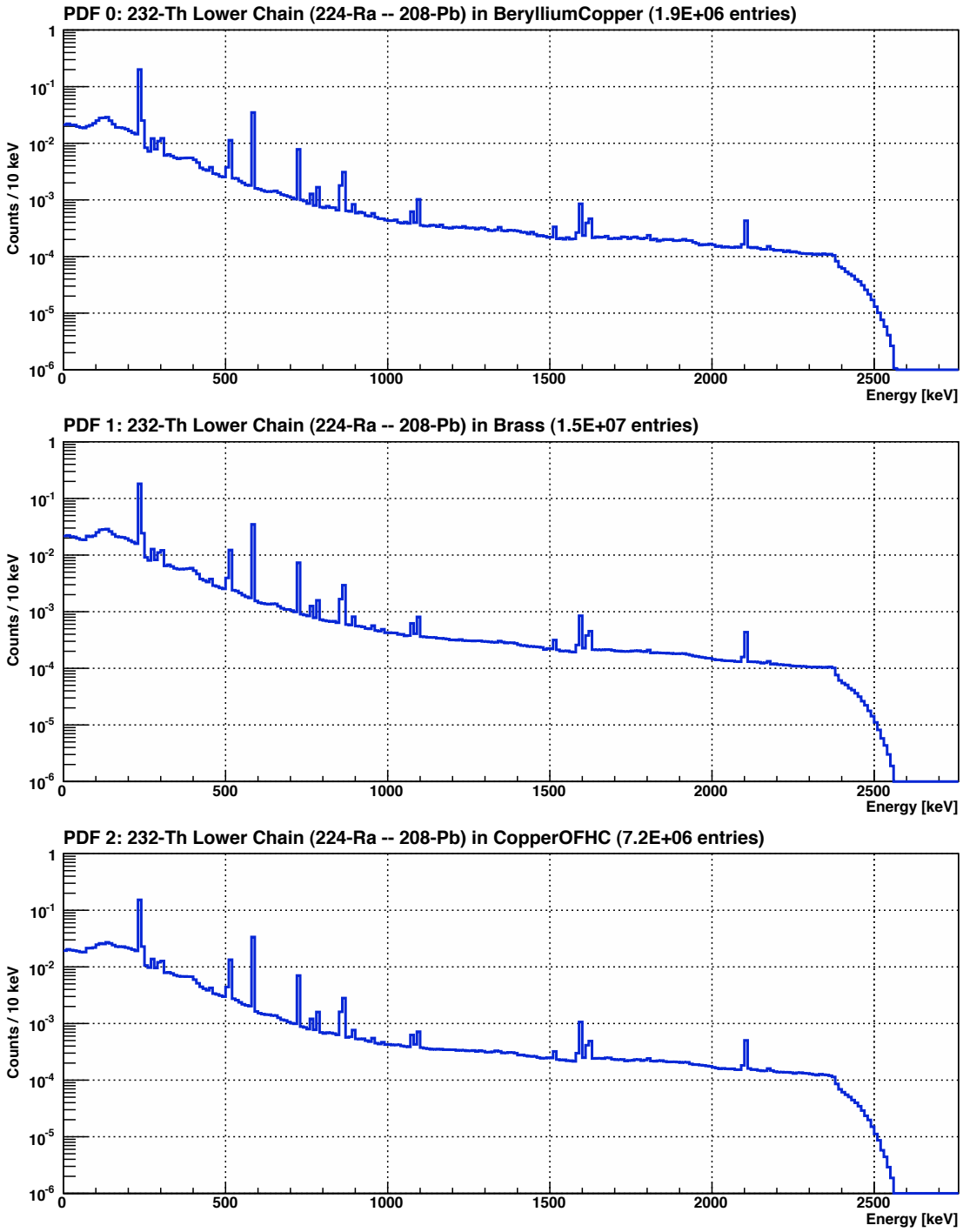

Figure L.1: Background model energy spectra histogram PDFs 0–2. Each PDF is normalized to unit area.

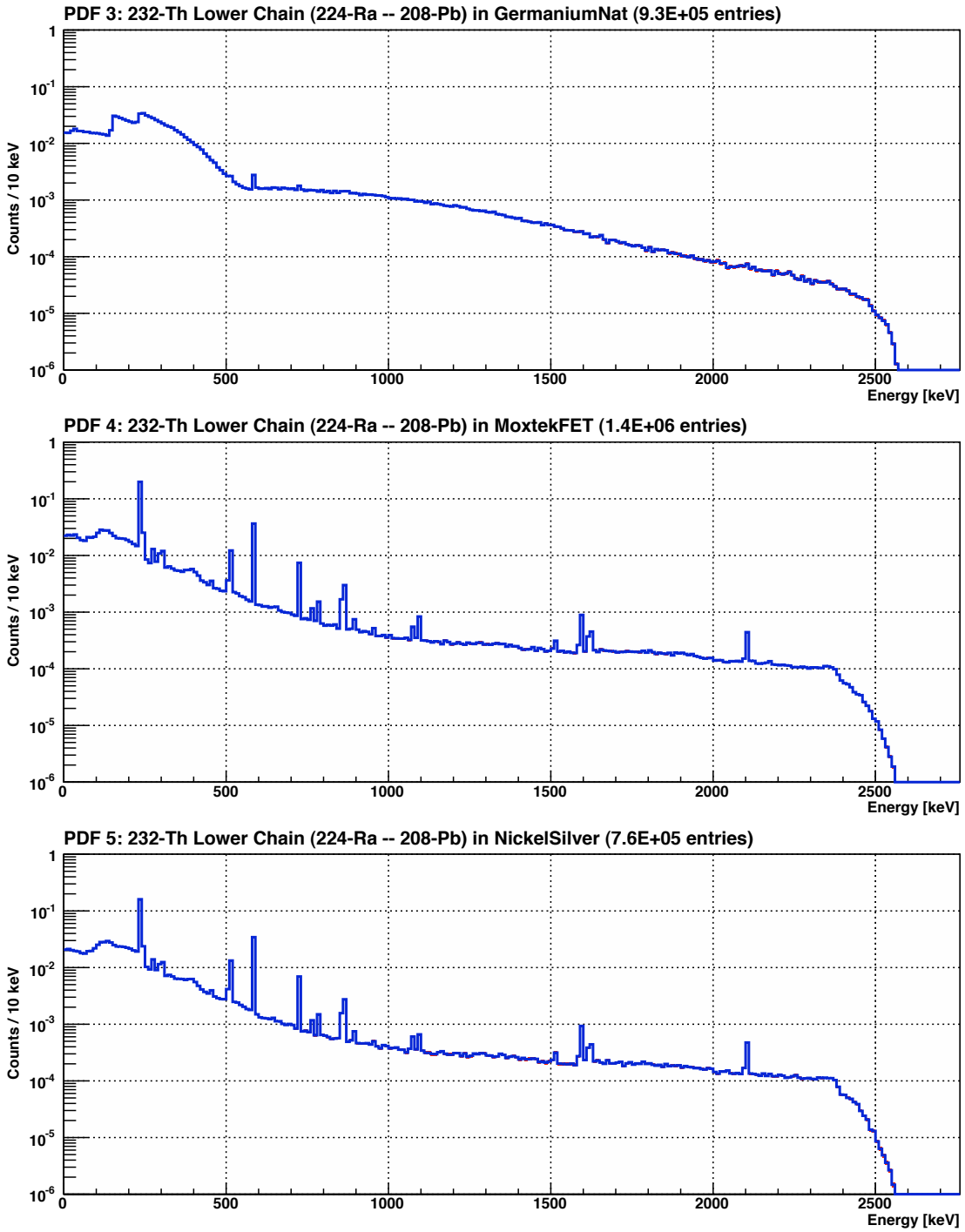

Figure L.2: Background model energy spectra histogram PDFs 3–5. Each PDF is normalized to unit area.

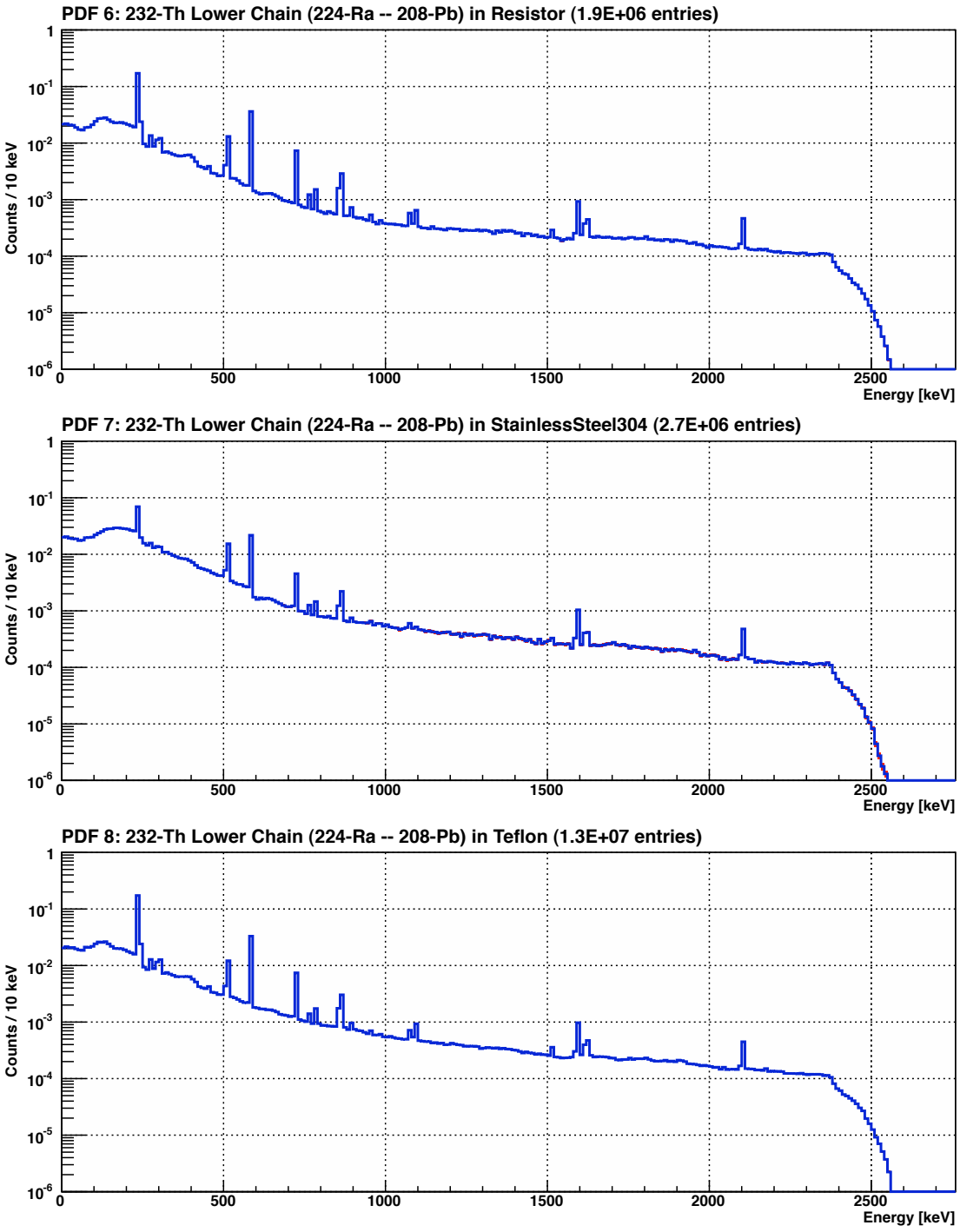

Figure L.3: Background model energy spectra histogram PDFs 6–8. Each PDF is normalized to unit area.

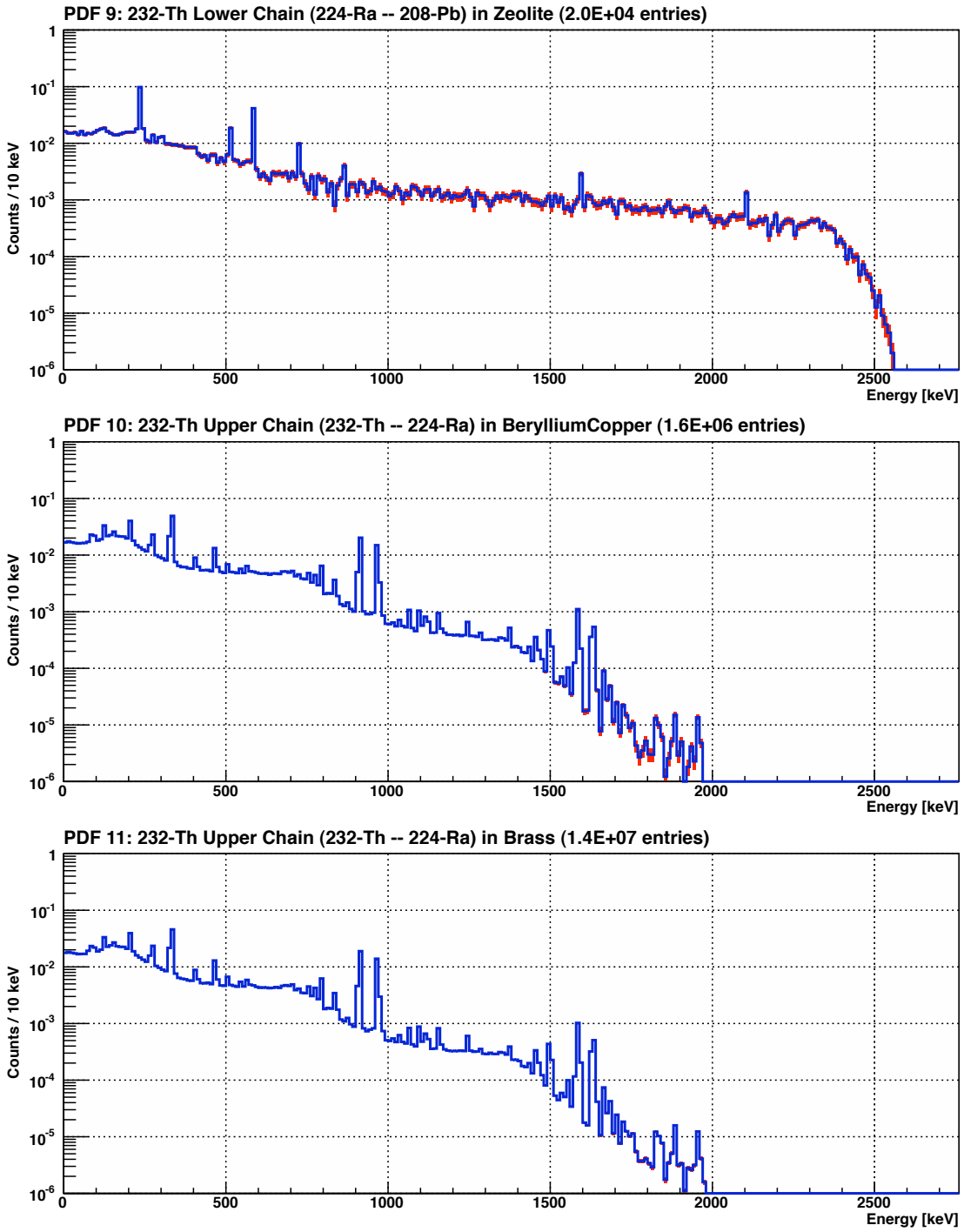

Figure L.4: Background model energy spectra histogram PDFs 9–11. Each PDF is normalized to unit area.

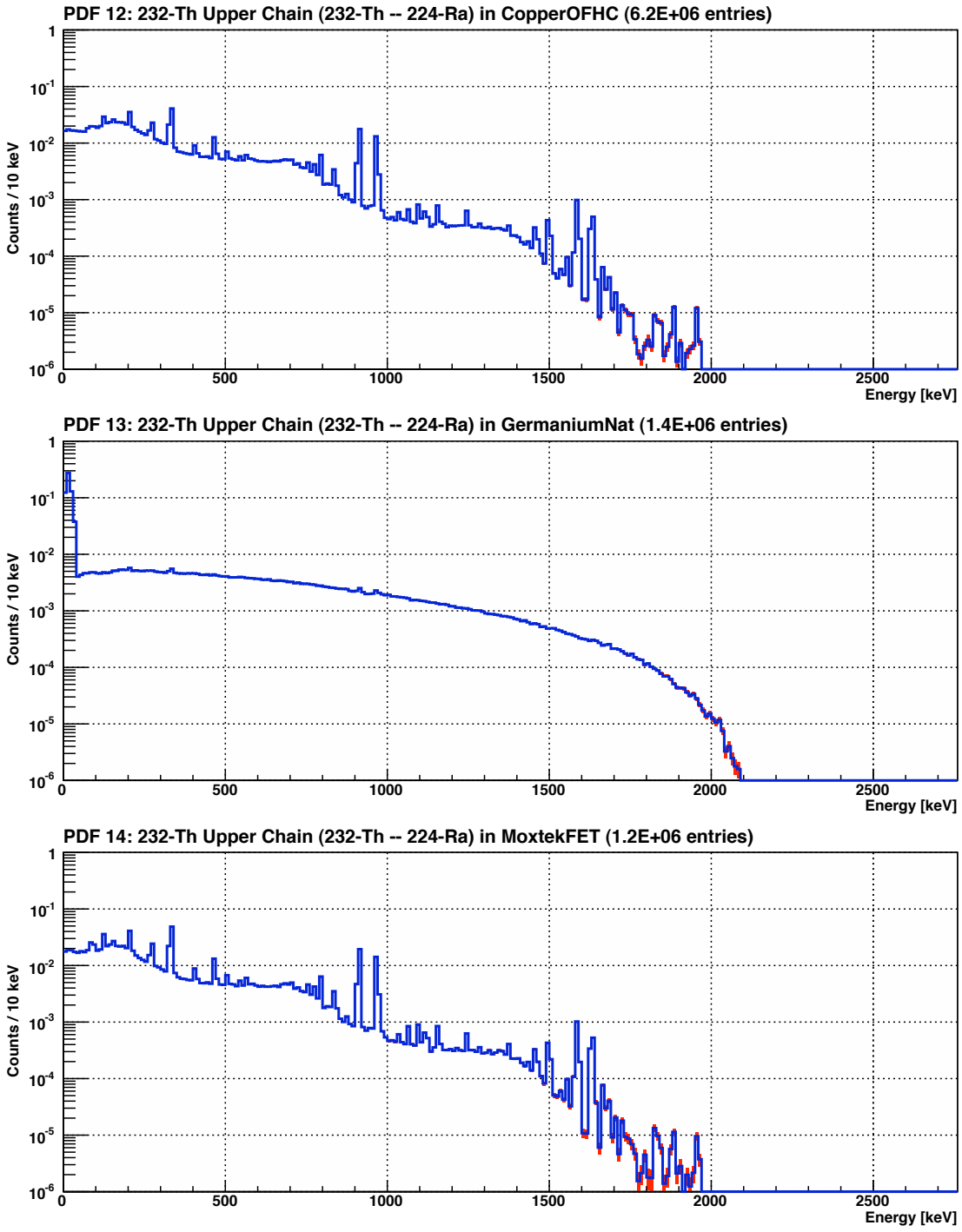

Figure L.5: Background model energy spectra histogram PDFs 12–14. Each PDF is normalized to unit area.

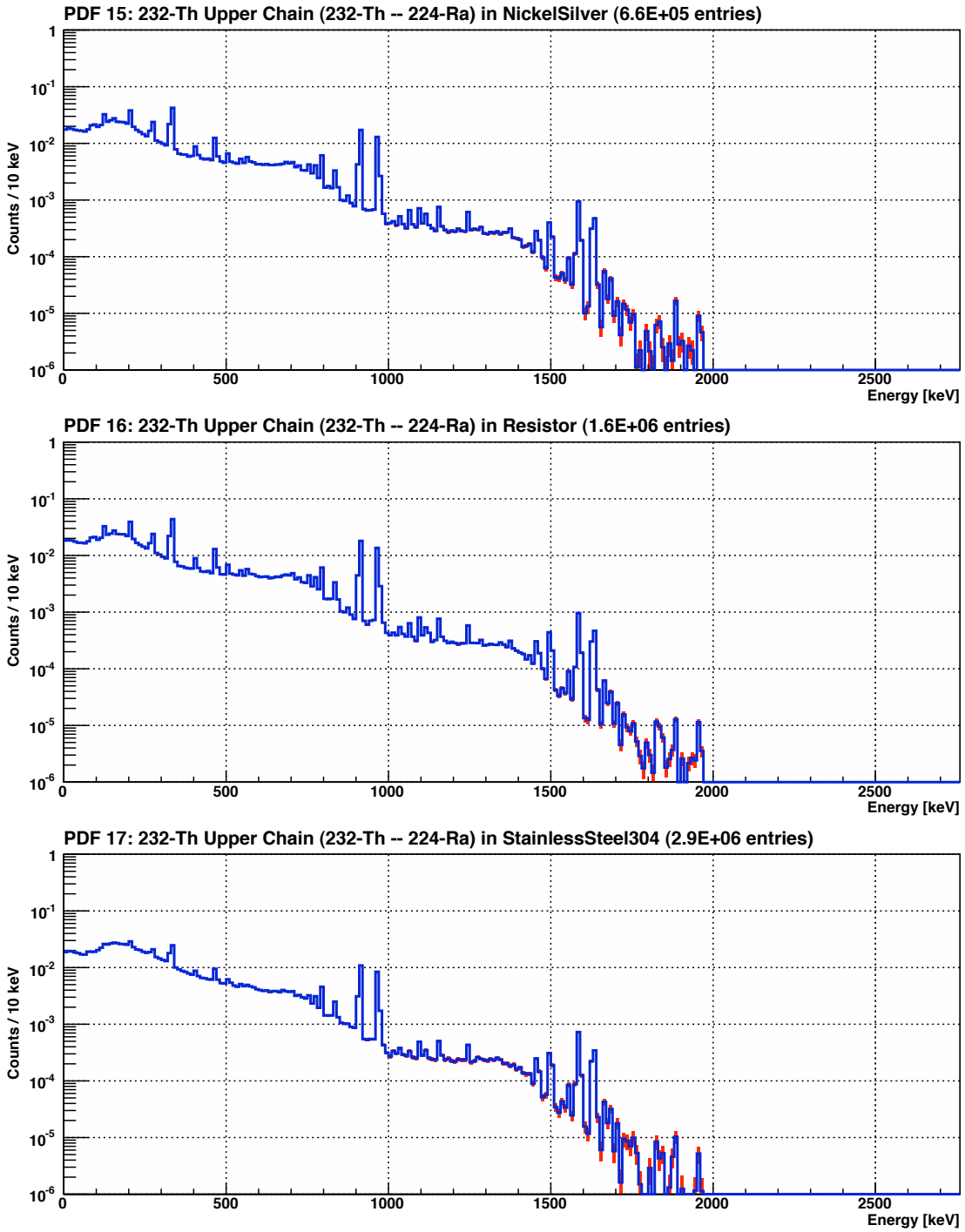

Figure L.6: Background model energy spectra histogram PDFs 15–17. Each PDF is normalized to unit area.

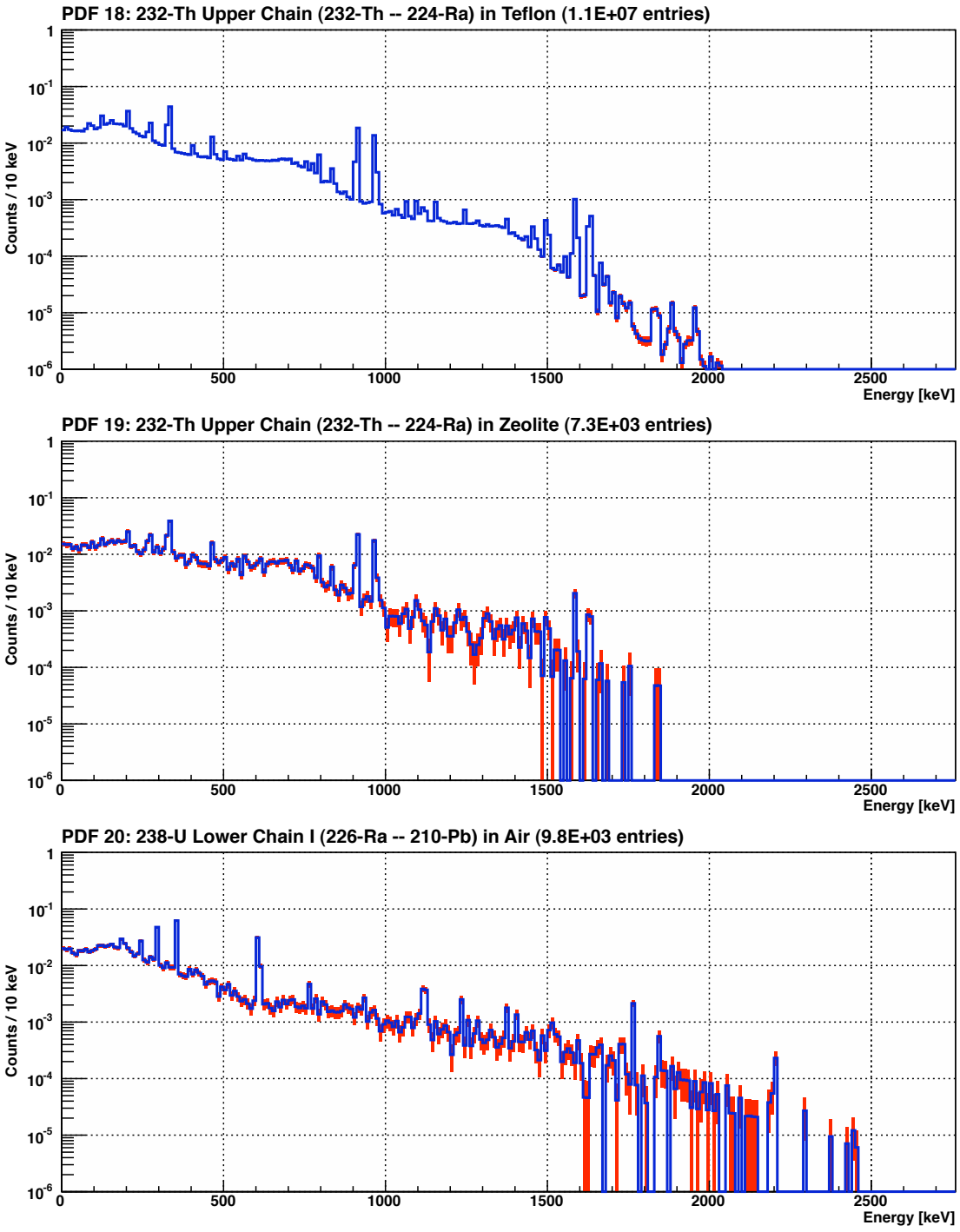

Figure L.7: Background model energy spectra histogram PDFs 18–20. Each PDF is normalized to unit area.

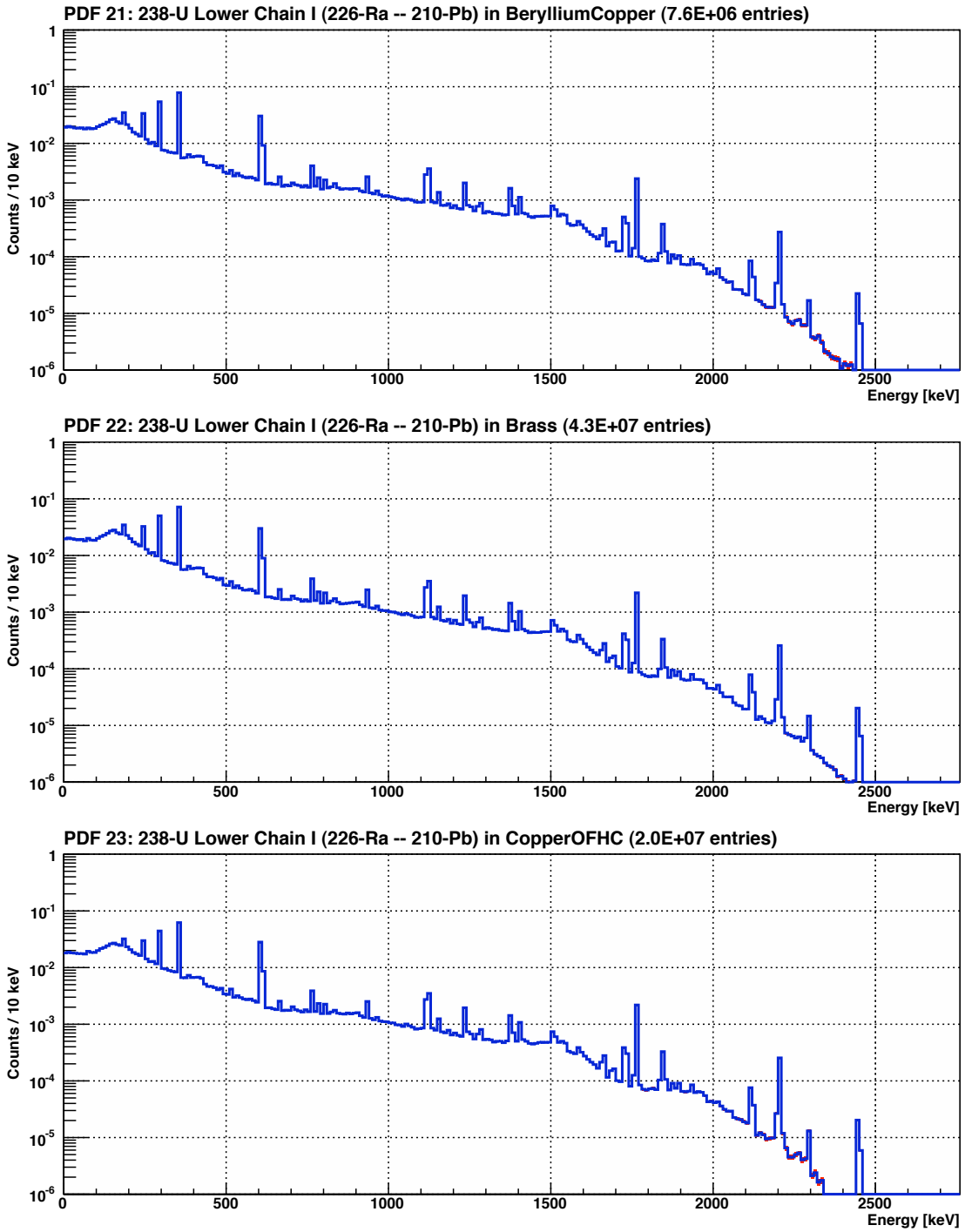

Figure L.8: Background model energy spectra histogram PDFs 21–23. Each PDF is normalized to unit area.

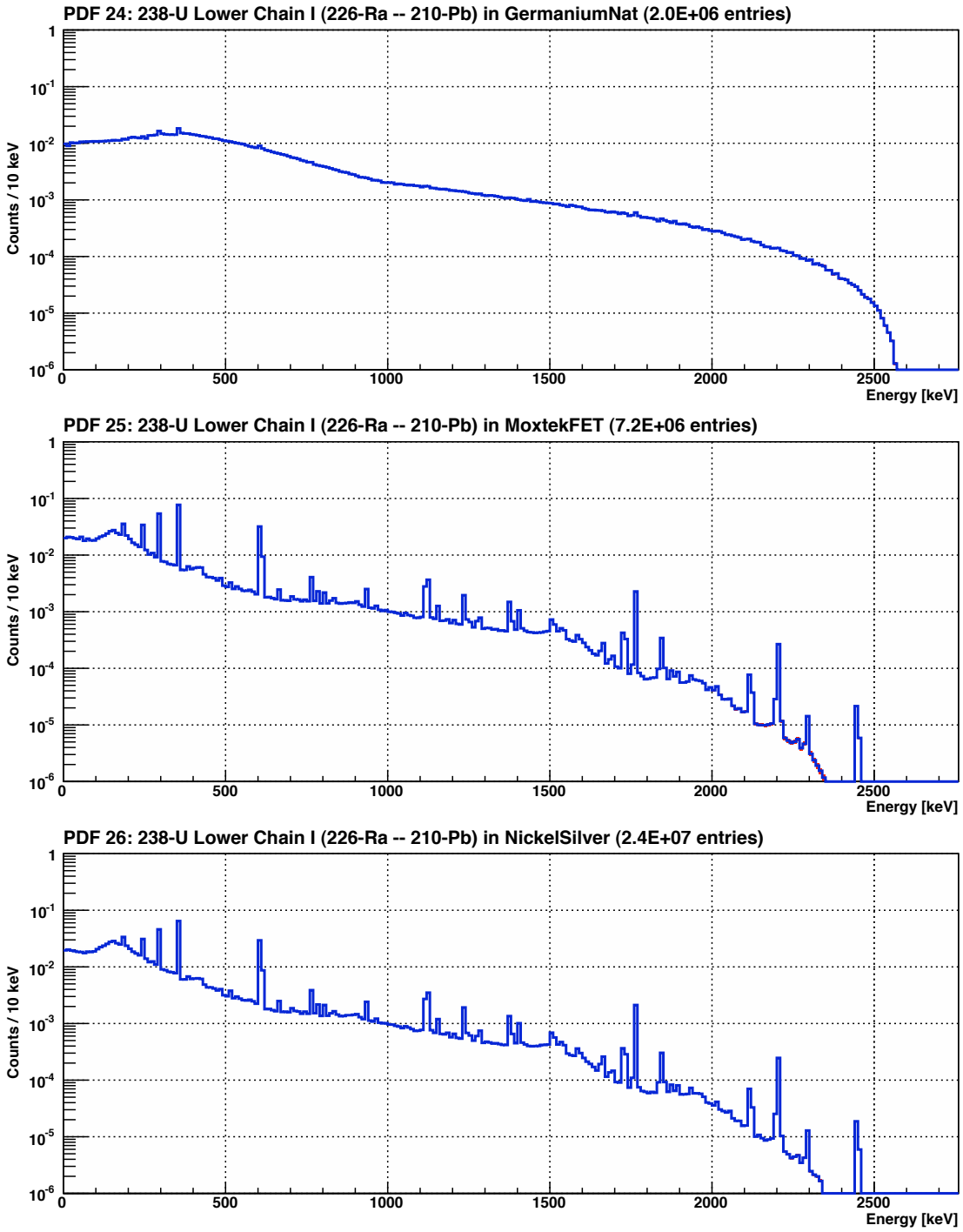

Figure L.9: Background model energy spectra histogram PDFs 24–26. Each PDF is normalized to unit area.

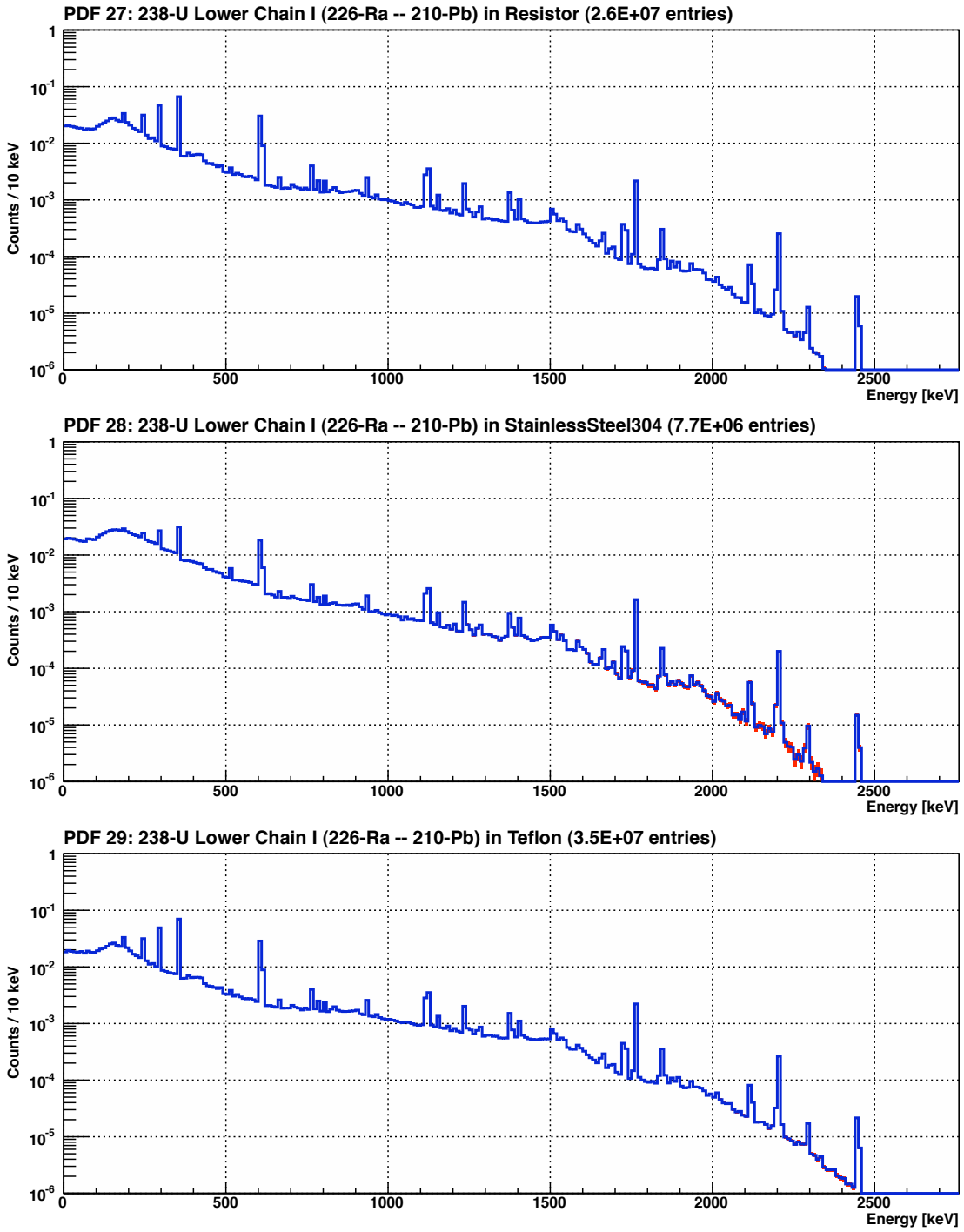

Figure L.10: Background model energy spectra histogram PDFs 27–29. Each PDF is normalized to unit area.

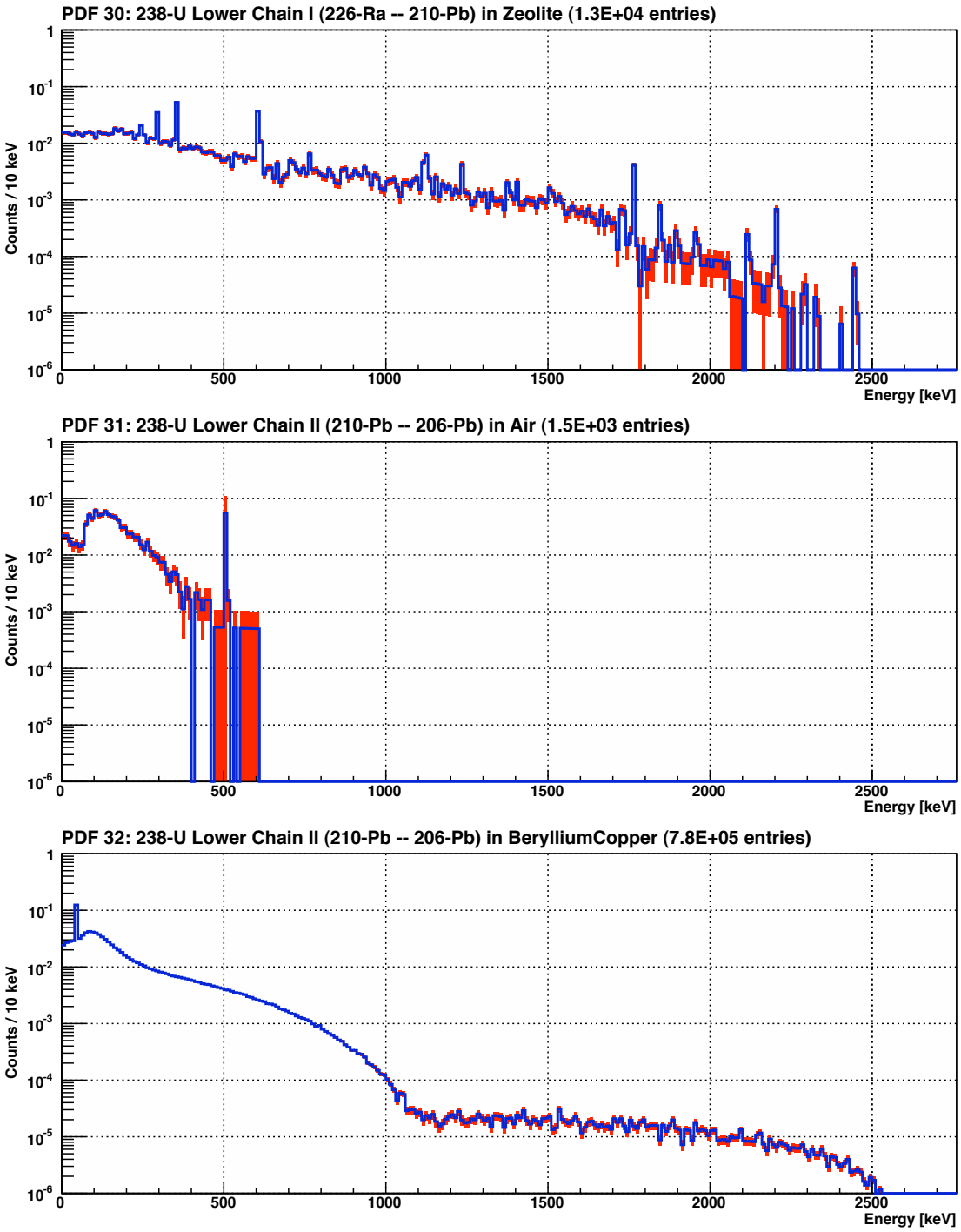

Figure L.11: Background model energy spectra histogram PDFs 30–32. Each PDF is normalized to unit area.

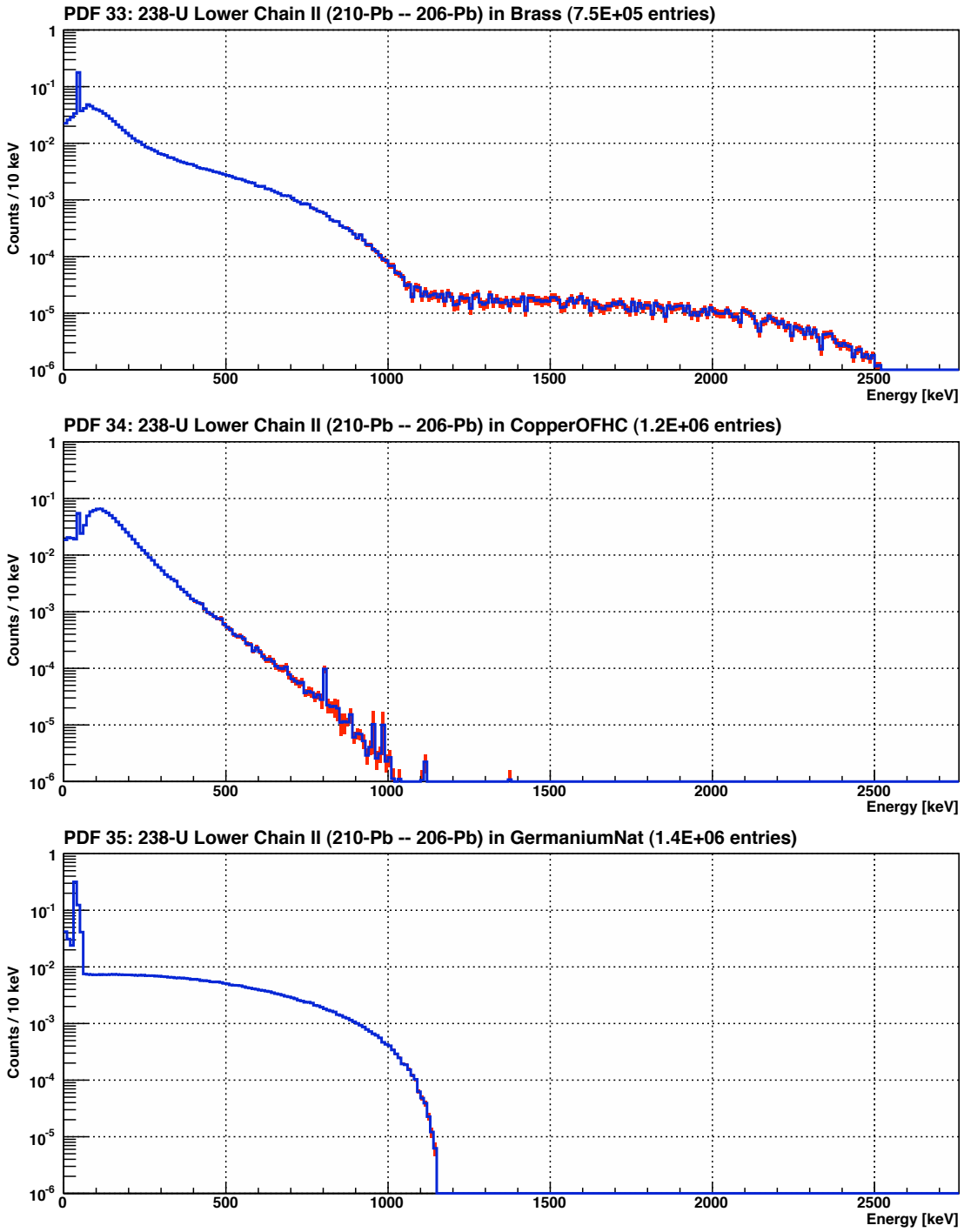

Figure L.12: Background model energy spectra histogram PDFs 33–35. Each PDF is normalized to unit area.

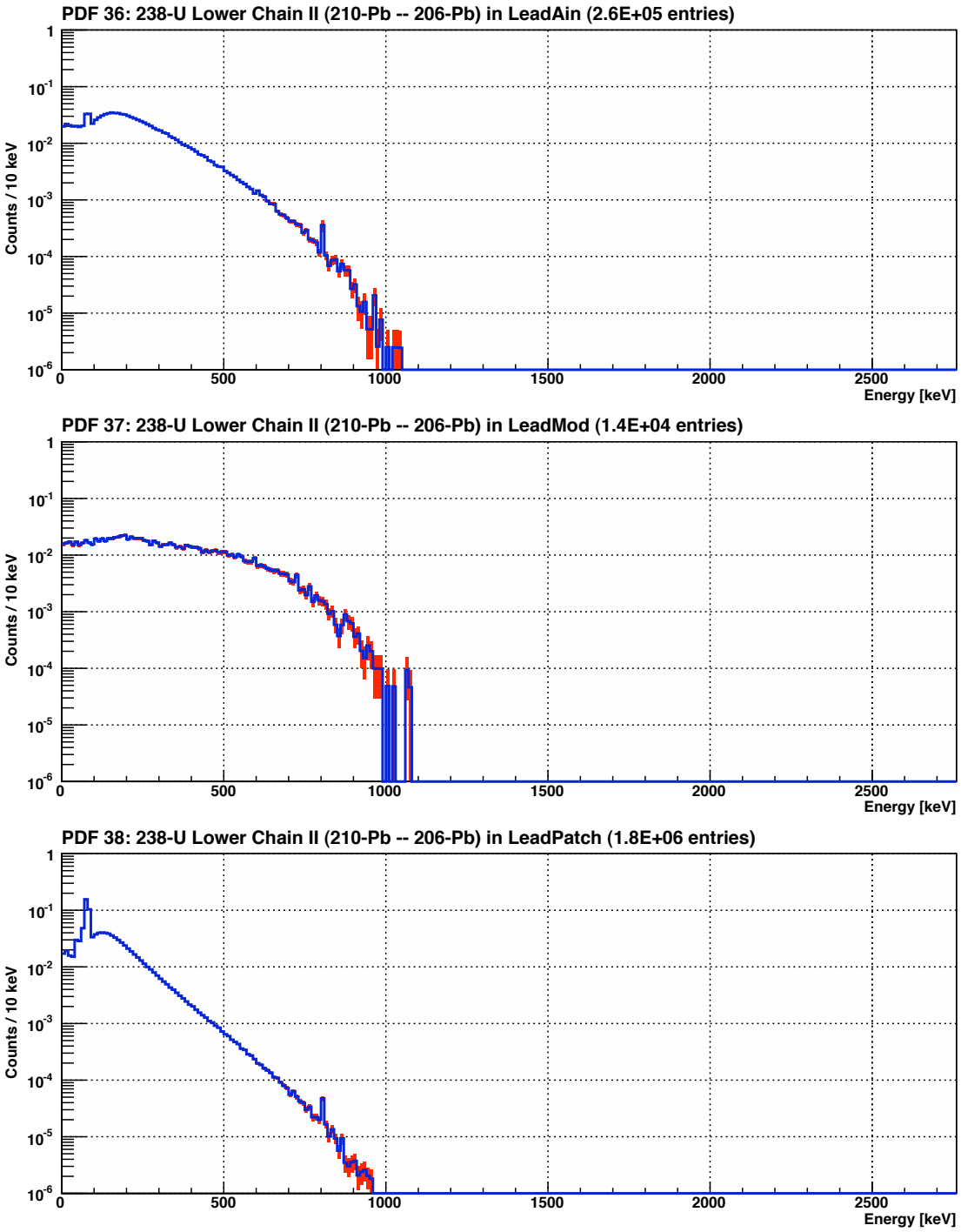

Figure L.13: Background model energy spectra histogram PDFs 36–38. Each PDF is normalized to unit area.

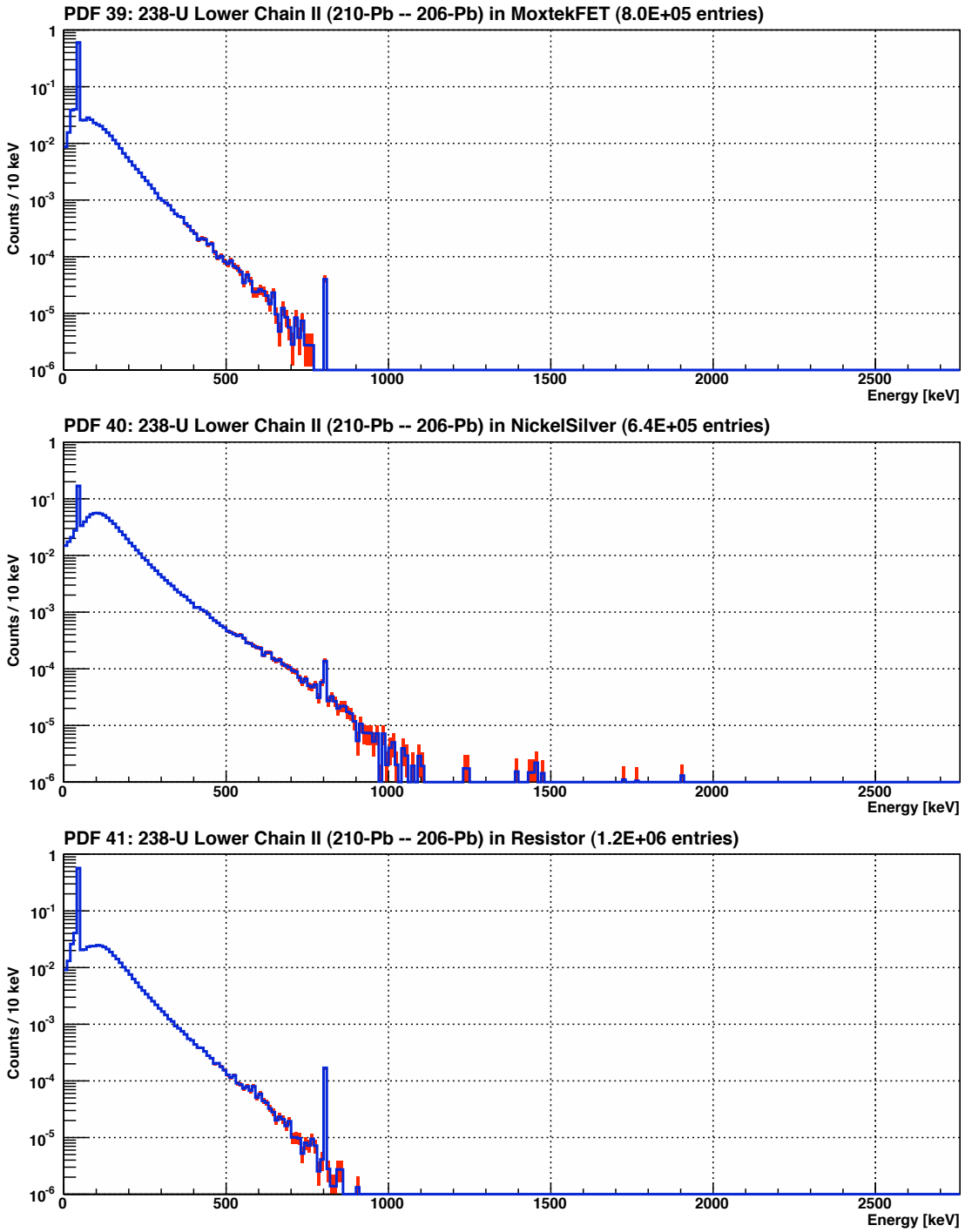

Figure L.14: Background model energy spectra histogram PDFs 39–41. Each PDF is normalized to unit area.

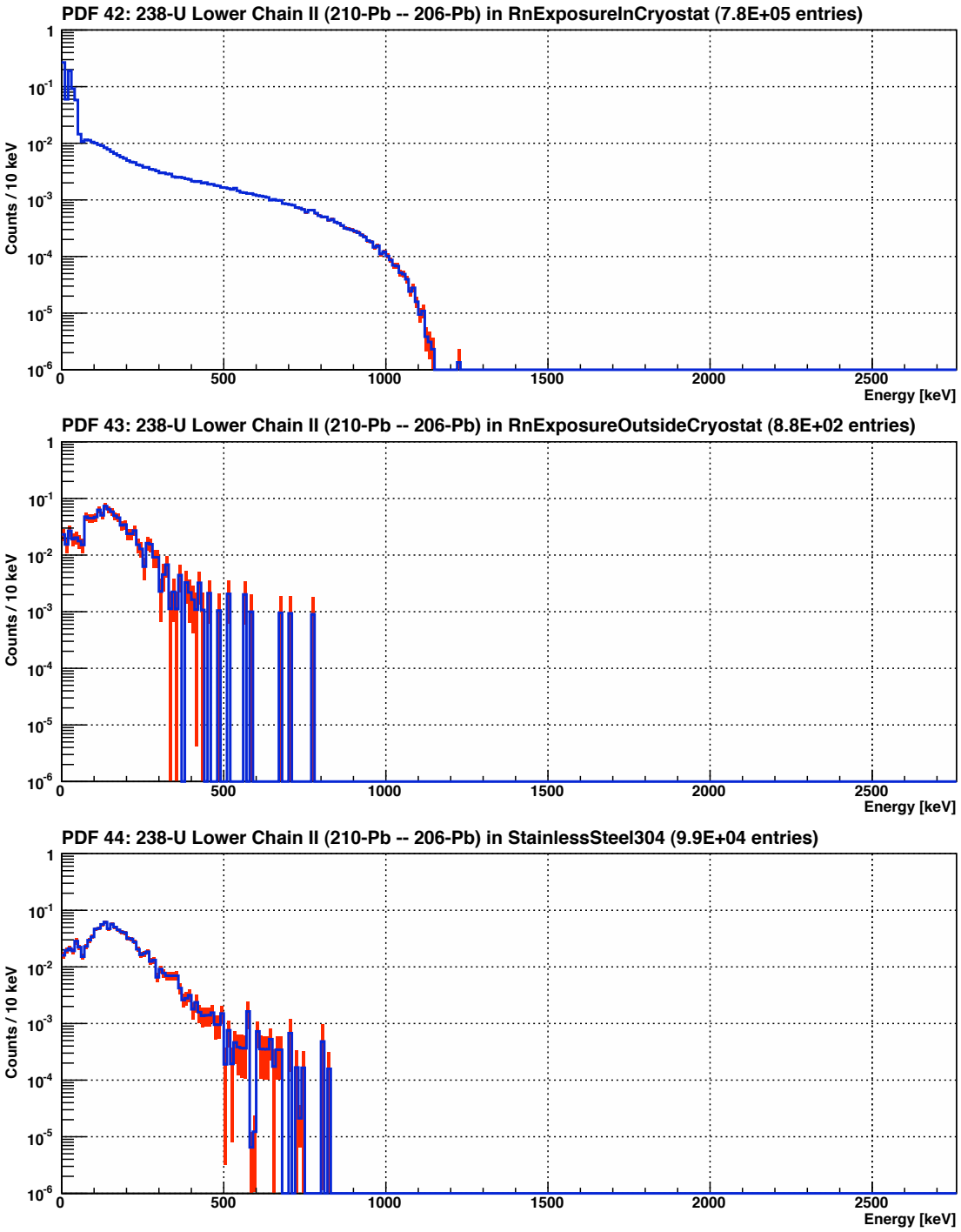

Figure L.15: Background model energy spectra histogram PDFs 42–44. Each PDF is normalized to unit area.

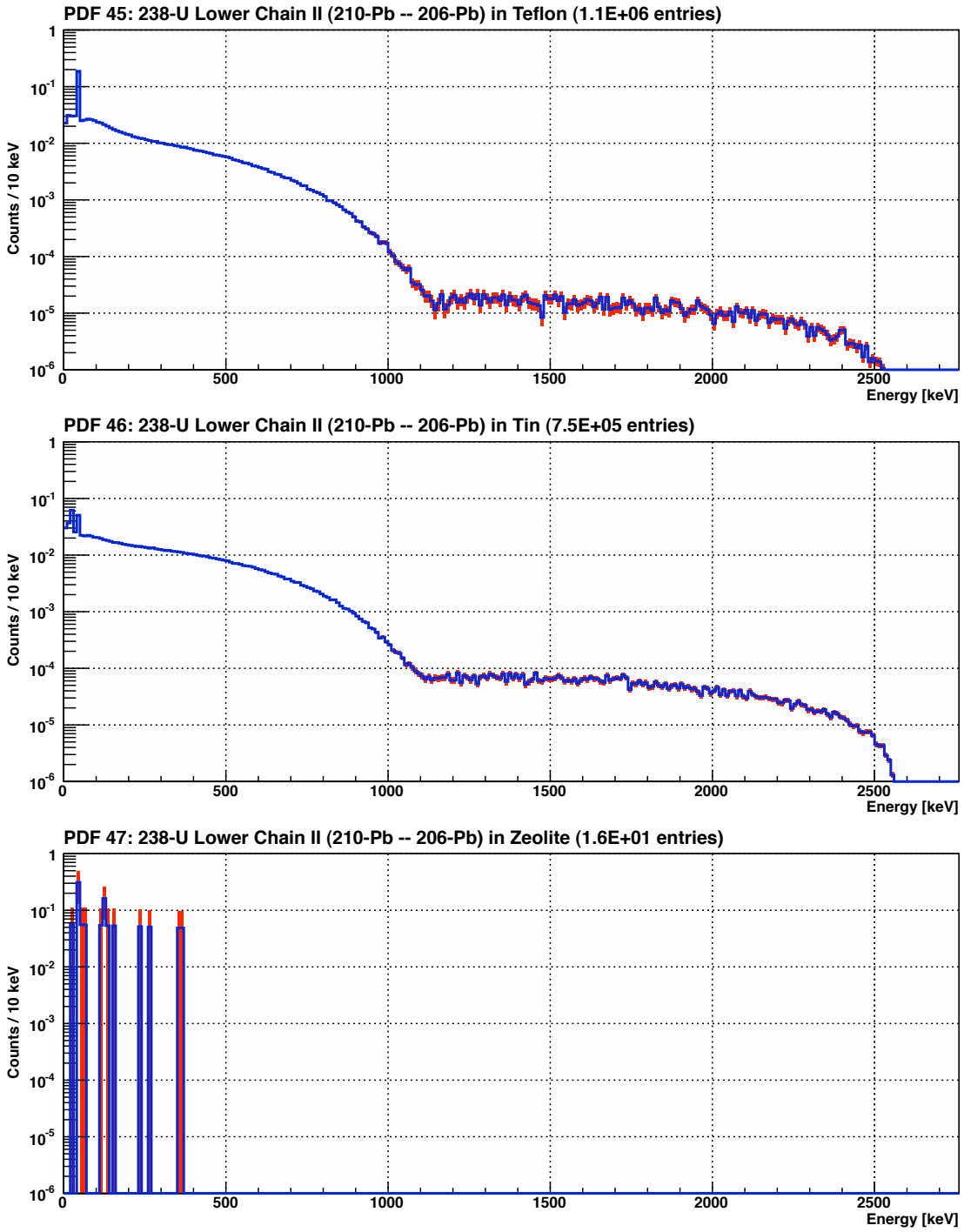

Figure L.16: Background model energy spectra histogram PDFs 45–47. Each PDF is normalized to unit area.

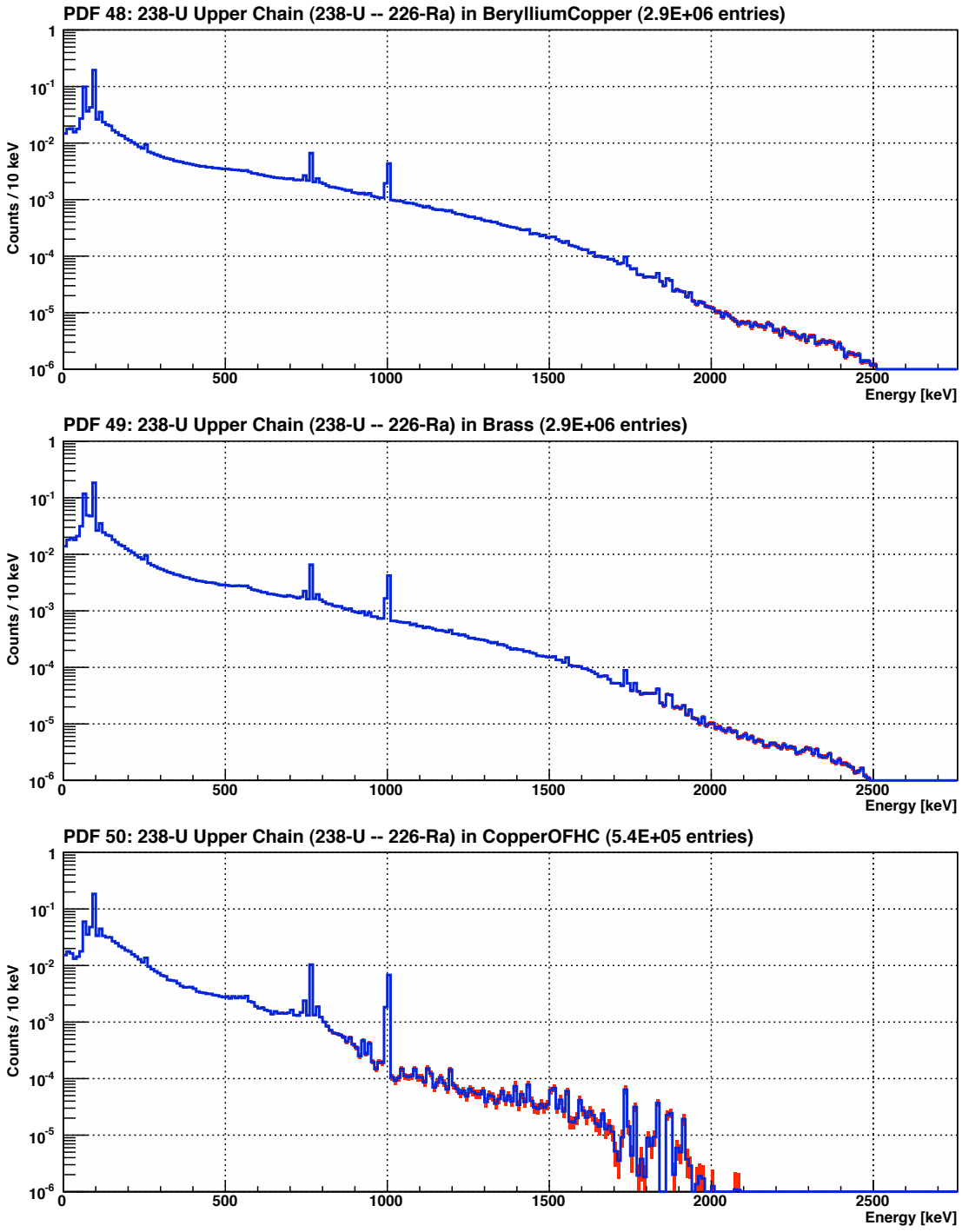

Figure L.17: Background model energy spectra histogram PDFs 48–50. Each PDF is normalized to unit area.

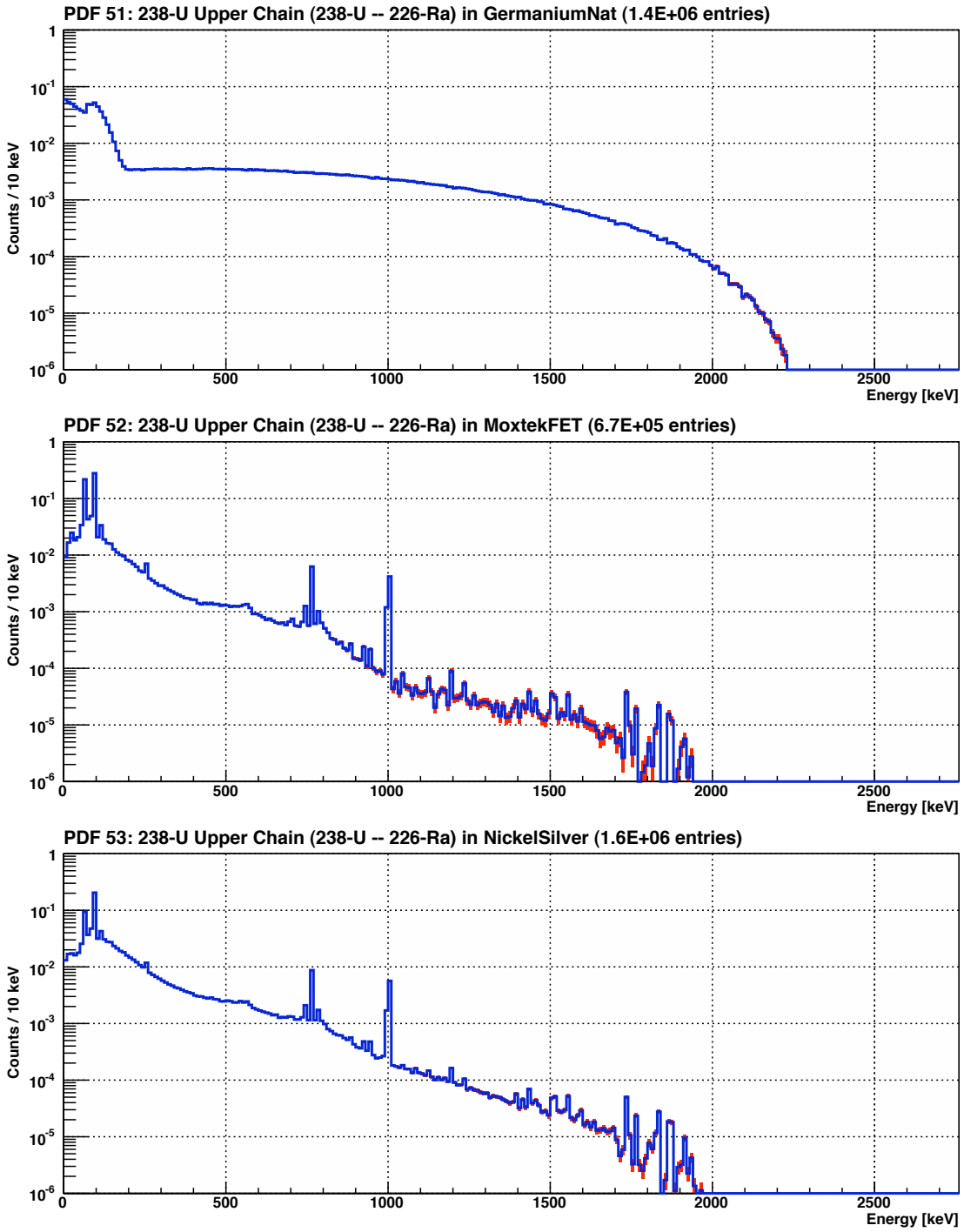

Figure L.18: Background model energy spectra histogram PDFs 51–53. Each PDF is normalized to unit area.

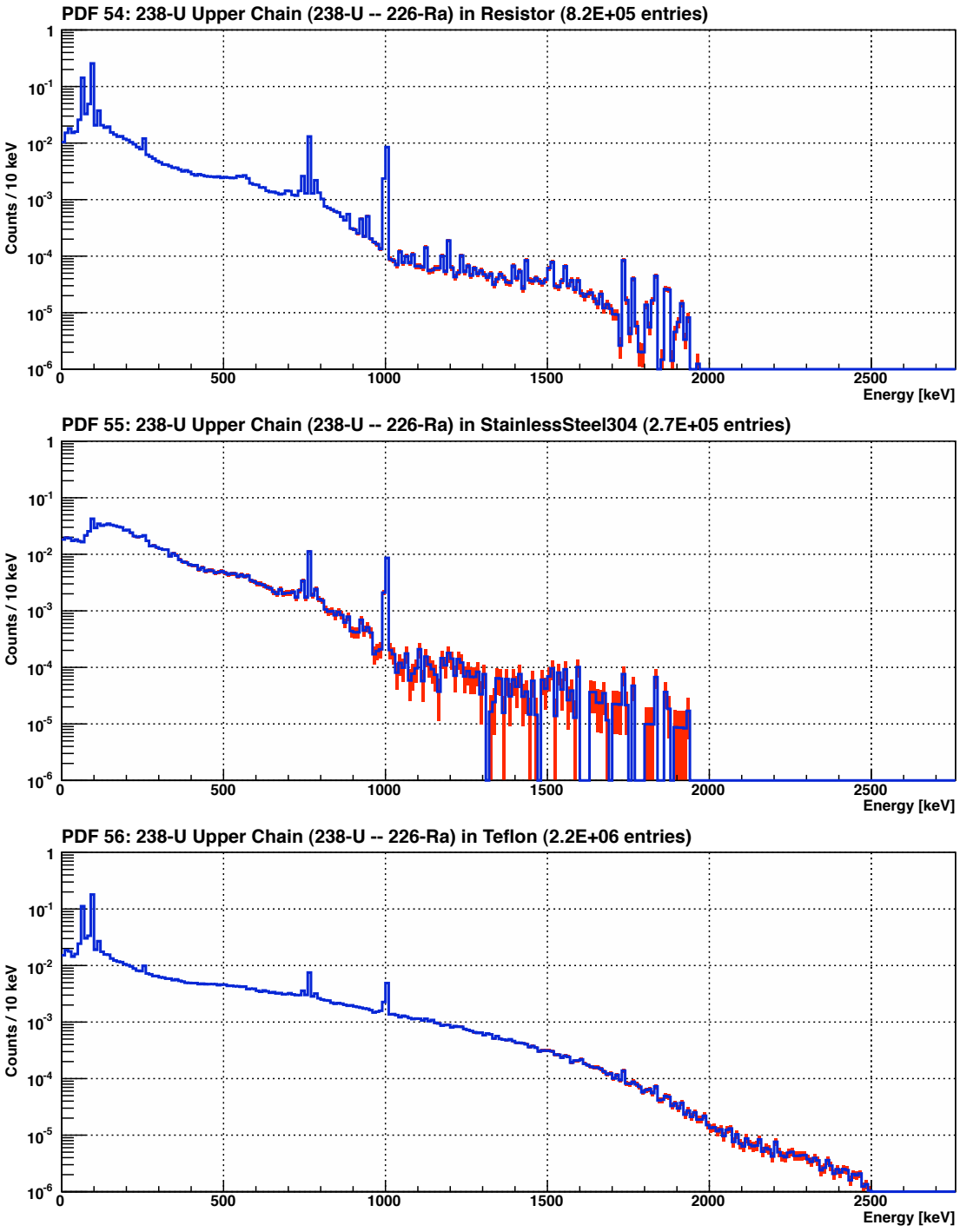

Figure L.19: Background model energy spectra histogram PDFs 54–56. Each PDF is normalized to unit area.

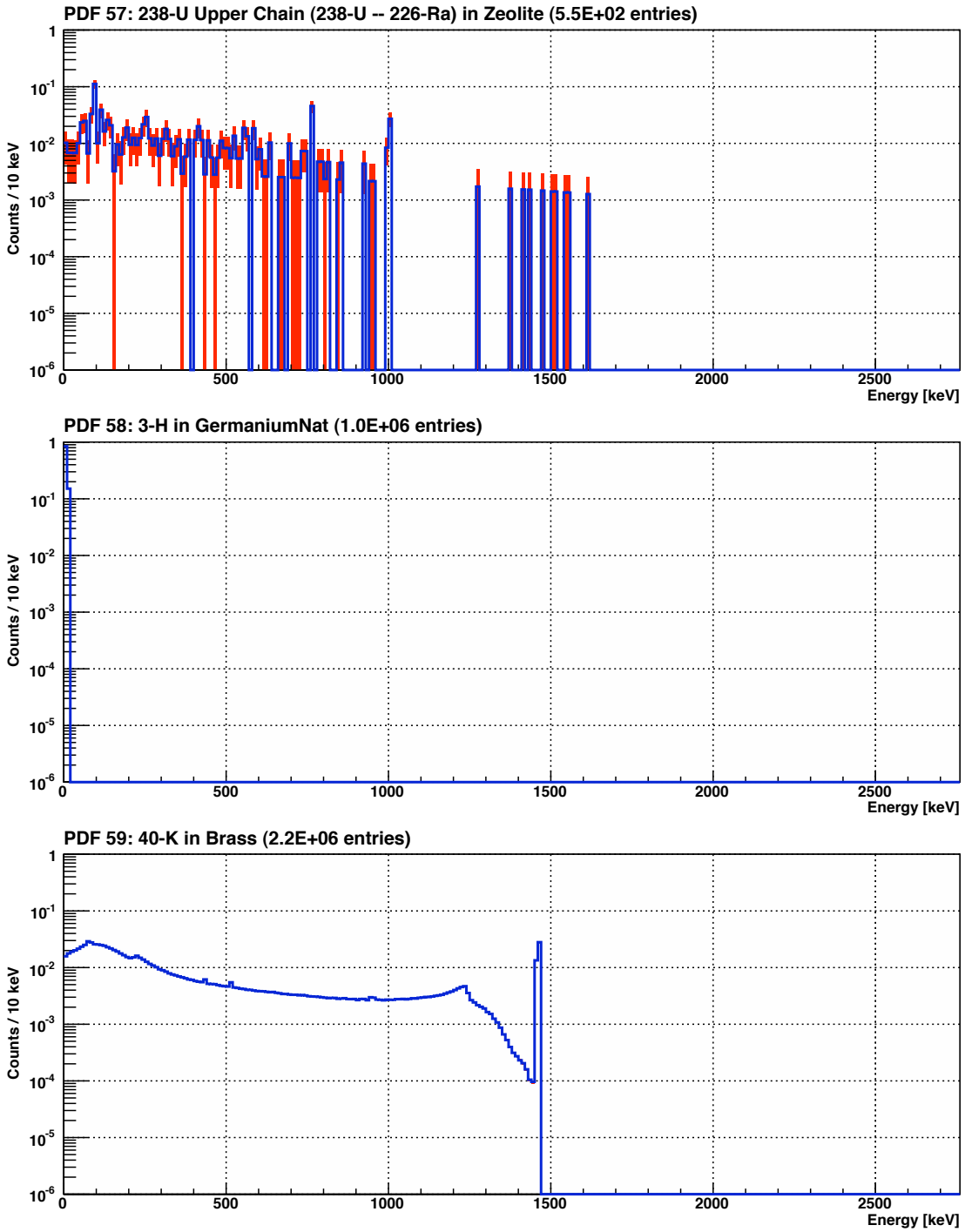

Figure L.20: Background model energy spectra histogram PDFs 57–59. Each PDF is normalized to unit area.

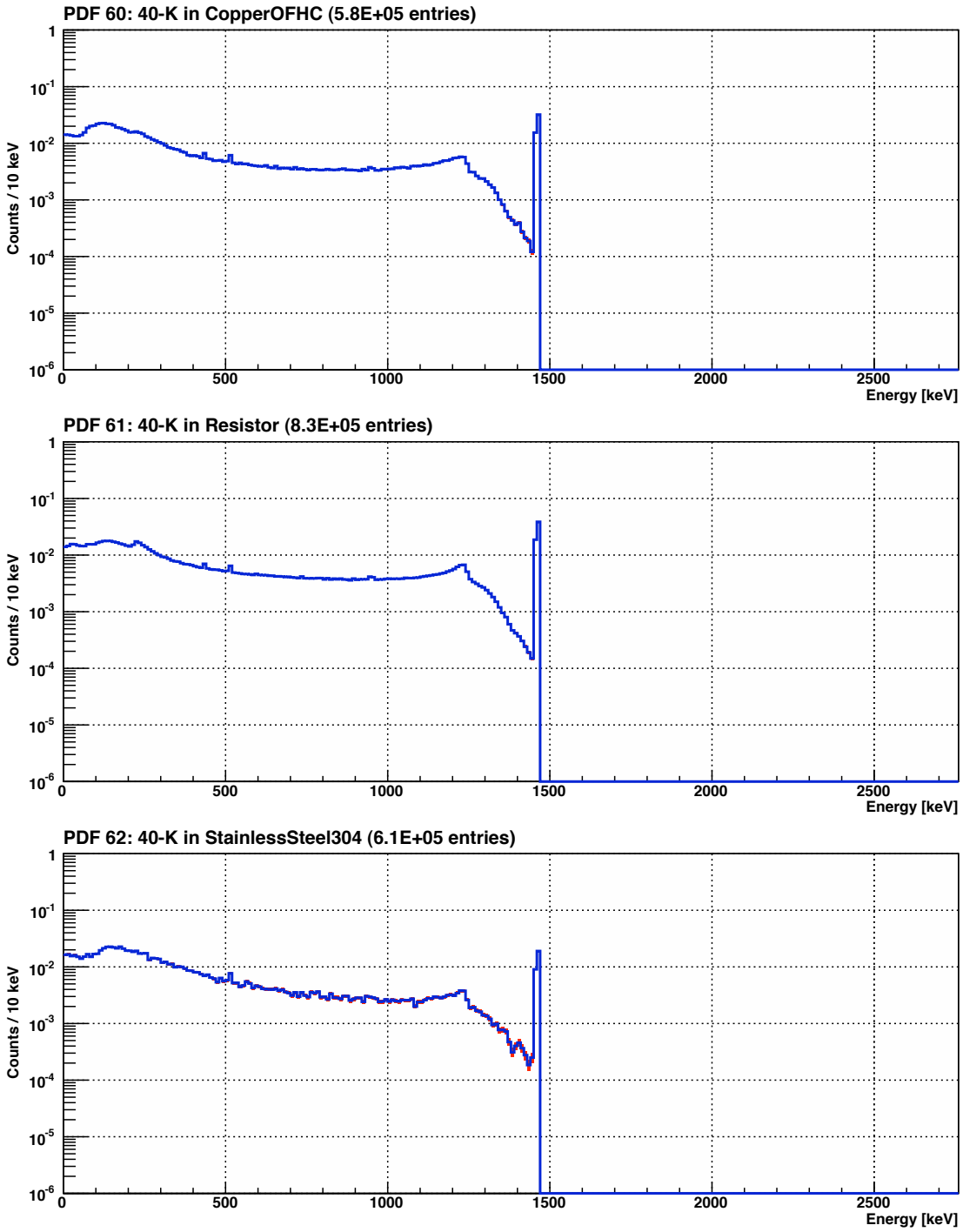

Figure L.21: Background model energy spectra histogram PDFs 60–62. Each PDF is normalized to unit area.

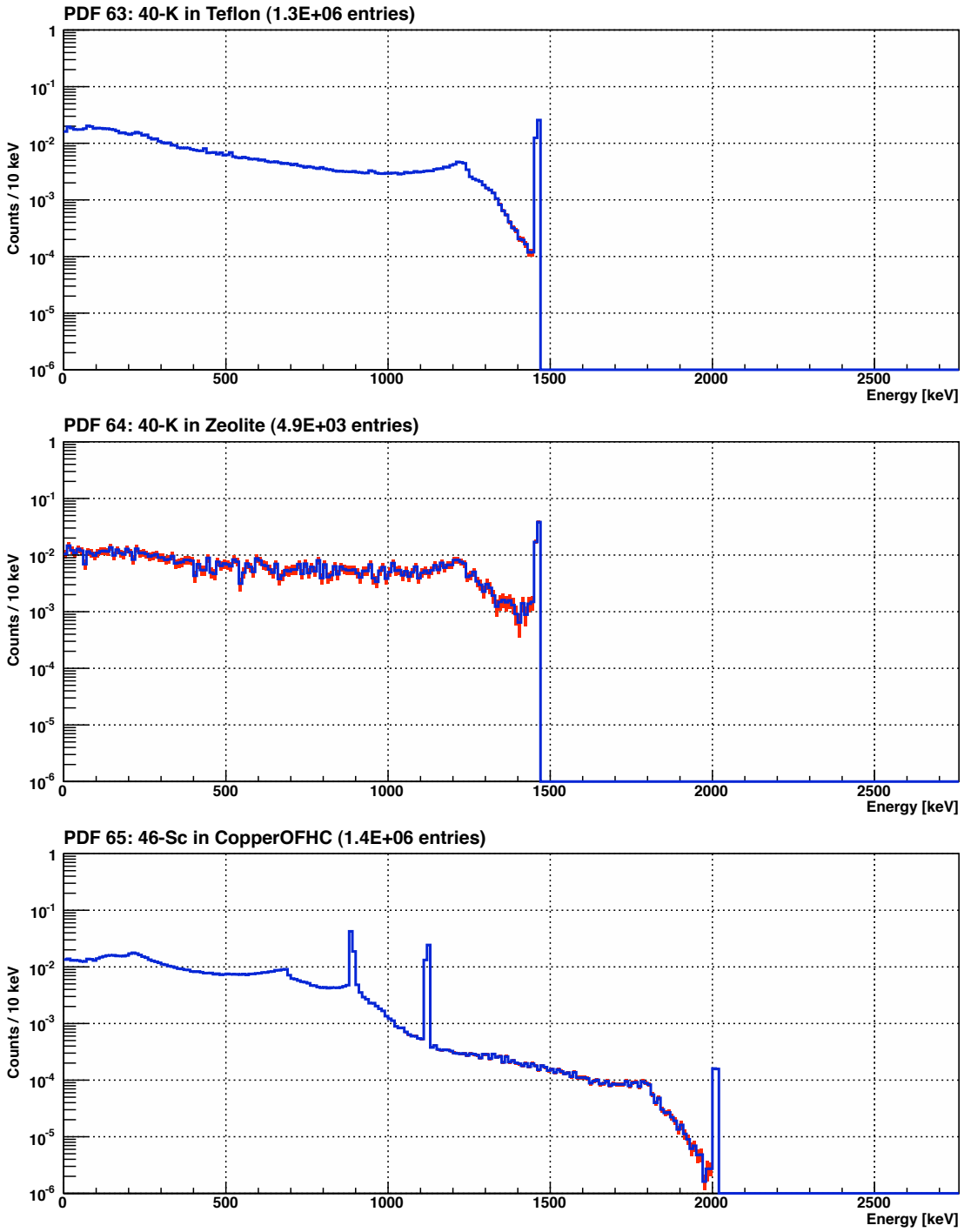

Figure L.22: Background model energy spectra histogram PDFs 63–65. Each PDF is normalized to unit area.

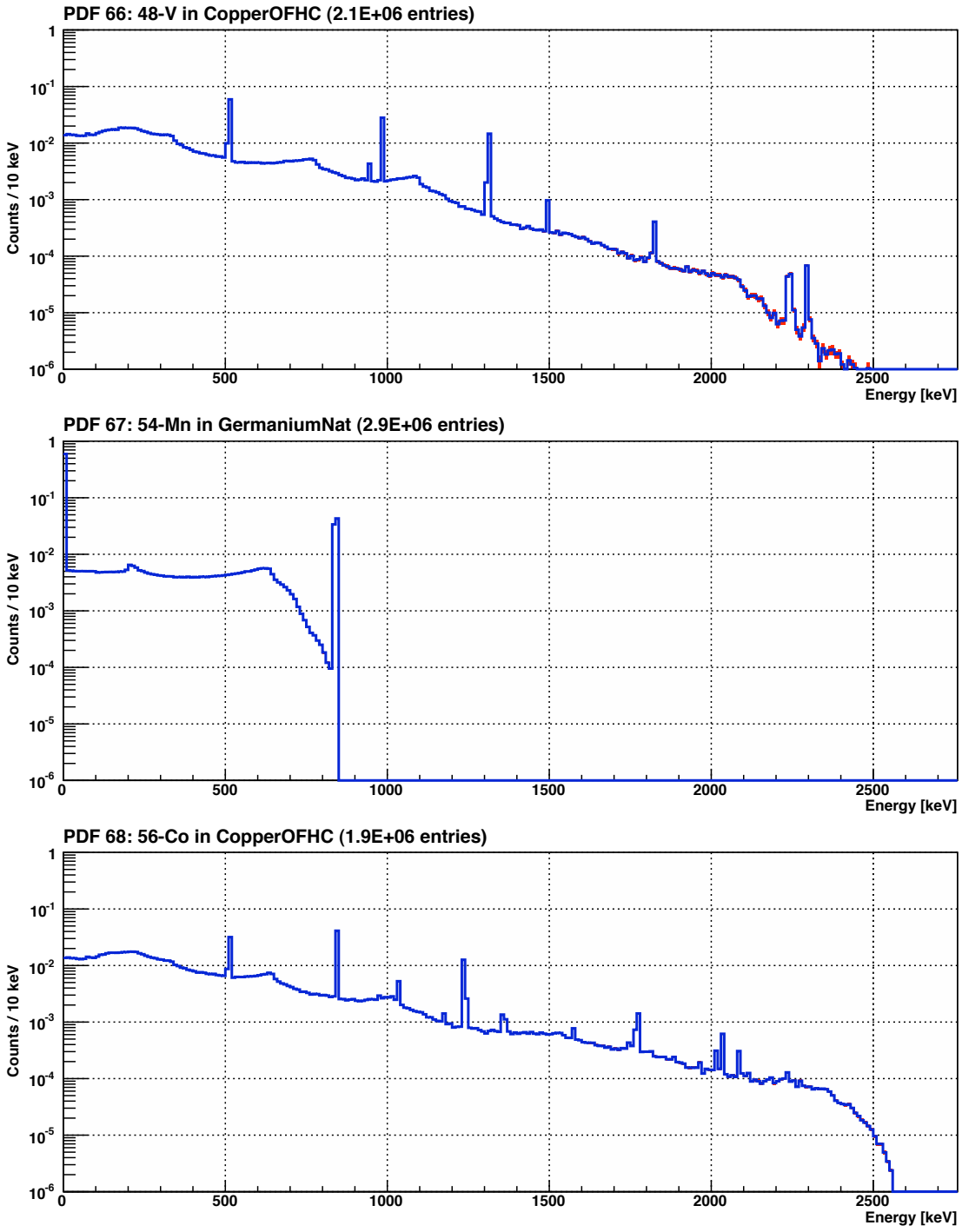

Figure L.23: Background model energy spectra histogram PDFs 66–68. Each PDF is normalized to unit area.

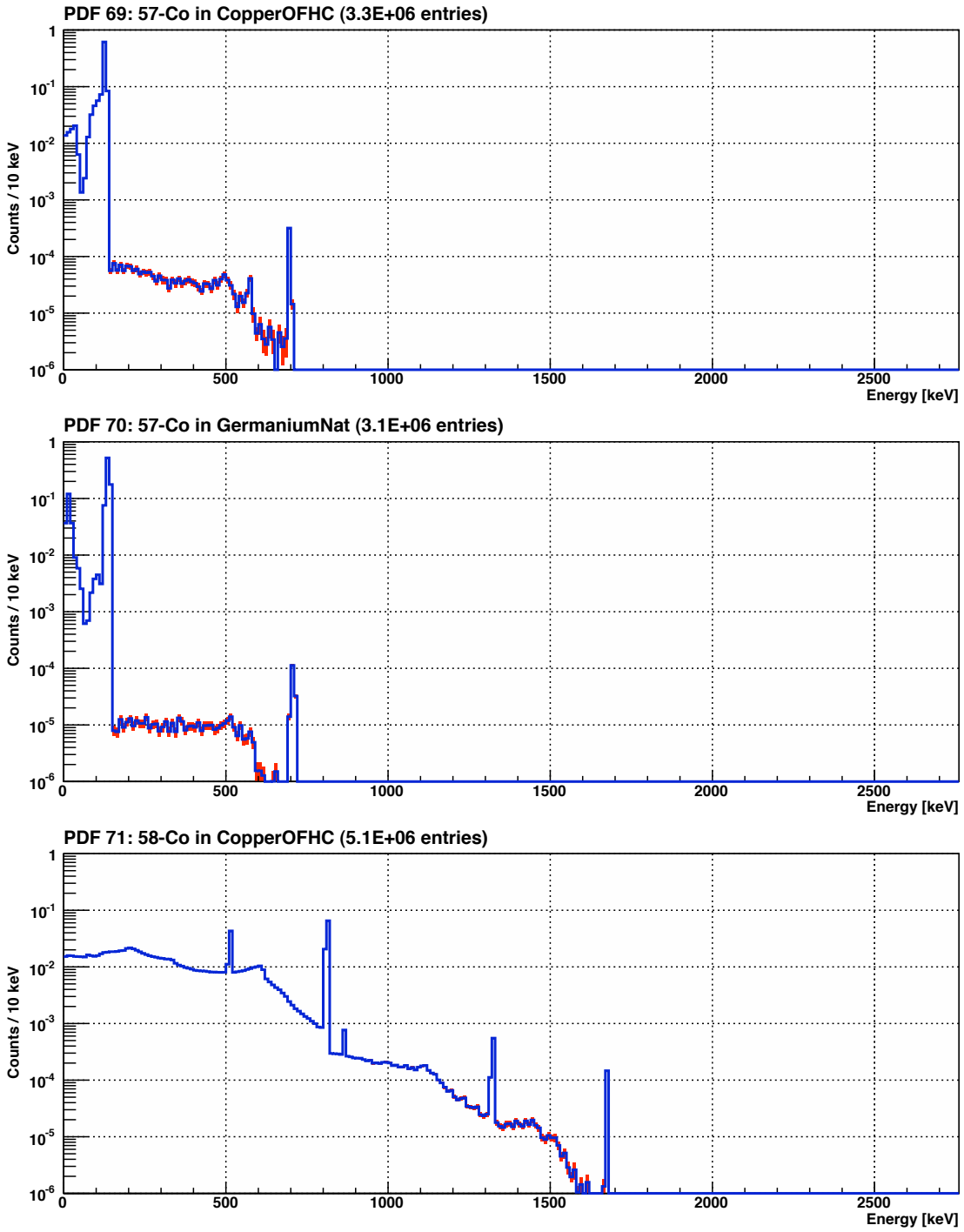

Figure L.24: Background model energy spectra histogram PDFs 69–71. Each PDF is normalized to unit area.

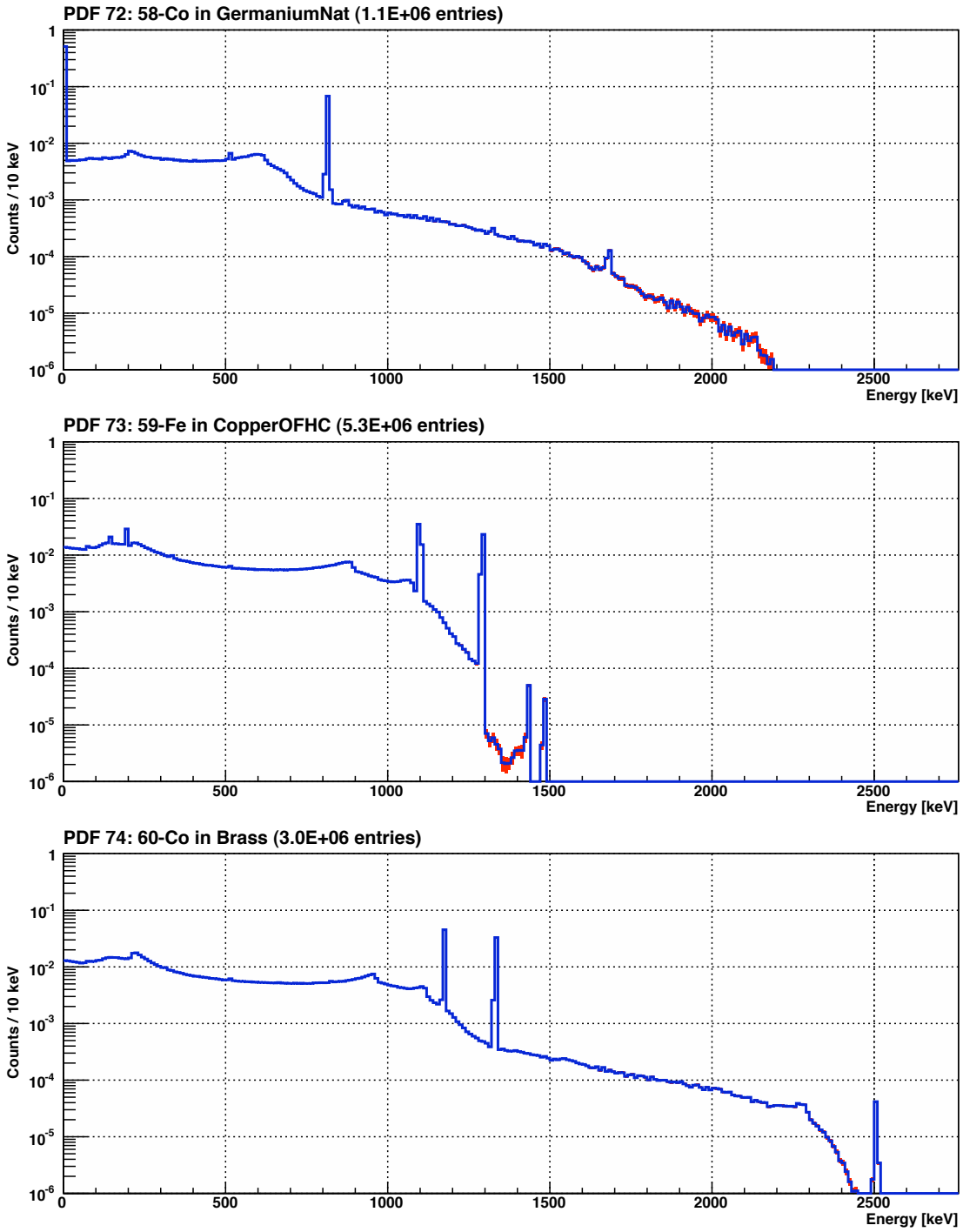

Figure L.25: Background model energy spectra histogram PDFs 72–74. Each PDF is normalized to unit area.

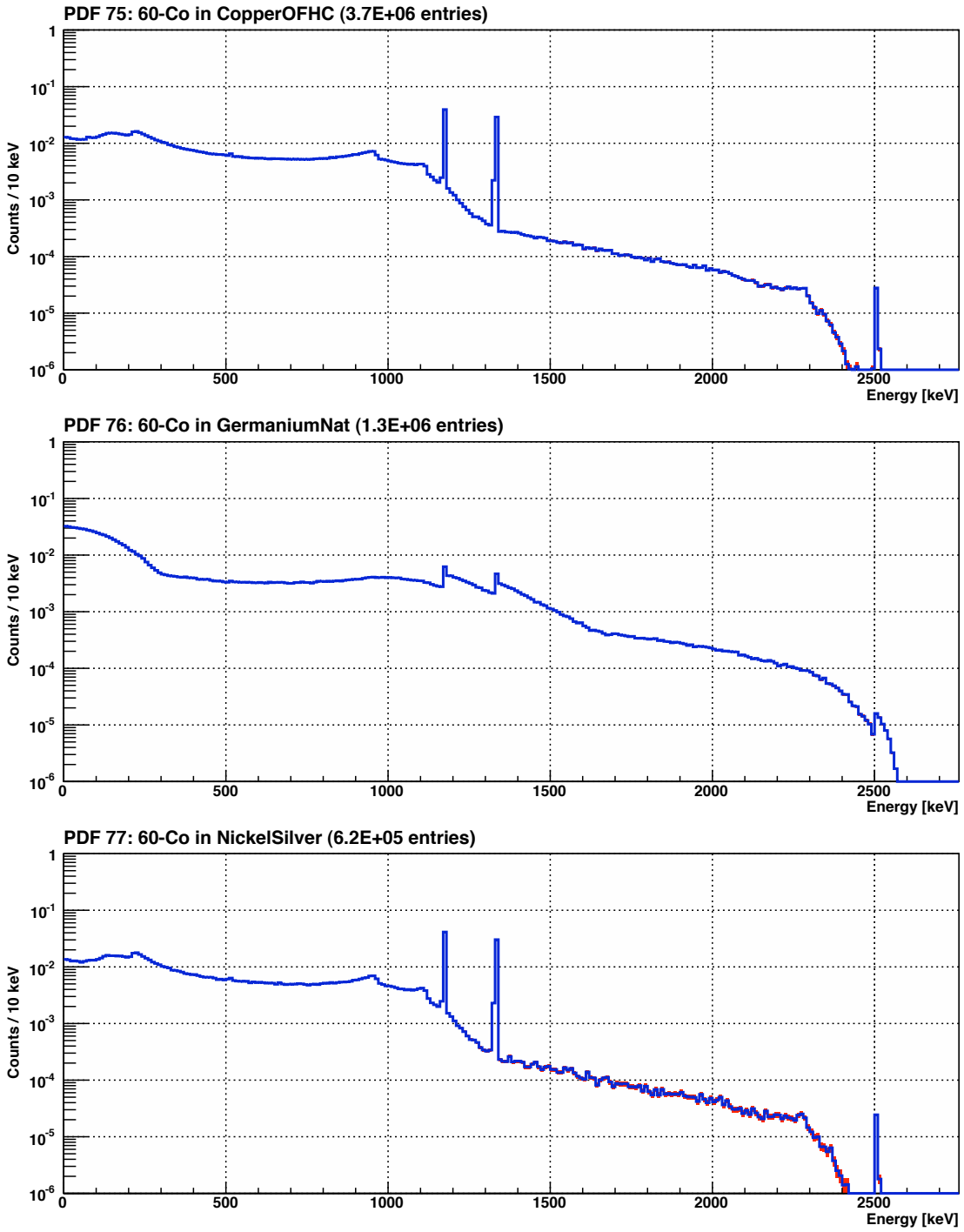

Figure L.26: Background model energy spectra histogram PDFs 75–77. Each PDF is normalized to unit area.

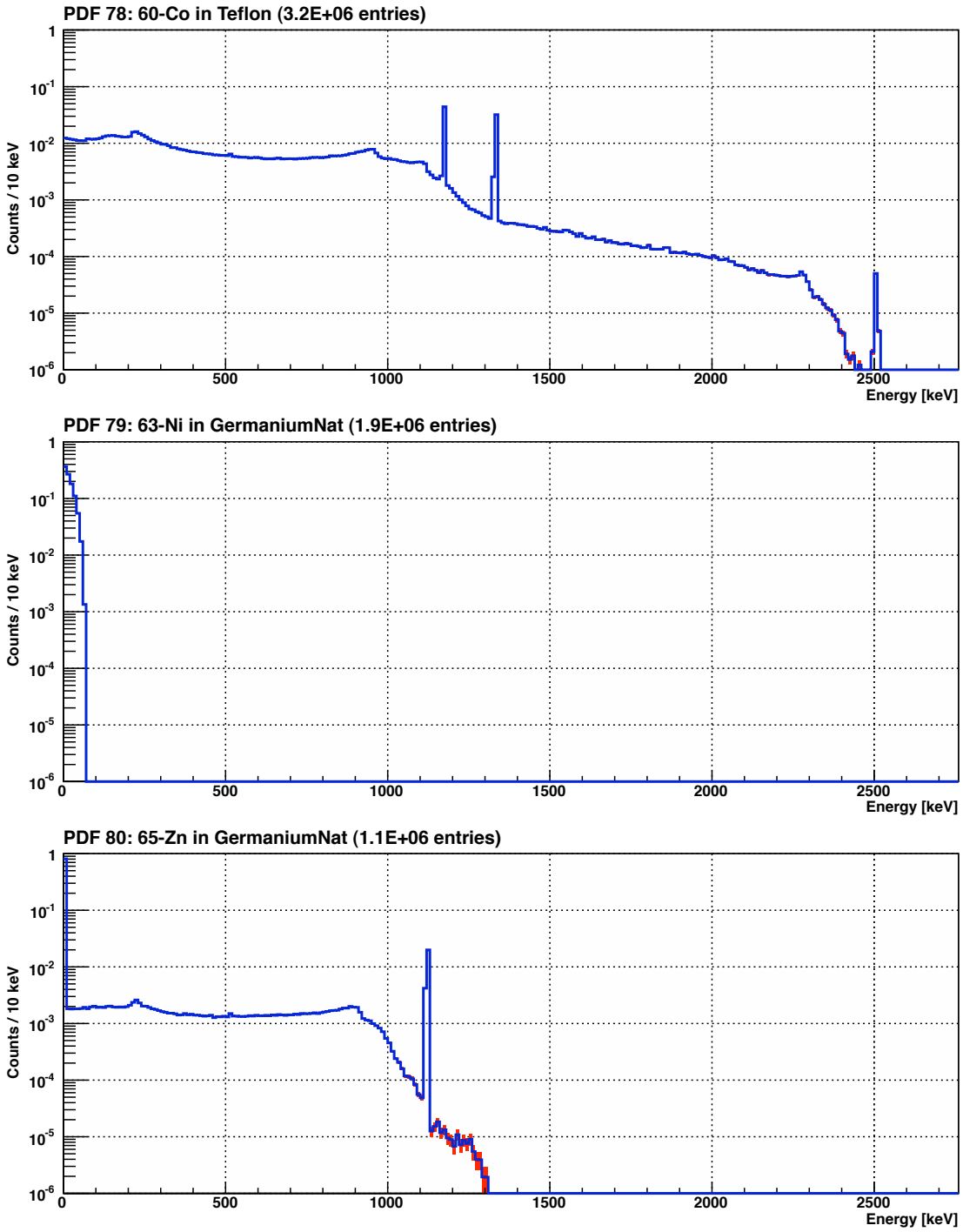

Figure L.27: Background model energy spectra histogram PDFs 78–80. Each PDF is normalized to unit area.

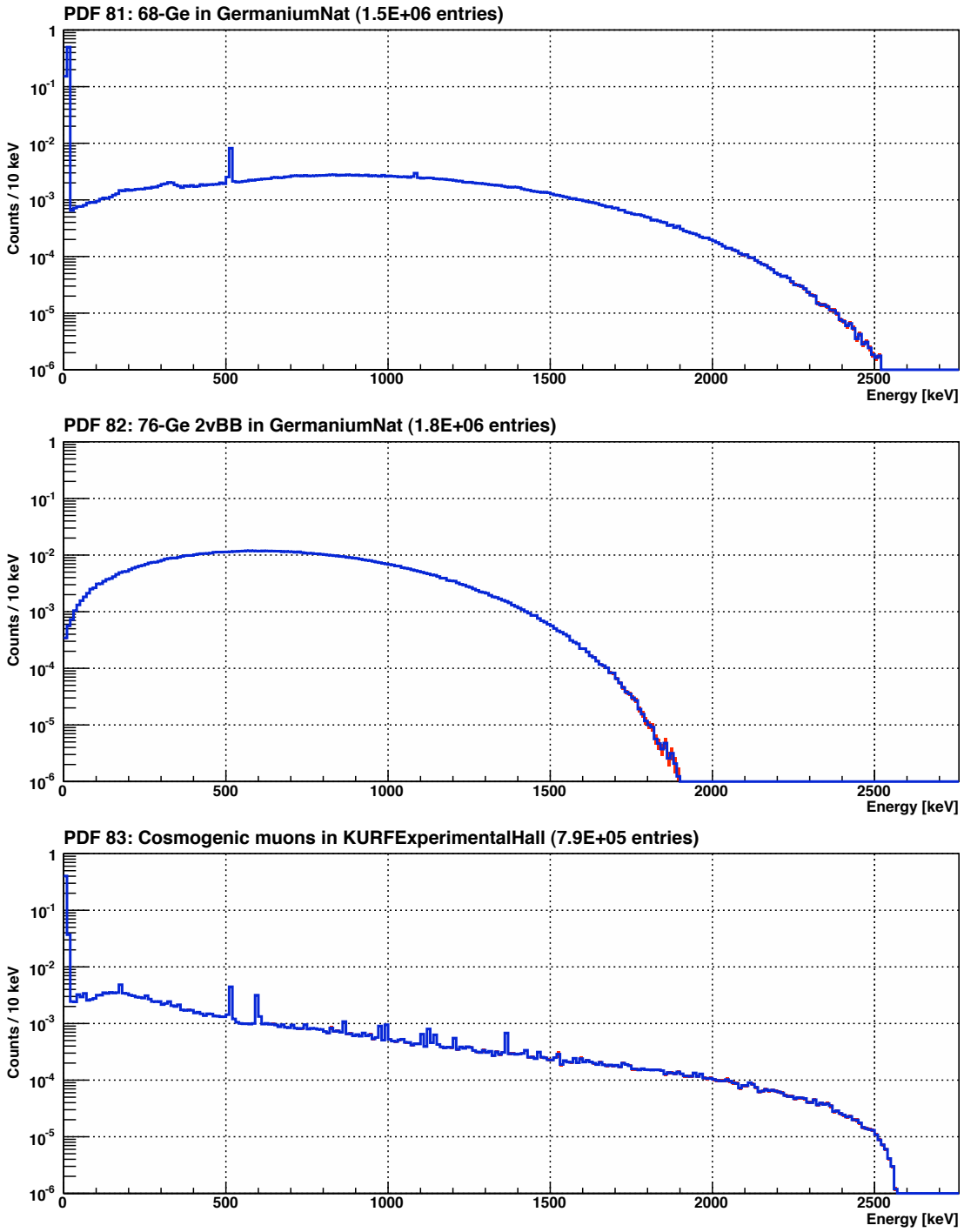

Figure L.28: Background model energy spectra histogram PDFs 81–83. Each PDF is normalized to unit area.

L.2 Dataset I fit results

Table L.1: Results from fit of background model to Dataset I energy spectrum. The fit was performed in the region from 10 to 2000 keV, using 10-keV bins. The first column of the table is an index used to identify the fit components. The third column is the number of counts expected from the predicted background energy spectrum.

	Description	**Prediction**	**Fit Result**
0	232-Th LC in BerylliumCopper	7.66×10^{1}	$\left(6.41\ ^{+6122775699.34}_{-0.00}\right) \times 10^{-8}$
1	232-Th LC in Brass	4.30×10^{0}	$\left(5.36\ ^{+6173736434.45}_{-0.00}\right) \times 10^{-8}$
2	232-Th LC in CopperOFHC	4.56×10^{-1}	$\left(6.67\ ^{+6230158866.28}_{-0.00}\right) \times 10^{-8}$
3	232-Th LC in GermaniumNat	8.92×10^{-3}	$\left(9.59\ ^{+3292222391.80}_{-3292222391.80}\right) \times 10^{-8}$
4	232-Th LC in MoxtekFET	9.03×10^{-3}	$\left(2.24\ ^{+5979860350.85}_{-0.00}\right) \times 10^{-8}$
5	232-Th LC in NickelSilver	4.58×10^{-4}	$\left(1.97\ ^{+5628690210.85}_{-0.00}\right) \times 10^{-8}$
6	232-Th LC in Resistor	2.86×10^{2}	$\left(1.48\ ^{+5533905604.82}_{-0.00}\right) \times 10^{-8}$
7	232-Th LC in StainlessSteel304	2.50×10^{1}	$\left(1.03\ ^{+521678479.50}_{-0.00}\right) \times 10^{-7}$
8	232-Th LC in Teflon	6.80×10^{1}	$\left(2.10\ ^{+665680170.03}_{-0.00}\right) \times 10^{-7}$
9	232-Th LC in Zeolite	9.32×10^{1}	$\left(1.46\ ^{+1.32}_{-0.00}\right) \times 10^{2}$
10	232-Th UC in BerylliumCopper	6.52×10^{1}	$\left(2.94\ ^{+2264294.96}_{-2264294.96}\right) \times 10^{-5}$
11	232-Th UC in Brass	1.31×10^{0}	$\left(7.45\ ^{+117628390.23}_{-0.00}\right) \times 10^{-6}$
12	232-Th UC in CopperOFHC	4.04×10^{-1}	$\left(7.46\ ^{+120949975.49}_{-0.00}\right) \times 10^{-6}$
13	232-Th UC in GermaniumNat	1.22×10^{-2}	$\left(4.13\ ^{+425663594.34}_{-425663594.34}\right) \times 10^{-7}$
14	232-Th UC in MoxtekFET	7.77×10^{-3}	$\left(1.30\ ^{+12618293.97}_{-0.00}\right) \times 10^{-5}$
15	232-Th UC in NickelSilver	3.99×10^{-4}	$\left(2.11\ ^{+24968579.09}_{-24968579.09}\right) \times 10^{-6}$
16	232-Th UC in Resistor	3.08×10^{2}	$\left(2.69\ ^{+23938937.96}_{-23938937.96}\right) \times 10^{-6}$
17	232-Th UC in StainlessSteel304	2.29×10^{1}	$\left(2.15\ ^{+6544500164.70}_{-0.00}\right) \times 10^{-8}$
18	232-Th UC in Teflon	5.87×10^{1}	$\left(2.64\ ^{+2365801.42}_{-2365801.42}\right) \times 10^{-5}$

Table L.1: continued

	Description	Prediction	Fit Result
19	232-Th UC in Zeolite	8.12×10^{1}	$\left(4.01\ ^{+14.35}_{-0.00}\right) \times 10^{1}$
20	238-U LC I in Air	3.02×10^{-4}	$\left(1.52\ ^{+37259.17}_{-37259.17}\right) \times 10^{-3}$
21	238-U LC I in BerylliumCopper	9.92×10^{2}	$\left(7.02\ ^{+20508.59}_{-20508.59}\right) \times 10^{-3}$
22	238-U LC I in Brass	5.48×10^{0}	$\left(3.68\ ^{+295781.42}_{-295781.42}\right) \times 10^{-4}$
23	238-U LC I in CopperOFHC	2.25×10^{0}	$\left(4.24\ ^{+17709094.05}_{-0.00}\right) \times 10^{-5}$
24	238-U LC I in GermaniumNat	3.56×10^{-2}	$\left(1.23\ ^{+0.34}_{-0.34}\right) \times 10^{3}$
25	238-U LC I in MoxtekFET	2.88×10^{-3}	$\left(2.64\ ^{+3.38}_{-0.00}\right) \times 10^{2}$
26	238-U LC I in NickelSilver	3.84×10^{-1}	$\left(3.82\ ^{+2739817.04}_{-2739817.04}\right) \times 10^{-5}$
27	238-U LC I in Resistor	3.01×10^{2}	$\left(5.79\ ^{+21055547.52}_{-0.00}\right) \times 10^{-5}$
28	238-U LC I in StainlessSteel304	1.77×10^{2}	$\left(8.93\ ^{+634198883.38}_{-0.00}\right) \times 10^{-7}$
29	238-U LC I in Teflon	9.88×10^{1}	$\left(6.01\ ^{+314644.69}_{-314644.69}\right) \times 10^{-4}$
30	238-U LC I in Zeolite	1.12×10^{2}	$\left(8.05\ ^{+0.00}_{-4.02}\right) \times 10^{2}$
31	238-U LC II in Air	3.35×10^{-6}	$\left(1.77\ ^{+19307956352.31}_{-0.00}\right) \times 10^{-9}$
32	238-U LC II in BerylliumCopper	2.41×10^{1}	$\left(2.80\ ^{+1429638157.96}_{-0.00}\right) \times 10^{-7}$
33	238-U LC II in Brass	5.30×10^{1}	$\left(3.01\ ^{+44841391.17}_{-44841391.17}\right) \times 10^{-6}$
34	238-U LC II in CopperOFHC	1.52×10^{-2}	$\left(4.68\ ^{+30048828122.66}_{-0.00}\right) \times 10^{-9}$
35	238-U LC II in GermaniumNat	4.20×10^{-2}	$\left(1.10\ ^{+0.92}_{-0.00}\right) \times 10^{2}$
36	238-U LC II in LeadAin	6.17×10^{1}	$\left(3.69\ ^{+33180116430.23}_{-33180116430.23}\right) \times 10^{-9}$
37	238-U LC II in LeadMod	6.09×10^{1}	$\left(2.31\ ^{+166697976.61}_{-0.00}\right) \times 10^{-6}$
38	238-U LC II in LeadPatch	2.30×10^{4}	$\left(2.10\ ^{+0.03}_{-0.00}\right) \times 10^{4}$
39	238-U LC II in MoxtekFET	5.33×10^{-5}	$\left(5.86\ ^{+0.90}_{-0.00}\right) \times 10^{2}$
40	238-U LC II in NickelSilver	4.57×10^{-1}	$\left(1.67\ ^{+5401456219.73}_{-0.00}\right) \times 10^{-8}$
41	238-U LC II in Resistor	1.01×10^{1}	$\left(1.42\ ^{+1449837621.68}_{-0.00}\right) \times 10^{-7}$
42	238-U LC II in RnExposureInCryostat	4.75×10^{-1}	$\left(5.15\ ^{+23889507553.27}_{-0.00}\right) \times 10^{-9}$
43	238-U LC II in RnExposureOutsideCryostat	1.92×10^{-2}	$\left(3.27\ ^{+23126555857.01}_{-0.00}\right) \times 10^{-9}$
44	238-U LC II in StainlessSteel304	3.84×10^{-1}	$\left(3.04\ ^{+21804112158.25}_{-21804112158.25}\right) \times 10^{-9}$

Table L.1: continued

	Description	Prediction	Fit Result
45	238-U LC II in Teflon	2.59×10^{0}	$\left(5.56\ ^{+249344878.13}_{-0.00}\right) \times 10^{-6}$
46	238-U LC II in Tin	1.38×10^{1}	$\left(3.38\ ^{+125854189.34}_{-0.00}\right) \times 10^{-6}$
47	238-U LC II in Zeolite	1.26×10^{-1}	$\left(1.74\ ^{+1.31}_{-1.29}\right) \times 10^{2}$
48	238-U UC in BerylliumCopper	4.37×10^{2}	$\left(7.83\ ^{+568475929.27}_{-0.00}\right) \times 10^{-7}$
49	238-U UC in Brass	5.26×10^{-1}	$\left(2.71\ ^{+103483853.55}_{-0.00}\right) \times 10^{-6}$
50	238-U UC in CopperOFHC	1.08×10^{-1}	$\left(8.43\ ^{+24253254363.96}_{-0.00}\right) \times 10^{-9}$
51	238-U UC in GermaniumNat	3.75×10^{-2}	$\left(1.48\ ^{+0.43}_{-0.42}\right) \times 10^{3}$
52	238-U UC in MoxtekFET	2.57×10^{-4}	$\left(6.12\ ^{+1.22}_{-0.00}\right) \times 10^{2}$
53	238-U UC in NickelSilver	2.25×10^{-2}	$\left(2.40\ ^{+3457865694.00}_{-0.00}\right) \times 10^{-8}$
54	238-U UC in Resistor	7.35×10^{0}	$\left(6.89\ ^{+4121995749.03}_{-0.00}\right) \times 10^{-8}$
55	238-U UC in StainlessSteel304	4.24×10^{0}	$\left(1.96\ ^{+2643971693.96}_{-0.00}\right) \times 10^{-8}$
56	238-U UC in Teflon	9.86×10^{1}	$\left(6.91\ ^{+93345561.61}_{-0.00}\right) \times 10^{-6}$
57	238-U UC in Zeolite	1.37×10^{0}	$\left(9.82\ ^{+1920711009.28}_{-0.00}\right) \times 10^{-8}$
58	3-H in GermaniumNat	1.04×10^{1}	$\left(1.90\ ^{+2.22}_{-2.22}\right) \times 10^{2}$
59	40-K in Brass	1.97×10^{-1}	$\left(1.30\ ^{+196654.43}_{-196654.43}\right) \times 10^{-4}$
60	40-K in CopperOFHC	4.68×10^{-1}	$\left(2.97\ ^{+1627741185.00}_{-0.00}\right) \times 10^{-7}$
61	40-K in Resistor	1.18×10^{2}	$\left(5.96\ ^{+1.03}_{-5.29}\right) \times 10^{2}$
62	40-K in StainlessSteel304	5.76×10^{0}	$\left(1.98\ ^{+104666418.42}_{-0.00}\right) \times 10^{-6}$
63	40-K in Teflon	2.54×10^{2}	$\left(2.71\ ^{+343010.73}_{-343010.73}\right) \times 10^{-4}$
64	40-K in Zeolite	4.36×10^{0}	$\left(7.63\ ^{+633720.62}_{-633720.62}\right) \times 10^{-4}$
65	46-Sc in CopperOFHC	3.24×10^{0}	$\left(2.00\ ^{+1.27}_{-1.27}\right) \times 10^{2}$
66	48-V in CopperOFHC	5.25×10^{-4}	$\left(4.30\ ^{+10.28}_{-0.00}\right) \times 10^{1}$
67	54-Mn in GermaniumNat	3.38×10^{1}	$\left(3.66\ ^{+3.99}_{-0.00}\right) \times 10^{1}$
68	56-Co in CopperOFHC	1.46×10^{1}	$\left(2.07\ ^{+381.63}_{-381.63}\right) \times 10^{-1}$
69	57-Co in CopperOFHC	1.85×10^{2}	$\left(1.21\ ^{+2222371527.88}_{-0.00}\right) \times 10^{-8}$
70	57-Co in GermaniumNat	6.14×10^{1}	$\left(3.61\ ^{+5.86}_{-0.00}\right) \times 10^{1}$

Table L.1: continued

	Description	Prediction	Fit Result
71	58-Co in CopperOFHC	4.93×10^{1}	$\left(6.61\ ^{+8.08}_{-0.00}\right) \times 10^{1}$
72	58-Co in GermaniumNat	9.66×10^{0}	$\left(2.63\ ^{+299139181.28}_{-0.00}\right) \times 10^{-7}$
73	59-Fe in CopperOFHC	5.28×10^{0}	$\left(1.92\ ^{+164046610.17}_{-0.00}\right) \times 10^{-7}$
74	60-Co in Brass	2.29×10^{0}	$\left(9.66\ ^{+7.75}_{-0.00}\right) \times 10^{1}$
75	60-Co in CopperOFHC	3.15×10^{2}	$\left(2.14\ ^{+18479.18}_{-0.00}\right) \times 10^{-2}$
76	60-Co in GermaniumNat	1.93×10^{1}	$\left(1.92\ ^{+229767.83}_{-229767.83}\right) \times 10^{-4}$
77	60-Co in NickelSilver	1.84×10^{-1}	$\left(5.41\ ^{+17828.57}_{-0.00}\right) \times 10^{-2}$
78	60-Co in Teflon	1.79×10^{2}	$\left(7.17\ ^{+171.27}_{-0.00}\right) \times 10^{0}$
79	63-Ni in GermaniumNat	9.76×10^{-1}	$\left(1.76\ ^{+293774719.35}_{-0.00}\right) \times 10^{-7}$
80	65-Zn in GermaniumNat	1.23×10^{2}	$\left(6.90\ ^{+6.35}_{-5.96}\right) \times 10^{1}$
81	68-Ge in GermaniumNat	3.92×10^{2}	$\left(5.60\ ^{+3.91}_{-3.91}\right) \times 10^{2}$
82	76-Ge 2vBB in GermaniumNat	1.26×10^{1}	$\left(2.32\ ^{+1.83}_{-1.84}\right) \times 10^{2}$
83	Cosmogenic muons in KURFExperimentalHall	4.64×10^{0}	$\left(3.78\ ^{+2211117.54}_{-0.00}\right) \times 10^{-4}$

The correlation coefficients between pairs of fit parameters are shown in Figure L.29 and Table L.2. A correlation coefficient is a dimensionless measure of the correlation between two parameters, i and j [85]:

$$\rho_{ij} = \frac{V_{ij}}{\sigma_i \sigma_j} \tag{L.1}$$

where V_{ij} is an element of the covariance matrix and σ_i and σ_j are the parameter uncertainties. The correlation coefficient has a value between -1 and 1.

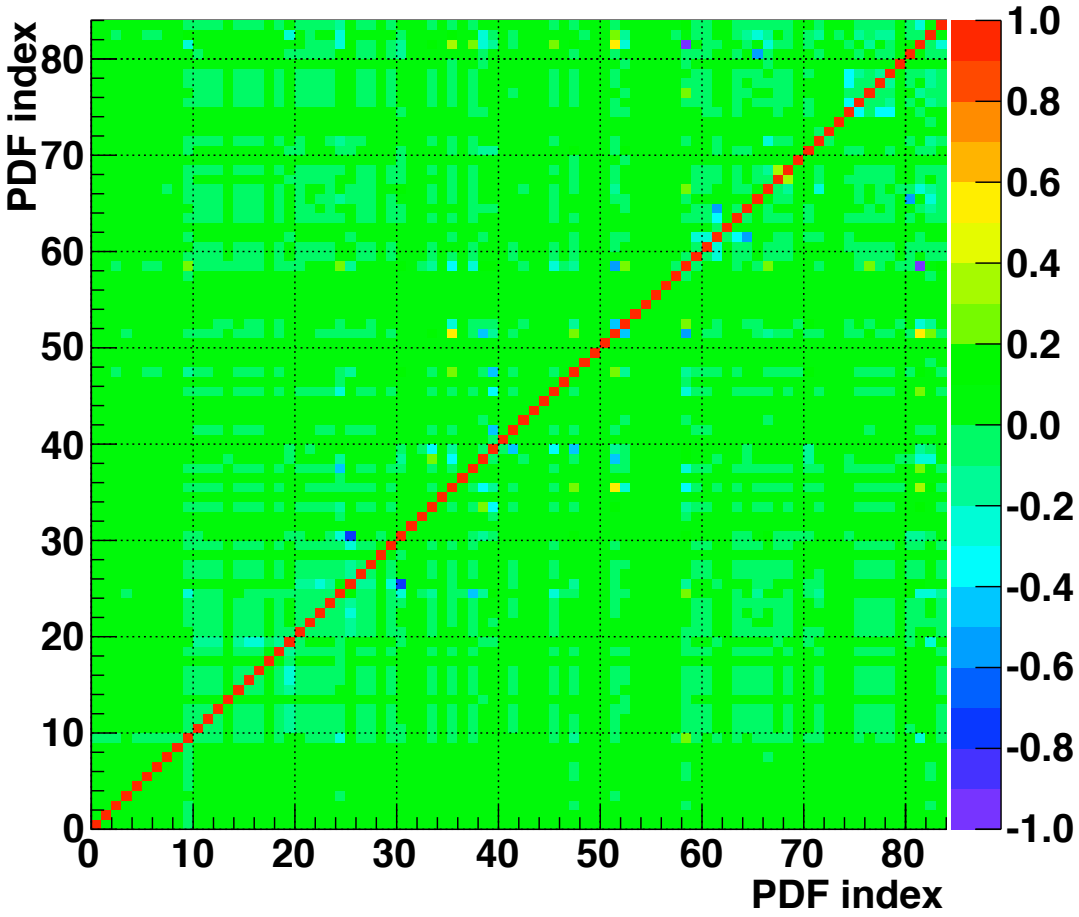

Figure L.29: Correlations between PDF pairs in Dataset I fit. This image represents the correlation coefficient matrix. It is symmetric about the diagonal. Each PDF is identified by an index listed in Table L.1.

Table L.2: Correlations between selected PDF pairs in Dataset I. The 12 pairs of PDFs for which the absolute value of the correlation coefficient is greater than 0.40 are listed.

	Description		**Description**	**Corr. coeff.**
24	238-U LC I in GermaniumNat	37	238-U LC II in LeadMod	-0.43
25	238-U LC I in MoxtekFET	30	238-U LC I in Zeolite	-0.74
35	238-U LC II in GermaniumNat	51	238-U UC in GermaniumNat	0.57
38	238-U LC II in LeadPatch	51	238-U UC in GermaniumNat	-0.40
39	238-U LC II in MoxtekFET	41	238-U LC II in Resistor	-0.47
39	238-U LC II in MoxtekFET	47	238-U LC II in Zeolite	-0.47
51	238-U UC in GermaniumNat	52	238-U UC in MoxtekFET	-0.49
51	238-U UC in GermaniumNat	58	3-H in GermaniumNat	-0.53
51	238-U UC in GermaniumNat	81	68-Ge in GermaniumNat	0.58
58	3-H in GermaniumNat	81	68-Ge in GermaniumNat	-0.98
61	40-K in Resistor	64	40-K in Zeolite	-0.54
65	46-Sc in CopperOFHC	80	65-Zn in GermaniumNat	-0.56

L.3 Energy regions of the Dataset I fit

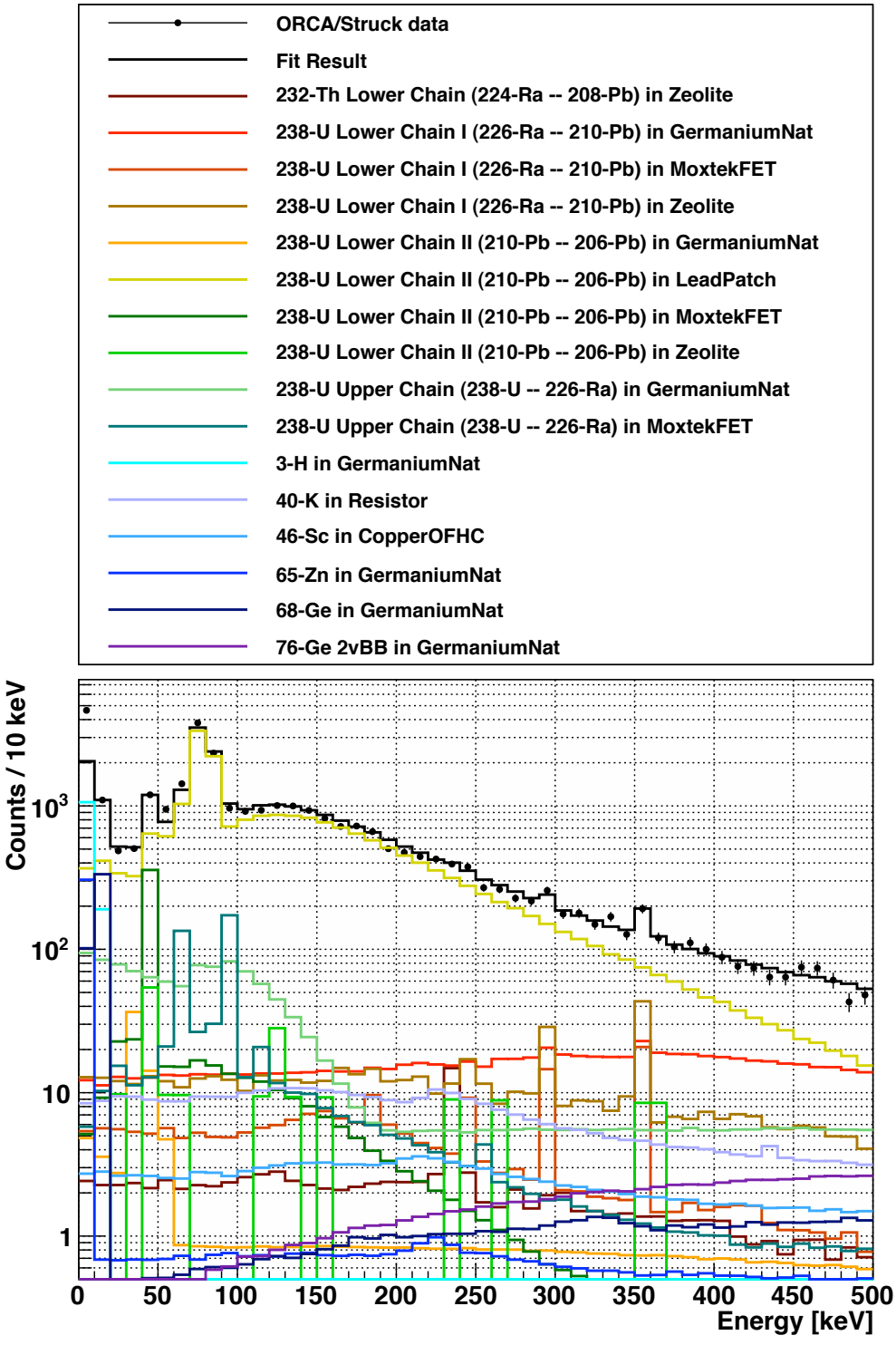

Figure L.30: Dataset I fit results in the region from 0 to 500 keV.

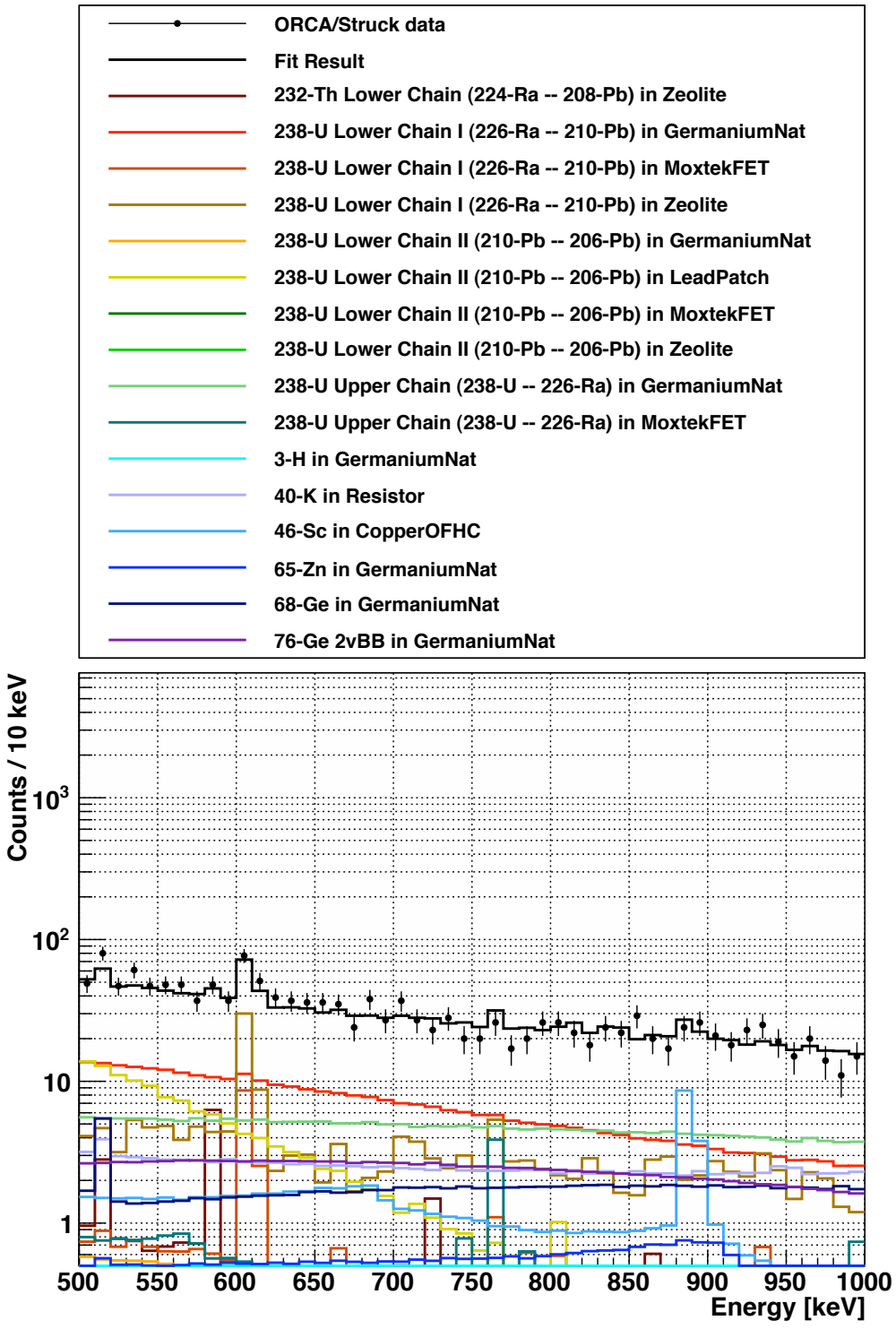

Figure L.31: Dataset I fit results in the region from 500 to 1000 keV.

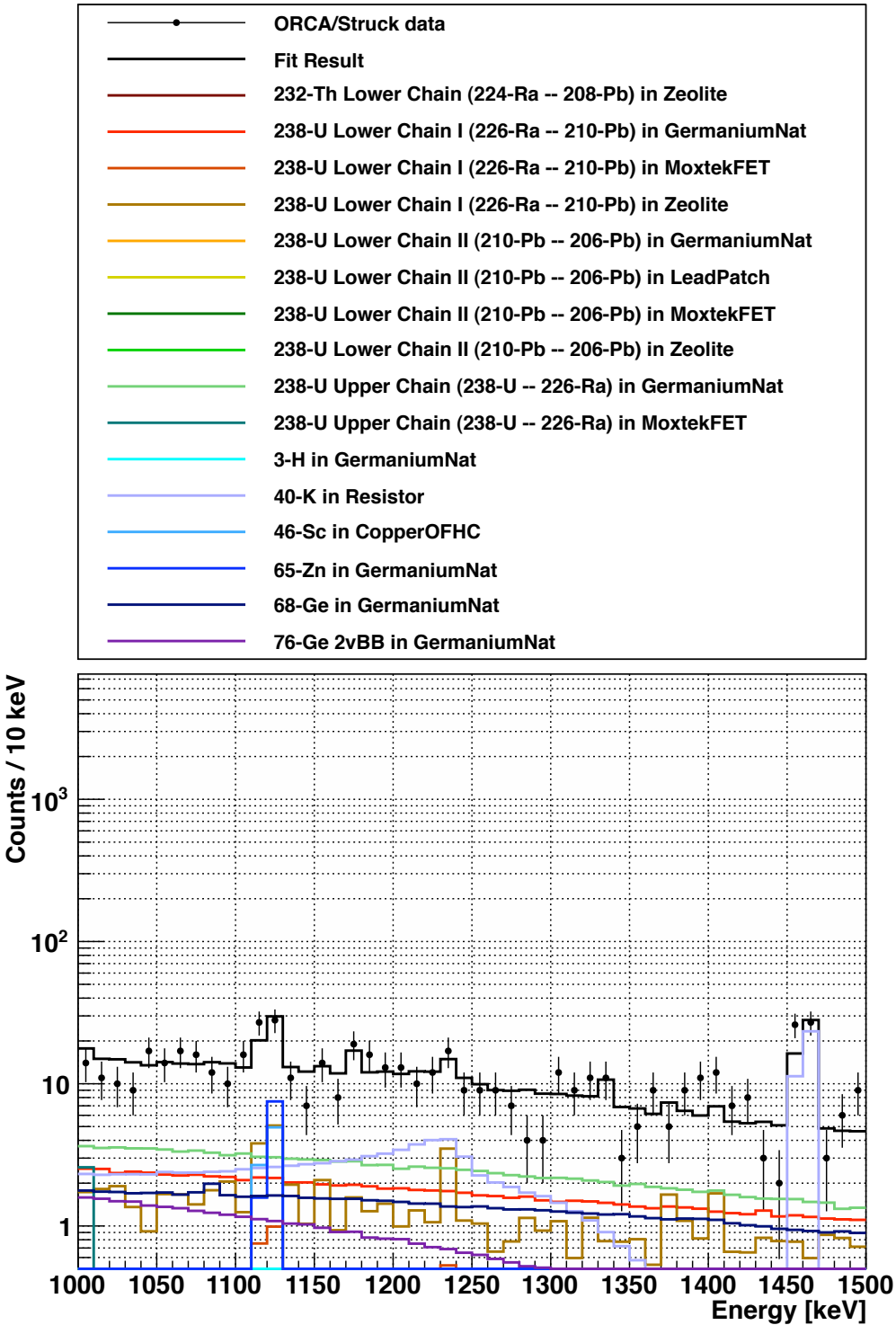

Figure L.32: Dataset I fit results in the region from 1000 to 1500 keV.

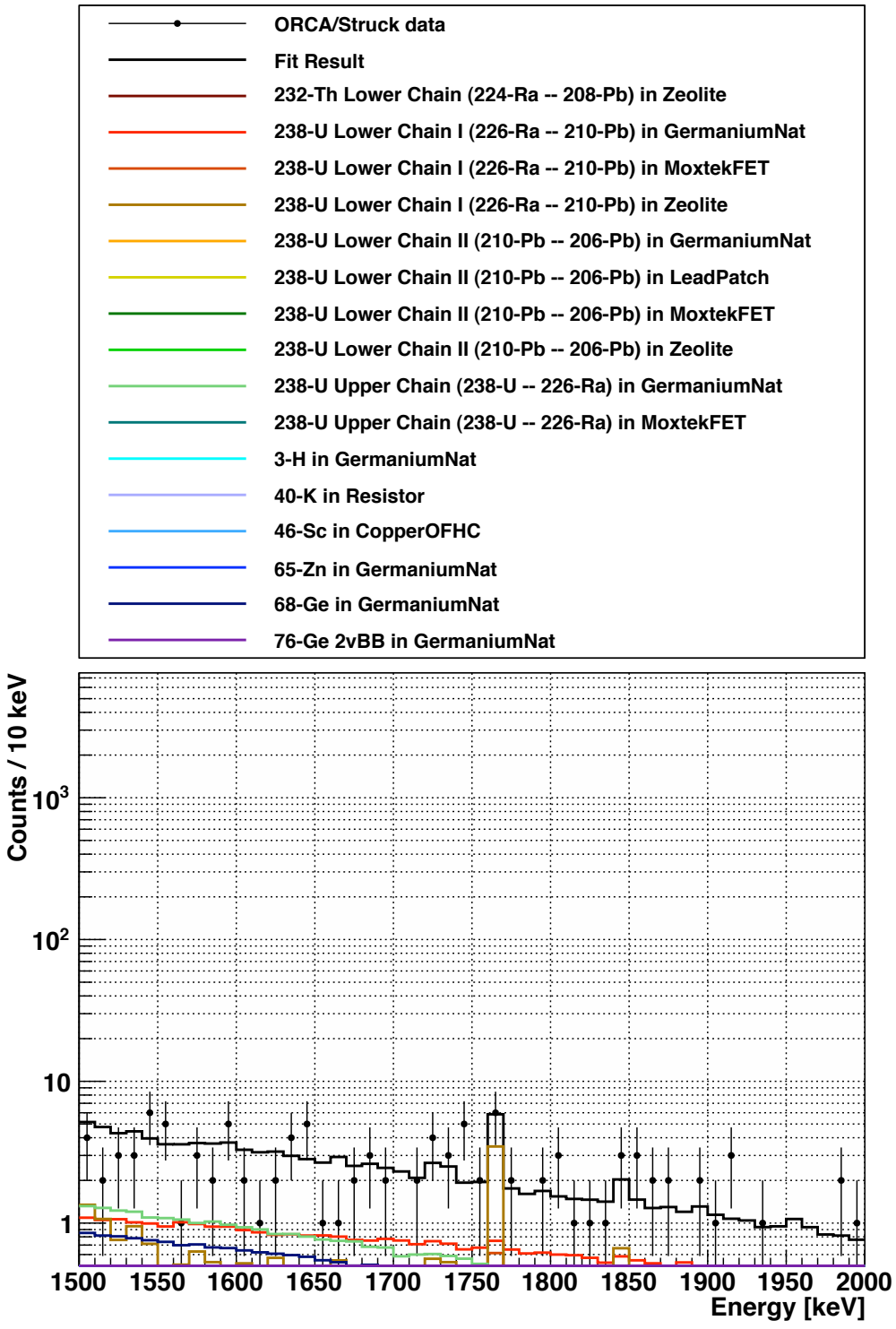

Figure L.33: Dataset I fit results in the region from 1500 to 2000 keV.

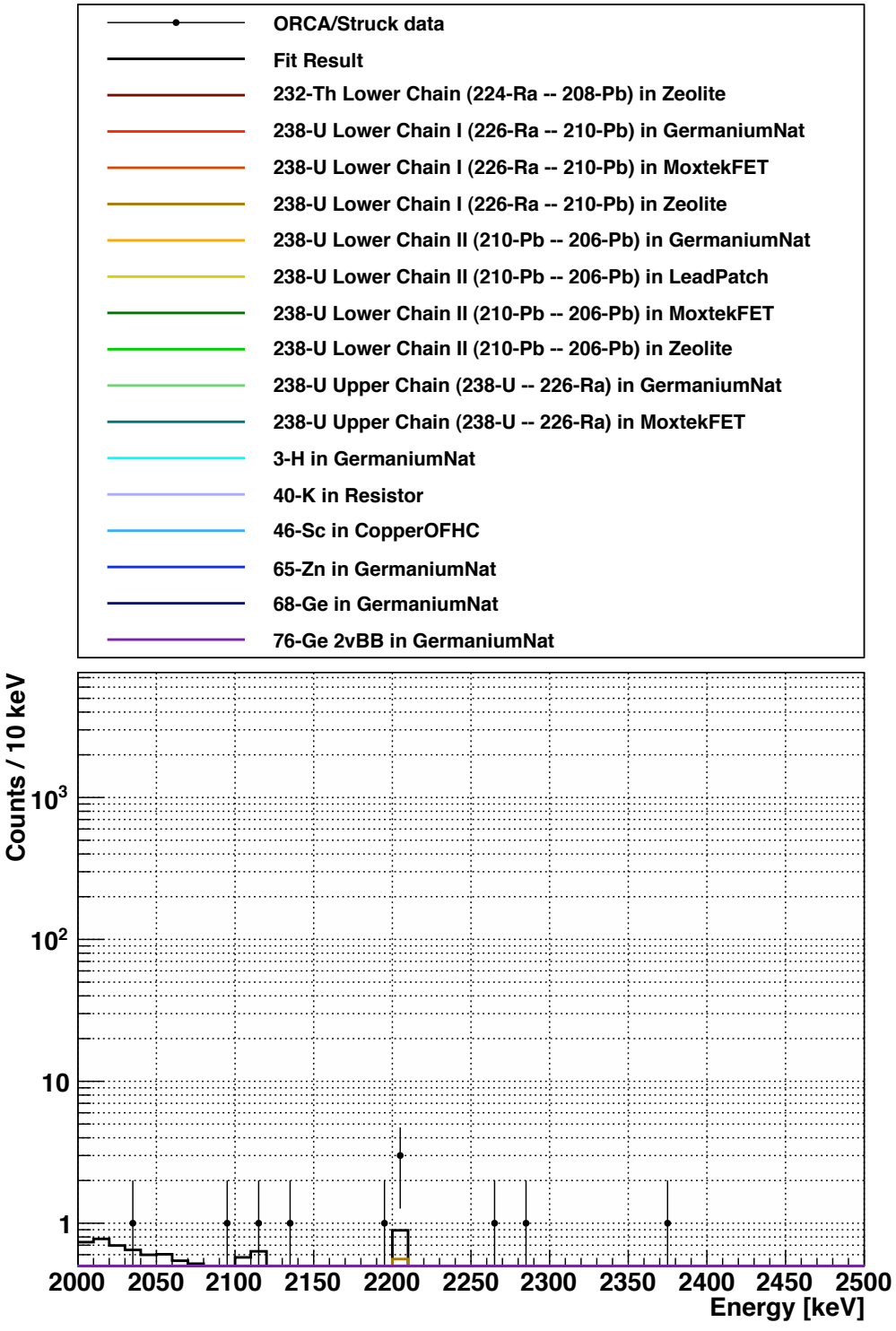

Figure L.34: Dataset I fit results in the region from 2000 to 2500 keV.

L.4 Dataset II fit results

Table L.3: Results from fit of background model to Dataset II energy spectrum. The fit was performed in the region from 10 to 2000 keV, using 10-keV bins. The first column of the table is an index used to identify the fit components. The third column is the number of counts expected from the predicted background energy spectrum.

	Description	**Prediction**	**Fit Result**
0	232-Th LC in BerylliumCopper	1.89×10^{2}	$\left(2.19\ ^{+3.05}_{-0.00}\right) \times 10^{2}$
1	232-Th LC in Brass	1.06×10^{1}	$\left(3.52\ ^{+14890.61}_{-14890.61}\right) \times 10^{-3}$
2	232-Th LC in CopperOFHC	1.13×10^{0}	$\left(7.67\ ^{+2059933741.41}_{-2059933741.41}\right) \times 10^{-7}$
3	232-Th LC in GermaniumNat	2.21×10^{-2}	$\left(2.18\ ^{+48948608335.80}_{-0.00}\right) \times 10^{-9}$
4	232-Th LC in MoxtekFET	2.23×10^{-2}	$\left(2.14\ ^{+12892.06}_{-12892.06}\right) \times 10^{-3}$
5	232-Th LC in NickelSilver	1.13×10^{-3}	$\left(1.13\ ^{+167157552.85}_{-0.00}\right) \times 10^{-6}$
6	232-Th LC in Resistor	7.08×10^{2}	$\left(1.06\ ^{+184630784.60}_{-0.00}\right) \times 10^{-6}$
7	232-Th LC in StainlessSteel304	6.18×10^{1}	$\left(6.43\ ^{+68042150783.17}_{-0.00}\right) \times 10^{-9}$
8	232-Th LC in Teflon	1.68×10^{2}	$\left(3.72\ ^{+155542.29}_{-155542.29}\right) \times 10^{-4}$
9	232-Th LC in Zeolite	2.30×10^{2}	$\left(6.38\ ^{+4.11}_{-4.16}\right) \times 10^{2}$
10	232-Th UC in BerylliumCopper	1.61×10^{2}	$\left(2.97\ ^{+176080920991.98}_{-0.00}\right) \times 10^{-9}$
11	232-Th UC in Brass	3.25×10^{0}	$\left(1.85\ ^{+1442924994.44}_{-0.00}\right) \times 10^{-7}$
12	232-Th UC in CopperOFHC	1.00×10^{0}	$\left(1.54\ ^{+1538060058.79}_{-1538060058.79}\right) \times 10^{-7}$
13	232-Th UC in GermaniumNat	3.01×10^{-2}	$\left(3.41\ ^{+5727922225.89}_{-0.00}\right) \times 10^{-8}$
14	232-Th UC in MoxtekFET	1.92×10^{-2}	$\left(2.16\ ^{+1526515301.81}_{-0.00}\right) \times 10^{-7}$
15	232-Th UC in NickelSilver	9.86×10^{-4}	$\left(1.63\ ^{+1151441891.08}_{-0.00}\right) \times 10^{-7}$
16	232-Th UC in Resistor	7.61×10^{2}	$\left(2.03\ ^{+1249526077.05}_{-0.00}\right) \times 10^{-7}$
17	232-Th UC in StainlessSteel304	5.65×10^{1}	$\left(2.62\ ^{+8765207510.69}_{-0.00}\right) \times 10^{-8}$
18	232-Th UC in Teflon	1.45×10^{2}	$\left(4.27\ ^{+183035782841.11}_{-0.00}\right) \times 10^{-9}$

Table L.3: continued

	Description	Prediction	Fit Result
19	232-Th UC in Zeolite	2.01×10^{2}	$\left(4.55\ ^{+2.43}_{-0.00}\right) \times 10^{2}$
20	238-U LC I in Air	7.46×10^{-4}	$\left(3.84\ ^{+2326248925.84}_{-0.00}\right) \times 10^{-7}$
21	238-U LC I in BerylliumCopper	2.45×10^{3}	$\left(2.08\ ^{+25464.40}_{-25464.40}\right) \times 10^{-3}$
22	238-U LC I in Brass	1.36×10^{1}	$\left(2.15\ ^{+29167.79}_{-29167.79}\right) \times 10^{-3}$
23	238-U LC I in CopperOFHC	5.56×10^{0}	$\left(5.32\ ^{+2262325052.76}_{-0.00}\right) \times 10^{-7}$
24	238-U LC I in GermaniumNat	8.80×10^{-2}	$\left(2.68\ ^{+0.48}_{-0.00}\right) \times 10^{3}$
25	238-U LC I in MoxtekFET	7.12×10^{-3}	$\left(2.53\ ^{+0.00}_{-1.82}\right) \times 10^{3}$
26	238-U LC I in NickelSilver	9.50×10^{-1}	$\left(3.05\ ^{+2208673638.77}_{-0.00}\right) \times 10^{-7}$
27	238-U LC I in Resistor	7.45×10^{2}	$\left(4.16\ ^{+2688615051.98}_{-2688615051.98}\right) \times 10^{-7}$
28	238-U LC I in StainlessSteel304	4.38×10^{2}	$\left(3.03\ ^{+8129847899.60}_{-0.00}\right) \times 10^{-8}$
29	238-U LC I in Teflon	2.44×10^{2}	$\left(9.04\ ^{+293382.40}_{-293382.40}\right) \times 10^{-4}$
30	238-U LC I in Zeolite	2.76×10^{2}	$\left(3.52\ ^{+0.72}_{-0.71}\right) \times 10^{3}$
31	238-U LC II in Air	8.29×10^{-6}	$\left(3.32\ ^{+54121608330.53}_{-0.00}\right) \times 10^{-9}$
32	238-U LC II in BerylliumCopper	5.95×10^{1}	$\left(1.18\ ^{+1851165410.64}_{-0.00}\right) \times 10^{-7}$
33	238-U LC II in Brass	1.31×10^{2}	$\left(2.35\ ^{+486468.15}_{-0.00}\right) \times 10^{-3}$
34	238-U LC II in CopperOFHC	3.76×10^{-2}	$\left(4.60\ ^{+367127202058.58}_{-0.00}\right) \times 10^{-10}$
35	238-U LC II in GermaniumNat	1.04×10^{-1}	$\left(5.21\ ^{+1.38}_{-1.37}\right) \times 10^{2}$
36	238-U LC II in LeadAin	1.53×10^{2}	$\left(2.72\ ^{+45644838315.20}_{-0.00}\right) \times 10^{-9}$
37	238-U LC II in LeadMod	1.51×10^{2}	$\left(8.67\ ^{+2407877964.58}_{-0.00}\right) \times 10^{-7}$
38	238-U LC II in LeadPatch	5.18×10^{4}	$\left(5.27\ ^{+0.04}_{-0.04}\right) \times 10^{4}$
39	238-U LC II in MoxtekFET	1.32×10^{-4}	$\left(1.42\ ^{+0.15}_{-0.19}\right) \times 10^{3}$
40	238-U LC II in NickelSilver	1.13×10^{0}	$\left(1.44\ ^{+6507260840.12}_{-0.00}\right) \times 10^{-8}$
41	238-U LC II in Resistor	2.50×10^{1}	$\left(9.89\ ^{+763073.61}_{-763073.61}\right) \times 10^{-5}$
42	238-U LC II in RnExposureInCryostat	1.17×10^{0}	$\left(2.64\ ^{+324380211.62}_{-0.00}\right) \times 10^{-7}$
43	238-U LC II in RnExposureOutsideCryostat	4.74×10^{-2}	$\left(4.29\ ^{+2750024838693.46}_{-0.00}\right) \times 10^{-11}$
44	238-U LC II in StainlessSteel304	9.50×10^{-1}	$\left(2.64\ ^{+268966659461.17}_{-0.00}\right) \times 10^{-10}$

Table L.3: continued

	Description	Prediction	Fit Result
45	238-U LC II in Teflon	6.40×10^{0}	$\left(1.02\ ^{+404112.05}_{-0.00}\right) \times 10^{-3}$
46	238-U LC II in Tin	3.41×10^{1}	$\left(1.79\ ^{+19157942052.85}_{-0.00}\right) \times 10^{-8}$
47	238-U LC II in Zeolite	3.12×10^{-1}	$\left(5.05\ ^{+2.17}_{-2.15}\right) \times 10^{2}$
48	238-U UC in BerylliumCopper	1.08×10^{3}	$\left(2.32\ ^{+7559880348.27}_{-0.00}\right) \times 10^{-8}$
49	238-U UC in Brass	1.30×10^{0}	$\left(1.61\ ^{+15184042904.19}_{-15184042904.19}\right) \times 10^{-8}$
50	238-U UC in CopperOFHC	2.68×10^{-1}	$\left(1.84\ ^{+3432624040709.95}_{-0.00}\right) \times 10^{-11}$
51	238-U UC in GermaniumNat	9.28×10^{-2}	$\left(2.82\ ^{+0.54}_{-0.53}\right) \times 10^{3}$
52	238-U UC in MoxtekFET	6.35×10^{-4}	$\left(1.31\ ^{+0.18}_{-0.18}\right) \times 10^{3}$
53	238-U UC in NickelSilver	5.56×10^{-2}	$\left(2.94\ ^{+484711791510.01}_{-0.00}\right) \times 10^{-10}$
54	238-U UC in Resistor	1.82×10^{1}	$\left(9.69\ ^{+678987584367.27}_{-0.00}\right) \times 10^{-10}$
55	238-U UC in StainlessSteel304	1.05×10^{1}	$\left(3.85\ ^{+43324171076.63}_{-0.00}\right) \times 10^{-9}$
56	238-U UC in Teflon	2.44×10^{2}	$\left(1.31\ ^{+1367993027.88}_{-0.00}\right) \times 10^{-7}$
57	238-U UC in Zeolite	3.37×10^{0}	$\left(4.62\ ^{+5130063215.18}_{-0.00}\right) \times 10^{-8}$
58	3-H in GermaniumNat	2.50×10^{1}	$\left(8.32\ ^{+0.54}_{-1.39}\right) \times 10^{2}$
59	40-K in Brass	4.87×10^{-1}	$\left(5.80\ ^{+201.06}_{-201.06}\right) \times 10^{-1}$
60	40-K in CopperOFHC	1.16×10^{0}	$\left(5.76\ ^{+1856152732.21}_{-0.00}\right) \times 10^{-7}$
61	40-K in Resistor	2.92×10^{2}	$\left(4.24\ ^{+6.67}_{-0.00}\right) \times 10^{2}$
62	40-K in StainlessSteel304	1.42×10^{1}	$\left(1.55\ ^{+133145362927.74}_{-0.00}\right) \times 10^{-9}$
63	40-K in Teflon	6.28×10^{2}	$\left(2.03\ ^{+1760.85}_{-1760.85}\right) \times 10^{-2}$
64	40-K in Zeolite	1.08×10^{1}	$\left(9.38\ ^{+0.00}_{-6.68}\right) \times 10^{2}$
65	46-Sc in CopperOFHC	1.88×10^{0}	$\left(8.00\ ^{+72858353215.22}_{-0.00}\right) \times 10^{-9}$
66	48-V in CopperOFHC	2.68×10^{-6}	$\left(1.93\ ^{+1.58}_{-1.51}\right) \times 10^{2}$
67	54-Mn in GermaniumNat	5.55×10^{1}	$\left(1.26\ ^{+0.65}_{-0.62}\right) \times 10^{2}$
68	56-Co in CopperOFHC	7.56×10^{0}	$\left(1.82\ ^{+774551843.40}_{-0.00}\right) \times 10^{-7}$
69	57-Co in CopperOFHC	2.86×10^{2}	$\left(2.45\ ^{+164787860953.20}_{-0.00}\right) \times 10^{-10}$
70	57-Co in GermaniumNat	9.50×10^{1}	$\left(3.13\ ^{+160541148449.91}_{-0.00}\right) \times 10^{-10}$

Table L.3: continued

	Description	Prediction	Fit Result
71	58-Co in CopperOFHC	2.25×10^{1}	$\left(1.92\ ^{+1.26}_{-1.68}\right) \times 10^{2}$
72	58-Co in GermaniumNat	4.40×10^{0}	$\left(3.84\ ^{+700926.34}_{-700926.34}\right) \times 10^{-5}$
73	59-Fe in CopperOFHC	1.29×10^{1}	$\left(1.60\ ^{+1148253.23}_{-0.00}\right) \times 10^{-4}$
74	60-Co in Brass	5.66×10^{0}	$\left(7.85\ ^{+10140.07}_{-10140.07}\right) \times 10^{-3}$
75	60-Co in CopperOFHC	7.27×10^{2}	$\left(7.81\ ^{+10836.22}_{-10836.22}\right) \times 10^{-3}$
76	60-Co in GermaniumNat	4.45×10^{1}	$\left(3.95\ ^{+162034413.86}_{-162034413.86}\right) \times 10^{-6}$
77	60-Co in NickelSilver	4.24×10^{-1}	$\left(1.99\ ^{+10992.06}_{-10992.06}\right) \times 10^{-3}$
78	60-Co in Teflon	4.43×10^{2}	$\left(2.09\ ^{+1.09}_{-0.00}\right) \times 10^{2}$
79	63-Ni in GermaniumNat	2.41×10^{0}	$\left(1.60\ ^{+415507985.03}_{-0.00}\right) \times 10^{-7}$
80	65-Zn in GermaniumNat	1.80×10^{2}	$\left(1.57\ ^{+0.80}_{-0.75}\right) \times 10^{2}$
81	68-Ge in GermaniumNat	6.10×10^{2}	$\left(1.61\ ^{+48814.09}_{-48814.09}\right) \times 10^{-4}$
82	76-Ge 2vBB in GermaniumNat	3.11×10^{1}	$\left(1.22\ ^{+0.34}_{-0.00}\right) \times 10^{3}$
83	Cosmogenic muons in KURFExperimentalHall	1.15×10^{1}	$\left(1.15\ ^{+92363558.27}_{-0.00}\right) \times 10^{-6}$

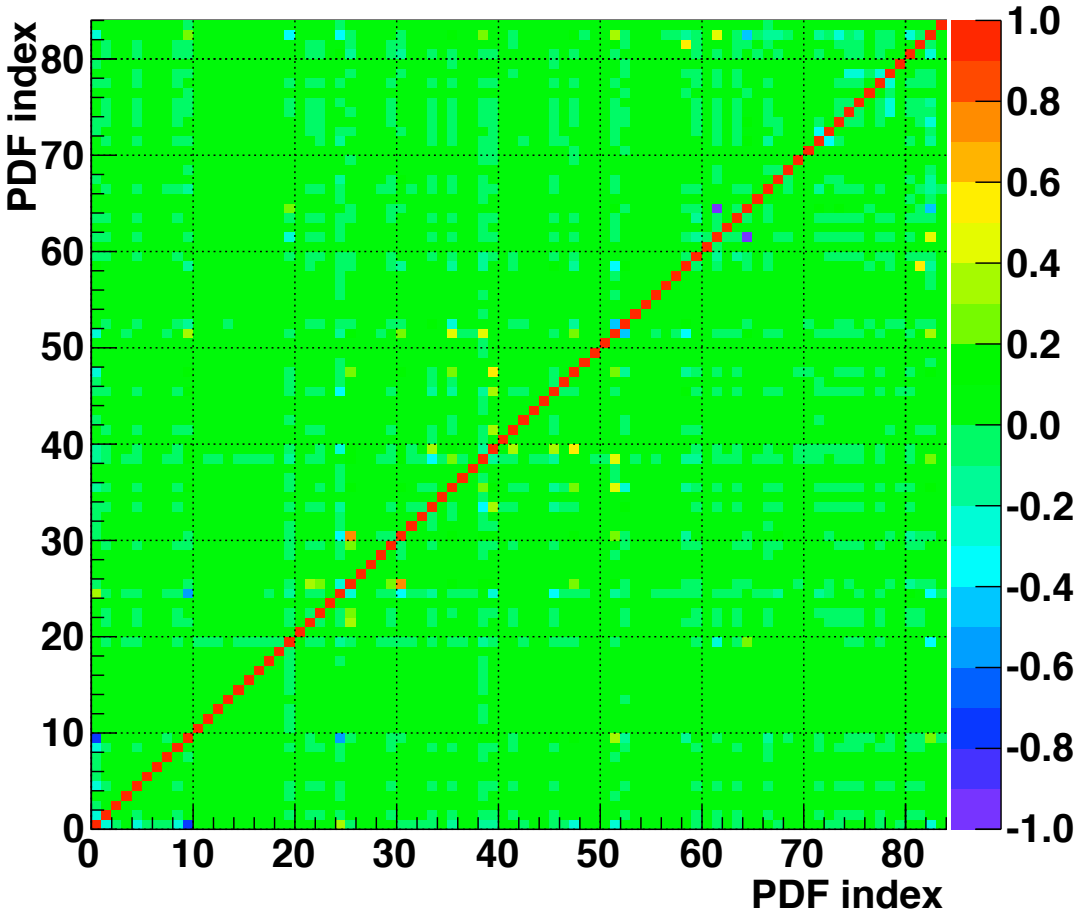

Figure L.35: Correlations between PDF pairs in Dataset II fit. This image represents the correlation coefficient matrix. It is symmetric about the diagonal. Each PDF is identified by an index listed in Table L.3.

Table L.4: Correlations between selected PDF pairs in Dataset II. The 11 pairs of PDFs for which the absolute value of the correlation coefficient is greater than 0.40 are listed.

	Description		**Description**	**Corr. coeff.**
0	232-Th LC in BerylliumCopper	9	232-Th LC in Zeolite	-0.74
9	232-Th LC in Zeolite	24	238-U LC I in GermaniumNat	-0.52
25	238-U LC I in MoxtekFET	30	238-U LC I in Zeolite	0.76
35	238-U LC II in GermaniumNat	51	238-U UC in GermaniumNat	0.48
38	238-U LC II in LeadPatch	51	238-U UC in GermaniumNat	0.40
39	238-U LC II in MoxtekFET	47	238-U LC II in Zeolite	0.50
51	238-U UC in GermaniumNat	52	238-U UC in MoxtekFET	-0.42
58	3-H in GermaniumNat	81	68-Ge in GermaniumNat	0.57
61	40-K in Resistor	64	40-K in Zeolite	-0.96
61	40-K in Resistor	82	76-Ge 2vBB in GermaniumNat	0.43
64	40-K in Zeolite	82	76-Ge 2vBB in GermaniumNat	-0.46

L.5 Dataset III fit results

Table L.5: Results from fit of background model to Dataset III energy spectrum. The fit was performed in the region from 10 to 2000 keV, using 10-keV bins. The first column of the table is an index used to identify the fit components. The third column is the number of counts expected from the predicted background energy spectrum.

	Description	**Prediction**	**Fit Result**
0	232-Th LC in BerylliumCopper	3.34×10^{2}	$\left(6.28\ ^{+18878.61}_{-18878.61}\right) \times 10^{-3}$
1	232-Th LC in Brass	1.88×10^{1}	$\left(6.09\ ^{+21570.83}_{-21570.83}\right) \times 10^{-3}$
2	232-Th LC in CopperOFHC	1.99×10^{0}	$\left(7.77\ ^{+27216.76}_{-27216.76}\right) \times 10^{-3}$
3	232-Th LC in GermaniumNat	3.90×10^{-2}	$\left(1.10\ ^{+1.05}_{-1.07}\right) \times 10^{3}$
4	232-Th LC in MoxtekFET	3.94×10^{-2}	$\left(2.86\ ^{+1851.25}_{-1851.25}\right) \times 10^{-2}$
5	232-Th LC in NickelSilver	2.00×10^{-3}	$\left(8.12\ ^{+259946.40}_{-259946.40}\right) \times 10^{-4}$
6	232-Th LC in Resistor	1.25×10^{3}	$\left(7.55\ ^{+235976.21}_{-235976.21}\right) \times 10^{-4}$
7	232-Th LC in StainlessSteel304	1.09×10^{2}	$\left(1.27\ ^{+2.36}_{-2.36}\right) \times 10^{3}$
8	232-Th LC in Teflon	2.97×10^{2}	$\left(4.42\ ^{+4.44}_{-0.00}\right) \times 10^{2}$
9	232-Th LC in Zeolite	4.07×10^{2}	$\left(9.42\ ^{+332.47}_{-332.47}\right) \times 10^{1}$
10	232-Th UC in BerylliumCopper	2.85×10^{2}	$\left(1.42\ ^{+481552.28}_{-481552.28}\right) \times 10^{-4}$
11	232-Th UC in Brass	5.74×10^{0}	$\left(1.65\ ^{+6265227.35}_{-0.00}\right) \times 10^{-4}$
12	232-Th UC in CopperOFHC	1.77×10^{0}	$\left(1.93\ ^{+56834.21}_{-56834.21}\right) \times 10^{-3}$
13	232-Th UC in GermaniumNat	5.32×10^{-2}	$\left(6.22\ ^{+14616452.03}_{-0.00}\right) \times 10^{-5}$
14	232-Th UC in MoxtekFET	3.39×10^{-2}	$\left(1.59\ ^{+488986.68}_{-488986.68}\right) \times 10^{-4}$
15	232-Th UC in NickelSilver	1.74×10^{-3}	$\left(1.18\ ^{+6183752.31}_{-0.00}\right) \times 10^{-4}$
16	232-Th UC in Resistor	1.34×10^{3}	$\left(1.09\ ^{+6026380.75}_{-0.00}\right) \times 10^{-4}$
17	232-Th UC in StainlessSteel304	9.98×10^{1}	$\left(1.34\ ^{+2.18}_{-0.00}\right) \times 10^{3}$
18	232-Th UC in Teflon	2.56×10^{2}	$\left(2.05\ ^{+53167.98}_{-53167.98}\right) \times 10^{-3}$

Table L.5: continued

	Description	Prediction	Fit Result
19	232-Th UC in Zeolite	3.55×10^{2}	$\left(8.91\ ^{+13.51}_{-13.51}\right) \times 10^{2}$
20	238-U LC I in Air	1.32×10^{-3}	$\left(5.35\ ^{+693269.05}_{-693269.05}\right) \times 10^{-4}$
21	238-U LC I in BerylliumCopper	4.33×10^{3}	$\left(1.47\ ^{+616689.10}_{-616689.10}\right) \times 10^{-4}$
22	238-U LC I in Brass	2.40×10^{1}	$\left(5.29\ ^{+662391.66}_{-662391.66}\right) \times 10^{-4}$
23	238-U LC I in CopperOFHC	9.83×10^{0}	$\left(1.37\ ^{+75815.99}_{-75815.99}\right) \times 10^{-3}$
24	238-U LC I in GermaniumNat	1.56×10^{-1}	$\left(1.42\ ^{+57350.69}_{-57350.69}\right) \times 10^{-3}$
25	238-U LC I in MoxtekFET	1.26×10^{-2}	$\left(5.42\ ^{+1.04}_{-1.04}\right) \times 10^{3}$
26	238-U LC I in NickelSilver	1.68×10^{0}	$\left(3.00\ ^{+724138.45}_{-724138.45}\right) \times 10^{-4}$
27	238-U LC I in Resistor	1.32×10^{3}	$\left(6.66\ ^{+700432.95}_{-700432.95}\right) \times 10^{-4}$
28	238-U LC I in StainlessSteel304	7.74×10^{2}	$\left(3.00\ ^{+2.10}_{-0.00}\right) \times 10^{3}$
29	238-U LC I in Teflon	4.31×10^{2}	$\left(2.60\ ^{+699117.43}_{-699117.43}\right) \times 10^{-4}$
30	238-U LC I in Zeolite	4.89×10^{2}	$\left(4.80\ ^{+612807.91}_{-612807.91}\right) \times 10^{-4}$
31	238-U LC II in Air	1.46×10^{-5}	$\left(1.20\ ^{+2.48}_{-0.00}\right) \times 10^{2}$
32	238-U LC II in BerylliumCopper	1.05×10^{2}	$\left(1.36\ ^{+35359.80}_{-35359.80}\right) \times 10^{-3}$
33	238-U LC II in Brass	2.31×10^{2}	$\left(3.36\ ^{+1.94}_{-0.00}\right) \times 10^{2}$
34	238-U LC II in CopperOFHC	6.64×10^{-2}	$\left(9.68\ ^{+362640.97}_{-362640.97}\right) \times 10^{-4}$
35	238-U LC II in GermaniumNat	1.83×10^{-1}	$\left(6.66\ ^{+10.13}_{-0.00}\right) \times 10^{1}$
36	238-U LC II in LeadAin	2.69×10^{2}	$\left(4.46\ ^{+2.31}_{-2.31}\right) \times 10^{3}$
37	238-U LC II in LeadMod	2.66×10^{2}	$\left(4.54\ ^{+0.87}_{-0.87}\right) \times 10^{3}$
38	238-U LC II in MoxtekFET	2.33×10^{-4}	$\left(7.64\ ^{+4887140378.61}_{-4887140378.61}\right) \times 10^{-9}$
39	238-U LC II in NickelSilver	2.00×10^{0}	$\left(4.06\ ^{+211615.56}_{-211615.56}\right) \times 10^{-4}$
40	238-U LC II in Resistor	4.41×10^{1}	$\left(1.01\ ^{+52482783.28}_{-52482783.28}\right) \times 10^{-7}$
41	238-U LC II in RnExposureInCryostat	2.07×10^{0}	$\left(2.17\ ^{+8082498.27}_{-0.00}\right) \times 10^{-5}$
42	238-U LC II in RnExposureOutsideCryostat	8.37×10^{-2}	$\left(4.09\ ^{+6.39}_{-0.00}\right) \times 10^{2}$
43	238-U LC II in StainlessSteel304	1.68×10^{0}	$\left(3.54\ ^{+52582218.13}_{-0.00}\right) \times 10^{-5}$
44	238-U LC II in Teflon	1.13×10^{1}	$\left(5.34\ ^{+2288814.18}_{-2288814.18}\right) \times 10^{-5}$

Table L.5: continued

	Description	Prediction	Fit Result
45	238-U LC II in Tin	6.02×10^{1}	$\left(2.13 \, ^{+618804.37}_{-618804.37}\right) \times 10^{-4}$
46	238-U LC II in Zeolite	5.51×10^{-1}	$\left(2.35 \, ^{+5364496304.02}_{-0.00}\right) \times 10^{-8}$
47	238-U UC in BerylliumCopper	1.91×10^{3}	$\left(5.23 \, ^{+215713.59}_{-215713.59}\right) \times 10^{-4}$
48	238-U UC in Brass	2.30×10^{0}	$\left(5.99 \, ^{+6.60}_{-6.60}\right) \times 10^{2}$
49	238-U UC in CopperOFHC	4.72×10^{-1}	$\left(6.48 \, ^{+7.38}_{-7.38}\right) \times 10^{2}$
50	238-U UC in GermaniumNat	1.64×10^{-1}	$\left(1.28 \, ^{+0.56}_{-0.00}\right) \times 10^{3}$
51	238-U UC in MoxtekFET	1.12×10^{-3}	$\left(9.48 \, ^{+10504395.88}_{-10504395.88}\right) \times 10^{-6}$
52	238-U UC in NickelSilver	9.81×10^{-2}	$\left(2.79 \, ^{+19812.71}_{-19812.71}\right) \times 10^{-3}$
53	238-U UC in Resistor	3.21×10^{1}	$\left(5.06 \, ^{+1363879.08}_{-1363879.08}\right) \times 10^{-5}$
54	238-U UC in StainlessSteel304	1.85×10^{1}	$\left(1.89 \, ^{+11.13}_{-11.13}\right) \times 10^{2}$
55	238-U UC in Teflon	4.31×10^{2}	$\left(6.78 \, ^{+2368362.11}_{-2368362.11}\right) \times 10^{-5}$
56	238-U UC in Zeolite	5.96×10^{0}	$\left(2.36 \, ^{+16739.86}_{-16739.86}\right) \times 10^{-3}$
57	3-H in GermaniumNat	4.21×10^{1}	$\left(6.15 \, ^{+5.97}_{-0.00}\right) \times 10^{2}$
58	40-K in Brass	8.62×10^{-1}	$\left(1.57 \, ^{+0.23}_{-0.00}\right) \times 10^{3}$
59	40-K in CopperOFHC	2.04×10^{0}	$\left(4.42 \, ^{+295287.21}_{-295287.21}\right) \times 10^{-4}$
60	40-K in Resistor	5.17×10^{2}	$\left(5.59 \, ^{+2466093.59}_{-2466093.59}\right) \times 10^{-5}$
61	40-K in StainlessSteel304	2.52×10^{1}	$\left(1.05 \, ^{+54317.16}_{-54317.16}\right) \times 10^{-3}$
62	40-K in Teflon	1.11×10^{3}	$\left(1.12 \, ^{+38947.74}_{-38947.74}\right) \times 10^{-3}$
63	40-K in Zeolite	1.91×10^{1}	$\left(4.89 \, ^{+2170964722.21}_{-0.00}\right) \times 10^{-7}$
64	46-Sc in CopperOFHC	1.44×10^{0}	$\left(1.35 \, ^{+2.07}_{-0.00}\right) \times 10^{2}$
65	48-V in CopperOFHC	3.15×10^{0}	$\left(1.03 \, ^{+182034.16}_{-0.00}\right) \times 10^{-3}$
66	54-Mn in GermaniumNat	4.84×10^{1}	$\left(4.78 \, ^{+9.82}_{-0.00}\right) \times 10^{1}$
67	56-Co in CopperOFHC	7.45×10^{0}	$\left(4.62 \, ^{+2.96}_{-3.00}\right) \times 10^{2}$
68	57-Co in CopperOFHC	2.26×10^{2}	$\left(1.81 \, ^{+0.53}_{-0.00}\right) \times 10^{2}$
69	57-Co in GermaniumNat	7.49×10^{1}	$\left(9.51 \, ^{+39570927.32}_{-0.00}\right) \times 10^{-6}$
70	58-Co in CopperOFHC	3.05×10^{1}	$\left(1.17 \, ^{+1.35}_{-1.35}\right) \times 10^{2}$

Table L.5: continued

	Description	Prediction	Fit Result
71	58-Co in GermaniumNat	5.98×10^{0}	$\left(2.07\ ^{+483689438.63}_{-483689438.63}\right) \times 10^{-7}$
72	59-Fe in CopperOFHC	2.27×10^{1}	$\left(3.21\ ^{+18.49}_{-18.49}\right) \times 10^{0}$
73	60-Co in Brass	1.00×10^{1}	$\left(3.05\ ^{+1750230.52}_{-1750230.52}\right) \times 10^{-5}$
74	60-Co in CopperOFHC	1.15×10^{3}	$\left(2.84\ ^{+19668657.08}_{-19668657.08}\right) \times 10^{-6}$
75	60-Co in GermaniumNat	7.00×10^{1}	$\left(9.91\ ^{+8.58}_{-8.53}\right) \times 10^{2}$
76	60-Co in NickelSilver	6.68×10^{-1}	$\left(2.69\ ^{+1.43}_{-0.00}\right) \times 10^{2}$
77	60-Co in Teflon	7.84×10^{2}	$\left(6.68\ ^{+17187.91}_{-17187.91}\right) \times 10^{-3}$
78	63-Ni in GermaniumNat	4.23×10^{0}	$\left(1.27\ ^{+13594754.79}_{-13594754.79}\right) \times 10^{-5}$
79	65-Zn in GermaniumNat	1.31×10^{2}	$\left(2.12\ ^{+0.00}_{-1.00}\right) \times 10^{2}$
80	68-Ge in GermaniumNat	4.83×10^{2}	$\left(1.80\ ^{+1.10}_{-1.11}\right) \times 10^{3}$
81	69-Ge in GermaniumNat	7.35×10^{0}	$\left(3.30\ ^{+20009280.32}_{-20009280.32}\right) \times 10^{-5}$
82	71-Ge in GermaniumNat	1.28×10^{2}	$\left(7.51\ ^{+40956.42}_{-40956.42}\right) \times 10^{-4}$
83	76-Ge 2vBB in GermaniumNat	5.51×10^{1}	$\left(1.92\ ^{+0.39}_{-0.40}\right) \times 10^{3}$
84	Cosmogenic muons in KURFExperimentalHall	2.04×10^{1}	$\left(7.79\ ^{+8.22}_{-8.22}\right) \times 10^{2}$

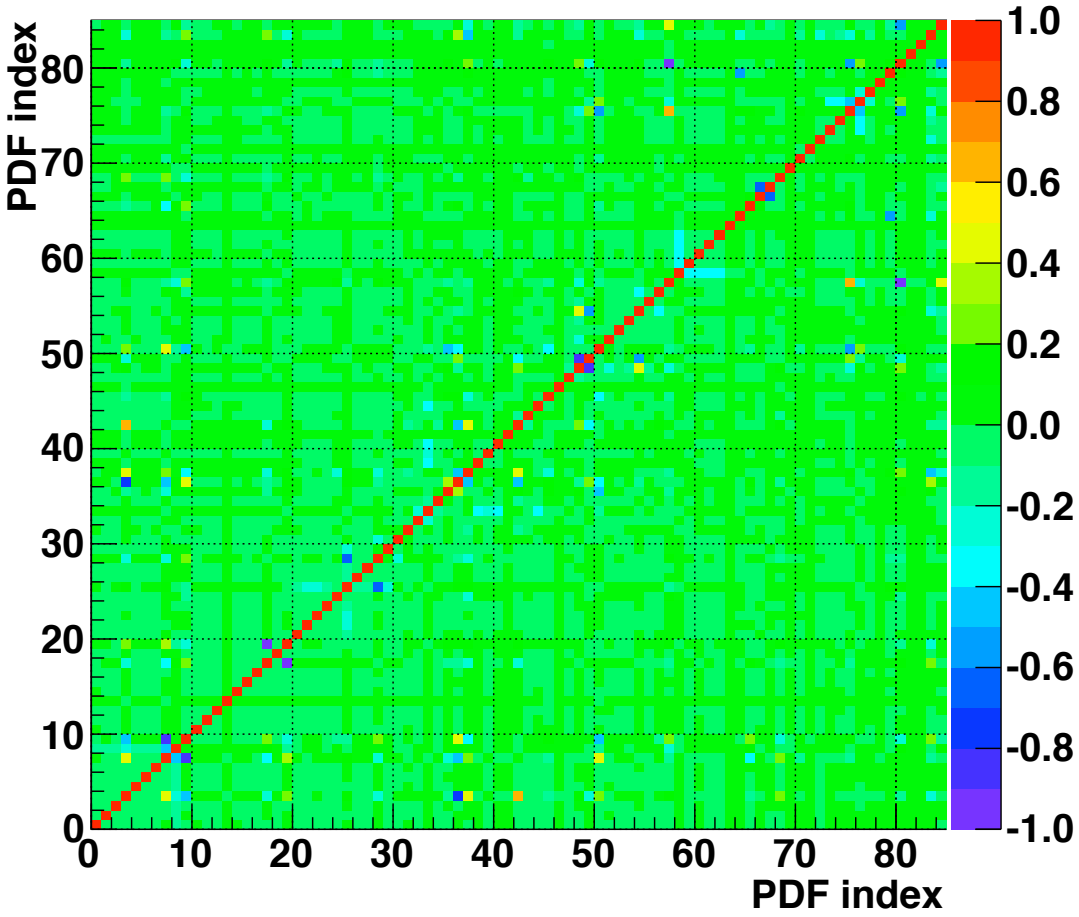

Figure L.36: Correlations between PDF pairs in Dataset III fit. This image represents the correlation coefficient matrix. It is symmetric about the diagonal. Each PDF is identified by an index listed in Table L.5.

Table L.6: Correlations between selected PDF pairs in Dataset III. The 30 pairs of PDFs for which the absolute value of the correlation coefficient is greater than 0.40 are listed.

	Description		**Description**	**Corr. coeff.**
3	232-Th LC in GermaniumNat	7	232-Th LC in StainlessSteel304	0.48
3	232-Th LC in GermaniumNat	9	232-Th LC in Zeolite	-0.43
3	232-Th LC in GermaniumNat	36	238-U LC II in LeadAin	-0.74
3	232-Th LC in GermaniumNat	37	238-U LC II in LeadMod	0.47
3	232-Th LC in GermaniumNat	42	238-U LC II in RnExposureOutsideCryostat	0.62
7	232-Th LC in StainlessSteel304	8	232-Th LC in Teflon	-0.41
7	232-Th LC in StainlessSteel304	9	232-Th LC in Zeolite	-0.86
7	232-Th LC in StainlessSteel304	36	238-U LC II in LeadAin	-0.46
7	232-Th LC in StainlessSteel304	50	238-U UC in GermaniumNat	0.48
9	232-Th LC in Zeolite	36	238-U LC II in LeadAin	0.42
9	232-Th LC in Zeolite	50	238-U UC in GermaniumNat	-0.44
17	232-Th UC in StainlessSteel304	19	232-Th UC in Zeolite	-0.92
25	238-U LC I in MoxtekFET	28	238-U LC I in StainlessSteel304	-0.67
35	238-U LC II in GermaniumNat	50	238-U UC in GermaniumNat	-0.41
36	238-U LC II in LeadAin	37	238-U LC II in LeadMod	-0.42
36	238-U LC II in LeadAin	42	238-U LC II in RnExposureOutsideCryostat	-0.47
37	238-U LC II in LeadMod	42	238-U LC II in RnExposureOutsideCryostat	0.45
37	238-U LC II in LeadMod	83	76-Ge 2vBB in GermaniumNat	-0.44
48	238-U UC in Brass	49	238-U UC in CopperOFHC	-0.85
48	238-U UC in Brass	54	238-U UC in StainlessSteel304	0.42
49	238-U UC in CopperOFHC	54	238-U UC in StainlessSteel304	-0.55
50	238-U UC in GermaniumNat	75	60-Co in GermaniumNat	-0.55
57	3-H in GermaniumNat	75	60-Co in GermaniumNat	0.62
57	3-H in GermaniumNat	80	68-Ge in GermaniumNat	-0.98
57	3-H in GermaniumNat	84	Cosmogenic muons in KURFExperimentalHall	0.42
64	46-Sc in CopperOFHC	79	65-Zn in GermaniumNat	-0.51
66	54-Mn in GermaniumNat	67	56-Co in CopperOFHC	-0.68
75	60-Co in GermaniumNat	76	60-Co in NickelSilver	-0.41
75	60-Co in GermaniumNat	80	68-Ge in GermaniumNat	-0.59
80	68-Ge in GermaniumNat	84	Cosmogenic muons in KURFExperimentalHall	-0.57